

A weakest-link based constant-life diagram for the probabilistic high-cycle fatigue assessment of notched metallic components

vom Fachbereich Maschinenbau und Verfahrenstechnik
der Technischen Universität Kaiserslautern
zur Verleihung des akademischen Grades
Doktor-Ingenieur (Dr.-Ing.)
genehmigte

Dissertation

Mark Alexander Klawonn, M.Sc.

Kaiserslautern, 2021

- D 386 -

Datum der Disputation: 20. Mai 2021
Dekan des Fachbereichs: Prof. Dr.-Ing. Tilmann Beck
Vorsitz der Kommission: Prof. Dr.-Ing. Ralf Müller
Erster Berichterstatter: Prof. Dr.-Ing. Tilmann Beck
Zweiter Berichterstatter: Prof. Dr. Hanno Gottschalk

Kurzfassung

Das Thema dieser Arbeit ist die probabilistische Bewertung der Betriebssicherheit von gekerbten metallischen Bauteilen unter periodischen Lasten mit konstanter Amplitude im Hinblick auf das Versagen durch hochzyklische Ermüdung. Letztgenanntes bezieht sich auf die Rissinitiierung im betrachteten Bauteil, welche von einer hohen Anzahl, üblicherweise mehreren Millionen, von Lastzyklen hervorgerufen wird, die sich durch eine, im Vergleich zur statischen Belastungsgrenze des Materials, kleine Amplitude auszeichnen.

Um die Versagenswahrscheinlichkeit aufgrund von hochzyklischer Ermüdung für ein spezifisches Bauteil unter gegebener Belastung bewerten zu können, wird ein neues empirisches Modell basierend auf der sogenannten weakest-link Theorie entwickelt, welches ein probabilistisches und Bauteil-spezifisches Festigkeitsschaubild für die angestrebte Auslegungslbensdauer beschreibt. Das konventionelle, nicht-probabilistische Festigkeitsschaubild beschreibt eine diskrete Auslegungsgrenze bezüglich Mittel- und Amplitudenspannung, welche üblicherweise auf Testergebnissen mit ungekerbten Prüfkörpern des betrachteten Materials basiert. Seine Anwendung auf die Auslegung von gekerbten Bauteilen wird dadurch realisiert, dass der Spannungszustand an der höchstbelasteten Stelle des Bauteils mit jenem identifiziert wird, welche in den ungekerbten Testproben der Ermüdungstests gewirkt haben. Unter dieser Annahme werden die kritischen Spannungen des Bauteils mit der Auslegungsgrenze des klassischen Festigkeitsschaubilds verglichen. Einflüsse, die auf diese Weise unberücksichtigt bleiben, wie etwa Kerbeinfluss und der statistische Größeneffekt, müssen durch entsprechende Korrekturfaktoren einbezogen werden. Das vorgeschlagene probabilistische Festigkeitsschaubild auf der anderen Seite beschreibt ein kontinuierliches Feld von Versagenswahrscheinlichkeiten im Raum der Entwurfsspannungen, wobei nicht nur die Spannungen an der kritischen Stelle des Bauteils berücksichtigt werden, sondern das gesamte zyklische Spannungsfeld. Auf diese Weise berücksichtigt die vorgeschlagene Methode unmittelbar Kerbeinfluss und statistischen Größeneffekt. Ermöglicht wird diese erweiterte Beschreibung durch den weakest-link Ansatz, welcher ein nicht-lokales stochastisches Modell zur Berechnung der Versagenswahrscheinlichkeit von belasteten Festkörpern darstellt. Die vier Modellparameter können basierend auf Fatigue Testdatensätzen mit völlig unzusammenhängenden Tests über beliebige Prüfkörpergeometrien kalibriert werden, womit das Verfahren unabhängig von der Verfügbarkeit von Testdaten gemäß Treppenstufen- oder Probit-Systematiken ist.

In dieser Arbeit ist die Formulierung, Analyse, Validierung sowie die Anwendung dieses Modells beschrieben. Nachdem es eingeführt und mit bestehenden Ansätzen verglichen wird, folgt seine Analyse im Hinblick auf die numerischen Eigenschaften bei Anwendung auf Finite Elemente Modelle, seine effiziente Kalibrierung sowie die resultierende Modellunsicherheit. Die Validierung wiederum ist in zwei Teilen dargestellt. Zunächst wird das Modell an Testdaten gefittet, welche mehrere gekerbte Prüfkörpertypen umfassen, und vorrangig elastisches Materialverhalten abbilden. In einem zweiten Schritt wird diese Einschränkung aufgehoben und das Modell wird zur Vorhersage des Versagens von Prüfkörpern verwendet, welche durch hohe Mittelspannungen hervorgerufene Kerbgrundplastifizierung erfahren. In beiden Fällen korrespondieren die Modellvorhersagen zum größten Teil mit der experimentell beobachteten Versagensstatistik der untersuchten Proben. Schlussendlich wird die Anwendbarkeit der vorgeschlagenen probabilistischen Methodik im Rahmen der Bauteilauslegung anhand des Beispiels eines Gasturbinen Kompressorblattes und der dazugehörigen Kompressorstufe demonstriert.

Abstract

The subject of this thesis is the probabilistic reliability assessment of notched metallic components under periodic constant-amplitude loads with respect to the failure mode of high-cycle fatigue. The latter refers to the crack initiation within the considered component caused by a high number, typically millions, of load cycles characterized by their small magnitude in terms of the material's static strength.

In order to estimate the probability of failure due to high-cycle fatigue for a specified component under given loads, a new empirical model based on weakest-link theory is developed which describes a probabilistic and component specific constant-life diagram with respect to the anticipated design life. A conventional, non-probabilistic constant-life diagram reflects a discrete design boundary in terms of mean stress and stress amplitude, typically based on test results with respect to unnotched coupons made from the material of interest. Its application to the design of a notched component is established by identifying the stress conditions at the component's hot spot with those acting in the smooth coupons during the tests, and comparing those hot-spot conditions with the design boundary described in the constant-life diagram. Disregarded influences, such as notch and statistical size effect have to be incorporated by respective correction factors. The proposed probabilistic model on the other hand describes a continuous field of failure probabilities in the design stress plane, taking into account not only the hot-spot stresses, but the entire cyclic stress field acting throughout the component. In this way, the methodology directly accounts for notch and statistical size effects. Responsible for providing this greater scope is the weakest-link concept, which represents a non-local stochastic approach for quantifying the failure probability of loaded solids. The four model parameters can be calibrated with fatigue test data sets containing entirely unrelated test results on arbitrary specimen geometries, obliterating the constraining need for test data following staircase or probit schemes.

This work contains the formulation, analysis, validation and application of the proposed model. After its introduction and a comparison with existing methods, it is analyzed in terms of its numerical properties when applied to finite element models, its efficient calibration and the corresponding model uncertainty. The validation is split into two parts. In a first analysis, the model is fitted to test data, containing results on several types of notched specimens, reflecting predominantly elastic material behavior. In a second step, this restriction is lifted and the model is used in order to predict the failure behavior of notched test specimens experiencing notch root plasticity due to high mean stresses. In both validation studies, the derived model predictions are, for the most part, well in line with the experimentally observed failure behavior of the test specimens. Finally, the applicability of the proposed probabilistic methodology in a design context is demonstrated on the example of a gas turbine compressor blade and the corresponding compressor stage.

Acknowledgment

This thesis is the result of my work at Siemens (Energy)¹ in Mülheim an der Ruhr from March 2018 until May 2021 under the academic guidance of Prof. Tilmann Beck from the Institute of Materials Science and Engineering at TU Kaiserslautern.

I am grateful for having been given the opportunity to do this work. The corresponding financial support by Siemens (Energy) AG is very much acknowledged. In this context, I want to thank Dr. Antje Hagenacker, my Siemens-internal supervisor, and Dr. Georg Rollmann, the lead of the Probabilistic Analytics team at Siemens Energy, for putting their trust in me, when they hired me for the position associated with this project.

Moreover, I want to express my sincere gratitude to Prof. Tilmann Beck for his continuous support in form of frequent discussions, valuable feedback on the current status of the project, and a collaborative atmosphere in the spirit of an open door policy. Due to our exchanges, I always felt certain to be standing on solid academic ground, which gave me the necessary confidence to experiment with new approaches. After the first version of the dissertation was finished, he also helped me in navigating the submission process and made sure that I was able to defend my thesis quickly afterwards. Thank you Prof. Beck for all your help!

I also want to thank Prof. Hanno Gottschalk from Bergische Universität Wuppertal, for assuming the role of the second assessor, and for his quick compilation of the assessment of this thesis. A big thank you also to Prof. Ralf Müller from TU Kaiserslautern for agreeing to act as the chairman in the defense of this thesis.

At Siemens, I was lucky to work in a team of great scientists and engineers, who helped me to gain a deeper understanding in both the different fatigue phenomena in metal components, as well as their assessment in probabilistic terms. In this context, I want to emphasize the professional discussions with Dr. Christian Amann, Dr. Dirk Kulawinski, Björn Sjödin, Dr. Florian Hiss, Dr. Sebastian Schmitz and (soon to be) Dr. Lucas Mäde. I very much enjoyed the working atmosphere in our team, and want to thank all my team members for contributing to this environment. In particular I want to thank my supervisor Dr. Antje Hagenacker, who made sure I had a good start at Siemens, by personally introducing me to a lot of helpful colleagues outside of our team, discussing the existing work in the field of high-cycle fatigue, and generally showing me the ropes around various processes and tools within the company. Thank you Antje!

Last but not least, I want to thank my parents Manfred and Ulrike, my brother Felix, my sister Ines, all of my friends and of course my lovely girlfriend Galit Goldstein for their spoken and unspoken encouragements during the last three years. Your support was particularly valuable for me since most of the writing part took place during the dreadful Corona-year 2020. You all helped me in keeping my spirits up and in mustering the necessary motivation to finish this work. Thank you!

Essen, May 2021
Alexander Klawonn

¹While I started this project as an employee of the Siemens AG, it was finished within the Siemens Energy AG after Siemens' energy division was encapsulated in an independent company.

Contents

1	Introduction	1
2	State of knowledge	6
2.1	Vibratory loads on axial-flow compressor blades	6
2.2	Fundamentals of cyclic stress fields	10
2.3	High-cycle fatigue of metals from a material perspective	14
2.4	The fatigue strength of an engineering component	18
2.5	Standard lifing diagrams in high-cycle fatigue	21
2.6	Fatigue strength testing	23
2.7	Deterministic vs. probabilistic design approaches	30
2.8	Current approaches to design against high-cycle fatigue	32
2.8.1	Local methods	32
2.8.2	Non-local methods	35
2.8.3	Weakest-link approach	37
3	Scope of work	42
4	Experimental data	43
4.1	SAE-4130	43
4.2	AL2024-T3	45
4.3	AL7075-T6	47
4.4	PH12-10Mo	48
5	Model development	50
5.1	Model formulation and fit	50
5.1.1	Probabilistic unit Haigh diagram	50
5.1.2	Probabilistic design Haigh diagram	52
5.1.3	Fitting strategy	55
5.2	Model discussion	57
5.2.1	Comparison with other approaches	57
5.2.2	On the equivalent stress models	59
5.2.3	On the integration domain	63
5.2.4	Model scope and limits	64
5.3	Numerical aspects	65
5.3.1	Quadrature rule	66
5.3.2	On the quadrature error	67
5.3.3	On the role of the mesh resolution	74
5.3.4	Summary and conclusion	80
5.4	Model fits assuming elastic material behavior	81
5.4.1	Used test data	81
5.4.2	Finite element models	83
5.4.3	Evaluation method	84
5.4.4	Results	85
5.4.5	Discussion	90
5.4.6	Summary and conclusion	92

5.5	On the selection of test data for the model fit	93
5.5.1	True model definition	93
5.5.2	Statistical analyses	95
5.5.3	Results	99
5.5.4	Discussion	103
5.5.5	Summary and conclusion	106
5.6	Model fits accounting for high mean stress plasticity	107
5.6.1	Material and test data	108
5.6.2	Finite element models	110
5.6.3	Evaluation method	112
5.6.4	Results and discussion	114
5.6.5	Summary and conclusion	123
5.7	On the model uncertainty	124
5.7.1	Model fit	125
5.7.2	General approach	128
5.7.3	Parametric bootstrapping	130
5.7.4	Markov chain Monte Carlo	133
5.7.5	Discussion	135
5.7.6	Summary and conclusion	136
6	Application	137
6.1	Probabilistic design of a compressor blade	137
6.2	Probabilistic assessment of a compressor stage	143
7	Summary and conclusion	145
8	References	148
	List of Figures	162
	List of Tables	167
	The author	169

Nomenclature

The following composition contains many, but not all symbols that appear in this work. Not included are those expressions which have a rather limited scope of use – for example symbols that are merely used over one paragraph and do not reoccur afterwards. In such cases, the respective definition is given locally. All other expressions that are repeatedly used throughout the text are compiled below. Note however, that not all variations of a given symbol with respect to its subscripts and superscript are listed. For easier orientation, the expressions are categorized with respect to the context they appear in.

Stress related expressions

$\boldsymbol{\sigma}, \boldsymbol{\sigma}(\mathbf{x}, t)$	Spatio-temporal Cauchy stress tensor function and its evaluation at location \mathbf{x} and point in time t , cf. Eq. (2.1). Sometimes, in order to prevent overloaded notation, the arguments of $\boldsymbol{\sigma}(\mathbf{x}, t)$ are omitted.
$\boldsymbol{\sigma}(\mathbf{x}, [0, T])$	Cauchy stress tensor at location \mathbf{x} as a function of time $t \in [0, T]$ assuming T -periodicity for each component, cf. Eq. (2.2).
$\boldsymbol{\sigma}_m, \boldsymbol{\sigma}_m(\mathbf{x})$	Mean stress tensor with respect to a given load cycle over $t \in [0, T]$, cf. Eq. (2.6) in the sense of Eq. (2.4) and its evaluation at location \mathbf{x} .
$\boldsymbol{\sigma}_a, \boldsymbol{\sigma}_a(\mathbf{x})$	Stress amplitude tensor with respect to a load cycle over $t \in [0, T]$, cf. Eq. (2.7) in the sense of Eq. (2.5) and its evaluation at location \mathbf{x} .
$\sigma, \sigma(\mathbf{x}, t)$	Spatio-temporal, scalar-valued (as opposed to tensor-valued) stress function and its evaluation at location \mathbf{x} and point in time t . In cases where the function σ is constant over space and time, it is identified with that constant as a scalar stress value.
$\sigma_m, \sigma_m(\mathbf{x})$	Spatial, scalar-valued mean stress function and its evaluation at location \mathbf{x} . Note that this notation does not specify how the mean stress is derived from $\boldsymbol{\sigma}(\mathbf{x}, [0, T])$.
$\sigma_a, \sigma_a(\mathbf{x})$	Spatial, scalar-valued stress amplitude function and its evaluation at location \mathbf{x} . Note that this notation does not specify how the stress amplitude is derived from $\boldsymbol{\sigma}(\mathbf{x}, [0, T])$.
$\sigma^{\text{vM}}, \sigma^{\text{vM}}(\boldsymbol{\sigma})$	Von Mises stress function and its evaluation for a given stress tensor $\boldsymbol{\sigma} = \boldsymbol{\sigma}(\mathbf{x}, t)$, cf. Eq. (2.11). In the latter case one will often find the compressed notation $\sigma^{\text{vM}}(\mathbf{x}, t) := \sigma^{\text{vM}}(\boldsymbol{\sigma}(\mathbf{x}, t))$.
$\sigma^{\text{mP}}, \sigma^{\text{mP}}(\boldsymbol{\sigma})$	Maximum or first principal stress function and its evaluation for a given stress tensor $\boldsymbol{\sigma} = \boldsymbol{\sigma}(\mathbf{x}, t)$, cf. Eq. (2.14).
$\sigma^{\text{oct}}, \sigma^{\text{oct}}(\boldsymbol{\sigma})$	Octahedral normal stress function and its evaluation for a given stress tensor $\boldsymbol{\sigma} = \boldsymbol{\sigma}(\mathbf{x}, t)$, cf. Eq. (2.12).
$\sigma^{\text{h}}, \sigma^{\text{h}}(\boldsymbol{\sigma})$	Hydrostatic stress function (identical with octahedral normal stress function σ^{oct}) and its evaluation for a given stress tensor $\boldsymbol{\sigma} = \boldsymbol{\sigma}(\mathbf{x}, t)$, cf. Eq. (2.12) and the elaborations below.
$I_1(\boldsymbol{\sigma}), I_2(\boldsymbol{\sigma})$	First and second invariant of a given stress tensor $\boldsymbol{\sigma} = \boldsymbol{\sigma}(\mathbf{x}, t)$, as defined in Eqs. (2.8) and (2.9).
$J_2(\boldsymbol{\sigma})$	Second invariant of the stress tensor deviator of $\boldsymbol{\sigma} = \boldsymbol{\sigma}(\mathbf{x}, t)$, as defined in Eq. (2.10).

$\sigma_n, \sigma_n(\boldsymbol{\sigma}, \mathbf{n})$	Normal stress function and its evaluation with respect to a given stress tensor $\boldsymbol{\sigma} = \boldsymbol{\sigma}(\mathbf{x}, t)$ and a normal vector \mathbf{n} , cf. Eq. (2.15).
$\sigma^{\text{eq}},$ $\sigma^{\text{eq}}(\boldsymbol{\sigma}(\mathbf{x}, [0, T]))$	Equivalent stress function and its evaluation for a considered load cycle at location \mathbf{x} , cf. Eq. (2.20).
$\sigma_m^{\text{eq}}, \sigma_a^{\text{eq}}, \sigma_{a,m}^{\text{eq}}$	Equivalent stress functions with respect to the mean stress and stress amplitude separately, see the examples in Eqs. (2.21) and (2.22), or for the mean stress corrected stress amplitude, compare with the example in Eq. (2.23).
σ^{eff}	Not further specified effective stress function.
$\sigma_m^{\text{nom}}, \sigma_a^{\text{nom}}$	Nominal mean stress and nominal stress amplitude.
$\sigma_m^{1,\text{nom}}, \sigma_a^{1,\text{nom}}$	Mean stress and stress amplitude field, normalized with the respective nominal stresses, cf. Eq. (5.12).
$\sigma_m^{\text{crit}}, \sigma_a^{\text{crit}}$	Mean stress and stress amplitude at the component's critical location. Also referred to as hot-spot stresses.
$\sigma_m^{1,\text{crit}}, \sigma_a^{1,\text{crit}}$	Mean stress and stress amplitude field, normalized with the respective hot-spot stresses, cf. Eq. (5.8).
$\sigma_m^{\text{notch}}, \sigma_a^{\text{notch}}$	Similar to σ_m^{crit} and σ_a^{crit} assuming the critical location is located in a specified notch of the considered structure.
$\sigma_{a,P_f}^{\text{crit}}$	Hot-spot stress amplitude that corresponds to the component's failure probability of P_f , cf. Eq. (5.11).
$\sigma_e, \sigma_e(\sigma_m)$	Fatigue strength function and its evaluation at σ_m , cf. Eq. (5.2).
$\hat{\sigma}_e, \hat{\sigma}_m$	Parameters of unit Haigh diagram denoting the two axis intercepts of the scale function, cf. Eq. (5.2) and Fig. 5.1. Note that $\hat{\sigma}_e$ is also used in the context of other general mean stress models.
$\sigma_{\text{th}}, \sigma_e^{\text{th}}$	Threshold stress parameter, see for example Eq. (2.55).
$\sigma_I, \sigma_{II}, \sigma_{III}$	Principal stresses of stress tensor with $\sigma_I > \sigma_{II} > \sigma_{III}$.
$\sigma_{\text{YS}}, \sigma_{\text{UTS}}$	Yield strength and ultimate tensile strength of a given material.
K_t, K_f	Elastic stress concentration factor with respect to the von Mises stress model, and notch fatigue factor, cf. Eq. (2.24).
$R, R(\mathbf{x})$	Nominal stress ratio, local stress ratio at location \mathbf{x} , cf. Eq. (2.17).

Geometry related expressions

C, G	Identifier of a structural component or test specimen geometry.
$\mathbf{n}, \Delta_{\mathbf{n}}$	Normal vector and cutting plane normal to \mathbf{n} .
Ω	Some subset of Ω_C , that is $\Omega \subseteq \Omega_C$.
Ω_C	Not further specified domain of component C . This domain might be the component's volume, surface or subdomains thereof.
Ω_1	Not further specified unit domain of a weakest-link model.
$\text{vol}(\Omega)$	General volume of Ω (volume or surface).
V_C, A_C	Volume or surface domain of the considered component C .
V_1, A_1	Unit volume and unit surface of a weakest-link model respectively.
\mathbf{x}	Spatial point on the considered component V_C .
\mathbf{x}_{crit}	Critical location on the considered component V_C , cf. Eq. (2.34).

Probability related expressions

α	Probability of accepting a proposed sample in the Metropolis-Hastings algorithm, cf. Eq. (5.75).
$\mathcal{B}(p)$	Bernoulli distribution with respect to probability p .
$F(x \theta)$	Parametric cumulative distribution function, given the parameters in model vector θ , evaluated at x .
$F_{\mathcal{W}}$	Cumulative distribution function of Weibull distribution.
$\ell(\theta), \mathcal{L}(\theta)$	Likelihood and log-likelihood function evaluated at model vector θ .
$\mathcal{N}(\mu, \text{sd})$	Normal distribution with location μ and standard deviation sd .
$P(A)$	Probability of event A .
P_f	Probability of failure.
P_f^1	Probability of failure for a considered unit domain in the framework of a weakest-link model, cf. Eqs. (2.55), (5.5), (5.18) and (5.19).
P_s	Probability of survival, probability of non-failure.
p, q	General notation for probabilities with $q = 1 - p$.
p^*	Probability used for the definition of the model uncertainty adjustment of the unit Haigh diagram, cf. Eq. (5.67).
Q_p	Empirical quantile function with respect to probability p , cf. Eq. (5.63).
\mathcal{U}_a^b	Uniform distribution over the interval $[a, b]$.
$\mathcal{W}(\lambda, k)$	Weibull distribution with scale λ and shape k .
X, Y	General notation for random variables.
X_e^{crit}	Random variable of the component's fatigue strength with respect to the hot-spot stress amplitude, cf. Eq. (5.10).
X_e^{nom}	Random variable of the component's fatigue strength with respect to the nominal stress amplitude, analogous to Eq. (5.10).

Expressions in numerical analyses

E	Absolute quadrature error between I and Q , cf. Eq. (5.24).
ε	Relative error, see for example Eq. (5.28).
I	Weakest-link integral, defined in Eq. (5.24).
\tilde{P}_f, \tilde{P}_s	Approximation of P_f and P_s respectively.
Φ	Transformation between an element's reference and mesh geometry.
Q	Approximation of I by numerical integration, cf. Eq. (5.24).
ρ_m, ρ_a	Relative variations of mean stress and stress amplitude in an element with respect to σ_m^{max} and σ_a^{max} respectively, cf. Eqs. (5.39) and (5.40).
$\sigma_m^{\text{max}}, \sigma_a^{\text{max}}$	Maximum mean stress and stress amplitude attained in an element, cf. Eqs. (5.39) and (5.40).
$\tilde{\sigma}_m, \tilde{\sigma}_a$	Approximations for the mean stress field and the stress amplitude field respectively derived from a finite element analysis.
w, \tilde{w}	Gaussian integration weight and adjusted Gaussian integration weight with respect deformed integration domain, cf. Eq. (5.27) and explanations below.

Other expressions

α	Mean stress factor in linear stress amplitude correction, cf. Eq. (2.37).
α_2, α_3	Ratio of second and third principal stress with respect to first principal stress, cf. Eqs. (5.20), (5.21), (5.22) and explanations above.
δ^{ref}	Adjusted failure flag with respect to N_{ref} , cf. Eq. (5.15).
E	Young's modulus of a considered material.
$\varepsilon, \varepsilon_p$	Total and plastic strain respectively.
\mathcal{G}	Set of considered specimen geometries.
γ	Exponent in Walker's mean stress model, cf. Eq. (2.36).
γ_s	Safety factor applied to simulation-derived stress amplitudes.
k	Fatigue strength scatter parameter, cf. Eqs. (5.5), (5.18) and (5.19).
L_m, L_a	Load representatives for the stationary and cyclic load components, see the elaborations above Eq. (5.7).
N_b	Number of blades in the considered compressor stage.
N_f	Number of load cycles until failure occurred.
N_{ref}	Reference number of cycles with respect to a fatigue strength or a constant-life diagram.
N_s	Number of generated samples.
n	Curvature parameter of the scale function of unit Haigh diagram, cf. Eq. (5.2). Sometimes also used as general natural number.
n_e	Number of elements in a finite element model.
n_g	Number of integration points (Gauss points) per element.
n_{ip}	Number of integration points in one dimension.
n_{res}	Finite element mesh-resolution parameter for a notched specimen which states the number of elements on the notch arc.
$\Sigma, \bar{\Sigma}$	Sum and mean value.
$\Sigma_C(L_m, L_a)$	Finite element analysis of component C based on loads defined by L_m and L_a , cf. Eq. (5.14).
T	Oscillatory period of a load cycle.
\mathcal{T}	Fatigue test data set.
Θ_s	Vector containing sampled parameter vectors, cf. Eq. (5.61).
θ	Model parameter vector of a considered parametric model.

Acronyms

EO	Engine order
FE	Finite element
ML	Maximum likelihood
MU	Model uncertainty
LCF	Low-cycle fatigue
HCF	High-cycle fatigue
VHCF	Very-high-cycle fatigue
NACA	National Advisory Committee for Aeronautics

1 Introduction

Since the industrial revolution in the 19th century enabled the economic manufacture of metallic machine components, engineers responsible for an application-appropriate design of such parts have been faced with the problem of metal fatigue. According to a historical review by Schütz [1], the first publication on this issue was put out in 1837 by Albert [2], a German mining engineer who was reporting on numerous in-service failures observed on metal conveyor chains in the mining operations of Clausthal, Germany. The term “fatigue” as a general label for the phenomenon described by Albert was first mentioned in a publication by Braithwaite [3] in 1854.

While there have been many applications, unexpected fatigue failures have been reported on in the first period of fatigue research – brewery equipment, water pumps, propeller shafts [3] – the most pressing issue of the time was associated with the numerous cases of often disastrous railway accidents [4, 5]. Many times, the cause of these accidents could be traced back to the fatigue-induced failure of train axles. On May 8th in 1842, for example, 60 people lost their lives after a broken locomotive axle led to a catastrophic derailment of a train in Versailles, France [6]. The extent of the problem might be further illustrated by the fact that, until 1887, English newspapers regularly reported on “the most serious railway accident of the week” [1]. It was around this time, in the late 1850s, when August Wöhler, by many considered the founding father of fatigue strength research [7], was assigned to investigate the origin of the problem. Several years later, after having conducted multiple extensive investigations [8–10], he summarized his findings in [11] to what is today often referred to as Wöhler’s law: “Material can be induced to fail by many repetitions of stresses, all of which are lower than the static strength. The stress amplitudes are decisive for the destruction of the cohesion of the material. The maximum stress is of influence only in so far as the higher it is, the lower are the stress amplitudes which lead to failure”.

Around a century after Wöhler had published his work, in the early 1950s, Coffin and Manson described the fatigue behavior of metals subjected to loads that resulted in a cyclic elasto-plastic material response [12, 13]. Their research marks the beginning of the formal distinction between low-cycle fatigue (LCF) on the one hand, and high-cycle fatigue (HCF) on the other. While low-cycle fatigue refers to failures encountered after the application of a rather low number of cycles, typically less than 10^4 , associated with loading conditions such as those investigated by Coffin and Manson, high-cycle fatigue is the terminology used for fatigue-induced fractures that do not occur before a comparably high number of cycles, usually 10^5 to 10^8 , at low load amplitudes in terms of the static strength has been accumulated [14].

The design against low-cycle fatigue is conceptually a finite life design, and therefore focused on the number of load cycles. From the requirements of the considered application, a minimum number of cycles is derived, the respective component has to survive. It is then the engineer’s job to provide a design that ensures that this minimum number is reached. The main design tool for this purpose is the strain-life or SN -diagram, relating a given strain amplitude to an expected number of cycles until failure. The latter is modeled as a random variable in probabilistic LCF-assessments [15, 16]. Characteristic for low-cycle fatigue problems is the rather easy characterization and countability of the individual load cycles. Examples are the start-stop cycles of a gas or steam turbine [17], the number of flights of an airplane [18] or the pressurization of vessels [19].

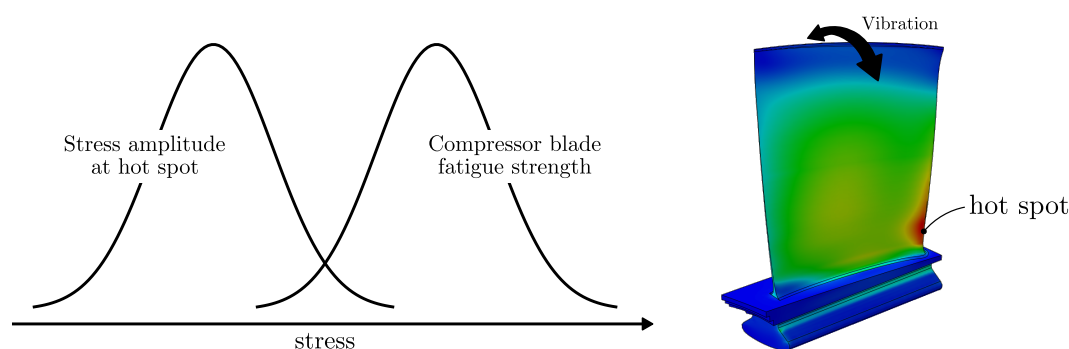


Figure 1.1: Schematic illustration emphasizing the statistical nature of the HCF-relevant compressor blade loading and its fatigue strength with respect to a given vibration mode.

The design against high-cycle fatigue on the other hand was historically conceptualized as an infinite life design [20]. In this framework one would assume that the considered material exhibits a characteristic fatigue limit [21] which could serve as a decision boundary separating acceptable from non-acceptable loads. Consequently, the fatigue limit was thought of to be a stress amplitude threshold defined by the characteristic that any given stress amplitude of smaller magnitude would not cause failure, no matter how many cycles would be applied. Even though fatigue research indicates that this model does not hold true for most materials – if only enough cycles are applied also stress amplitudes below a potential fatigue limit will lead to failure [22, 23] – the concept of emphasizing the stresses rather than the number of cycles is still the guiding motive in design against high-cycle fatigue. Today, the notion of a fatigue limit has mostly been replaced by the fatigue strength, which is always corresponding to a specific design life. Characteristic for many problems associated with high-cycle fatigue is a high loading frequency, emphasized mean stresses and a more difficult characterization and countability of the individual load cycles. Other than for low-cycle fatigue application, the major design tool for high-cycle fatigue problems is not the SN -diagram, but the constant-life diagram [24], relating a given mean stress to a maximum acceptable stress amplitude with respect to the anticipated design life. In probabilistic HCF-methodologies it is usually the fatigue strength, not the resulting life, that is modeled as a random variable [25]. Typical examples for applications where high-cycle fatigue has to be accounted for are gear drives [26, 27], railway wheels [28, 29], crankshafts [30] or suspension arms [31].

Another example for a component that has to be designed against high-cycle fatigue, which will be focused on in this work, is a compressor blade of a gas or steam turbine [32]. While being subjected to considerable mean stresses introduced by the centrifugal forces of the rotor’s rotation and the mean pressure of the passing airflow, cyclic loads are generated by variations in the flow pressure caused by the stationary vanes before and behind the row of blades. When the resulting excitation frequency approaches a blade eigenfrequency, the airfoil will resonate, resulting in vibratory stresses that have to be checked with respect to the possibility of high-cycle fatigue [33].

The reliability of a compressor blade is influenced by many parameters of emphasized statistical nature [33, 34]. They mostly relate to the expected loads on the one hand, and to the fatigue strength of the component on the other, see Fig. 1.1. With respect to the anticipated loading conditions, small manufacturing induced variations in geometry and material properties between the individual airfoils in a single compressor stage [35],

result in different resonance behaviors in terms of the stress levels around hot spots. But even if all blades were geometrical identical with similar vibratory characteristics, the material inherent scatter with respect to the local fatigue properties, caused by microstructural differences, would still lead to a scatter in the resulting compressor blade lives. In the light of these probabilistic boundary conditions, it is surprising, that the design of a compressor blade is still conducted using deterministic models in combination with rather large safety factors throughout industry practice today [36]. Not only do sound probabilistic design frameworks allow for the reduction of overly conservative design margins, fostering a more efficient material use. They also enable component optimization in terms of their reliability, allow for the identification of major risk sources, and generally increase the understanding of applications that are governed by influences of statistical nature, cf. [37].

The forgoing of probabilistic approaches in the design process of compressor blades cannot be explained with a lack of corresponding methods. At the time, this thesis was written, several methodologies for assessing high-cycle metal fatigue with probabilistic content have been published, see for example [38–42]. In some cases, these methods explicitly focused on the design of compressor blades [33, 34]. However, their practical utilization remains limited. Several reasons have been pointed out in the literature for this apparent reluctance, see for example [36]. They range from a higher complexity of the probabilistic approach, over unavailable finite element post-processing routines, to a lack in required material data. Especially the last point constitutes an effective obstacle since additional material tests are expensive. Another important reason that goes mostly unmentioned is the inertia of traditional design methodologies when it comes the proposal of conceptionally different approaches. While the former represents a well-established way of assessing a given design, validated by the products in operation that did not fail, a novel probabilistic method, unproven by experience with the product, might be looked upon with some skepticism by the responsible designers. This situation often prevents the transfer of available probabilistic methods into design practice.

In view of the aforementioned hurdles for probabilistic approaches with respect to the high-cycle fatigue design of metal components in general, and the corresponding design of gas turbine compressor blades in particular, it is the goal of this work to develop a probabilistic framework for the high-cycle fatigue assessment of metal components – particularly compressor blades – which can be easily incorporated into existing non-probabilistic design procedures. In order to achieve this goal, the anticipated model is supposed to satisfy two criteria. At first, it is intended to be conceptually related to the traditional design method based on constant-life diagrams. Secondly, the requirements with respect to the test data needed for calibrating the model are supposed to be as low as possible. This last point is intended to ensure the compatibility of the model with most test databases, and to keep the need for additional tests as low as possible.

The stated requirements are translated into a probabilistic Haigh diagram based on a weakest-link model and finite element stress field data. A (conventional) Haigh diagram is a constant-life diagram, where the fatigue strength corresponding to the respective design life is expressed as a function of the acting mean stress, see Fig. 1.2a. It is a classic high-cycle fatigue design tool, typically used with respect to the stresses attained at the most severely stressed location on the considered component, the so-called hot spot, cf. Fig. 1.1. If the expected stress amplitude at this location, usually multiplied with a safety factor, does not exceed the fatigue strength corresponding to the hot-spot

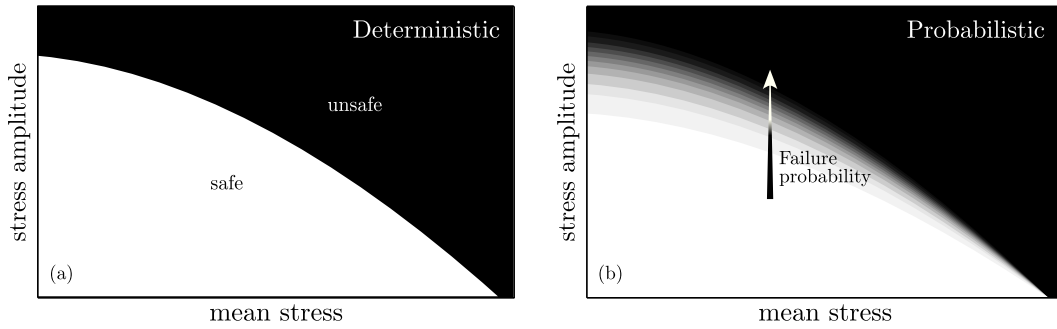


Figure 1.2: Schematic illustration of a deterministic and a probabilistic Haigh diagram.

mean stress based on the Haigh diagram, the design is accepted. If this condition is not satisfied, the design is rejected. With this binary view it therefore corresponds to a traditional deterministic approach. The weakest-link model on the other hand represents the door opener for the probabilistic treatment of the Haigh diagram, see Fig. 1.2b. Instead of assessing the severity of the cyclic load based on the hot-spot stresses, the weakest-link model represents an integral approach, which evaluates the probability of failure over the entire component domain. Depending on the model, this can be the component surface, its entire volume or subdomains thereof. The considered domain is partitioned into small interconnected subdomains (the links), and component failure is assumed as soon as one of these subdomains fails (the weakest link). Combining the weakest-link model with the concept of a constant-life diagram allows for the derivation of component specific probabilistic Haigh diagrams that can be used in a design context in a very similar fashion as the traditional deterministic Haigh diagrams.

It will be shown how the four parameters of the model can be calibrated with almost arbitrary data sets of constant-amplitude fatigue tests from the HCF-relevant load range. In contrast to other approaches which require test data in a specific format – one may think of Dixon and Mood’s popular method [43] for deriving a fatigue strength distribution, which requires test data that was generated following a specific staircase scheme – the presented approach has no such constraints. It is even possible to combine test data obtained for different specimen geometries in the model calibration. The latter is realized by a simple maximum likelihood fit for test data where each data point is either left or right censored. Even though the requirements on the test data for calibrating the four model parameters are low, some data sets will still be better suited to do so than others. This topic is addressed in two separate investigations. The first study focuses on the question concerning which kind of test data should be included in the model calibration in order to obtain parameter estimates with narrow confidence intervals. In the second study, a fixed data set is considered, and the question is addressed on how to quantify the resulting model uncertainty. Both subjects are relevant in a design context.

After its proposal, and a comparison with existing approaches, the model is analyzed in terms of its numerical properties, when applied to stress field data obtained from finite element simulations. The focus is put on the error in the predicted failure probability that results when either the used finite element mesh is too coarse, or the underlying quadrature rule is insufficient. It is the goal to provide guidelines how the model should be used in a design context without underestimating the failure probability due to approximation errors.

The model is validated in several studies based on tension-compression fatigue test data for different types of smooth and notched specimens as well as different kinds of materials. The latter comprise one high-strength precipitation hardened steel (PH12-10Mo), one more ductile low-alloy steel (SAE-4130) and two aluminum alloys (AL2024-T3 and AL7075-T6). A two-step calibration/prediction methodology has been applied. At first the four model parameters are calibrated using a subset of the considered data pool containing only test results on two of the available specimen types. In a second step the calibrated model is used to predict the failure behavior of the remaining specimen geometries, the test data of which has not been used in the calibration step. The model prediction can then be compared with the experimentally observed test outcomes. In the first study, the considered test data is still restricted to predominantly elastic material behavior. Since the stress amplitudes are always small in the context of HCF, this restriction is mostly constraining the superimposed mean stress to small and moderate magnitudes. However, when the mean stress is high, as it is often the case in HCF-relevant applications, notched components subjected to small amplitude loads might experience a plasticity induced stress redistribution in the notch root over the first few cycles. In order to account for such effects, a model extension based on non-linear finite element simulations is introduced in a second study.

At last, the applicability of the proposed model in a design context is demonstrated for the example of a gas turbine compressor blade. First, the probability of failure for a single blade with respect to different vibration modes for a range of rotor speeds is evaluated. Afterwards, a simple probabilistic methodology based on Monte Carlo simulations is presented showing how the single-blade risk can be used in order to quantify the probability of failure for an entire compressor stage containing numerous blades.

The material presented in this thesis is structured as follows. The current state of knowledge with respect to high-cycle metal fatigue and design strategies aiming to avoid this type of failure in metallic engineering components is summarized in Section 2. Based on the obtained picture, the scope of this work is derived and formulated in Section 3. An overview of the used fatigue test data and the corresponding materials is compiled in the following Section 4. The major part of this thesis is presented in Section 5 which contains the model development, including the analyses on the numerical properties and the model uncertainty, as well as the two validation studies outlined above. Section 6 contains the application of the proposed methodology to the design case of a gas turbine compressor blade. Finally, a concluding summary, including open questions for future research activities, is given in Section 7.

2 State of knowledge

This chapter outlines the current state of research in the field of high-cycle metal fatigue as far as it relates to the objectives pursued in this work. In Section 2.1 the most important characteristics of the vibratory loading conditions typically experienced by gas turbine compressor blades are discussed. The following Section 2.2 will introduce some basic terminology when describing the stress fields in components that are subjected to cyclic loads. After introducing this formal framework, Section 2.3 will focus on the physical mechanisms that lead to high-cycle fatigue. These mechanisms are typically affected by several influences that have to be accounted for when designing a specific structure against high-cycle fatigue. These influences are discussed in Section 2.4 in terms of the fatigue strength of an engineering component. A common means to account for these effects during the design phase are life diagrams. After introducing the two most important representatives of such diagrams in Section 2.5, the following Section 2.6 describes how they are determined experimentally. The remaining part focuses on the design process itself. In Section 2.7 the general concepts underlying traditional deterministic and probabilistic approaches are compared. Finally, in Section 2.8 specific methodologies for the design against high-cycle fatigue are presented.

2.1 Vibratory loads on axial-flow compressor blades

While the methods developed in this work, which are aiming to assess the probability for high-cycle fatigue of a considered metallic component under a given loading, are generally applicable to many different respective design problems, the motivating and therefore guiding application will be the design of a gas turbine compressor blade. The purpose of this section is to introduce some of the most important characteristics of this application that have to be taken into account when assessing the probability of failure due to high-cycle fatigue. Much more details and in-depth explanation on this specific case can be found for example in Chapter 7 of [44] or Chapter 6 of [45].

An axial-flow compressor, as an integral component of a gas turbine, produces a stream of pressurized air which is required by the combustor for the burning process. It consists of several sequentially installed stages, where each stage contains one row of rotating airfoils (blades) and one following row of stationary airfoils (vanes), see Fig. 2.1. While the fluid passes through the stages its static pressure as well as its temperature successively increases. During this process the interaction with the rotating blades increases mostly the kinetic energy of passing air, while the following interaction with the static vanes decelerates the fluid, resulting in an increase of static pressure. Note that in most land-based applications the gas temperature remains too low for material creep effects to occur during this process. After passing the last compressor stage, the air enters a diffuser, once again converting the air's velocity into static pressure. Finally, it enters the combustor for the fuel injection and the burning process.

Compressor blades are often made from titanium alloys for use in aero-engines, mostly due to their high strength-to-weight ratio and good temperature resistance, while high strength steels are used for applications in land-based heavy duty gas turbines [46, 47]. These steels often contain chromium, carbon, nickel or molybdenum, resulting in a high tensile strength and HCF resistance after appropriate heat treatment [47]. Both types of material have in common that their manufacturing process produces a polycrystalline microstructure, resulting in macroscopically mostly isotropic material properties, cf. [48].

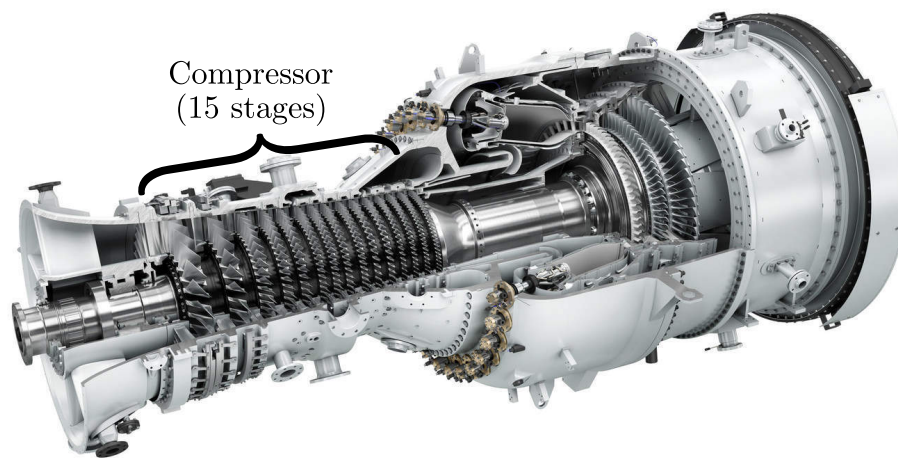


Figure 2.1: Gas turbine (SGT-800) containing a 15-stage compressor [49].

During normal operation, the loads acting on the compressor blades, i.e. the rotating airfoils, are originating from two major sources. First, there is the rotation of the rotor, the blades are mounted upon. This rotation results in high centrifugal forces acting onto the blades, leading to high mean stresses particularly in their fixture. Secondly, there is the airflow which is constantly passing the blade. Triggered by the relative motion with respect to the stationary row of vanes in front of and behind the row of blades, the airflow will have certain cyclic characteristics. These cyclic properties are majorly defined by the numbers of vanes in the adjacent rows, as well as the rotational speed of the rotor. As a consequence, next to a certain static component, the passing airflow will apply highly dynamic, cyclic loads on each compressor blade. However, compared with the static strength of the blade material, the amplitudes of these cyclic loads are typically rather small.

In many cases, that is under many different operation conditions, the dynamic loads will be too small to represent a source of hazard for the structural integrity of a compressor blade. However, under certain conditions this can change. Typically, these conditions are reached when a major frequency in the dynamic load spectrum comes close to an eigenfrequency of the compressor blade. If this happens, the blade structure is likely to resonate in the corresponding eigenmode, resulting in dynamic blade loads, which in many cases, although still small compared with the static strength of the material, cannot be neglected anymore. The resulting load case is a typical high-cycle fatigue problem, i.e. high stationary loads, combined with comparably small but numerous cyclic components. The high number of cycles is explained by the fact that, due to the usually high eigenfrequencies of the blades, load cycles accumulate quickly.

One of the unpleasant characteristics of this load case is that it is typically not possible to avoid it entirely. Compressor blades have several eigenmodes with relevant eigenfrequencies, and the state space of possible operation conditions, and consequently possible excitation frequencies, is large. The problem is additionally amplified by the circumstance that due to manufacturing deviations and material scatter, the compressor blades contained in a considered row are not all identical. As a consequence, each blade will have slightly different eigenfrequencies than any other blade. Finally, it should be

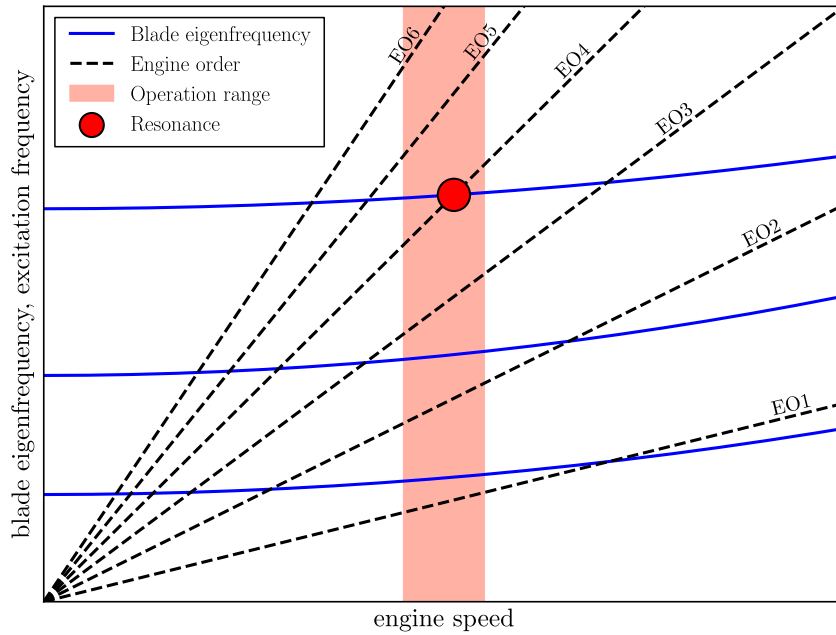


Figure 2.2: Generic Campbell diagram used for the design of compressor blades.

pointed out that all of these eigenfrequencies are influenced by the operating conditions such as temperature (material properties) and rotation speed (blade stiffening).

In the design phase of a compressor blade this resonance problem is often visualized in a so-called Campbell diagram [50], see Fig. 2.2. Such a diagram contains the relevant nominal blade eigenfrequencies as a function of the engine speed, next to the excitation frequencies of different engine orders (EOs). In this context, an engine order is simply a multiple of the rotation frequency of the rotor. For example, the fifth engine order EO5 refers to an excitation frequency of five times the current engine speed. Whenever the graphs of a blade eigenfrequency crosses the graph of an engine order, one can expect an excitation event, that is a potential problem, under the corresponding engine speed. As depicted in Fig. 2.2 one will always find several crossings. However, not all of these crossings are relevant or even critical. Only those will matter, which are located in an engine speed interval which is frequently visited during operation, such as normal stationary operation, start-ups or shutdowns. The most important speed interval is of course the one corresponding to the most frequently used normal operation mode. Any compressor design has to ensure that no blade resonance will occur under these conditions. Otherwise, due to the fast accumulation of cycles, one will almost certainly encounter early blade failure. Transient events, such as start-ups and shutdowns, on the other hand, cover much larger speed intervals. In a start-up, for example, the machine starts at speed zero, and gradually accelerates to the operation speed. It is therefore much more difficult to prevent resonance events for these scenarios. In most designs, one will have to accept a few resonance crossing during transient events. Fortunately, resonance conditions in transient events are only effective for a short period of time, so that only a limited number of load cycles is applied to the blades. However, if the respective machine is operated in a rather fluctuating manner, with many start-ups and shutdowns, it is still possible to accumulate enough cycles for making it necessary to conduct a high-cycle fatigue analysis.

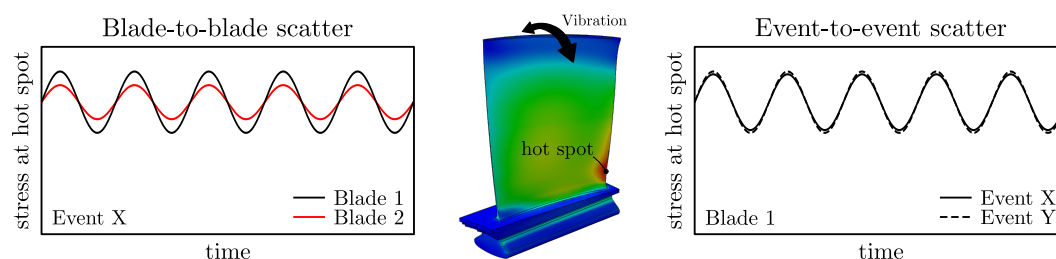


Figure 2.3: On the scatter in the blade response in terms of the hot-spot stress between different compressor blades of the same stage (blade-to-blade scatter) and repeated resonance events (event-to-event scatter). Typically the former is considerably greater than the latter.

Resonance conditions are always associated with a specific stage, since different stages contain different blades. In many cases, all blades contained within a specific stage are nominally identical. This means, when resonance conditions are reached for one of the compressor stages, all blades within that stage will resonate at the same time. In this context, one has to distinguish two kinds of scatter with respect to the resonance response of the individual blade, cf. Fig. 2.3. Note that the resonance response is understood as the magnitude of the cyclic stress field that emerges in a blade as a result of the vibration. The first kind is the variability of the response of a single blade from one resonance event to another. One may refer to this kind of variability as the event-to-event scatter. The second type refers to the scatter of the resonance response during a single resonance event between different blades. This second type may be called blade-to-blade scatter. Measurements on the vibration characteristics of compressor blades in several Siemens gas turbines generally show a rather small event-to-event scatter of the individual blade, as long as the operation conditions, which cause the resonance are repeated. In other words, the compressor blade responds in a quantitatively very similar fashion when exposed to similar resonance conditions. The blade-to-blade scatter on the other hand is typically much greater. When the rotor speed crosses a frequency resulting in resonance conditions in one of the compressor stages, the stress levels in the individual blades will generally differ. Typically, there are blades that exhibit a rather high stress level, while others show much lower magnitudes. This behavior is mostly caused by small differences in the geometry of the manufactured blades, as well as slightly different distributions of local material properties over the blades.

As already pointed out at the beginning of this section, the loading conditions that have to be anticipated in the design of a gas turbine compressor blade, will serve as a motivating example for the development of the probabilistic method in this work. In summary, the corresponding stress fields are characterized by the following features. First of all, the vibration of a single blade eigenmode represents a proportional load case. No phase shifts between simultaneously acting stress fields have to be considered. The second major characteristic is the approximately constant stress amplitude for an individual blade between repeated resonance events. This eliminates the need for variable amplitude considerations. On the other hand, high mean stresses have to be anticipated mostly caused by the centrifugal loads. However, due to the moderate temperatures, no creep effects have to be expected. Additionally, considering the shape of the airfoils, it is important to account for stress concentrations at structural discontinuities. Finally, the used material types allow for an isotropic material model relating stresses to strains.

2.2 Fundamentals of cyclic stress fields

Stress fields that form in a structural component as a result of external cyclic loading will assume a central role in the considered methodologies throughout this work. It is the purpose of this section to establish a common basis with respect to the required concepts and the respective terminology for describing and evaluating those stress fields.

Consider an engineering component C with volumetric domain V_C that is subjected to the continuously repeated application of an external load. Due to the cyclic nature of this type of loading, the resulting stress field within the component will be cyclic as well. Consequently, it will be called a cyclic stress field. A cyclic stress field, which will be generally denoted as $\boldsymbol{\sigma}$, is understood as a spatio-temporal function on $V_C \times \mathbb{R}$ with the characteristic that its restriction to any point $\mathbf{x} \in V_C$ describes a continuous T -periodic tensor-valued function, $T \in \mathbb{R}_+$. The tensor $\boldsymbol{\sigma}(\mathbf{x}, t)$ in the image of $\boldsymbol{\sigma}$ is the Cauchy stress tensor [51], which is a symmetric tensor of second order in three dimensions and can thus be represented by six scalar values. In more formal terms one would have $\boldsymbol{\sigma} : V_C \times \mathbb{R} \rightarrow \mathbb{R}^6$ such that $\boldsymbol{\sigma}(\mathbf{x}, t) = \boldsymbol{\sigma}(\mathbf{x}, t + T)$ for all $t \in \mathbb{R}$. By denoting the individual component functions of $\boldsymbol{\sigma}$ as σ_{ij} with $i, j \in \{1, 2, 3\}$ one can express $\boldsymbol{\sigma}(\mathbf{x}, t)$ in matrix notation via

$$\boldsymbol{\sigma}(\mathbf{x}, t) = \begin{pmatrix} \sigma_{11}(\mathbf{x}, t) & \sigma_{12}(\mathbf{x}, t) & \sigma_{13}(\mathbf{x}, t) \\ * & \sigma_{22}(\mathbf{x}, t) & \sigma_{23}(\mathbf{x}, t) \\ * & * & \sigma_{33}(\mathbf{x}, t) \end{pmatrix}. \quad (2.1)$$

where the asterisks represent the symmetric components of $\boldsymbol{\sigma}(\mathbf{x}, t)$. Note that in order to avoid overloaded formulas, the arguments (\mathbf{x}, t) of $\boldsymbol{\sigma}(\mathbf{x}, t)$ and its components $\sigma_{ij}(\mathbf{x}, t)$ may be omitted at times, see for example Eqs. (2.8) to (2.10) below.

In most considerations, one does not refer to the full cyclic stress field $\boldsymbol{\sigma}$ but only to certain restrictions. On the one hand, from a time perspective, it suffices to consider a single load period $[0, T)$ in order to analyze the properties of a cyclic stress field. On the other hand, from a spatial perspective, one might be considering only the stresses in a certain subdomain $\Omega \subseteq V_C$. Formally, these restrictions will be denoted as

$$\boldsymbol{\sigma}(\Omega, [0, T)) : \Omega \times [0, T) \rightarrow \mathbb{R}^6, (\mathbf{x}, t) \mapsto \boldsymbol{\sigma}(\mathbf{x}, t). \quad (2.2)$$

The most frequently used notation in this context will be $\boldsymbol{\sigma}(\mathbf{x}, [0, T)) := \boldsymbol{\sigma}(\{\mathbf{x}\}, [0, T))$ which refers to the stress cycle at a given location $\mathbf{x} \in V_C$.

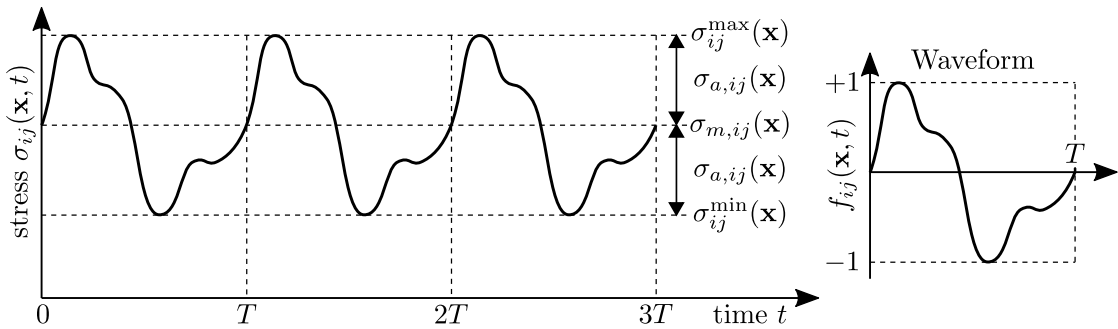


Figure 2.4: On the used terminology in the context of cyclic stresses.

The full load cycle $\boldsymbol{\sigma}(\mathbf{x}, [0, T])$ at a given location $\mathbf{x} \in V_C$ is typically viewed from a perspective that distinguishes between stationary and time-dependent components. With respect to the component functions given in Eq. (2.1) one defines

$$\sigma_{ij}(\mathbf{x}, t) = \sigma_{m,ij}(\mathbf{x}) + \sigma_{a,ij}(\mathbf{x})f_{ij}(\mathbf{x}, t) \quad i, j \in \{1, 2, 3\}. \quad (2.3)$$

where $f_{ij} : \{\mathbf{x}\} \times [0, T) \rightarrow [-1, 1]$ is a time-dependent continuous function describing the normalized waveform of the stress component's cycle at location $\mathbf{x} \in V_C$, cf. Fig. 2.4. Note that in the case of sinusoidal and proportional loads the waveform reduces to $f_{ij}(\mathbf{x}, t) = \sin(\omega t)$ with $\omega = 2\pi/T$. The two time-independent stress components $\sigma_{m,ij}(\mathbf{x})$ and $\sigma_{a,ij}(\mathbf{x})$ are called the mean stress and the stress amplitude respectively. Given the definition of f_{ij} they are computed via

$$\sigma_{m,ij} = \frac{1}{2} \left(\sigma_{ij}^{\max}(\mathbf{x}) + \sigma_{ij}^{\min}(\mathbf{x}) \right) \quad (2.4)$$

$$\sigma_{a,ij} = \frac{1}{2} \left(\sigma_{ij}^{\max}(\mathbf{x}) - \sigma_{ij}^{\min}(\mathbf{x}) \right) \quad (2.5)$$

where $\sigma_{ij}^{\max}(\mathbf{x}) := \max_{t \in [0, T)} \sigma_{ij}(\mathbf{x}, t)$ and $\sigma_{ij}^{\min}(\mathbf{x}) := \min_{t \in [0, T)} \sigma_{ij}(\mathbf{x}, t)$, see also Fig. 2.4. Mean and amplitude stress components are summarized in the local mean stress tensor $\boldsymbol{\sigma}_m(\mathbf{x})$ and the local stress amplitude tensor $\boldsymbol{\sigma}_a(\mathbf{x})$ which are Cauchy stress tensors themselves and, in matrix notation, are expressed as

$$\boldsymbol{\sigma}_m(\mathbf{x}) = \begin{pmatrix} \sigma_{m,11}(\mathbf{x}) & \sigma_{m,12}(\mathbf{x}) & \sigma_{m,13}(\mathbf{x}) \\ * & \sigma_{m,22}(\mathbf{x}) & \sigma_{m,23}(\mathbf{x}) \\ * & * & \sigma_{m,33}(\mathbf{x}) \end{pmatrix} \quad (2.6)$$

$$\boldsymbol{\sigma}_a(\mathbf{x}) = \begin{pmatrix} \sigma_{a,11}(\mathbf{x}) & \sigma_{a,12}(\mathbf{x}) & \sigma_{a,13}(\mathbf{x}) \\ * & \sigma_{a,22}(\mathbf{x}) & \sigma_{a,23}(\mathbf{x}) \\ * & * & \sigma_{a,33}(\mathbf{x}) \end{pmatrix}. \quad (2.7)$$

Generally, a Cauchy stress tensor like $\boldsymbol{\sigma}(\mathbf{x}, t)$, $\boldsymbol{\sigma}_m(\mathbf{x})$ or $\boldsymbol{\sigma}_a(\mathbf{x})$ is associated with several characteristic values and invariants [51]. The most important invariants for the purposes of this work are

$$I_1(\boldsymbol{\sigma}) = \sigma_{11} + \sigma_{22} + \sigma_{33} \quad (2.8)$$

$$I_2(\boldsymbol{\sigma}) = \sigma_{11}\sigma_{22} + \sigma_{11}\sigma_{33} + \sigma_{22}\sigma_{33} - \sigma_{12}^2 - \sigma_{13}^2 - \sigma_{23}^2 \quad (2.9)$$

$$J_2(\boldsymbol{\sigma}) = \frac{1}{3}I_1(\boldsymbol{\sigma})^2 - I_2(\boldsymbol{\sigma}). \quad (2.10)$$

The values $I_1(\boldsymbol{\sigma})$ and $I_2(\boldsymbol{\sigma})$ are simply called the first and second invariant of $\boldsymbol{\sigma}$, while $J_2(\boldsymbol{\sigma})$ is referred to as the second invariant of the deviator of $\boldsymbol{\sigma}$.

When dealing with cyclic stress fields in the context of high-cycle fatigue assessment, one will often reduce the complexity of the corresponding tensor fields by mapping them into scalar valued fields of so-called effective stresses. In this sense, an effective stress is supposed to translate the tensor valued stress state at a given location on the considered component to a scalar value representing the severity of the local stress conditions. In a not entirely correct use of the term, one can think of the effective stress as a local stress norm. More formally, an effective stress is understood as a function

$\sigma : \mathbb{R}^6 \rightarrow \mathbb{R}$, $\boldsymbol{\sigma} \mapsto \sigma(\boldsymbol{\sigma})$. An important group of effective stresses is based on the stress invariants, stated before. One defines

$$\sigma^{\text{vM}}(\boldsymbol{\sigma}) = \sqrt{3J_2(\boldsymbol{\sigma})} \quad (2.11)$$

$$\sigma^{\text{oct}}(\boldsymbol{\sigma}) = \frac{1}{3}I_1(\boldsymbol{\sigma}) \quad (2.12)$$

$$\tau^{\text{oct}}(\boldsymbol{\sigma}) = \sqrt{\frac{2}{3}J_2(\boldsymbol{\sigma})} \quad (2.13)$$

where σ^{vM} is referred to as von Mises stress, σ^{oct} denotes the octahedral normal stress and τ^{oct} the octahedral shear stress. Note that the octahedral normal stress is also often called the hydrostatic stress σ^{h} in the literature. Another frequently used invariant-based effective stress is the maximum or first principal stress. This stress refers to the maximum of the eigenvalues of a given stress tensor. Note that due to the symmetry of the Cauchy stress tensor, all eigenvalues are always real. Therefore, the maximum principal effective stress can be expressed via

$$\sigma^{\text{mP}}(\boldsymbol{\sigma}) = \max \left\{ \lambda \in \mathbb{R} : \exists \mathbf{v} \in \mathbb{R}^3 \setminus \{0\} : \boldsymbol{\sigma} \mathbf{v} = \lambda \mathbf{v} \right\}. \quad (2.14)$$

Another group of effective stresses is derived from geometric considerations with respect to an imaginary cutting plane intersecting the component. Consider a location $\mathbf{x} \in V_C$ and a plane $\Delta_{\mathbf{n}}$ containing \mathbf{x} with a unit normal vector $\mathbf{n} \in \mathbb{R}^3$. The stress state in $\mathbf{x} \in V_C$ at a given instance $t \in [0, T)$ may be expressed in terms of

$$\sigma_n(\boldsymbol{\sigma}, \mathbf{n}) = \mathbf{n}^T \boldsymbol{\sigma} \mathbf{n} \quad (2.15)$$

$$\tau(\boldsymbol{\sigma}, \mathbf{n}) = \|\boldsymbol{\sigma} \mathbf{n} - (\mathbf{n}^T \boldsymbol{\sigma} \mathbf{n}) \mathbf{n}\|_2 \quad (2.16)$$

where $\|\cdot\|_2$ denotes the Euclidean norm. The local stress tensor is decomposed into a normal and a tangential component with respect to the cutting plane $\Delta_{\mathbf{n}}$. The magnitudes of these projections are given by $\sigma_n(\boldsymbol{\sigma}, \mathbf{n})$ and $\tau(\boldsymbol{\sigma}, \mathbf{n})$ respectively.

By means of an effective stress model σ in combination with the time-independent stress tensors $\boldsymbol{\sigma}_m(\mathbf{x})$ and $\boldsymbol{\sigma}_a(\mathbf{x})$, see Eqs. (2.6) and (2.7), one can define an effective mean stress $\sigma_m(\mathbf{x}) = \sigma(\boldsymbol{\sigma}_m(\mathbf{x}))$ and an effective stress amplitude $\sigma_a(\mathbf{x}) = \sigma(\boldsymbol{\sigma}_a(\mathbf{x}))$ for any location $\mathbf{x} \in V_C$. In this context, one often encounters the so-called stress ratio $R(\mathbf{x}) \in [-1, 1]$ which is related to mean stress and stress amplitude via

$$R(\mathbf{x}) = \frac{\sigma_m(\mathbf{x}) - \sigma_a(\mathbf{x})}{\sigma_m(\mathbf{x}) + \sigma_a(\mathbf{x})} \quad (2.17)$$

$$\sigma_m(\mathbf{x}) = \frac{1 + R(\mathbf{x})}{1 - R(\mathbf{x})} \sigma_a(\mathbf{x}) \quad (2.18)$$

$$\sigma_a(\mathbf{x}) = \frac{1 - R(\mathbf{x})}{1 + R(\mathbf{x})} \sigma_m(\mathbf{x}) \quad (2.19)$$

where the last two expressions only make sense for $R < 1$ (non-zero stress amplitude) and $R > -1$ (non-zero mean stress) respectively. Note that the stress ratio R is generally a function of $\mathbf{x} \in V_C$. However, in many applications it is defined either with respect to a specific location, or in terms of nominal stresses.

A notion conceptually related to the effective stress is the equivalent stress. While the effective stress function is translating a single tensor $\boldsymbol{\sigma}(\mathbf{x}, t)$ into a scalar value, the equivalent stress function, denoted as σ^{eq} , does the same with a spatio-temporal tensor field $\boldsymbol{\sigma}(\Omega, [0, T])$ where $\Omega \subseteq V_C$, cf. Eq. (2.2). Formally, this is expressed as

$$\boldsymbol{\sigma}(\Omega, [0, T]) \mapsto \sigma^{\text{eq}}(\boldsymbol{\sigma}(\Omega, [0, T])) \in \mathbb{R}. \quad (2.20)$$

The idea behind the concept of the equivalent stress is to reduce the complex stress cycle experienced by the considered component under a specific design load case to a single stress value that can be compared with material properties which typically refer to experimental fatigue tests under much simpler loading conditions. In the case of high-cycle fatigue one often compares the component loading with the fatigue strength of a smooth test specimen. When the latter is defined in terms of mean stress and stress amplitude like in a Haigh diagram, see Section 2.5, the equivalent stresses must also be expressed as equivalent mean stress σ_m^{eq} and equivalent stress amplitude σ_a^{eq} . Oftentimes, however, the fatigue strength of a smooth specimen is known only for zero mean stress. In this case one has to define an equivalent stress amplitude which inherently accounts for the mean stress influence, so that it can be compared with the zero-mean-stress fatigue strength of the smooth specimen. Such an equivalent stress amplitude will be denoted as $\sigma_{a,m}^{\text{eq}}$. Note that the equivalent stress is primarily understood as a formal concept. It can be defined in numerous ways. Whether or not a computed equivalent stress for a loaded component actually relates to the fatigue strength of a smooth component depends of course on a physically meaningful definition.

A simple way to define an equivalent mean stress σ_m^{eq} and an equivalent stress amplitude σ_a^{eq} for a loaded component C is to focus on a specific location $\tilde{\mathbf{x}} \in V_C$ and compute an effective stress with respect to the local mean stress and stress amplitude tensor, cf. Eqs. (2.6) and (2.7). For example

$$\sigma_m^{\text{eq}}(\boldsymbol{\sigma}(\tilde{\mathbf{x}}, [0, T])) = \sigma^{\text{oct}}(\boldsymbol{\sigma}_m(\tilde{\mathbf{x}})) \quad (2.21)$$

$$\sigma_a^{\text{eq}}(\boldsymbol{\sigma}(\tilde{\mathbf{x}}, [0, T])) = \sigma^{\text{vM}}(\boldsymbol{\sigma}_a(\tilde{\mathbf{x}})). \quad (2.22)$$

These stresses could now be compared with the design boundary in a Haigh diagram, see Section 2.5, referring to the smooth reference specimen. Such a definition would make sense, if one could assume that the stress state in $\tilde{\mathbf{x}} \in V_C$ was crucial for the fatigue assessment of the entire component.

Another equivalent stress definition, relating to the case where the mean stress influence is incorporated into the equivalent stress amplitude, is given by Walker's model [52]. Focusing again on a specific location $\tilde{\mathbf{x}} \in V_C$ it is defined by

$$\sigma_{a,m}^{\text{eq}}(\boldsymbol{\sigma}(\tilde{\mathbf{x}}, [0, T])) = \sigma(\boldsymbol{\sigma}_a(\tilde{\mathbf{x}})) \left(\frac{2}{1 - R(\tilde{\mathbf{x}})} \right)^\gamma \quad (2.23)$$

where σ is some effective stress function, $\boldsymbol{\sigma}_a(\tilde{\mathbf{x}})$ denotes the local stress amplitude tensor at $\tilde{\mathbf{x}} \in V_C$, $R(\tilde{\mathbf{x}})$ is the local stress ratio, also defined by effective stresses, and $\gamma \in (0, 1]$ represents a material parameter. The resulting stress amplitude could then be compared with the fatigue strength of the smooth reference specimen at zero mean stress.

More specific examples for equivalent stresses will be presented in Section 2.8 when discussing design approaches with respect to high-cycle fatigue.

2.3 High-cycle fatigue of metals from a material perspective

After having presented a motivating application and the required stress-related terminology in the context of high-cycle fatigue, the purpose of this section is to provide some background on the physical mechanisms governing a metallic material's failure due to cyclic low-amplitude loads. In order to emphasize the characteristics of high-cycle fatigue, the first part of this section provides a brief comparison with the failure mode of low-cycle fatigue. Most of the remaining part will then be focused on the crack initiation process under cyclic low amplitude loading which is the crucial failure mechanism with respect to high-cycle fatigue. Finally, the notion of the fatigue limit will be discussed.

Since the mid 1950s, after Coffin and Manson developed a methodology to describe the fatigue behavior of metals under elasto-plastic strain amplitudes [12, 13], mechanical fatigue phenomena have roughly been classified into low-cycle fatigue (LCF) and high-cycle fatigue (HCF) [1]. While the first kind, low-cycle fatigue, was referring to fatigue failure due to the application of a comparably low number, typically less than 10^4 , of rather severe load cycles, high-cycle fatigue was the terminology used for the remaining cases where failure was associated with a high number, usually 10^5 to 10^8 , of load cycles with comparably small amplitudes. Around fifty years later, beginning with the Giga-cycle Fatigue conference 1998 in Paris, a third category coined very-high-cycle fatigue (VHCF) emerged, covering fatigue cases with even longer lives than usually treated under the classical HCF umbrella [23]. Note in this context, that the previously stated life domains merely serve as a means for a rough categorization, which additionally leave gaps in the transition intervals where a distinct identification is not meaningful.

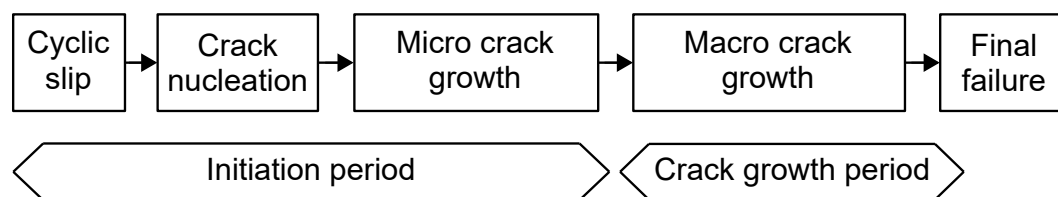


Figure 2.5: On the different phases of fatigue life in metals, taken from [14].

Independent from its classification into LCF, HCF or VHCF, fatigue failure in a polycrystalline metal is generally considered to be a phenomenon that can be split up into two phases, whose individual durations are strongly dependent on the considered loading conditions, cf. Section 2.2 in [14] and Fig. 2.5. The first phase comprises various processes leading to the initiation of a so-called micro-crack, and the first stages of its often irregular growth (initiation period). Note that in order for fatigue to occur the initiation of at least one micro-crack is required, but oftentimes several of these micro-cracks will form at different initiation sites more or less simultaneously. After such a micro-crack has reached a certain size the second phase begins, which is characterized by a comparably regular growth of the, now called, macro-crack (propagation period). The macro-crack will grow until the remaining un-cracked material is not able to withstand the applied loads anymore, followed by fracture.

Depending on the amplitude of the cyclic load, that means depending on whether one is considering an LCF or (V)HCF typical fatigue process, the role of the two described phases is very different. In a low-cycle fatigue context, the cyclic loads are typically high enough for many micro-cracks to form and grow into macro-cracks after a short

amount of time compared to the full life span. The remaining part of the life is spent in the propagation period, where the macro-cracks will continuously grow, until the most critical one will eventually lead to fracture. In other words, in an LCF setup, most of the life is spent in the phase of crack propagation, while the initiation phase is short. In a high-cycle fatigue context on the other hand, the role of the two fatigue phases is conceptually inverse. The stress fields encountered under HCF relevant load conditions are typically low enough for the processes of the crack initiation phase to be significantly retarded compared to the case of low-cycle fatigue. As a result, many more load cycles are required for a micro-crack to form and grown into a macro-crack. However, once such a macro-crack has emerged, the remaining number of cycles spent in crack propagation will be short compared to the time spent in crack initiation, and hence short compared to the entire life span. In other words, in an HCF setup most of the life is spent in the phase of crack initiation, while the following propagation phase is short, compare also Chapters 2 and 4 in [53]. While this qualitative description holds for the high-cycle fatigue setup, it is even more emphasized in the very-high-cycle fatigue context, cf. [54].

Since the crack initiation period is the most important one under (V)HCF load conditions, the corresponding physical processes will be described in more detail. The first aspect, that should be highlighted in this context is the location of where the crack initiates within the considered material. Three qualitative initiation sites are distinguished. Crack initiation at the surface, slightly below the surface and in the bulk of the material. The question on which of these three locations will host the fatigue-determinating crack is closely related to the mechanism that is dominating the initiation process in the considered material. This mechanism, in turn, depends on both the microstructure of the material as well as the amount of energy introduced into the material by the applied loads. With respect to the microstructure, an often cited classification proposed by Mughrabi [23] distinguishes two kinds of materials. The first kind, which is referred to as type I or single-phase, is a ductile material which does not contain any (effective) inclusions or equivalent imperfections. The second kind, consequently labeled as type II or multi-phase, corresponds to brittle materials such as high strength steels that do contain effective non-metallic inclusions. One can understand this distinction as a means to differentiate between materials where the fatigue mechanism can be influenced by the presence of inclusions (type II) versus materials where this is not the case (type I). In

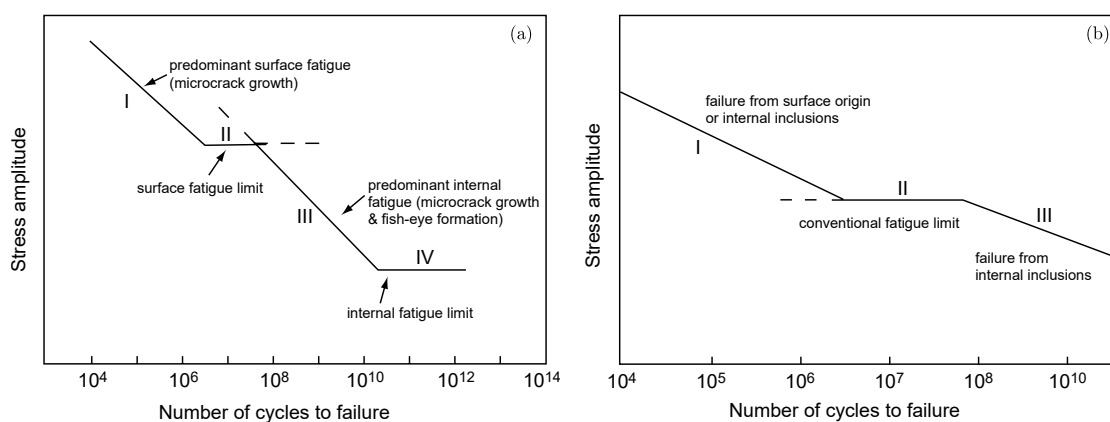


Figure 2.6: On the location of the critical fatigue crack for materials with a conventional fatigue limit (first plateau of the shown SN -curves), taken from [22].

order to return to the initially discussed crack initiation site, it has to be pointed out, that type I materials will typically fail from cracks that initiated at the surface, while more brittle materials, which do contain damage relevant inclusions (type II) might experience fatigue-determinating crack initiation either from the inclusion-free surface or from a non-metallic inclusion located at the surface, the sub-surface or even the bulk of the material. Hence, in the case of type II materials, two competing crack initiation mechanisms exist. The answer to the question on which of these mechanisms will actually lead to failure qualitatively depends on the number and size distribution of the non-metallic inclusions as well as on the applied loading. As a rule of thumb it can be said that – assuming failure occurs – the lower the number of inclusions, the larger their sizes and the lower the applied loads, the more likely it is that the fatigue critical crack initiates in the sub-surface or the bulk of the material originating from an inclusion. On the other hand, the higher the inclusion density, the smaller their size and the higher the loads, the more likely is a surface related failure mechanism, cf. [23]. Note that the role of the number of inclusions is explained by the probability of finding an inclusion at the surface, where the initiation process is faster than in the bulk of the material. The higher the number of inclusions, the higher the probability of finding a surface defect. With respect to the role of the applied loads, one can say, that inclusion-caused failures from within the material are typically associated with the very high-cycle fatigue domain, while failures originating from the surface are the typical failure mode associated with the classical high-cycle fatigue regime, see also Fig. 2.6.

After the location of the crack initiation has been discussed, the focus should be shifted to the actual physical mechanisms that drive the initiation process. The elaborations below are mostly based on the explanations in Chapter 2 of [14]. Even though the macroscopic stress amplitudes in the context of (very-) high-cycle fatigue are far below the material yield strength, the crack initiation process is generally a consequence of local cyclic plasticity, often referred to as cyclic slip, see also Fig. 2.5. In the absence of any inclusions of relevant size, cyclic slip will first occur in a small number of grains on crystallographic planes that are characterized by a combination of low slip resistance and a comparably high shear stress acting on them. The lowest resistance against cyclic slip is typically found in favorably oriented grains located at the free surface of the material, where neighboring grains are not constraining slip movements in all directions. If one

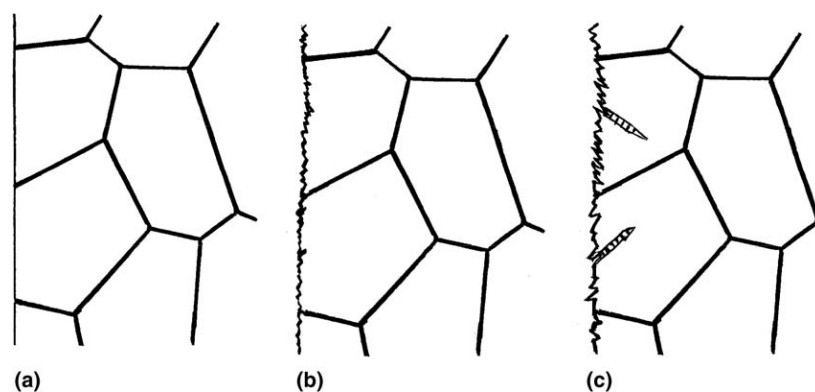


Figure 2.7: On the initiation process of surface cracks due to cyclic loading, taken from [23]. The smooth surface in the initial state (a) is successively roughening (b) until the first persistent slip bands form (c).

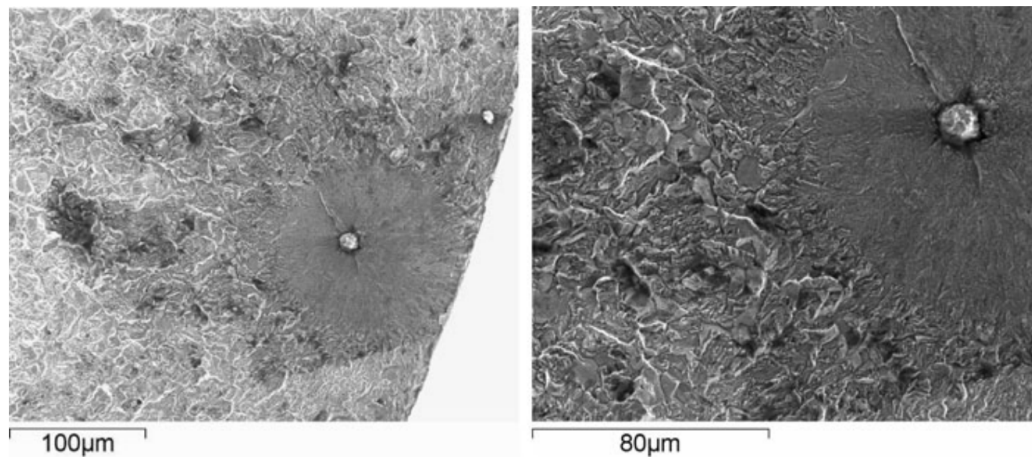


Figure 2.8: Typical fracture surface of a fish-eye crack, which formed at a non-metallic inclusion within a cylindrical test specimen of steel SNCM439, taken from [55].

of these weak grains allows for cyclic slip to occur, a step will be generated on the free surface of this grain. In most applications, the free surface will be surrounded by a gas or a liquid which will react with the fresh surface exposed by the step resulting in an oxide layer almost instantly covering the step. Due to the oxide layer and the additional effect of strain hardening on the acting slip plane, the step will not be fully reversed during the following load reversal. Instead the acting shear stress will be increased due to the additional constraint. As a consequence, slip processes on parallel planes might be activated, leading to a successive progression of step generations on the free surface. Eventually, the stress concentrations at the roots of these steps will trigger the activation of slip systems at adjacent grains in the subsurface regions, leading to the generation of a macro-crack and concluding the phase of crack initiation.

In the case, where the critical crack initiates at a non-metallic inclusion – typically between 10 to 100 μm of size [14] – the initiation process is governed by an interaction between cyclic slip in the grains, and the inclusion itself. The presence of the inclusion influences the stress distribution on a micro level and often leads to the formation of so-called fish-eye structures, as shown in Fig. 2.8, often in combination with a surrounding thin layer of submicron-sized grains (fine granular area, optical dark area). The details of the internal crack initiation process are still a subject of research and are not fully understood yet, see also the corresponding discussion in [56].

The initiation of a crack under low-amplitude loads is often considered a threshold problem. While failure under high-amplitude loads (LCF), as a process driven by crack propagation, is essentially just a matter of time, high-cycle fatigue is conditioned on whether or not the applied loads are high enough for at least one micro-crack to overcome the obstacles of its surrounding microstructure, and grow into a macro-crack. An important term, frequently encountered in this context is the fatigue limit, sometimes also called endurance limit. The notion of a fatigue limit, which goes back to the work of Wöhler [11], reflects the idea, that, for certain materials, there exists a threshold stress, which is defined by the characteristic, that cyclic loads with an amplitude larger than the fatigue limit will eventually lead to failure, while cyclic loads of lower amplitude will not, no matter how many stress cycles are applied. In a stress-life plot (SN -diagram), more

elaborately introduced in Section 2.5, the fatigue limit was typically associated with lives around 10^6 cycles, see also the “conventional fatigue” limit in Fig. 2.6. Consequently, the stress associated with approximately 10^6 cycles by the SN -curve was considered a good estimate for the fatigue limit. Today, many researchers in the field of high-cycle and especially very-high-cycle fatigue share the opinion, that if a considered material attributes a fatigue limit, then it will be associated with much higher lives than 10^6 cycles, see for example [21, 22, 57]. In this understanding, the classical fatigue limit is merely a plateau in the SN -curve, followed by a further decrease of the graph as shown in Fig. 2.6. For many applications, however, the classical fatigue limit remains a useful design parameter. This holds true, particularly for those applications, where the anticipated number of collected load cycles is highly unlikely to surpass the life associated with the conventional fatigue limit. That being said, there still remains a number of situations where this estimate cannot be made, and the accumulated number of cycles might very well end up in the gigacycle regime, far beyond the conventional fatigue limit.

It must be pointed out that not all metals exhibit a conventional fatigue limit, meaning a distinct plateau in the SN -curve after a few million cycles. This kind of SN -curve characteristic is associated with metals that show a body-centered cubic lattice structure with interstitially dissolved atoms [21]. Typical representatives are ferritic steels and titanium alloys. On the other hand, metals with a face-centered cubic lattice structure are associated with the lack of a classic fatigue limit. Instead, their SN -curve exhibits a continuous decrease, in the region where the classical fatigue limit is typically encountered [21]. Typical representatives for this second class are austenitic steel and aluminum alloys, see also Chapter 2 in [58]. In this work, the term “fatigue limit” will be mostly avoided. Instead, the more general notion of a N_{ref} -fatigue strength will be used, which simply refers to a stress or specified load amplitude, which, when applied to the considered structure, results in an expected life of N_{ref} cycles. For the benefit of a simpler notation, the term will be frequently used without the N_{ref} -prefix, that is “fatigue strength” instead of “ N_{ref} -fatigue strength”. However, even when not mentioned explicitly, the fatigue strength always relates to a reference number of cycles N_{ref} . The notion of the fatigue strength will be discussed in more details in the next section.

2.4 The fatigue strength of an engineering component

The fatigue strength of a material is often determined by conducting fatigue tests on unnotched test specimens under simple loads in ambient conditions, see also Section 2.6. However, when considering an engineering component subjected to its application-typical loads, one usually finds a very different situation compared with the one tested in the laboratory. These different conditions can be described in terms of influences that affect the fatigue strength. It is the purpose of this section to provide a brief overview of the most important effects among these influences. Emphasis is put on geometry related and mean stress effects, which are addressed by the model presented in this work.

The probably most striking difference between the laboratory tests on the one hand, and the loaded engineering component on the other, is the typically very different geometry of the component compared to the test specimen. While the latter is often a small unnotched cylindrical or sheet-like coupon, the former is usually of much more irregular shape featuring several structural discontinuities such as notches, fillets or steps. When the component is subjected to some kind of design load, the structural features result in

complex stress fields forming throughout the component, exhibiting stress concentrations around structural discontinuities. The severity of notch-induced stress concentrations in terms of their effect on the fatigue strength of the notch-containing component is frequently described using the two parameters

$$K_t = \frac{\text{peak stress at notch root}}{\text{average section stress}} \quad \text{and} \quad K_f = \frac{\text{fatigue strength without notch}}{\text{fatigue strength with notch}} \quad (2.24)$$

where K_t is called the elastic stress concentration factor and K_f the notch fatigue factor, cf. Chapter 5 in [53]. While both parameters are well defined for notched test specimens, it is often difficult to define them for components that look very different. With respect to K_t it might be problematic to identify a notch section for averaging the stress, while it may be unclear how to define the considered component “without notch” considering the definition of K_f . However, for several components these parameters are useful, hence they still appear in design codes, see for example [59]. The existence of a notch almost always reduces the fatigue strength, so that $K_f \geq 1$. The greater K_f the more severe the effect of the notch. An upper limit is established by the elastic stress concentration factor, so that $K_f \in [1, K_t]$. The case $K_f = K_t$ corresponds to the rather conservative assumption where the fatigue strength is a local quality, i.e. a geometry independent material property, so that only the peak stress at the notch root determines whether or not the component fails. This can be the case for very brittle materials. In most cases, however, one finds $K_f < K_t$ – an effect which is referred to as the notch support effect.

When the fatigue strength is not considered a local quantity, it has to be stated in non-local terms. In practice, this means that the fatigue strength of a component, which is a scalar value, has to be interpreted as the magnitude of a specific design load or corresponding stress field. In the case of a notched test specimen under uniaxial tension-compression loads this reference is typically provided by nominal stresses, i.e. the average mean stress and the average stress amplitude in the notch root section. In the case of a compressor blade which is vibrating in a specific eigenmode, say mode 1, one could use the effective stresses at a predefined monitor point, say point P , to describe the fatigue strength. More specifically, one could express the fatigue strength of the compressor blade under mode-1 vibrations by stating: The mode-1 fatigue strength of the compressor blade is reached when the von Mises stress amplitude in monitor point P reaches 100 MPa while vibrating in mode 1. In other words, the fatigue strength of a component must always be expressed in the context of the corresponding load case.

Next to its different shape, the component is often of considerably different size, i.e. has a smaller or greater volume than the test specimen. In this context one has to make the following distinction. While the total volume of most components is greater compared to the typically small test specimens, the highly stressed volume around stress concentrations in notched components is often much smaller than the test specimen volume. The influence of these size-related aspects on the fatigue strength is commonly referred to as size effect. In a narrower sense, the size effect refers to the variation of the fatigue strength of a specified component under a given loading, when scaling both, geometry and load at the same time, so that the stress state at each point remains the same. The resulting effect may be categorized into the statistical, geometrical, technological and surface-technological size effect, cf. [60, 61]. The latter two effects refer to the manufacturing process. With increasing dimensions of the semi-finished product, the fatigue strength decreases as it becomes more difficult to ensure the same tolerances and

surface conditions for larger components compared with smaller ones. The statistical size effect accounts for the increased probability to find a critical defect in the highly stressed region of the component when its size increases. The geometrical size effect on the other hand refers to the decrease of spatial stress gradients in non-constant stress fields with increasing component size. As a result, the fatigue strength decreases, since the supporting effect of the gradient is reduced, compare also [62].

The second major influence to be addressed, next to the geometry related contributions, is the mean stress effect. As it was described in Section 2.2, the mean stress quantifies the stationary part of the stress history during one load cycle. It plays an emphasized role in the assessment of many high-cycle fatigue related applications, since it typically has a detrimental effect on the fatigue strength. More precisely, a tensile mean will in most cases reduce the fatigue strength of a metal component, while a compressive mean stress typically increases it. This influence will be discussed in more detail in Section 2.5. For many high-cycle fatigue phenomena encountered in turbomachinery, like the vibration of compressor blades as discussed in Section 2.1, the magnitude of the mean stress is closely related to the rotor speed, and therefore easier to predict than the stress amplitudes [63]. With respect to the last paragraph, it should be pointed out, that also the mean stress has to be considered in context of its load shape when referring to a notched component. If tensile mean stresses become very high, especially under high temperatures and long periods of application, the material might creep [63], which poses a non-trivial problem in its own right, and is outside of the scope of this work.

Two other influences related to the applied loading are the waveform and the load frequency. The waveform or waveshape relates to the graph of the dynamic part of the load, see Fig. 2.4. In fatigue testing one typically applies the cyclic loads with an approximately sinusoidal waveform. However, in practice, the encountered shapes might be very different. Saw tooth or block shaped waves are just two examples. The effect on the fatigue strength is hard to quantify, and depends on the specific application. In many cases, no test data will be available on this specific effect. Considering the vibration of a gas turbine compressor blade, measurements conducted at Siemens – where the author was employed during the work on this thesis – show, that a sinusoidal waveform is a good approximation. In the literature, the influence of the waveform is associated mostly with low-cycle fatigue [64], particularly in the context of corrosion effects cf. [14], Section 2.5.7. The general situation appears to be clearer when considering the effect of the load frequency. In most analyses reported in the literature it is found that the fatigue strength increases with increasing load frequency. For example, Harris demonstrated this effect for the aluminum alloy AlCuMg2, while Morrissey et al. reported the same trend for the titanium alloy Ti-6Al-4V [65]. In other studies, such as the one by Beck et al. regarding the ferritic-martensitic steel X10CrNiMoV12-2-2 [66], no significant frequency effect were measured. The frequency influence becomes relevant, when the load frequencies of the considered application are very different, especially when they are lower, compared to the test-load frequencies used to determine the materials' fatigue strength.

The last load-related influence to be addressed is the effect of additional cyclic load components with different amplitudes than the one considered in the high-cycle fatigue design. Under these circumstances, which occur – at least to some extent – in almost all applications, one is no longer facing a constant-amplitude but a variable-amplitude load case. In the high-cycle fatigue related literature, the corresponding effects are frequently discussed in terms of HCF-LCF interactions, see for example [67, 68], as well as random

load spectra, see [69, 70]. It is typically difficult to account for such conditions in the design phase, since it requires both detailed knowledge on the expected loading as well as a validated material model for variable-amplitude loads. As a consequence, the participating fatigue modes are often considered individually in the framework of conservative constant-amplitude assessments. In this work, effects resulting from variable-amplitude loads are not accounted for.

The next influence to be covered is the temperature effect. Since most material properties change with temperature it is not surprising that the fatigue strength as a strongly material dependent property is a function of temperature as well. The effect of a, compared with ambient conditions, elevated temperature on the fatigue strength is usually detrimental with very few exceptions, cf. Chapter 17 in [14]. Consequently, it is important to conduct a fatigue assessment based on test data that corresponds to the temperature encountered in the considered application. In combination with elevated mean stresses applied over long periods of time, high temperatures, as mentioned before, can result in creep phenomena.

Another important influence to be mentioned is the condition of the component surface, see for example [71]. As discussed in Section 2.3 cracks often initiate at or close to the surface, hence it comes at no surprise, that the state of the surface has an influence on the fatigue strength. In order to obtain a component with a high fatigue strength it is important to ensure a smooth component surface, without scratches or pits. This is typically achieved by polishing the surface. However, one has to take into account that this initial state of the component is likely to change during operation. Consequently, one cannot design a component assuming a polished surface at all times, even if this is its initial state. Next to the surface finish, the surface condition can be manipulated in other ways. By surface treatments like nitriding or shot peening one can alter the surface properties chemically or by introducing compressive residual stresses. Another approach is to apply a coating to protect the surface during operation. Obviously such surface enhancements need to be accounted for in the design phase.

Finally, it should be mentioned that for several applications also influences from the environment exist. A typical example is the medium (air, fresh or salt water, etc.) surrounding the component, which additionally might promote corrosion of the considered material. Another example is the interaction with debris, like sand – a typical problem in the design of aircraft jet engines [72].

2.5 Standard lifing diagrams in high-cycle fatigue

High-cycle fatigue test data is often presented in lifing diagrams. The purpose of these diagrams is to graphically show the influence of specific parameters on the fatigue strength of a test specimen – in many cases an unnotched coupon. In this section, two of the most common lifing diagrams used in the field of high-cycle fatigue will be introduced, the stress-life diagram and the Haigh diagram.

The stress-life diagram, frequently called SN -diagram or – mostly in the German literature – Wöhler diagram, reflects the relationship between the stress amplitude (S) which is applied to the considered test specimen, and the resulting number of load cycles (N) until failure occurs. The latter is commonly referred to as the specimen life and often denoted by N_f . Obviously, the expected life increases with a decreasing stress amplitude. In this context, one finds that for most metals there exists a life interval I_{HCF} in the

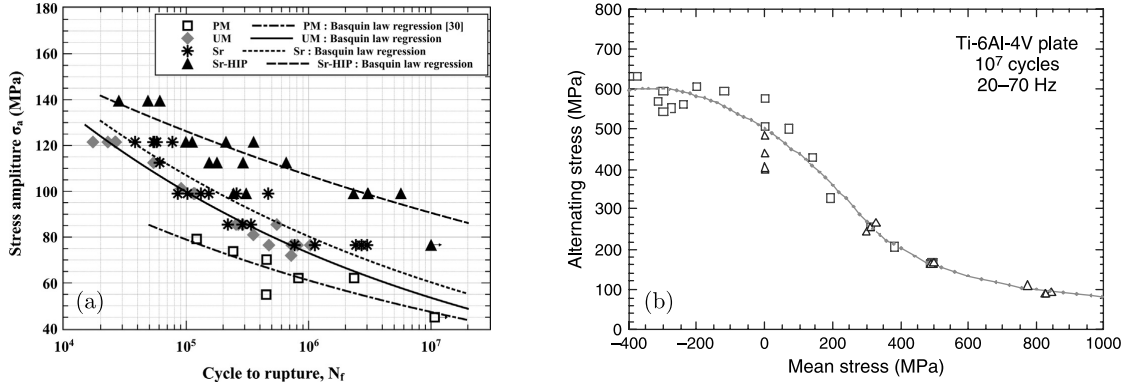


Figure 2.9: A typical SN -diagram (a) with Basquin fits for different aluminum alloys, taken from [74], and a Haigh diagram (b) for a titanium alloy, taken from [53].

high-cycle fatigue regime $I_{HCF} \subset [10^5, 10^8]$, where this general trend of “the lower the stress amplitude, the longer the life” can be adequately described by a simple power law

$$\sigma_a = aN_f^b \quad \text{for } N_f \in I_{HCF} \quad (2.25)$$

when the two parameters $a > 0$ and $b < 0$ are fitted to the test data, see Fig. 2.9a for some examples. Since Eq. (2.25) describes an affine function in the $\log \sigma_a$ - $\log N_f$ space, such a fit can be obtained by simple linear regression. While Eq. (2.25) is frequently referred to as Basquin’s law [73], the two parameters a, b are sometimes called Basquin coefficient and Basquin exponent respectively. It should be pointed out that both parameters are functions of the various influence parameters that have been mentioned in Section 2.4, which means that they vary for example with mean stress or temperature.

The second lifing diagram that should be discussed is the Haigh diagram [75], see Fig. 2.9b. A Haigh diagram is a so-called constant-life diagram, see also [24], meaning that it refers to a fixed value of N_f in contrast to the SN -diagram. In this work, the reference life of a Haigh diagram is denoted as N_{ref} . In the example shown in Fig. 2.9b one finds this reference life N_{ref} stated in the upper right corner ($N_{\text{ref}} = 10^7$). The diagram itself shows the influence of the mean stress, which is displayed on the horizontal axis, on the fatigue strength of the tested specimens, shown on the vertical axis. Note that in the example given in Fig. 2.9b the mean stress covers both compressive and tensile stresses. As mentioned before in Section 2.4, compressive stresses typically have a beneficial effect on the fatigue strength, while tensile mean stresses are almost always detrimental. It turns out that for many applications the tensile region is more important than the compressive part, which is the reason why many Haigh diagrams only show the positive part of the mean stress axis.

Several empirical formulas have been proposed aiming to describe the influence of the mean stress on the fatigue strength which is reflected by the test results, see also [24, 76]. Some of the most popular expressions, which are still used today, are the straight line approximations of Goodman [77] and Soderberg [78], as well as Gerber’s parabola [79]. They can all be expressed by the common expression

$$\left(\frac{\sigma_e}{\widehat{\sigma}_e}\right) + \left(\alpha \frac{\sigma_m}{\sigma_{\text{UTS}}}\right)^n = 1 \quad (2.26)$$

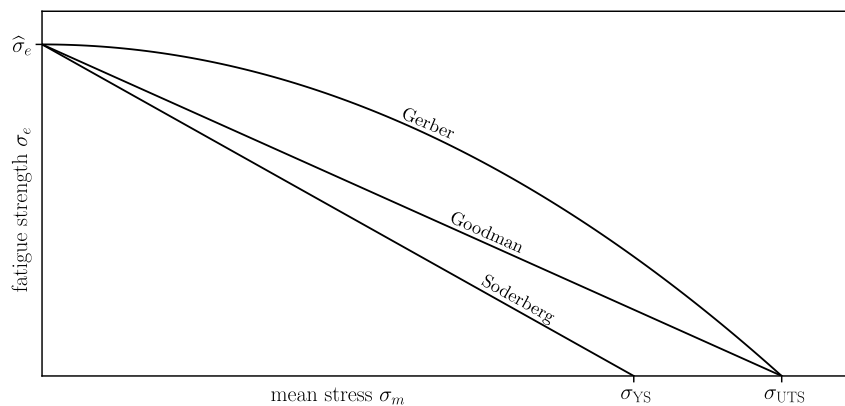


Figure 2.10: Haigh diagram with graphs representing the empirical formulas of Goodman [77], Soderberg [78] and Gerber [79].

where σ_e denotes the fatigue strength at mean stress σ_m , $\hat{\sigma}_e$ is the fatigue strength for zero mean stress and σ_{UTS} the ultimate tensile strength with respect to the considered material. Considering the two remaining parameters, one obtains the Goodman line when setting $\alpha = n = 1$, while Soderberg's formula corresponds to $\alpha = \sigma_{UTS}/\sigma_{YS}$ and $n = 1$. Finally, Gerber's parabola results from the parameter pair $\alpha = 1$ and $n = 2$. The respective graphs are shown in Fig. 2.26.

While several empirical models for describing the fatigue strength over the mean stress exist, it is often difficult to fit them to available test data. In Section 2.7 of [53] Nicholas points out “While attempts have been made to define the equation which best represents the data on a Haigh diagram [...] variability from material to material, scatter in the data, and lack of sufficient data in many cases prevent the fitting of an equation to such data.” The problem of experimentally determining the fatigue strength is addressed in the following section in more detail.

2.6 Fatigue strength testing

Any high-cycle fatigue assessment of an engineering component has to be based on some kind of test data with respect to the used material. The result derived from such test data is typically a quantification of the material's fatigue strength that corresponds to the considered design case. It is the purpose of this section to provide a brief overview on the different experimental methods that are being used to derive the fatigue strength of a given material with respect to the considered application.

In order to determine the fatigue strength of an engineering component subjected to a specified load case, generally two approaches exist. In the first approach – the direct approach – the component is fatigue tested itself [80]. The corresponding test campaign requires several replica of the component, which likely will be destroyed during the tests. While sometimes being applied for central components that are crucial from an economical or health-and-safety perspective, for example aircraft wings [81] or wind turbine blades [82], this option is not feasible in most applications for obvious reasons. Neither can it be economically justified to destructively test multiple replica of each component subjected to cyclic loads, nor is it always possible to accurately reproduce the anticipated load conditions in a test laboratory. In the second approach – the indirect approach – one therefore refrains from testing the component itself, and rather focuses

on tests with geometrically much simpler test specimens. The results of these tests are then used in the framework of specific fatigue models to infer the fatigue strength of the considered component. Due to the significantly reduced costs compared with direct component testing, the indirect approach is the standard way for most applications in terms of how the results of fatigue tests are utilized in component design. The following elaborations are therefore all relating to simple specimen fatigue tests.

The specimens, sometimes also called coupons or members, which are tested in a laboratory can have different geometries. Typically, they have a test gauge which is based either on a cylindrical or a sheet-like shape. Additionally, the test gauge might feature steps, fillets or notches, in order to experimentally study the influence of stress concentrations. If no structural discontinuities are present, the coupon is often referred to as a smooth specimen. Examples for respective specimen geometries can be found in Fig. 4.7 for cylindrical specimens, and in Fig. 4.2 regarding sheet specimens.

With respect to the test loads, one generally distinguishes between constant-amplitude tests and variable-amplitude tests. The former refers to tests where the applied stress amplitude remains constant during the test, while the latter, consequently, corresponds to test where the stress amplitude varies in time. In this work, only test results from constant-amplitude tests will be considered. Next to the stress amplitude, the second most important load parameter is the mean stress, particularly in high-cycle fatigue tests. The consideration of mean stress effects is often incorporated into the test campaigns by conducting multiple tests with different stress amplitudes either at a fixed mean stress, or at a fixed stress ratio R . Both strategies are reflected in Figs. 4.1, 4.3 and 4.4.

Another category with respect to the test loads might be referred to as the loading type. The most common loading types are tension-compression, torsion, plane-bending and rotating-bending. In tension-compression tests, sometimes also called push-pull tests, the test force is applied in the direction of the long axis of the coupon. In the case sheet specimens are used, guides might be required to prevent the specimens from buckling. For unnotched specimens, this type of test results in a uniaxial stress field throughout the test gauge. Torsion fatigue tests are conducted by realizing a cyclic torsion moment, aligned with the long axis of the, typically cylindrical specimen. Note, that the resulting stress field within the specimen is not homogeneous in this type of test. In bending fatigue tests, the test force is applied orthogonal to the long axis, resulting in a bending moment and the corresponding inhomogeneous stress field in the test gauge. While the moment vector remains constant over time in plane-bending tests, it is continuously rotating in rotating-bending tests – typically realized by rotating the specimen. Finally, it is also possible to combine different loading types in a single test. The resulting multiaxial stress fields, possibly with phase shifts and different frequencies of the contributing load types, are often much more complex than test with single load types. However, in this work, only results from tension-compression tests will be used.

In the scope of high-cycle fatigue testing, constant-amplitude, tension-compression experiments are typically conducted using servo-hydraulic, electromagnetic or piezoelectric test machines. Modern servo-hydraulic devices typically allow test frequencies around 50 Hz – in special cases up to 1 kHz [83]. Electromagnetic resonance systems are usually operating between 100 and 200 Hz, cf. [84]. Piezoelectric machines, which have been developed primarily for tests reaching into the gigacycle domain, allow frequencies of more than 20 kHz [85]. Due to specimen heating these devices are mostly operated in a pulse-pause mode, resulting in effective frequencies of 1 to 5 kHz.

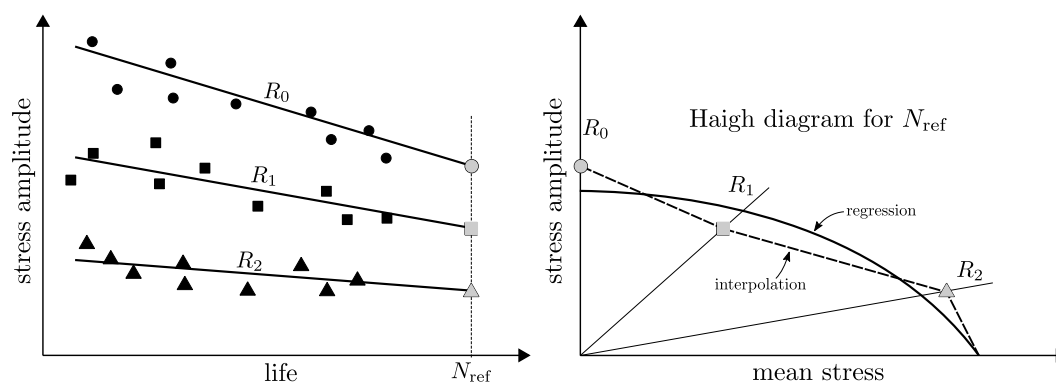


Figure 2.11: On the extrapolation method to derive a Haigh diagram from SN -curves.

When an individual specimen is tested, it is clamped into the test machine, and the loads corresponding to the stresses to be tested – mean stress and stress amplitude – are applied, typically following a sinusoidal waveform [14]. The load cycle is repeated, either until the specimen fails, or until a predefined maximum number of cycles N_{max} is reached. The latter is defined at the beginning of the test campaign due to economical reasons, and typically reflects the reference number of cycles, the fatigue strength should be derived for, i.e. $N_{\text{ref}} = N_{\text{max}}$. A specimen which did not fail before reaching N_{max} cycles is reported as a runout. In high-cycle fatigue tests, the failure of a specimen is commonly defined as its complete fracture. Since the time spent in crack propagation is typically short, cf. Section 2.3, the number of cycles until the specimen fails can be used as a reasonable approximation for the time required for crack initiation.

The test procedure described above has the fatigue life of a specimen as an outcome. However, most high-cycle fatigue assessments pivot around the notion of the fatigue strength, which is a stress value. The question arises, how test results providing the former can be used to infer the latter. In this context, it should be pointed out that it can be seen as a general inconvenience of fatigue strength testing, that it is not possible – at least not without considerable altering the testing procedure as described by the accelerated test methods presented later in this section – to experimentally obtain a realization of the fatigue strength of a test specimen in the same way as one can obtain a realization of its fatigue life. In other words, one cannot enter a specific fatigue life into the test machine, press the start button, and obtain a realization of the corresponding fatigue strength as the outcome of the following experiment. Nonetheless, several approaches have been developed in order to determine the fatigue strength of a given specimen type under these boundary conditions. They should be briefly discussed in the following paragraphs. Emphasis will be put on the so-called staircase method, since this type of testing will be addressed later in Section 5.5.

The first approach to be considered here is based on the extrapolation of an experimentally determined SN -curve, cf. Section 2.5, at the number of cycles N_{ref} the fatigue strength should be evaluated at, see for example [86]. Fatigue tests are conducted at several stress amplitudes, aiming to provide a reliable basis for a fit of the corresponding Basquin parameters, see Eq. (2.25). After the parameters are determined based on the obtained test results, the N_{ref} -fatigue strength is estimated via

$$\sigma_e(N_{\text{ref}}) = aN_{\text{ref}}^b. \quad (2.27)$$

In order to provide an estimate of the full Haigh diagram, this procedure has to be repeated for several mean stress levels or multiple stress ratios. Fig. 2.11 illustrates this process using Basquin fits for three different stress ratios. Each resulting SN -curve is evaluated at N_{ref} and the corresponding stress amplitudes – which are now interpreted as the N_{ref} -fatigue strengths – are copied into the Haigh diagram at the respective stress ratios. Finally, the design line is obtained by either defining some kind of regression with respect to the derived data points, or by linearly interpolating between them. The advantages of this deterministic method, cf. Section 2.7, are its simplicity with respect to the required tests – no specific test procedure must be followed – and its conservativeness. The reason for the latter is due to the typically decreasing slope of the SN -curve in the high-cycle fatigue regime, cf. Fig. 2.6, which might end up being close to horizontal for materials with a conventional fatigue limit. In these cases, the fatigue strength will likely be underestimated when extrapolating it with Eq. (2.27). While this conservativeness can be seen as an advantage, making the method save to use in a design context, it must also be considered a disadvantage regarding its tendency to over-engineering.

The next approach to be discussed refers to a group of procedures that are summarized under the term of accelerated or rapid test methods, see Chapter 3 in [53]. Two popular representatives of this group are the methods of Prot [87] and the step-method introduced by Nicholas [88]. Also the fatigue limit estimation associated with the more recently published PhyBal method [89] should be mentioned in this context. The concept of Prot's method is to fatigue test a specimen beginning with a stress amplitude that is expected to be smaller than its fatigue strength, while increasing the stress amplitude during the test at a given rate until failure occurs. This test procedure is repeated for several specimens, using progressively smaller stress rates. By assuming a relationship between the corresponding fracture stresses, the numbers of cycles to failure and the stress rates, the fatigue strength can be estimated. In Nicholas' step-method, on the other hand, only one specimen is required to derive a realization of the corresponding fatigue strength. Over several test blocks, the specimen is tested in conventional constant-amplitude fatigue tests for N_{ref} cycles. Beginning with a stress amplitude that is expected to be lower than the fatigue strength, it is increased after each block that the specimen survives. Eventually, the specimen will fail and the correspondingly interpolated stress amplitude will be interpreted as its fatigue strength. More details can be found in [53, 86]. The major advantage of these methods is the significantly reduced number of required test specimens. The disadvantages include the more complicated test procedure, and possible understressing effects of the stress history on the fatigue strength. Especially the last point, which is also referred to as coxing, is discussed at length by Nicholas in [53]. One has to make sure that the fatigue strength is not increased by the previous loads below the fatigue strength, which would lead to its overestimation. In [86] it is shown, that this does not seem to be the case for the investigated titanium alloy. However, when applied for a new material, one will first have to experimentally show, that the method is safe to use by comparing it with conventional methods. When used for the determination of the full Haigh diagram, several tests have to be conducted under multiple mean stresses or stress ratios. The results can then be used for regression or interpolation models as discussed in the extrapolation method above, and as illustrated in the right plot of Fig. 2.11.

The last two approaches were aiming to provide a single value for the fatigue strength under specific load conditions. The next two methods, on the other hand, are aiming

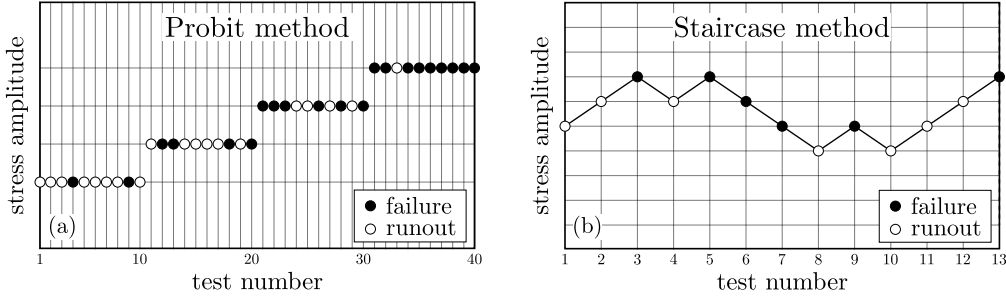


Figure 2.12: On the test schemes used in the probit method [90] and the staircase method [43] in order to determine the fatigue strength distribution.

to determine the fatigue strength in terms of an underlying distribution, assuming that the fatigue strength of the considered specimen can be modeled as a random variable. In the literature, mostly two types of distributions are used in order to describe the scatter in the fatigue strength – the normal distribution, see for example [91], and the extreme value distribution, typically in the form of a two- or three-parameter Weibull distribution, cf. [92]. The latter is defined in terms of its distribution function $F_{\mathcal{W}}$ by

$$F_{\mathcal{W}}(\sigma_e | \hat{\sigma}_e, \sigma_e^{\text{th}}, k) = 1 - \exp \left\{ - \left(\frac{\langle \sigma_e - \sigma_e^{\text{th}} \rangle}{\hat{\sigma}_e} \right)^k \right\} \quad (2.28)$$

where σ_e denotes the fatigue strength, $\hat{\sigma}_e$ the fatigue limit scale, σ_e^{th} the fatigue limit threshold and k the fatigue limit scatter parameter. The operator $\langle \cdot \rangle$, sometimes referred to as Macaulay brackets, is defined by $\langle x \rangle = \max\{x, 0\}$. Note that in many cases, a two-parameter instead of a three-parameter Weibull distribution is considered, which is characterized by $\sigma_e^{\text{th}} = 0$.

A classic approach for determining the fatigue strength distribution is the so-called probit method, which was introduced by Finney [90, 93] in the context of the analysis of toxicity data. An application with respect to fatigue strength testing can be found in [94, 95]. It is a quantal response analysis based on repeated testing under the same conditions, see Fig. 2.12a. At the beginning of the tests, a number of m load levels $\sigma_{a,i}$ with $i \in \{1, \dots, m\}$ regarding the applied stress amplitude are defined. Each of these load levels will then be tested for a specified number of test specimens. The outcome of each test is interpreted from a binary perspective with respect to the predefined runout number of cycles N_{max} . If a specimen fails before reaching N_{max} , it is considered a failure. The specific number of cycles until failure, however, is not of interest. If the specimen does not fail before accumulating N_{max} cycles, it is reported as a runout. This binary data is then used to derive the observed failure probabilities $P_{f,i}^{\text{exp}}$ for each load level $i \in \{1, \dots, m\}$. The latter can be computed either directly in terms of the empirical failure probabilities, or they can be estimated for example using median ranked probabilities, cf. [96]. The observed failure probabilities can then be used as a basis for fitting a parametric probability distribution F , for example by using linear regression on probability paper, or – more formally – by minimizing the error function

$$E(\theta) = \sum_{i=1}^m \left(P_{f,i}^{\text{exp}} - F(\sigma_{a,i} | \theta) \right)^2 \quad (2.29)$$

where θ denotes the parameter vector of the considered distribution F . For example, in case of a Weibull distribution Eq. (2.28) one would have $\theta = (\hat{\sigma}_e, \sigma_e^{\text{th}}, k)$. Note however, that the probit method is typically associated with a normal or log-normal distribution. In order to approximate the full Haigh diagram, the procedure has to be repeated for several mean stresses or stress ratios. The design curves can then be obtained by interpolation or regression with respect to specific quantiles. Conceptually very similar to the probit approach are the two-point method [96, 97] and the $\text{ArcSin}\sqrt{P}$ -method [98], which also rely on empirical probabilities derived from repeated testing of different load levels.

The last approach presented here, is called staircase testing, sometimes also referred to as up-and-down testing, cf. [43, 99–101]. Beginning with an arbitrary stress amplitude, typically reflecting the best guess for the fatigue strength median, specimens are tested sequentially by means of constant-amplitude tests with a predefined maximum number of cycles N_{max} . After a test has finished, the applied stress amplitude of the next test is determined depending on the outcome of the previous test, cf. Fig. 2.12. In case of a previous failure the stress amplitude of the following test is reduced by a predefined step size, while the stress amplitude is analogously increased if the last test specimen survived the maximum number of cycles, cf. Section 3.4 in [53]. After all tests have been conducted, the underlying fatigue strength distribution – which is assumed to be a normal distribution with mean value $\sigma_{e,\mu}$ and standard deviation sd – is determined via

$$\sigma_{e,\mu} = \sigma_a^{\text{min}} + \left(\frac{B}{A} \pm 0.5 \right) s \quad \text{and} \quad \text{sd} = 1.62 \left(\frac{AC - B^2}{A^2} + 0.029 \right) s \quad (2.30)$$

$$\text{with} \quad A = \sum_{i=0}^{i_{\text{max}}} f_i \quad B = \sum_{i=0}^{i_{\text{max}}} i f_i \quad C = \sum_{i=0}^{i_{\text{max}}} i^2 f_i.$$

The above formulas, which reflect an approximation of a maximum likelihood estimate [43], are applied with respect to the test result that occurred less often during the tests. If failures occur less often, the equation for $\sigma_{e,\mu}$ must be used with the “+” sign, otherwise with the “−” sign. In Eq. (2.30) σ_a^{min} denotes the stress amplitude of the lowest stress level where the specified outcome occurred at least once. The index $i \in \{0, \dots, i_{\text{max}}\}$ enumerates the stress levels beginning from $i = 0$ at σ_a^{min} to i_{max} as the highest stress level that includes the considered outcome, while the integers f_i represent the respective numbers of occurrence. The remaining parameter $s > 0$ denotes the step size, that is the difference between the equidistant load levels. Finally, it should be pointed out that the formula for sd is only applicable if $(AC - B^2)/A^2 > 0.3$ holds. More details can be found in [43, 53, 102]. Similar to the approaches presented before, the staircase test method has to be conducted for several mean stress levels or stress ratios in order to obtain a basis for an approximation of the full Haigh diagram.

Since the staircase method will be in the focus of Section 5.5, some more detailed background information should be provided at this point. The staircase approach is often associated with the names Dixon and Mood, who were the first to analyze the method from a statistical point of view in the context of explosives testing in 1948 [43] and who proposed the evaluation using Eq. (2.30). The authors claimed that it required fewer tests, than the probit method, which was the respective reference at the time. It was not until the 1970s when the method was associated with fatigue strength testing, dating back to several publications of Little [100, 100, 103]. In their original work, Dixon and Mood, who assumed the variate of interest to be normally distributed, analyzed stair-

cases with numbers of tests in the order of 40 to 50. Since these were rather large sample sizes for many applications (resulting in high costs), efforts were focused on the suitability of smaller sample sizes with respect to their potential of inferring the underlying distribution. Brownlee et al. [99] pointed out that the Dixon and Mood method provided reasonable estimates for the expected value of the underlying distribution, when sample sizes of only 5 to 10 tests were used. This result, however, was conditioned on good choices of both the first test value, and the step size. If these requirements were not met, it was found that the Dixon and Mood estimate for the expected value suffered from a bias. Proposals for a correction of this bias were published by Brownlee et al. [99] as well as by Dixon [104] and Little [103]. Since then, the problem of estimating the distribution mean by evaluating a staircase scheme is considered to be adequately solved, cf. Chapter III in [105] and the more recently published study by Müller et al. [106].

However, while the work on a staircase based mean estimation is considered mostly concluded, the situation is very different with respect to the estimation of the fatigue strength scatter parameter. While analyzing the Dixon and Mood method, Brownlee et al. [99] pointed out that even under optimal conditions over 200 test points would be required to estimate the standard deviation of the underlying normal distribution within 20% at a confidence of 95%. Consequently, since Little's Bias correction in 1972, most of the proposed improvements of the staircase methodology were aiming to augment its poor estimation qualities considering the scatter parameter. In context of the Dixon and Mood framework, Svensson et al. [107] proposed a correction of the estimated standard deviation as a function of the number of tested specimens. Braam and van der Zwaag [98] considered a correction based on both step size and number of specimens. Fang et al. [108] corrected the Dixon and Mood standard deviation estimate by taking into account the SN -behavior of the considered material, while Rabb [109] proposed to include the statistical size effect. Pollak [105], who evaluated the previously mentioned corrections, excluding the approaches of Fang et al. and Rabb, proposed a standard deviation correction of his own, where he used an analytical expression to alleviate the bias, and a bootstrapping approach to reduce the estimate scatter, cf. [105, 110]. However, in spite of all the proposed scatter corrections, a simulation study published by Wallin in 2010 [111] comes to the conclusion that "the normal staircase test is not capable of providing reliable information regarding the scatter or underlying distribution". A quite similar result was obtained in 2017 by Müller et al. [106] whose comparison study also included evaluation techniques from German literature, such as the approach proposed by Deubelbeiss [112] and Hück [113]. A bad estimate of the scatter parameter translates into bad estimates for small fatigue strength quantiles, which are of interest to the designer of a component. This is the reason why the quality of the scatter parameter estimate is important. Note that the drawback of the staircase method concerning the estimation of the scatter parameter persists when the considered variate follows a non-normal distribution like the Weibull distribution stated in Eq. (2.28).

A major disadvantage of both the staircase evaluation as well as analyses based on experimentally observed failure probabilities in the context of applying them to existing test databases, is the requirement of test data with a specific format. The probit methods and related approaches require test results from repeated tests at several load levels, while the staircase approach expects the test data to follow its characteristic up-and-down system. If the available test data is not in the respective format, these evaluation methods cannot be applied.

2.7 Deterministic vs. probabilistic design approaches

While the previous sections have mostly been focused on load conditions and the corresponding material strength in the context of high-cycle fatigue, this section, and the following one, will be discussing how both of these aspects can be brought together in the framework of a component's design. The current section will approach this problem from a more general perspective, considering what might be referred to as the underlying design strategy or design mode. In this context, mostly two strategies exist – the deterministic and the probabilistic design approach. Since this work is specifically focused on a probabilistic method, the corresponding advantages and disadvantages compared to the deterministic alternative will be outlined and discussed.

In the field of engineering, a probabilistic design approach [114] describes a way to assess the adequacy of a proposed design with respect to the expected load conditions in terms of a continuous measure regarding the probability of failure, in contrast to a binary adequate/non-adequate assessment. The latter is often referred to as the deterministic method. More precisely, the result of a probabilistic design assessment with respect to a given component is a probability of failure $P_f \in (0, 1)$ or, alternatively, a probability of survival $P_s \in (0, 1)$. The latter, which is often referred to as the component's reliability, is related to the component's failure probability P_f via $P_s = 1 - P_f$. The deterministic method can be interpreted in these probabilistic terms, by describing its result as a prediction of definite failure $P_f = 1$ or definite survival $P_f = 0$. In this way, the difference between both methods may be expressed via

$$\begin{array}{ll} P_f \in (0, 1) & P_f \in \{0, 1\} \\ \text{(probabilistic)} & \text{(deterministic)} \end{array} \quad (2.31)$$

where the round braces indicate an open interval, while the curly braces denote a set. Principally, $P_f \in \{0, 1\}$ are valid outcomes of a probabilistic analysis as well. However, they will almost never be obtained for the assessment of a real-world design problem, since they reflect no remaining uncertainty, which is a deterministic characteristic.

Probabilistic design approaches, or more generally risk assessment approaches [115], are not unique to the fatigue design of structures. While originally introduced in an engineering context by the nuclear energy industry in the 1950s and 1960s, cf. [37] and [116], today, they can be found over a broad spectrum of engineering disciplines, such as the aerospace [117] or energy sector [118] as well as in civil [119] and chemical engineering [120].

According to a literature study conducted by Doorn and Hansson [37] the most frequently mentioned advantages of probabilistic approaches to risk assessment can be summarized within four, sometimes overlapping, categories.

1. **Improved model precision** By describing design parameters as random variables with an underlying probability distribution (a typical feature of a probabilistic design approach) as opposed to a constant value, a physically more adequate and therefore more precise model is obtained.
2. **Economic optimization** In order to save resources and avoid unnecessarily conservative designs, probabilistic approaches – which in this context need to claim to be more accurate – allow for the reduction of large safety factors associated with deterministic approaches.

3. **Optimization capability** Since the derived overall risk for the considered application is in most cases the composition of several sub-risks stemming from different sources, a probabilistic analysis enables the identification of the largest contributors. These insights can then be used to focus on specific mitigations or for setting up corresponding maintenance schemes. Moreover, in a design context, these risk sensitivities can be used for optimization purposes.
4. **Decoupled decision making** Since the result of a probabilistic assessment is a failure probability, a second step is required in order to decide if the risk is acceptable or not. This division, so the argument, decouples the scientific risk analysis from the non-scientific process of decision making. Through this constellation, the assessment procedure should be protected from being manipulated in order to meet predetermined decision objectives.

In their analysis of these four arguments, Doorn and Hansson arrive at the conclusion, that in many applications only the capability of sensitivity studies (the third point above) is valid, while the other three arguments are often not justified. The reason why these other arguments often fail to hold, especially the first two, can be traced back to a common cause, which is in many cases the central problem of a probabilistic assessments. Since this point is also important for the considerations undertaken in this work, it should be clearly emphasized here. Probabilistic assessments can only be as precise as the input data is able to reflect its most important statistical properties, and as the used models are adequate for describing the considered phenomenon. However, both the input data as well as the utilized models are often associated with considerable uncertainty, due to either a lack of data, a lack of insight into the modeled problem or both. The missing information with respect to the input data is often substituted with best guesses disguised under the term of “expert knowledge”, cf. [121]. This means that both the distributions used for describing the sparsely or even unavailable input data as well as their defining parameters are chosen by the person who performs the assessment. Maybe even more problematic is the compensation for a lack of insight in the problem at hand. The solution is often a considerably simplified model which is used with little or even entirely without validation. Almost all non-trivial probabilistic assessments will have some of these ingredients to a certain amount. After all, each model is a simplification of the physical reality, and each input distribution will merely approximate the available data. However, if these properties dominate the probabilistic input, the produced results of the assessment are virtually meaningless. It is hence crucial for the value of the result of a probabilistic assessment to critically evaluate the processed input as well as the used models with respect to their inherent uncertainty. If reliable input is provided and validated models are being used, the first two advantages of probabilistic assessments listed above certainly hold.

Considering the last point stated in the aforementioned list, Doorn and Hansson found that the promoted separation of risk assessment and decision making is often found to be non-existent. In fact, in many cases they examined, the same people who conducted the risk assessment were also responsible for the following decision making. This, however, is typically not the case when it comes to probabilistic design in engineering applications. Here, a related but different problem arises. Even though failure probability for a new design might be available, the lack of an agreed risk threshold (acceptable risk) prevents the explicit consideration of the derived probabilities.

2.8 Current approaches to design against high-cycle fatigue

In today's industrial design practice with respect to high-cycle fatigue, different methodologies are in use, compare [122]. The specific choice of the approach, depends on many factors like the load conditions encountered in the respective field of application, the component's geometry, the amount and type of available material test data, or even the design methodology that has been used in the past.

The various methods can be categorized from several perspectives. One possibility, which has been discussed in the previous Section 2.7, is the distinction between probabilistic and deterministic methods. Another differentiation, which is considered in this section, refers to the scope of spatial stress information, that is taken into account by the corresponding design approach. In this context, one might distinguish between local and non-local methods. In local approaches, each location on the component is assessed individually without taking into account the variation of the stress state in its vicinity. These approaches will be discussed in Section 2.8.1. Non-local approaches on the other hand typically have a broader scope and take into account specific features of the component's highly stressed regions. A brief survey on these approaches, focusing on deterministic representatives, is provided in Section 2.8.2. The central methodology with respect to this work is the so-called weakest-link approach. It can be interpreted as a probabilistic non-local method. Due to its central role for this thesis, it is discussed separately in Section 2.8.3, covering both a formal introduction of the underlying theory as well as a concise literature review focused on recent developments.

2.8.1 Local methods

Due to their conceptual simplicity and conservative tendency, many design approaches that are used in industry are based on local methods – often in combination with non-local corrections as it will be discussed in Section 2.8.2. Local methods are characterized by their property of assessing the sufficiency of a component's fatigue strength in a point-wise fashion. Several specific examples are given in this section.

Consider an engineering component C with volumetric domain $V_C \subset \mathbb{R}^3$ under a design load resulting in the stress tensor field $\boldsymbol{\sigma}$, see Eq. (2.1). In a local assessment, the component is expected to withstand the design load if the condition

$$\gamma_s \sigma_a^{\text{eq}}(\boldsymbol{\sigma}(\mathbf{x}, [0, T])) \leq \sigma_e(\sigma_m^{\text{eq}}(\boldsymbol{\sigma}(\mathbf{x}, [0, T]))) \quad \forall \mathbf{x} \in V_C \quad (2.32)$$

is satisfied. Here, $\sigma_a^{\text{eq}}(\boldsymbol{\sigma}(\mathbf{x}, [0, T]))$ denotes the equivalent stress amplitude, see Section 2.2, at $\mathbf{x} \in V_C$ while $\sigma_e(\sigma_m^{\text{eq}}(\boldsymbol{\sigma}(\mathbf{x}, [0, T])))$ refers to the material's fatigue strength which might be expressed as a function of the equivalent mean stress at the considered location. The remaining parameter $\gamma_s \geq 1$ is a safety factor, depending on the respective application. The condition in Ineq. (2.32) expresses that the local equivalent stress amplitude must remain below the corresponding fatigue strength at all locations of the considered component. It should be pointed out, that the general condition given in Ineq. (2.32) is often expressed in the more specific form

$$\gamma_s \sigma_{a,m}^{\text{eq}}(\boldsymbol{\sigma}(\mathbf{x}, [0, T])) \leq \sigma_e \quad \forall \mathbf{x} \in V_C \quad (2.33)$$

where the mean stress dependence of the material's fatigue strength is accounted for in the correspondingly adjusted equivalent stress amplitude $\sigma_{a,m}^{\text{eq}}(\boldsymbol{\sigma}(\mathbf{x}, [0, T]))$, cf. Eq. (2.23).

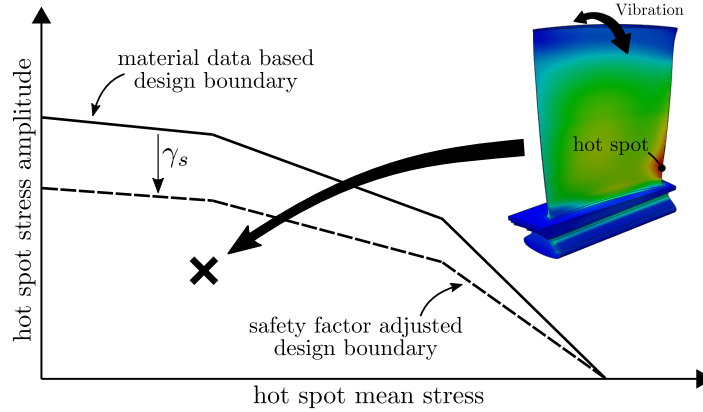


Figure 2.13: The concept of the local design approach using the hot-spot stresses in combination with a Haigh diagram. In this case, the design would be accepted since the hot-spot stresses indicated by the cross lie within the design bounds represented by the dashed line.

While the conditions expressed in Ineqs. (2.32) and (2.33) require an examination of all $\mathbf{x} \in V_C$, in practice, this check often reduces to a single point – the critical location. Using Ineq. (2.33), the critical location $\mathbf{x}_{\text{crit}} \in V_C$, which is also called hot or weak spot in the literature, is defined by

$$\sigma_{a,m}^{\text{eq}}(\boldsymbol{\sigma}(\mathbf{x}_{\text{crit}}, [0, T])) = \max_{\mathbf{x} \in V_C} \left\{ \sigma_{a,m}^{\text{eq}}(\boldsymbol{\sigma}(\mathbf{x}, [0, T])) \right\}. \quad (2.34)$$

Note that a component under a given loading might contain more than one critical location. This situation is often encountered in symmetric structures. However, in many cases there is only one critical point. Its location is either obvious – for example when there is only one major notch – or can be identified with a finite element analysis of the considered component under the given loading.

One of the most elementary local methods utilizes constant-life diagrams such as the Haigh diagram, which was introduced in Section 2.5. A Haigh diagram, which is typically derived from smooth specimen tests, provides a design curve where the fatigue strength of the test specimen is expressed as a function of the applied mean stress $\sigma_e(\sigma_m)$. When used in a design context, see Fig. 2.13, the corresponding design condition is identical with Ineq. (2.32), which, in combination with the critical location, reads

$$\gamma_s \sigma_a^{\text{eq}}(\boldsymbol{\sigma}(\mathbf{x}_{\text{crit}}, [0, T])) \leq \sigma_e(\sigma_m^{\text{eq}}(\boldsymbol{\sigma}(\mathbf{x}_{\text{crit}}, [0, T]))) \quad (2.35)$$

A common way to evaluate this expression is to use the time-independent tensors $\boldsymbol{\sigma}_m$ and $\boldsymbol{\sigma}_a$ given in Eqs. (2.6) and (2.7) in combination with effective stress functions. If, for example, the mean stress at the critical location was evaluated using the maximum principle stress, while the stress amplitude was derived by means of the von Mises model, Ineq. (2.35) would reduce to $\gamma_s \sigma^{\text{vM}}(\boldsymbol{\sigma}_m(\mathbf{x}_{\text{crit}})) \leq \sigma_e(\sigma^{\text{mP}}(\boldsymbol{\sigma}_m(\mathbf{x}_{\text{crit}})))$. Depending on the material and load conditions, other effective stress functions might be used in practice.

While the previous method was based on a constant-life diagram, the following approach is based on an SN -model. While originally introduced in the context of low-cycle fatigue stress- or strain-life models, the mean stress corrections of Walker [52] as well as Smith, Watson and Topper [123] have also been applied in the high-cycle fatigue regime,

cf. [53, 124]. In this context, the Smith, Watson and Topper (SWT) model is a special case of Walker's correction, so that the focus will put here on the latter. Expressed as a local method with respect to the critical location, Walker's model reads

$$\gamma_s \sigma_a^{\text{eq}}(\boldsymbol{\sigma}(\mathbf{x}_{\text{crit}}, [0, T])) \left(\frac{2}{1 - R(\mathbf{x}_{\text{crit}})} \right)^\gamma \leq \sigma_e^{\text{W}} \quad (2.36)$$

where $\gamma \in (0, 1]$ and $\sigma_e^{\text{W}} > 0$ are model parameters that need to be calibrated with test data. Note that one obtains the SWT-model by setting $\gamma = 0.5$. The term on the left-hand side of Ineq. (2.36) can be interpreted as a mean stress corrected equivalent stress amplitude, compare Eq. (2.23).

Another family of local methods, which are encountered particularly in the broad field of multiaxial high-cycle fatigue assessment, can be summarized as linear stress amplitude corrections. Using the critical point concept, they can be expressed via

$$\gamma_s \left(\sigma_a^{\text{eq}}(\boldsymbol{\sigma}(\mathbf{x}_{\text{crit}}, [0, T])) + \alpha \sigma_m^{\text{eq}}(\boldsymbol{\sigma}(\mathbf{x}_{\text{crit}}, [0, T])) \right) \leq \sigma_e \quad (2.37)$$

where α and σ_e are considered material parameters that have to be calibrated with test data. Note, that the safety factor might also be applied to the stress amplitude only [42]. One of the oldest representatives of this type of approach is Sines' method [125, 126] published in 1955. His condition is based on invariants of the tensors $\boldsymbol{\sigma}_m$, $\boldsymbol{\sigma}_a$ given in Eqs. (2.6), (2.7), and, in combination with the concept of the critical location, reads

$$\gamma_s \left(\sqrt{J_2(\boldsymbol{\sigma}_a(\mathbf{x}_{\text{crit}}))} + \alpha_S I_1(\boldsymbol{\sigma}_m(\mathbf{x}_{\text{crit}})) \right) \leq \sigma_e^{\text{S}}. \quad (2.38)$$

Note that by adjusting the parameters α_S and σ_e^{S} Sines' criterion can be equivalently expressed as $\gamma_s (\sigma^{\text{VM}}(\boldsymbol{\sigma}_a(\mathbf{x}_{\text{crit}})) + \alpha_S \sigma^{\text{oct}}(\boldsymbol{\sigma}_m(\mathbf{x}_{\text{crit}}))) \leq \sigma_e$, cf. Section 2.2. Another approach, very similar to Sines' proposal, is Crossland's criterion [127]. It reads

$$\gamma_s \left(\sqrt{J_2(\boldsymbol{\sigma}_a(\mathbf{x}_{\text{crit}}))} + \alpha_C \max_{t \in [0, T]} I_1(\boldsymbol{\sigma}(\mathbf{x}_{\text{crit}}, t)) \right) \leq \sigma_e^{\text{C}}. \quad (2.39)$$

The only difference to Sines' model is the mean stress term, which in Crossland's model corresponds to the maximum hydrostatic stress encountered over the entire load cycle, while Sines' model evaluates the respective mean value, cf. Eq. (2.4).

Another subgroup of linear stress correction are based on the notion of the critical plane, cf. [128, 129]. In these approaches, the stress $\boldsymbol{\sigma}(\mathbf{x}, t)$ at a fixed point $\mathbf{x} \in V_C$ is expressed with respect to a cutting plane $\Delta_{\mathbf{n}}$ with normal vector \mathbf{n} intersecting $\mathbf{x} \in V_C$, see also Section 2.2. A classic example for a critical-plane approach is Findley's criterion [130]. Similar to the criteria presented above it features two model parameters σ_e^{F} , α_F , and is expressed as

$$\gamma_s \max_{\|\mathbf{n}\|_2=1} \left\{ \tau_a^{\text{eq}}(\boldsymbol{\sigma}(\mathbf{x}_{\text{crit}}, [0, T]), \mathbf{n}) + \alpha_F \max_{t \in [0, T]} \sigma_n(\boldsymbol{\sigma}(\mathbf{x}_{\text{crit}}, t), \mathbf{n}) \right\} \leq \sigma_e^{\text{F}}. \quad (2.40)$$

In this approach, the critical plane is identified as the one that maximizes the expression given in curly brackets, which is a linear combination of equivalent shear stress amplitude and normal stress, cf. Eqs. (2.15) and (2.16). The equivalent shear stress amplitude τ_a^{eq} can be determined using the minimum-circumscribed-circle method as described in [129].

Another example for a critical-plane approach is Matake's criterion [131]. Using the two model parameters σ_e^M and α_M , the critical point concept is expressed as

$$\gamma_s \left(\tau_a^{\text{eq}}(\boldsymbol{\sigma}(\mathbf{x}_{\text{crit}}, [0, T]), \mathbf{n}^*) + \alpha_M \max_{t \in [0, T]} \sigma_n(\boldsymbol{\sigma}(\mathbf{x}_{\text{crit}}, t), \mathbf{n}^*) \right) \leq \sigma_e^M \quad (2.41)$$

where the normal vector \mathbf{n}^* is defined by the plane $\Delta_{\mathbf{n}^*}$ that is critical in that sense, that it maximizes the equivalent shear stress amplitude. More formally, one defines

$$\tau_a^{\text{eq}}(\boldsymbol{\sigma}(\mathbf{x}_{\text{crit}}, [0, T]), \mathbf{n}^*) = \max_{\|\mathbf{n}\|_2=1} \left\{ \tau_a^{\text{eq}}(\boldsymbol{\sigma}(\mathbf{x}_{\text{crit}}, [0, T]), \mathbf{n}) \right\}. \quad (2.42)$$

The major drawback shared by all local methods used without non-local corrections is their high degree of conservativeness when applied to components with stress concentrations. The critical location of a notched component is assumed to behave like a smooth test, or in other words $K_f = K_t$, cf. Eq. (2.24) and the discussion below. The stress field surrounding the critical point is entirely ignored. Since this framework almost always leads to an underestimation of the component's fatigue strength, most local methods used in practice are corrected in some form that is accounting for the stress field the critical point is embedded in. Corresponding methods are part of the following section.

2.8.2 Non-local methods

Instead of using the stress values taken directly from the critical location $\mathbf{x}_{\text{crit}} \in V_C$ of the loaded component V_C , non-local methods for designing against high-cycle fatigue are using stress information including the stress field in the vicinity of \mathbf{x}_{crit} . The result is typically a reduction of the equivalent loading compared to the local methods. Most of the non-local approaches can be categorized as gradient-based approaches, stress averaging methods, critical distance models and highly loaded region frameworks.

The concept of gradient-based approaches, cf. [53, 58], is a reduction of the local equivalent stress amplitudes presented in the previous section, based on the local stress gradient. Throughout the literature, absolute and relative stress gradients, defined as

$$\chi_{\text{abs}}(\mathbf{x}) = \|\nabla \sigma_{a,m}^{\text{eq}}(\boldsymbol{\sigma}(\mathbf{x}, [0, T]))\|_2 \quad \text{and} \quad \chi_{\text{rel}}(\mathbf{x}) = \frac{\|\nabla \sigma_{a,m}^{\text{eq}}(\boldsymbol{\sigma}(\mathbf{x}, [0, T]))\|_2}{\sigma_{a,m}^{\text{eq}}(\boldsymbol{\sigma}(\mathbf{x}, [0, T]))} \quad (2.43)$$

are being used. Depending on the specific method, the gradients defined above are employed for different types of corrections. In an approach proposed by Siebel and Stieler [132], for example, the relative gradient is used for computing the fatigue notch factor, see Eq. (2.24), by introducing

$$K_f = \frac{K_t}{n_\chi} \quad \text{with} \quad n_\chi = 1 + \sqrt{s_g \chi_{\text{rel}}(\mathbf{x}_{\text{crit}})}. \quad (2.44)$$

where K_t is the stress concentration factor and s_g represents a material parameter. In a study presented by Norberg and Olsson [133], the gradient was used to directly correct the equivalent stress amplitude at the critical location. Using Ineq. (2.33), this reads

$$\gamma_s \left(\sigma_{a,m}^{\text{eq}}(\boldsymbol{\sigma}(\mathbf{x}_{\text{crit}}, [0, T])) - \beta \chi(\mathbf{x}) \right) \leq \sigma_e \quad (2.45)$$

where $\chi(\mathbf{x})$ can be defined either as the relative or absolute stress gradient, see Eq. (2.43), and $\beta > 0$ is a material parameter, compare also [62].

In stress averaging approaches, the equivalent stress amplitude that is compared with material data is not associated with some critical location. Instead, the stress field of the component is averaged in some form, typically over a small subdomain in the vicinity of the critical location. The classic example for a stress averaging method is Neuber's line method [134]. Starting from the assumption that the peak stress attained at the critical location in a real component – typically a notch root – does not reach the value predicted by continuum mechanics, he proposed to compute a reference stress averaged over a short line beginning at the notch root, perpendicular to the surface, directed into the bulk of the material. Similar considerations can be made by replacing Neuber's line by a correspondingly defined surface, or volume [135, 136]. Formally, one can summarize such approaches via

$$\frac{\gamma_s}{\text{vol}(\Omega)} \int_{\Omega} \sigma_{a,m}^{\text{eq}}(\boldsymbol{\sigma}(\mathbf{x}, [0, T])) \, d\Omega(\mathbf{x}) \leq \sigma_e \quad (2.46)$$

where $\Omega \subset V_C$ is either a one, two or three dimensional subdomain of the considered component with the length, area or volume $\text{vol}(\Omega)$ respectively.

Closely related to stress averaging approaches is the theory of critical distances. The underlying concept was initially introduced by Peterson [137] and later systematically extended by Taylor [135]. In this framework, a central role is assumed by a distance parameter d^* , called the critical distance, which is supposed to be characteristic for the considered material. In the classic approach proposed by Peterson, the critical distance is used to determine the equivalent stress amplitude close underneath the surface at a distance of d^* from the stress concentration apex. This stress amplitude, which will be smaller than the one at the critical location, is then used for the design condition

$$\gamma_s \max_{\mathbf{x} \in \Omega^*} \sigma_{a,m}^{\text{eq}}(\boldsymbol{\sigma}(\mathbf{x}, [0, T])) \leq \sigma_e \quad \text{with} \quad \Omega^* = \{\mathbf{x} \in V_C : \|\mathbf{x} - \mathbf{x}_{\text{crit}}\|_2 = d^*\}. \quad (2.47)$$

Other variations utilize the critical distance as a measure determining the integration domain Ω from Eq. (2.46) in order to average the stresses [136].

The last type of non-local methods presented in this section evolves around the notion of a highly stressed region, cf. [61, 138–140]. In this approach not the most critical stress conditions themselves are focused on, but the size of the region where these stress conditions are attained. The highly stressed region typically refers to a volume or surface domain around the stress concentration apex. A frequently used definition refers to the highly stressed domain (volume or surface) as that region on the component where an equivalent stress amplitude of at least 90% of the amplitude at the critical location is attained. However, the choice of 90% is somewhat arbitrary, and also other definitions like 80% or 95% can be found in the literature, cf. [141]. In a similar fashion as the gradient based adjustment stated in Eq. (2.44) the highly stressed region approach can be used to compute the fatigue notch factor by setting

$$K_f = \frac{K_t}{n_{90\%}} \quad \text{with} \quad n_{90\%} = 1 + \left(\frac{\Omega_{90\%}}{\Omega_{\text{ref}}} \right)^m \quad (2.48)$$

where $\Omega_{90\%}$ refers to the highly stressed domain [61]. The reference domain Ω_{ref} and m are considered material parameters that have to be calibrated with test data.

2.8.3 Weakest-link approach

The weakest-link approach can be seen as a probabilistic, non-local methodology with respect to the assessment of high-cycle fatigue. Similar to the previously discussed approaches it assumes that the considered component fails from a global perspective, as soon as failure initiates locally. However, in contrast to the methods presented above it does not assume where this location will be.

In the corresponding literature, one mostly encounters two approaches in order to introduce the weakest-link concept. The first one considers the problem from the perspective of spatial statistics and describes the phenomenon of local failure as a Poisson point process [142]. Examples can be found in [15] considering a low-cycle fatigue application, as well as in [143] with respect to high-cycle fatigue. The other approach might be described as the incremental model. In this framework, the component domain – typically its volume or surface – is described as an interconnected partition of a finite number of volume or surface increments. The resulting expression for the failure probability can then be analyzed for the limit case of infinitesimally small increments. Examples for this second deduction method are provided in [92] or [144]. The introduction presented below will be based on the incremental model.

Any weakest-link model is based on a description of the failure probability of some reference domain in terms of the considered load parameters. In the case discussed here, the reference domain will be an arbitrarily defined unit volume, denoted as V_1 , while the load parameters are defined as the uniaxial mean stress σ_m and the uniaxial stress amplitude σ_a of a corresponding cyclic load. One may think of V_1 as a smooth test specimen that is subjected to external loads resulting in σ_m and σ_a in the course of a constant-amplitude fatigue test. Assume that the survival probability of V_1 under these load conditions can be described with some parametric distribution function as

$$P_s^1(\sigma_m, \sigma_a | \theta) \quad (2.49)$$

where θ represents the parameter vector of the distribution function. The corresponding probability of failure will be denoted as $P_f^1(\sigma_m, \sigma_a | \theta)$. From the perspective of the weakest-link model, the reference domain V_1 is considered as an interconnected partition of smaller subvolumes, which determine whether the specimen fails or survives, cf. Fig. 2.14. More specifically, the weakest-link assumption states, that the specimen fails, if at least one of its subvolumes fails. Conversely, the specimen can only survive if all subvolumes survive. Assuming both that the unit volume consists of n subvolumes of equal size $\Delta V = V_1/n$ and that the failure behavior of each ΔV is statistically independent from the failure behavior of the other increments, this translates into

$$P_s^1(\sigma_m, \sigma_a | \theta) = P_{s,\Delta V}(\sigma_m, \sigma_a)^n = P_{s,\Delta V}(\sigma_m, \sigma_a)^{\frac{V_1}{\Delta V}} \quad (2.50)$$

where $P_{s,\Delta V}(\sigma_m, \sigma_a)$ denotes the survival probability of a single subvolume of size ΔV under the considered load conditions. The latter may be interpreted as a local survival probability. Using the above Eq. (2.50), this local survival probability $P_{s,\Delta V}(\sigma_m, \sigma_a)$ can be expressed in terms of the global survival probability of V_1 as in

$$P_{s,\Delta V}(\sigma_m, \sigma_a) = P_s^1(\sigma_m, \sigma_a | \theta)^{\frac{\Delta V}{V_1}}. \quad (2.51)$$

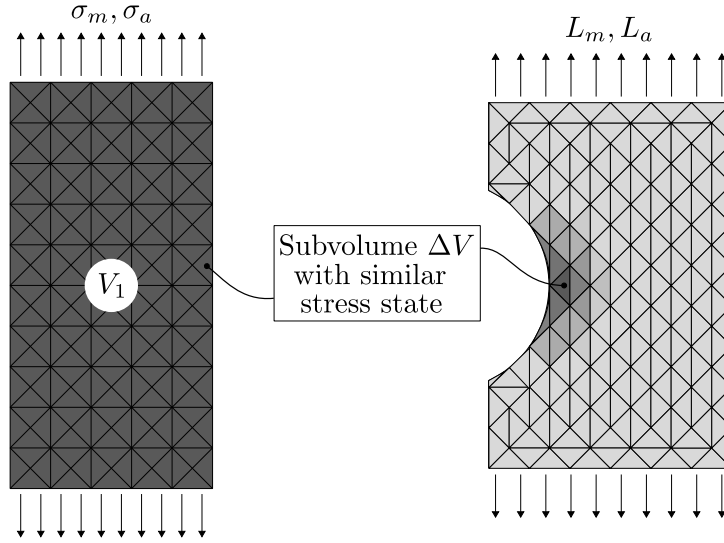


Figure 2.14: On the weakest-link concept.

Now the focus will be shifted to an engineering component with volume V subjected to some design load. The latter will be expressed using the load amplitude representative L_a and the mean load representative L_m , cf. Fig. 2.14. Assuming the weakest-link perspective, this component may be seen as a number of N interconnected, statistically independent subvolumes. In contrast to the previous situation, each of these subvolumes may now be of different size and will be subjected to a different equivalent stress state. By enumerating the volume increments ΔV_i from $i = 1$ to N , the corresponding average stresses over the individual increments will be denoted as $\sigma_{m,i}^{\text{eq}}$ and $\sigma_{a,i}^{\text{eq}}$. In this way, the probability of survival with respect to the considered component can be expressed as

$$P_s(L_m, L_a) = \prod_{i=1}^N P_{s,\Delta V_i}(\sigma_{m,i}^{\text{eq}}, \sigma_{a,i}^{\text{eq}}) \quad (2.52)$$

in analogy to Eq. (2.50). By combining the two previous Eqs. (2.52), (2.51) and applying the logarithm on both sides of the equation one obtains

$$\log P_s(L_m, L_a) = \sum_{i=1}^N \log P_s^1(\sigma_{m,i}^{\text{eq}}, \sigma_{a,i}^{\text{eq}} | \theta) \frac{\Delta V_i}{V_1}. \quad (2.53)$$

Finally, when considering the limit case of $N \rightarrow \infty$ and applying some simple rearrangements, one arrives at the expression

$$P_f(L_m, L_a) = 1 - \exp \left\{ \int_V \log(1 - P_f^1(\sigma_m^{\text{eq}}(\mathbf{x}), \sigma_a^{\text{eq}}(\mathbf{x}) | \theta)) \frac{dV(\mathbf{x})}{V_1} \right\} \quad (2.54)$$

where $\sigma_m^{\text{eq}}(\mathbf{x})$ and $\sigma_a^{\text{eq}}(\mathbf{x})$ denote local equivalent stresses. In many cases they will be defined as effective stresses with respect to the two stress tensors given in Eqs. (2.6) and (2.7). In Eq. (2.54) the whole component volume V was considered as the domain for the weakest-link assessment. In a similar fashion, this method can also be applied on the surface, or on any other subdomain of the component. With respect to the

question on which domain should be chosen for a high-cycle fatigue assessment, no definitive answer is given in the literature, cf. [145]. Some argue, that only the surface should be considered, since most cracks in high-cycle fatigue applications initiate at or very close to the surface [146]. However, the surface weakest-link model is unable to explain the typically different fatigue strengths of a smooth specimen when subjected to push-pull and rotating-bending loads respectively [147]. Within the framework of a volume weakest-link model this inconsistency is resolved. However, in this model a volume increment within the bulk of the material is considered equivalent in terms of the corresponding failure probability to a volume increment at the free surface when subjected to the same stress state. With respect to the fact that for many materials most high-cycle fatigue induced cracks in smooth test specimens initiate at or very close to the surface, compare Section 2.3, this equivalence seems to be inappropriate. Also combinations of volume and surface models can be found in the literature [148]. From a practical perspective the volume model is typically easier to implement based on standard finite element results, since no surface identification is required. It should be pointed out however, that especially in safety-related applications, the argument of practicality should not decide on which method to choose.

In order to apply the weakest-link model expressed in Eq. (2.54) one has to describe the failure behavior P_f^1 in terms of a distribution function. In many applications P_f^1 is modeled as a two or three-parameter Weibull distribution, cf. Eq. (2.28), via

$$P_f^1(\sigma_m, \sigma_a | \theta) = 1 - \exp \left\{ - \left(\frac{\langle \sigma_{a,m}^{\text{eq}} - \sigma_e^{\text{th}} \rangle}{\hat{\sigma}_e} \right)^k \right\} \quad (2.55)$$

where $\sigma_{a,m}^{\text{eq}} = f(\sigma_m, \sigma_a, \theta)$ denotes some equivalent stress amplitude accounting for the mean stress influence. Common choices are for example Sines' or Crossland's stress, but also critical-plane models like Findley's or Matake's stress are used, cf. [41, 133]. Note that in these two references, it is shown, that the specific choice of the stress model used for computing $\sigma_{a,m}^{\text{eq}}$ has only a small influence on the resulting weakest-link model in terms of the computed failure probabilities, when fitted to the same data.

Combining Eqs. (2.54) and (2.55), one obtains the Weibull weakest-link model

$$P_f(L_m, L_a) = 1 - \exp \left\{ - \int_V \left(\frac{\langle \sigma_{a,m}^{\text{eq}}(\boldsymbol{\sigma}(\mathbf{x}, [0, T])) - \sigma_e^{\text{th}} \rangle}{\hat{\sigma}_e} \right)^k \frac{dV(\mathbf{x})}{V_1} \right\}. \quad (2.56)$$

It should be emphasized that the failure probability expressed in Eqs. (2.54) and (2.56) implicitly accounts for the statistical size effect and the notch effect, compare Section 2.4. The statistical size effect is captured by integrating over the entire component volume V . Indeed, let $P_{f,V}$ denote the failure probability for the considered component with volume V as expressed in Eq. (2.56). On the other hand, let $P_{f,cV}$ denote the failure probability for the same component with a geometry scaled by the factor $c > 0$. Moreover, assume for the second case that the load representatives L_m and L_a are scaled in a way, that the stress field remains similar. Under these conditions one obtains

$$P_{f,cV} = 1 - (1 - P_{f,V})^c. \quad (2.57)$$

If $c > 1$, that is, when the component size is increased, the failure probability increases as well. Conversely, in the case of $0 < c < 1$, that is, when the component is scaled down, the failure probability decreases. The effect of stress concentration on the other hand is captured by the averaging effect resulting from the integral appearing in Eq. (2.56). Regions of high stresses are usually of rather small volume, while regions of lower stresses cover larger volumes. Since both quantities, volume and stress contribute to the failure probability, the overall failure probability of a notched component computed by Eq. (2.56) is lower than the failure probability one would obtain by merely assessing the peak stress in the notch root.

At this point, the weakest-link theory has been outlined to an extent that is sufficient for the purpose of this work. In order to conclude this section, a brief historical review on the use of the weakest-link model in the context of high-cycle metal fatigue should be provided. Emphasis is put on more recent contributions.

The first application of the weakest-link concept in the context of material failure analysis was the description of the static strength of brittle solids, such as ceramics, presented by Weibull [149] in 1939. It is important to point out, that even though Weibull utilized weakest-link theory in his work from 1939 (and further popularized it in his classic paper [150] from 1951, introducing the distribution which is today bearing his name), he did not originally propose it. This concept was already known by the time he published his paper. Neither is weakest-link theory a derivative of Weibull statistics, nor are Weibull statistics based on weakest-link theory. Both notions represent independent concepts – as shown in the derivations presented above – even though they are sometimes used synonymously in the literature, cf. [144].

Beginning in the early 1960s with a publication of Kuguel [138] several researchers transferred the concept behind the weakest-link idea to the statistical description of the fatigue behavior of metals [139, 145, 146, 148, 151–158]. However, as one would expect when considering the transfer of a conceptual model from one field to another, those first publications primarily focused on the general usability of the weakest-link model in the context of metal fatigue. The details and pitfalls of its practical application to components were discussed only briefly.

In the early 2000s this focus shifted to some extent. After it was shown in several publications over the previous decades, that the weakest-link model was often – however not always [146] – capable of describing the scatter in the fatigue behavior of metal components, efforts were increasingly aiming to show how the methodology could be used in an industrial context, both with respect to specific applications as well as to its non-trivial implementation as a finite element post-processor. From 2004 to 2007, during his PhD work [40], Wormsen et al. published several research papers [92, 159–161] focusing on the weakest-link approach in the context of both life and fatigue strength prediction of notched metal components. While using a combination of Walker’s [52] and Sines’ [126] stress model to incorporate the mean stress effect they touched upon several topics such as first cycle notch root plasticity [161] and variable-amplitude loading [160]. The most comprehensive work is provided in [92], which, based on its detailed descriptions of both physical foundations, and implementation, can be considered a standard reference considering the application of weakest-link theory to high-cycle metal fatigue.

Around the same time, in 2007, Norberg and Olsson [133, 162] published a study comparing the volume based weakest-link model against the more conventional point and gradient approaches in the context of different effective stress models. The results

showed that independent of the used effective stress model, the weakest-link methods were most consistent with the analyzed test data.

During the PhD studies of Karlen [163–166] from 2008 until 2012, the weakest-link approach was applied to situations with competing notches. Test specimens of a specific geometry containing two different notches were manufactured and experimentally fatigue tested. While being able to explain the test results for a single notch, the weakest-link model was seemingly unable to describe the test results when failure was likely in both notches. Additionally, Karlen also considered a finite life model combined with a fatigue limit model in the context of a weakest-link approach, see [164].

In yet another PhD project, Sadek [167, 168] compared the volume-based weakest-link model against several novel volumetric methods, that were inspired by the theory of critical distances in combination with highly-stress volume approaches. He found that in several cases the proposed models showed better predictive capabilities than the classic weakest-link approach.

Only a few years ago, in his PhD work from 2014 until 2017, Sandberg [33, 42, 96, 169] studied the volumetric weakest-link model in the context of its applicability to a gas turbine compressor blade. The focus was put on applications related questions such as mesh studies, efficient testing and transferability from specimen to component. All of these investigations were conducted using classical stress amplitude corrections focusing on Sines' or Crossland's model in combination with fitting approaches based on experimentally determined failure probabilities.

3 Scope of work

Despite the fact that probabilistic methods for the assessment of high-cycle metal fatigue based on weakest-link models are available for quite some time – at least since the 1990s – their utilization in an industry design context still appears to be rather limited. Considering the major advantages of weakest-link approaches of being more accurate than conventional hot-spot methods, and having a stronger physical foundation, this situation seems to be somewhat puzzling.

Several reasons have been pointed out in the literature for this apparent reluctance regarding the use of weakest-link approaches in component design. They range from the comparably high complexity of the method itself, over a lack of required finite element post-processing routines, to unavailable statistical fatigue strength data. Especially the latter represents an impediment which is often difficult to overcome without investing in additional systematic test efforts focused on the fatigue strength distribution. In many cases, merely some constant-amplitude fatigue test data describing the material's *SN*-behavior will be available, which, unfortunately, is difficult to utilize in order to determine a material's fatigue strength in terms of its statistical properties.

Another hurdle for the application of probabilistic design methods in general, and weakest-link models in particular, is the conceptional difference of these probabilistic methods compared with conventional deterministic approaches based on safety factors. While the latter often represents a well-established process of assessing a given design, validated by the components in operation which did not fail, a novel probabilistic method, unproven by field experience, might be looked upon with some skepticism by the responsible designers. This circumstance additionally hampers the transfer of available probabilistic methods into design practice.

In view of this situation, it is the goal of this work to propel the use of probabilistic weakest-link methodologies in the design process against high-cycle metal fatigue by developing and validating a corresponding model with the following properties.

1. The model can be calibrated with rather unsystematic constant-amplitude fatigue test data. This means that the impediment of relying on systematic test campaigns aiming to determine the fatigue strength distribution, like staircase tests or probit approaches, should be alleviated. Uncertainties associated with the proposed calibration method should be addressed.
2. The model bears a conceptual resemblance to existing design approaches against high-cycle fatigue, in order to simplify the adaption of the proposed methodology into existing design processes.

The practical application that originally motivated this work is the design of a gas turbine compressor blade with respect to high-cycle fatigue. Consequently, the developed model should be applicable to this specific case, which requires an emphasized focus on the mean stress effect. Therefore, both of the targeted model properties stated above have to be addressed in this context, that is accounting for the mean stress influence.

With that being said, it should also be stated what is outside the scope of this work. No efforts are being made to account for inherently time-dependent phenomena, such as the influence variable-amplitude loads, creep effects or surface degradation. Also the influences of multiaxial fatigue phenomena resulting from multiple simultaneously acting load sources with or without phase-differences are not being considered.

4 Experimental data

In this section, the fatigue test data which is used for the validation of the proposed method in this work is presented. All data sets refer to stress-controlled push-pull tests at ambient conditions with a constant nominal stress amplitude often in combination with a fixed superimposed nominal mean stress.

The test data is presented with respect to the corresponding material, the used specimen geometries and the stress conditions – mean stress and stress amplitude – the tests were conducted under. The selection of test data was motivated by three main requirements. First of all, since the mean stress influence was a main focus of this work, the test data had to contain test at both zero and non-zero mean stress levels at otherwise similar test conditions such as temperature and surface quality. Secondly, in order to investigate the transfer capabilities of the considered methods, meaning the inference from laboratory test results to the assessment of an engineering component, tests on both smooth and notched specimens of the same material had to be contained in the data sets. Finally, accounting for the stochastic nature of the studied approaches, the number of available test points had to be high enough to be suitable for statistical analysis. Note, that it was not a requirement to focus on materials for compressor blade application only. Even if this is an emphasized design case in this work, the conceptual validation of the proposed methods can also be performed with other metallic materials.

The selection presented in the next sections, contains both literature data and a test data from the Siemens test database. While the latter has to be adequately censored in this publicly available document, the literature data is presented without any restrictions.

4.1 SAE-4130

The low-alloy, normalized steel SAE-4130 was studied with respect to its fatigue properties in several test campaigns conducted by the US National Advisory Committee for Aeronautics (NACA) in the early 1950s, see [170–173]. Their investigation was a reaction to a wartime survey that revealed a lack of information on the fatigue properties of materials that were used in airframe construction at the time. Next to SAE-4130, two aluminum alloys were studied, which are presented in the following two Sections.

Taking a particular interest in the application of stressed skin constructions, tests were conducted using thin sheet specimens, either notched or unnotched. The tests were conducted on a direct repeated-stress testing machine, using guides to prevent specimens from buckling in tension-compression tests, see [170]. The used loading frequency was approximately 1100 cycles per minute (18.3 Hz), while the tests were set up aiming to produce specimen failure at lives in the range of 10^4 to 10^7 cycles. All specimens were polished electrolytically. After polishing, they were coated with Vinylseal to protect them against corrosion and any surface damage that might result from handling. This coating was removed with acetone just before the specimen was tested.

The chemical composition of SAE-4130 is given in Table 4.1. Note, that the stated values are not taken from the NACA reports as they were not included. Instead they were taken from [174]. While the alloying elements chromium and molybdenum act as strengthening agents [174], the normalization of the material contributes to an improved ductility. According to [174] the resulting material shows a good combination of static and fatigue strength as well as toughness and ductility. In the list of materials considered in this work, SAE-4130 is one of the more ductile representatives. In [170] its basic

SAE-4130 (steel)	Element	C	Mn	P	S	Si	Cr	Mo
	Mass-%	0.3	0.5	0.04	0.04	0.25	0.95	0.2

Table 4.1: Chemical composition of SAE-4130 (typical values taken from [174]).

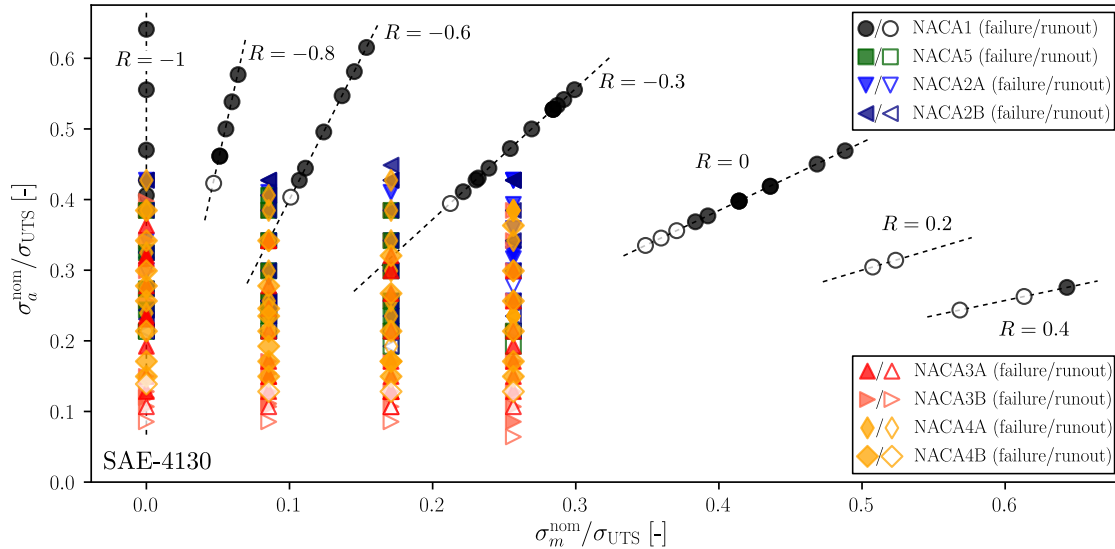


Figure 4.1: Available fatigue test data on SAE-4130 in a nominal Haigh plane ($N_{\text{ref}} = 5 \cdot 10^6$).

mechanical properties in the longitudinal axis of the manufactured tests specimens, which was the rolling direction of the original sheets, are given as presented in Table 4.3.

The used test specimen geometries are shown in Fig. 4.2. For SAE-4130 their thickness was 0.075 in (≈ 1.9 mm). The provided test data with respect to these specimen types is summarized in Table 4.2 and visually presented in the overview plot shown in Fig. 4.1. Note that the almost smooth NACA1 type was tested for constant stress ratios, while the notched geometries were tested at constant mean stresses. Only test results with $N_f > 10^4$ and without reported test irregularities like specimen buckling were used.

	Identifier	Type	Notch radius	K_t	#Tests
SAE-4130 (steel)	NACA 1	sheet/dogbone	305 mm	1.03	48 (11)
	NACA 2A	sheet/edge-cut notch	19 mm	1.62	24 (5)
	NACA 2B	sheet/edge-cut notch	9.5 mm	2.17	41 (6)
	NACA 3A	sheet/edge-cut notch	1.4 mm	4.46	38 (5)
	NACA 3B	sheet/edge-cut notch	0.8 mm	5.85	29 (4)
	NACA 4A	sheet/fillet-type notch	4.4 mm	2.20	31 (5)
	NACA 4B	sheet/fillet-type notch	0.5 mm	4.73	31 (4)
	NACA 5	sheet/hole-type notch	38 mm	2.11	22 (5)

Table 4.2: Summary of used test data for SAE-4130. The stated K_t is derived from FE-calculations and refers to the von Mises stress. The number in parentheses given in the column with the number of tests (#Tests) states the number of runouts with respect to $N_{\text{ref}} = 5 \cdot 10^6$ cycles. For example, 48 tests with specimen NACA 1 were used, 11 of which collected more than $5 \cdot 10^6$ load cycles.

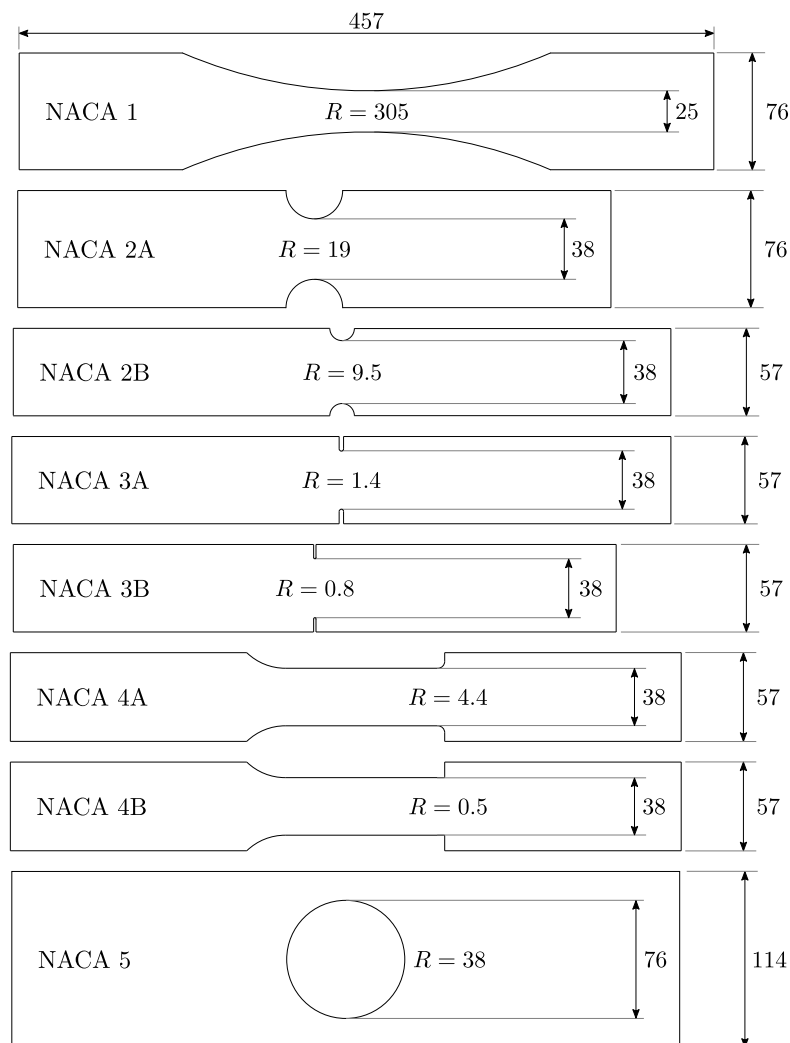


Figure 4.2: Overview of used test sheet specimen geometries for NACA test data, cf. [170–173]. Dimensions are given in mm (original values are given in inches). R denotes the notch radius.

4.2 AL2024-T3

The aluminum alloy AL2024-T3 is a high strength material frequently used for structural applications with weight constraints, such as encountered in the aerospace industry. While showing good fatigue properties, it shows a rather poor corrosion resistance [176]. Its basic mechanical properties after T3 tempering are presented in Table 4.3. An excerpt of its chemical composition is given in Table 4.4. The primary alloying element of this alloy series is copper. Additionally, its quasi-static stress-strain curve is shown in Fig. 4.5. Note that the latter was not provided by the original NACA reports, so that it had to be taken from another source which was found in [175].

The fatigue test data on AL2024-T3 was taken from the same sources as the test data on SAE-4130, see Section 4.1. As a consequence, similar specimen geometries have been used. The only difference to the SAE-4130 specimens is the slightly increased sheet thickness of the AL2024-T3 specimens with 0.090 in (≈ 2.3 mm). The used test data is summarized in Table 4.5 and shown in the overview plot in Fig. 4.3.

	SAE-4130	AL2024-T3	AL7075-T6
σ_{YS} [170]	98.5 ksi (679.1 MPa)	54.0 ksi (372.3 MPa)	76.0 ksi (524.0 MPa)
σ_{UTS} [170]	117.0 ksi (806.7 MPa)	73.0 ksi (503.3 MPa)	82.5 ksi (568.8 MPa)
E [170, 175]	30400 ksi (209.6 GPa)	10200 ksi (70.3 GPa)	10200 ksi (70.3 GPa)

Table 4.3: Tensile strength (σ_{UTS}), 0.2% yield strength (σ_{YS}) and Young’s modulus (E) in rolling direction of the base sheets of the three materials considered in the NACA test campaigns. Note that the stated Young’s modulus for SAE-4130 refers to compression, as it was not given as a tensile property in the reports.

AL2024-T3 (Al-alloy)	Element	Al	Cu	Mg	Mn	Fe
	Mass-%	93	4.4	1.5	0.6	<0.5

Table 4.4: Chemical composition of AL2024-T3 (typical values taken from [176]).

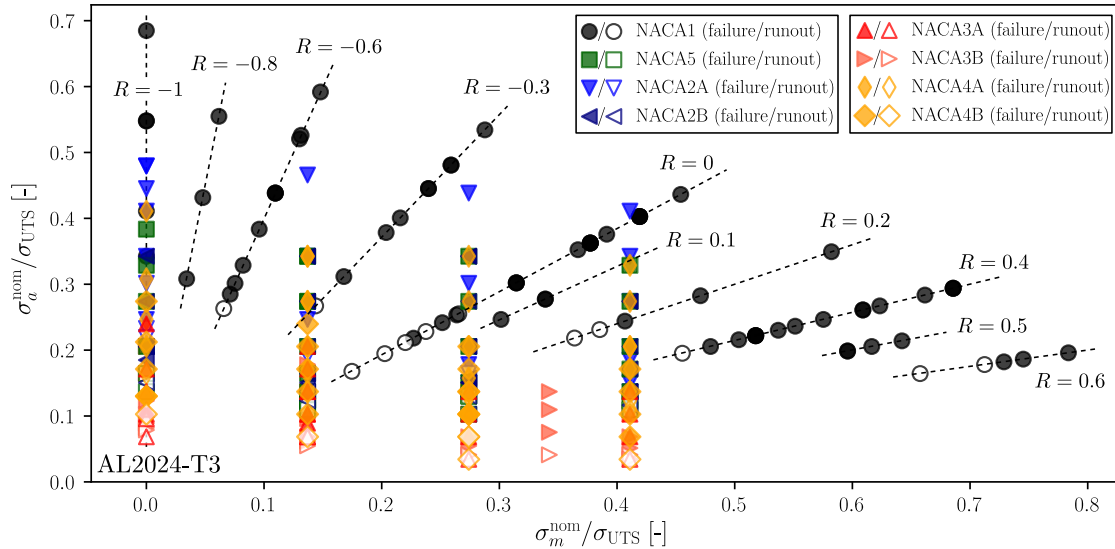


Figure 4.3: Available fatigue test data on AL2024-T3 in a nominal Haigh plane ($N_{ref} = 5 \cdot 10^6$).

AL2024-T3 (Al-alloy)	Identifier	Type	Notch radius	K_t	#Tests
	NACA 1	sheet/dogbone	305 mm	1.03	84 (12)
	NACA 2A	sheet/edge-cut notch	19 mm	1.62	29 (7)
	NACA 2B	sheet/edge-cut notch	9.5 mm	2.17	32 (6)
	NACA 3A	sheet/edge-cut notch	1.4 mm	4.46	24 (6)
	NACA 3B	sheet/edge-cut notch	0.8 mm	5.85	27 (7)
	NACA 4A	sheet/fillet-type notch	4.4 mm	2.20	28 (6)
	NACA 4B	sheet/fillet-type notch	0.5 mm	4.73	27 (5)
	NACA 5	sheet/hole-type notch	38 mm	2.11	31 (8)

Table 4.5: Summary of used test data for AL2024-T3, cf. Table 4.2.

4.3 AL7075-T6

The aluminum alloy AL7075-T6 is another high strength material often used for highly stressed structural parts with weight constraints. It shows good fatigue properties and improved corrosion fatigue resistance compared with AL2024-T3. Additionally, it is less ductile than AL2024-T3 [177]. An excerpt of its chemical composition is given in Table 4.7. The primary alloying element of this series is zinc. Its quasi-static stress-strain curve is shown in Fig. 4.5. Similar as for the previous case of AL2024-T3, the stress-strain curve was not provided by the original NACA reports, so that it had to be taken from another source [175].

The fatigue test data on AL7075-T6 was taken from the same sources as the test data on SAE-4130 and AL2024-T3, see Sections 4.1 and 4.2. Again, similar specimen geometries have been used with the same sheet thickness as the AL2024-T3 specimens, that is 0.090 in (≈ 2.3 mm). The used test data is summarized in Table 4.6 and shown in the overview plot in Fig. 4.4.

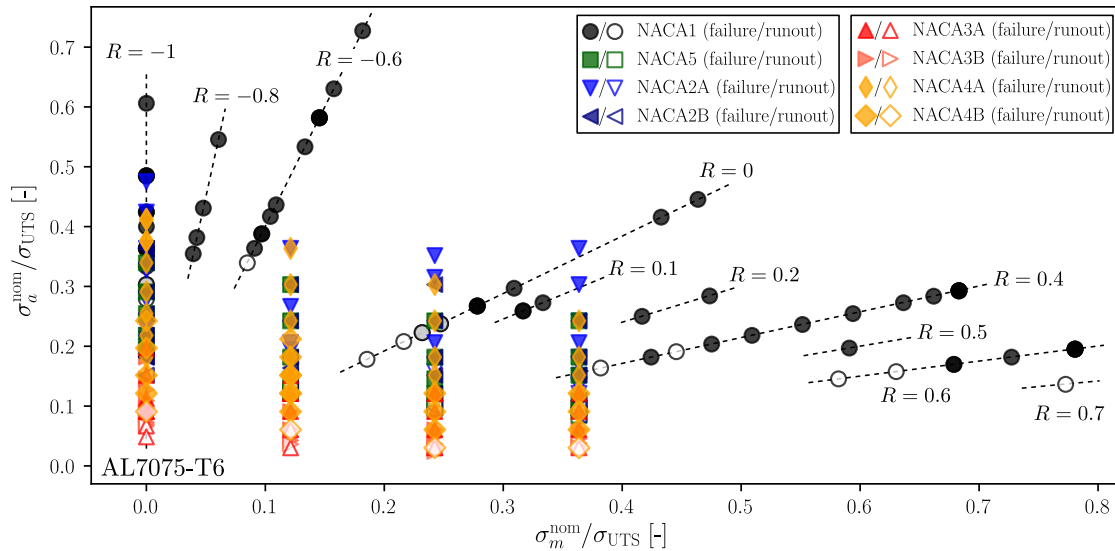


Figure 4.4: Available fatigue test data on AL7075-T6 in a nominal Haigh plane ($N_{\text{ref}} = 5 \cdot 10^6$).

	Identifier	Type	Notch radius	K_t	#Tests
AL7075-T6 (Al-alloy)	NACA 1	sheet/dogbone	305 mm	1.03	72 (12)
	NACA 2A	sheet/edge-cut notch	19 mm	1.62	31 (5)
	NACA 2B	sheet/edge-cut notch	9.5 mm	2.17	27 (6)
	NACA 3A	sheet/edge-cut notch	1.4 mm	4.46	25 (6)
	NACA 3B	sheet/edge-cut notch	0.8 mm	5.85	28 (7)
	NACA 4A	sheet/fillet-type notch	4.4 mm	2.20	26 (3)
	NACA 4B	sheet/fillet-type notch	0.5 mm	4.73	21 (4)
	NACA 5	sheet/hole-type notch	38 mm	2.11	23 (4)

Table 4.6: Summary of used test data for AL7075-T6, cf. Table 4.2.

AL7075-T6 (Al-alloy)	Element	Al	Zn	Mg	Cu	Fe
	Mass-%	89	5.6	2.5	1.6	<0.5

Table 4.7: Chemical composition of AL7075-T6 (typical values taken from [177]).

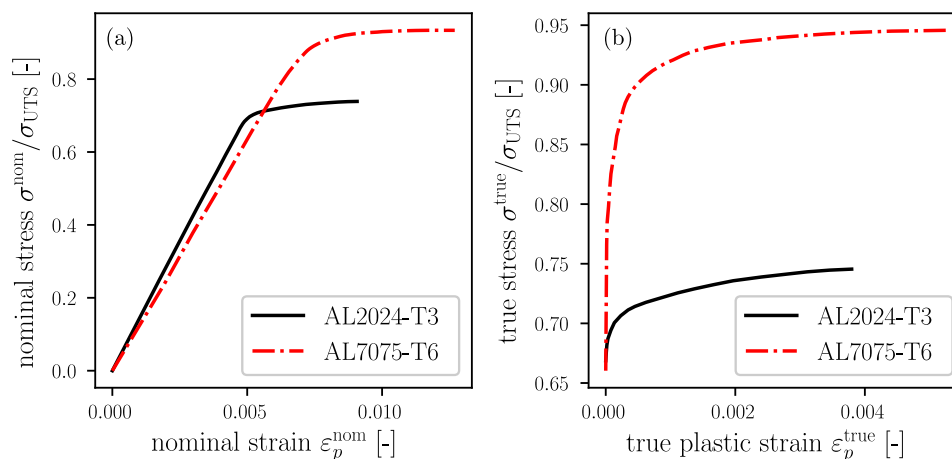


Figure 4.5: Plot (a) shows the static nominal stress-strain curves at room temperature for both considered materials taken from page 31 in [175]. Plot (b) shows the derived relationship of true stress over true plastic strain. Note that the stresses on the vertical axis are normalized to the respective value of σ_{UTS} , see Table 4.3.

4.4 PH12-10Mo

The high strength precipitation hardened (PH) steel PH12-10Mo with a yield strength class of $\sigma_{\text{YS}} \approx 1200$ MPa was in the center of recent research efforts at Siemens in the course of developing suitable materials with respect to applications for low pressure steam turbine end stage blades under increased loading conditions, cf. [178]. This material shows improved low-cycle and high-cycle fatigue behavior (with respect to the baseline materials) while preserving good stress corrosion cracking resistance and corrosion fatigue properties. An excerpt of its chemical composition is presented in Table 4.8.

The available test data (push-pull tests) for PH12-10Mo is summarized in Table 4.9. It contains 41 data points, 11 of which correspond to test specimens that did not fail during the tests (runouts). Three cylindrical specimen types have been used, one smooth and two notched geometries, see also Fig. 4.7. All tests were conducted in ambient conditions on high frequency pulsating machines with loading frequency of 100 – 150 Hz. An overview of the stress conditions, that is mean stress and stress amplitude of the different tests is presented in the overview plot shown in Fig. 4.6.

PH12-10Mo (steel)	Element	Cr	Ni	Mo	Al	Ti
	Mass-%	12	10	2	1	0.35

Table 4.8: Chemical composition of PH12-10Mo (average values), cf. [178].

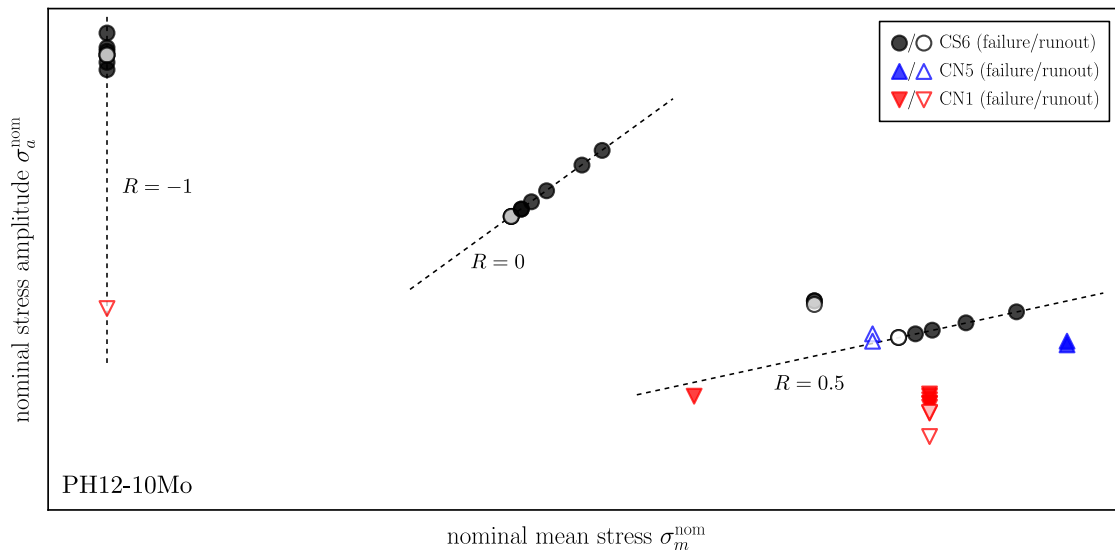


Figure 4.6: Available fatigue test data on PH12-10Mo in a nominal Haigh plane ($N_{\text{ref}} = 10^8$).

	Identifier	Type	Notch radius	K_t	#Tests
PH12-10Mo (steel)	CS6	cylindrical/smooth	∞	1.00	26 (6)
	CN5	cylindrical/notched	5 mm	1.27	4 (2)
	CN1	cylindrical/notched	1 mm	1.99	11 (3)

Table 4.9: Summary of available test data (Siemens) for PH12-10Mo. The stated K_t is derived from FE-calculations and refers to the von Mises stress. The number in parentheses given in the column with the number of tests (#Tests) states the number of runouts ($N_f > 10^8$). For example, 26 tests with specimen CS6 are available, 6 of which were runouts.

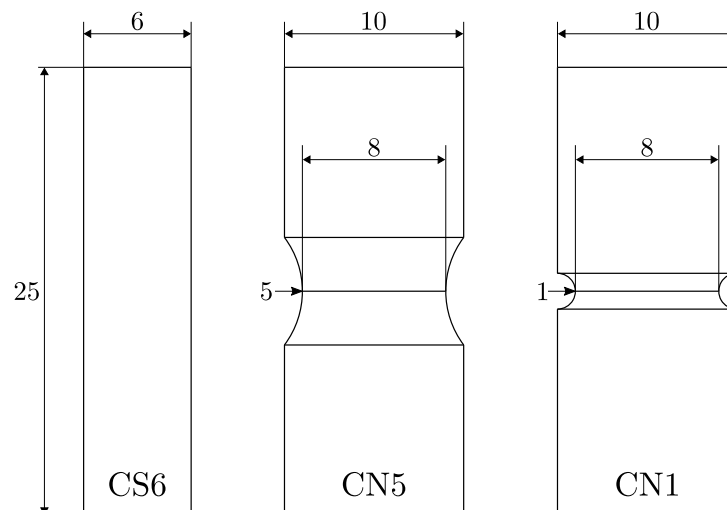


Figure 4.7: Overview of cylindrical test specimen geometries for Siemens test data. Note that only the relevant test gauge is shown, i.e. no clamping structure. Dimensions are stated in mm.

5 Model development

In many applications, design against high-cycle fatigue utilizes Haigh diagrams as a means to assess the expected stress amplitudes with respect to the component's fatigue strength under the anticipated mean stresses. In the conventional approach, a cyclic design load is accepted when the stress amplitude at the critical location does not exceed the corresponding fatigue strength, and rejected in the opposite case. As an alternative to this binary approach, a probabilistic methodology is presented in this section, that allows to quantify the probability of failure resulting from a given design load based on a probabilistic Haigh diagram for a unit domain in combination with a weakest-link model. Major parts of the presented material below have been published in [179–181].

5.1 Model formulation and fit

The model will be introduced in two steps. First, a four-parameter probabilistic Haigh diagram for a unit domain will be described. Note, that the term domain is used as a representative for a geometric entity derived from the considered component, like its volume or surface. Such a description with respect to a unit or reference domain is typical for weakest-link models, as discussed in Section 2.8.3. The corresponding Haigh diagram, which is in the focus of Section 5.1.1, assumes a homogeneous stress state in the unit domain, and will be referred to as the probabilistic unit Haigh diagram, or simply unit Haigh diagram. The transfer of the information reflected by the unit Haigh diagram to the description of the failure probability of an engineering component is achieved by means of a weakest-link approach. This is the content of the second step. The result will be a probabilistic Haigh diagram that refers to the – typically inhomogeneously stressed – component instead of merely a homogeneously stressed unit domain. Since this diagram can be used for design purposes, it is labeled probabilistic design Haigh diagram, or simply design Haigh diagram. It will be introduced in Section 5.1.2.

Any model can only be of value for practical purposes if it can be readily calibrated to available test data. The estimation of the four parameters of the unit Haigh diagram is the content of Section 5.1.3. The presented fitting strategy is a special case of a maximum likelihood fit, where each test data point is either left or right censored.

5.1.1 Probabilistic unit Haigh diagram

In the past, the influence of the mean stress on the fatigue strength has been expressed, depending on the considered material, in different empirically derived formulas. Two of the most popular ones are the Goodman line and Gerber's parabola, cf. Section 2.6. Marin [182] pointed out that many of these empirical relationships can be summarized using the common expression

$$\left(\frac{\sigma_e}{\hat{\sigma}_e}\right)^m + \left(\alpha \frac{\sigma_m}{\sigma_{\text{UTS}}}\right)^n = 1 \quad (5.1)$$

where σ_e denotes the fatigue strength at mean stress σ_m , $\hat{\sigma}_e$ is the fatigue strength for zero mean stress and σ_{UTS} the ultimate tensile strength of the considered material. The three parameters m , n and α are to be chosen depending on the considered model. For example, one obtains the Goodman line when setting $\alpha = n = m = 1$ while Gerber's parabola results from the parameter triple $\alpha = m = 1$, $n = 2$.

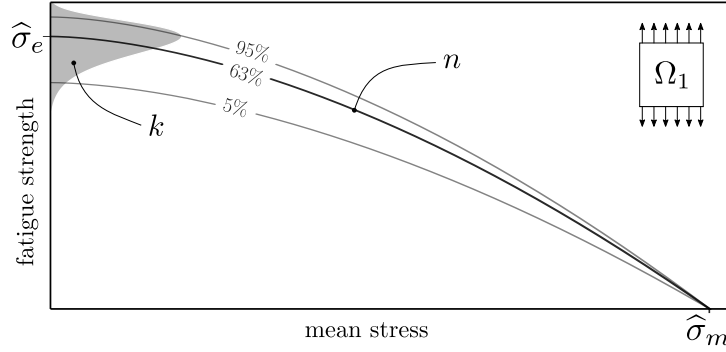


Figure 5.1: Probabilistic unit Haigh diagram for unit domain Ω_1 . The function of the Weibull scale, representing the $1 - 1/e \approx 63\%$ percentile, is determined by the axis intercepts $\hat{\sigma}_e$, $\hat{\sigma}_m$ and the curvature n . The scatter, on the other hand, is defined by the constant shape parameter k .

Typically, Eq. (5.1) is used to describe a deterministic Haigh diagram derived from smooth specimen tests. After the parameters are chosen to be consistent with the obtained test data, the resulting function $\sigma_e(\sigma_m)$ described by Eq. (5.1) can be understood as a mean stress dependent fatigue strength. Load conditions corresponding to peak stresses (σ_a, σ_m) with $\sigma_a > \sigma_e(\sigma_m)$ are interpreted to exceed the material's fatigue strength, while loads resulting in $\sigma_a \leq \sigma_e(\sigma_m)$ are considered to be acceptable.

In the approach presented here, on the other hand, the fatigue strength is understood as a random variable with respect to a predefined reference or unit domain Ω_1 (e.g. volume or surface), instead of being a fixed, geometry independent material property, as suggested by the conventional local interpretation. In this framework, Marin's expression Eq. (5.1) will be used to describe the mean stress dependent location parameter $\sigma_e(\sigma_m)$ of a fatigue strength distribution with respect Ω_1 . To that end set $m \equiv 1$ as well as $\hat{\sigma}_m := \sigma_{\text{UTS}}/\alpha$ and solve Eq. (5.1) for σ_e which results in

$$\sigma_e(\sigma_m) = \hat{\sigma}_e \left\langle 1 - \left\langle \frac{\sigma_m}{\hat{\sigma}_m} \right\rangle^n \right\rangle. \quad (5.2)$$

Note that two Macaulay brackets $\langle x \rangle = \max\{x, 0\}$ have been added. The outer one formally prevents negative fatigue strengths for $\sigma_m > \hat{\sigma}_m$. The inner one on the other hand inhibits the possible increase of the fatigue strength for $\sigma_m < 0$, which represents a conservative assumption. High-cycle fatigue phenomena which are dominated by compressive mean stresses are hence out of the scope of this model.

Throughout this work, a two-parameter Weibull distribution, abbreviated as $\mathcal{W}(\lambda, k)$ where λ is the scale and k the shape parameter, will be used to describe the fatigue strength distribution, see also Eq. (2.28). A three-parameter Weibull distribution, which is often used in the literature, see for example [183], was not considered, mostly in order to keep the number of parameters low and the model simple.

While Eq. (5.2) is used to describe the scale parameter as a function of mean stress, the remaining shape parameter k of the Weibull distribution will be assumed to be constant. This choice was made for the sake of model simplicity. Additionally, it should be considered, that the scatter parameter of a distribution is typically much more difficult to estimate with high confidence than its location parameter. Compare for example with the discussion of the difficulties encountered in the staircase method with respect to the estimation of the fatigue strength scatter parameter described in Section 2.6. It was

therefore assumed that the reliable determination of a possible trend in k over σ_m would likely require more test data, than one could usually provide.

With these two definitions for the Weibull scale and shape respectively, one can express the fatigue strength of a unit domain Ω_1 under mean stress σ_m as the random variable

$$X_e^1 \sim \mathcal{W}(\sigma_e(\sigma_m), k). \quad (5.3)$$

The corresponding distribution function is given by Eq. (2.28) with $\sigma_e^{\text{th}} = 0$. One hence ends up with three parameters describing the fatigue strength scale of Ω_1 over the mean stress ($\hat{\sigma}_e$, $\hat{\sigma}_m$ and n), while the scatter is controlled by a single parameter k . For easier reference the four model parameters will be summarized in the model parameter vector

$$\theta = (\hat{\sigma}_e, \hat{\sigma}_m, n, k). \quad (5.4)$$

For a given model parameter vector θ and a homogeneous loading in form σ_m and σ_a , the failure probability of the unit domain Ω_1 , by means of Eqs. (2.28) and (5.2), becomes

$$P_f^1(\sigma_m, \sigma_a \mid \theta) = 1 - \exp \left\{ - \left(\frac{\sigma_a}{\hat{\sigma}_e \left\langle 1 - \left\langle \frac{\sigma_m}{\hat{\sigma}_m} \right\rangle^n \right\rangle} \right)^k \right\}. \quad (5.5)$$

One can use Eq. (5.5) to compute the stress amplitude resulting in a given P_f^1 with respect to a considered mean stress σ_m by solving Eq. (5.5) for σ_a . This results in

$$\sigma_{a, P_f^1}(\sigma_m \mid \theta) = \hat{\sigma}_e \left\langle 1 - \left\langle \frac{\sigma_m}{\hat{\sigma}_m} \right\rangle^n \right\rangle \left(\log \frac{1}{1 - P_f^1} \right)^{\frac{1}{k}}. \quad (5.6)$$

Since Eq. (5.6) can be employed to describe a Haigh diagram for the unit domain Ω_1 in form of P_f -quantile lines, compare Fig. 5.1, Eq. (5.6) will be referred to as the probabilistic unit Haigh diagram or simply unit Haigh diagram.

5.1.2 Probabilistic design Haigh diagram

The unit Haigh diagram, describing a homogeneously stressed unit volume as presented in the previous Section 5.1.1, cannot be used for component design, since components typically feature structural discontinuities resulting in inhomogeneous stress fields. In order to assess the failure probability of a component, the unit Haigh diagram will be combined with the weakest-link model discussed in Section 2.8.3.

To that end, consider an engineering component C with domain Ω_C (volume, surface, etc.) that is subjected to some cyclic design load, expressed by the two load representatives L_m and L_a , compare with Section 2.8.3. While the former is supposed to reflect the stationary load component, the latter is assumed to describe the cyclic load contribution. These design loads will result in a cyclic stress field $\boldsymbol{\sigma} : \Omega_C \times [0, T) \rightarrow \mathbb{R}^6$ throughout the component's domain Ω_C , which can be translated into an equivalent local mean stress field $\sigma_m^{\text{eq}} : \Omega_C \ni \mathbf{x} \mapsto \sigma_m^{\text{eq}}(\mathbf{x}) := \sigma_m^{\text{eq}}(\boldsymbol{\sigma}(\mathbf{x}, [0, T)))$ and an equivalent local stress amplitude field of $\sigma_a^{\text{eq}} : \Omega_C \ni \mathbf{x} \mapsto \sigma_a^{\text{eq}}(\mathbf{x}) := \sigma_a^{\text{eq}}(\boldsymbol{\sigma}(\mathbf{x}, [0, T)))$, cf. Section 2.2. As described in Section 2.8.3, these two stress fields can now be used in combination with a description of the failure probability P_f^1 of a respective unit domain to set up a

corresponding weakest-link model. By using Eq. (5.5) as the model for the unit domain, and combining it with the weakest-link model stated in its volumetric formulation in Eq. (2.54), one can express the the component's failure probability via

$$P_f(L_m, L_a) = 1 - \exp \left\{ - \int_{\Omega_C} \left(\frac{\sigma_a^{\text{eq}}(\mathbf{x})}{\widehat{\sigma}_e \left\langle 1 - \left\langle \frac{\sigma_m^{\text{eq}}(\mathbf{x})}{\widehat{\sigma}_m} \right\rangle^n \right\rangle} \right)^k \frac{d\Omega_C(\mathbf{x})}{\text{vol}(\Omega_1)} \right\}. \quad (5.7)$$

For the further discussion of Eq. (5.7) it will be assumed that a variation in the load parameters L_m and L_a will merely result in a scaling of the resulting stress fields σ_m^{eq} and σ_a^{eq} , while preserving their shapes. This means that the ratios $\sigma_m^{\text{eq}}(\mathbf{x}; L_{m,1})/\sigma_m^{\text{eq}}(\mathbf{x}; L_{m,2})$ and $\sigma_a^{\text{eq}}(\mathbf{x}; L_{a,1})/\sigma_a^{\text{eq}}(\mathbf{x}; L_{a,2})$ are constant for all $\mathbf{x} \in \Omega_C$ and for any two values of $L_{m,1}, L_{m,2}$ and $L_{a,1}, L_{a,2}$ respectively. Such a situation is encountered in all linear-elastic problems in combination with equivalent stress models that preserve scalar multiplication. The latter refers to the property $\sigma^{\text{eq}}(\alpha \boldsymbol{\sigma}(\mathbf{x}, [0, T])) = \alpha \sigma^{\text{eq}}(\boldsymbol{\sigma}(\mathbf{x}, [0, T]))$ which is satisfied, for example, when defining the equivalent stress function by means of the von Mises, maximum principal or hydrostatic effective stress model, cf. Section 2.2.

Under these conditions, two special cases for the load representatives L_m and L_a should be introduced. The first one refers to the equivalent stresses at the critical location $\mathbf{x}_{\text{crit}} \in \Omega_C$, cf. Section 2.8.1. By defining $\sigma_m^{\text{crit}} := \sigma_m^{\text{eq}}(\mathbf{x}_{\text{crit}})$ as well as $\sigma_a^{\text{crit}} := \sigma_a^{\text{eq}}(\mathbf{x}_{\text{crit}})$ the two equivalent stress fields can be expressed via

$$\begin{aligned} \sigma_m^{\text{eq}}(\mathbf{x}) &= \sigma_m^{\text{crit}} \sigma_m^{1,\text{crit}}(\mathbf{x}) \\ \sigma_a^{\text{eq}}(\mathbf{x}) &= \sigma_a^{\text{crit}} \sigma_a^{1,\text{crit}}(\mathbf{x}) \end{aligned} \quad (5.8)$$

where $\sigma_m^{1,\text{crit}}(\mathbf{x})$ and $\sigma_a^{1,\text{crit}}(\mathbf{x})$ refer to the normalized equivalent stress fields, that – due to the normalization – assume unity in the critical location $\mathbf{x}_{\text{crit}} \in \Omega_C$. In this setup, the two equivalent stresses at the critical location can be used as the load representatives, hence $L_m = \sigma_m^{\text{crit}}$ and $L_a = \sigma_a^{\text{crit}}$. By referring to this interpretation, and by using the factorizations expressed in Eq. (5.8) in Eq. (5.7), one can rewrite the latter as

$$\begin{aligned} P_f(\sigma_m^{\text{crit}}, \sigma_a^{\text{crit}}) &= 1 - \exp \left\{ - \left(\frac{\sigma_a^{\text{crit}}}{\sigma_e^{\text{crit}}(\sigma_m^{\text{crit}})} \right)^k \right\} \\ \text{with } \sigma_e^{\text{crit}}(\sigma_m^{\text{crit}}) &= \widehat{\sigma}_e \left(\int_{\Omega_C} \left(\frac{\sigma_a^{1,\text{crit}}(\mathbf{x})}{\left\langle 1 - \left\langle \frac{\sigma_m^{\text{crit}} \sigma_m^{1,\text{crit}}(\mathbf{x})}{\widehat{\sigma}_m} \right\rangle^n \right\rangle} \right)^k \frac{d\Omega_C(\mathbf{x})}{\text{vol}(\Omega_1)} \right)^{-\frac{1}{k}}. \end{aligned} \quad (5.9)$$

Note that Eq. (5.9) describes a cumulative Weibull distribution function of the fatigue strength for the considered component with respect to the load representatives $L_m = \sigma_m^{\text{crit}}$ and $L_a = \sigma_a^{\text{crit}}$. This means the fatigue strength of the considered component in terms of σ_a^{crit} can be expressed as the random variable

$$X_e^{\text{crit}} \sim \mathcal{W}(\sigma_e^{\text{crit}}(\sigma_m^{\text{crit}}), k) \quad (5.10)$$

in analogy to Eq. (5.3). It should be emphasized, that Eq. (5.9) is formulated using equivalent stress values from the critical location \mathbf{x}_{crit} but refers to the non-local failure

probability of the entire component. The equivalent stresses at the critical location are merely used as references to scale the stress fields. The fatigue strength described by Eq. (5.10) can be interpreted as a non-local component fatigue strength that reflects both material properties and the component's geometry.

In analogy to Eq. (5.6), the expression stated in Eq. (5.7) allows for the computation of the load representative $L_a = \sigma_a^{\text{crit}}$ that corresponds to a specific failure probability. By solving Eq. (5.7) for σ_a^{crit} one obtains

$$\sigma_{a,P_f}^{\text{crit}}(\sigma_m^{\text{crit}} | \theta) = \hat{\sigma}_e \left(\frac{1}{\alpha} \log \frac{1}{1 - P_f} \right)^{\frac{1}{k}}$$

$$\text{with } \alpha = \int_{\Omega_C} \left(\frac{\sigma_a^{1,\text{crit}}(\mathbf{x})}{\left\langle 1 - \left\langle \frac{\sigma_m^{\text{crit}} \sigma_m^{1,\text{crit}}(\mathbf{x})}{\hat{\sigma}_m} \right\rangle^n \right\rangle} \right)^k \frac{d\Omega_C(\mathbf{x})}{\text{vol}(\Omega_1)}. \quad (5.11)$$

Since Eq. (5.11) describes a Haigh diagram for the considered component under the given design load in terms of P_f -quantiles with respect to the load representatives $L_m = \sigma_m^{\text{crit}}$ and $L_a = \sigma_a^{\text{crit}}$ it will be referred to as the probabilistic hot-spot design Haigh diagram, or simply (hot-spot) design Haigh diagram. Note that it can be used in the same fashion as a conventional Haigh diagram. As a designer, one just has to identify the equivalent stresses at the critical location, in order to look up the corresponding failure probability.

Next to the definition of L_m and L_a as hot-spot stresses, one can also define the load representatives in terms of nominal stresses such as the average stresses in the notch root section of notched members. The corresponding stress field factorization reads

$$\begin{aligned} \sigma_m^{\text{eq}}(\mathbf{x}) &= \sigma_m^{\text{nom}} \sigma_m^{1,\text{nom}}(\mathbf{x}) \\ \sigma_a^{\text{eq}}(\mathbf{x}) &= \sigma_a^{\text{nom}} \sigma_a^{1,\text{nom}}(\mathbf{x}) \end{aligned} \quad (5.12)$$

where σ_m^{nom} , σ_a^{nom} are the two nominal stresses, while $\sigma_m^{1,\text{nom}}$, $\sigma_a^{1,\text{nom}}$ denote the correspondingly normalized equivalent stress fields. In this case, one defines $L_m = \sigma_m^{\text{nom}}$ and $L_a = \sigma_a^{\text{nom}}$ as the load parameters. In the same way as discussed before, one can derive analogous expressions to Eqs. (5.9), (5.10) and (5.11) in terms of the nominal instead of equivalent hot-spot stresses. The respective formulas are obtained by substituting the superscripts “crit” by “nom” in the aforementioned equations. The corresponding probabilistic Haigh diagram will be referred to as the nominal design Haigh diagram.

In the remaining part of this section, the case will be discussed where a variation in the design load parameters L_m and L_a does not merely scale the stress fields but also leads to a change in their shapes. This situation is encountered when nonlinear effects play a role in the load-stress relationship, such as elasto-plastic material behavior. Under these circumstances, Eq. (5.7) still holds, but the design Haigh diagram cannot be derived anymore via Eq. (5.11), because the equivalent stress fields cannot be factorized with load shapes independent of L_m and L_a . Instead, for each combination of the design load parameters L_m and L_a the resulting equivalent stress fields σ_m^{eq} and σ_a^{eq} have to be computed using a nonlinear component-specific function Σ_C , formally expressed via

$$\begin{pmatrix} \sigma_m^{\text{eq}} \\ \sigma_a^{\text{eq}} \end{pmatrix} = \Sigma_C(L_m, L_a). \quad (5.13)$$

In a practical context, one may think of Σ_C as a formalization of a corresponding finite element analysis. The only possibility to derive a probabilistic design Haigh diagram in this framework, is by utilizing numerical means. A p -quantile line of the design Haigh diagram can be derived by numerically solving

$$P_f\left(\Sigma_C(L_m, L_a)\right) - p = 0 \quad (5.14)$$

for L_a over the relevant interval for L_m . Note, that for a fixed mean load L_m Eq. (5.14) implicitly defines the component's fatigue strength distribution in terms of L_a . In contrast to the linear case discussed before, where the fatigue strength could be described by a Weibull distribution, cf. Eq. (5.10), the distribution implicitly defined by Eq. (5.14) will, generally, not be of Weibull type.

5.1.3 Fitting strategy

In order to use the probabilistic Haigh diagram in a design context, the four model parameters $\hat{\sigma}_e$, $\hat{\sigma}_m$, n and k , summarized in the model vector θ , see Eq. (5.4), have to be calibrated for the considered material with test data. It should be emphasized, that the test data used for this purpose is assumed to be constant-amplitude fatigue test data with respect to a common test temperature. Test results from considerably different temperatures should not be mixed, as the derived model parameters will, in general, be different for different temperatures. It is, however, possible to mix test results from different specimen types, such as smooth and notched specimens. In this section, nominal stresses will be used as load representatives, see Eq. (5.12).

Principally, the model calibration could be conducted in a similar fashion as described in Section 2.6 when discussing the probit method. This approach and related variants are based on experimentally observed failure probabilities derived from repeated testing under similar conditions, cf. Fig. 2.12. The corresponding calibration can then be achieved by minimizing the error function expressed in Eq. (2.29). This approach has been used in many publications for the calibration of weakest-link high-cycle fatigue models, see for example [33, 34, 41, 96, 163, 165, 168, 169]. As mentioned before, this method cannot be applied to test data sets without repeated tests because the experimental failure probabilities cannot be determined. In order to avoid this problem, an alternative approach that does not rely on experimental probabilities is presented here.

Consider a test data set of $r \in \mathbb{N}$ individual constant-amplitude fatigue tests containing test results on one or multiple specimen types. A single test $i \in \{1, \dots, r\}$ is characterized by the corresponding nominal mean stress $\sigma_{m,i}^{\text{nom}}$, the nominal stress amplitude $\sigma_{a,i}^{\text{nom}}$ and the specimen geometry G_i . The result of a fatigue test is given by the number of applied load cycles N_i and a binary failure flag $\delta_i \in \{0, 1\}$ indicating whether the considered specimen has failed after it had accumulated N_i load cycles ($\delta_i = 1$) or not ($\delta_i = 0$). With respect to the reference number of cycles N_{ref} the probabilistic Haigh diagram should refer to, cf. Section 2.5, the N_{ref} -adjusted failure flag δ_i^{ref} is then defined via

$$\delta_i^{\text{ref}} = \begin{cases} 1, & \text{if } N_i \leq N_{\text{ref}} \text{ and } \delta_i = 1 \\ 0, & \text{if } N_i = N_{\text{ref}} \text{ and } \delta_i = 0 \\ 0, & \text{if } N_i > N_{\text{ref}}. \end{cases} \quad (5.15)$$

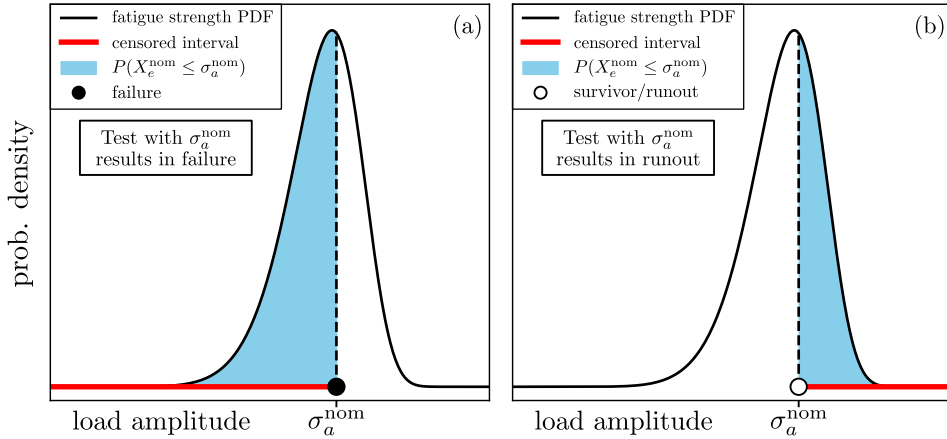


Figure 5.2: On the interpretation of specimens that failed (a) and specimens that survived (b) in a constant-amplitude fatigue test with respect to the censored fatigue strength information.

Test results that do not match any of the three criteria stated in Eq. (5.15), i.e. test points with $N_i < N_{\text{ref}}$ and $\delta_i = 0$ – one might call these tests early runouts – cannot be considered in the calibration, since they provide no information on whether the corresponding specimens would have survived N_{ref} load cycles or not. In the following discussion it is assumed that the considered data set does not contain early runouts. If one now describes an individual test point by the summarizing vector $(\sigma_{m,i}^{\text{nom}}, \sigma_{a,i}^{\text{nom}}, G_i, \delta_i^{\text{ref}})$, the entire test data set may be referred to as $\mathcal{T} := \{(\sigma_{m,i}^{\text{nom}}, \sigma_{a,i}^{\text{nom}}, G_i, \delta_i^{\text{ref}})\}_{i=1}^r$.

In order to fit the model parameter vector θ based on a given test data set \mathcal{T} , a maximum likelihood approach for censored data is applied, cf. [184]. An analogous approach was taken by Dixon and Mood [43] as a means to derive their evaluation method for the results of staircase tests. Other applications in the same context can be found for example in [106, 111]. All of these studies have in common, that they are focused on the evaluation of single-type specimen tests considering a fixed mean stress.

As it was already pointed out in Section 2.6, the problem in determining the fatigue strength of a specimen from an experimental point of view is that it cannot be measured directly in a conventional constant-amplitude fatigue test. The outcome of such a test is a fatigue life, not a fatigue strength. However, even if it is not possible to measure the fatigue strength directly, the outcome of these tests does contain censored information about the fatigue strength that can be used to calibrate the model. In the previous Section 5.1.2 it was described that the N_{ref} -fatigue strength of a test specimen can be considered a random variable with a corresponding underlying distribution. While it is not possible to measure the realization of this fatigue strength in a considered specimen, the outcome of a fatigue test reveals if the fatigue strength was smaller or greater than the tested nominal stress amplitude. Assume the considered specimen is tested with the nominal stress amplitude σ_a^{nom} . The applied mean stress is irrelevant for this consideration. If the specimen fails before accumulating N_{ref} load cycles, one concludes that the specimen's nominal fatigue strength must have been smaller than σ_a^{nom} . This scenario corresponds to a left-censored data point with respect to the nominal fatigue strength distribution, see Fig. 5.2a. On the other hand, if the specimen survives N_{ref} load cycles, it reveals that its fatigue strength was greater than the applied stress amplitude σ_a^{nom} . This corresponds to a right-censored data point, see Fig. 5.2b.

In this interpretation, denoting the random variable of the fatigue strength of specimen i as $X_{e,i}^{\text{nom}}$, one can formulate the corresponding likelihood function ℓ , which in this case is solely established by censored data points, as

$$\begin{aligned}\ell(\theta | N_{\text{ref}}) &= \prod_{i=1}^r P(X_{e,i}^{\text{nom}} \leq \sigma_{a,i}^{\text{nom}} | \theta)^{\delta_i^{\text{ref}}} P(\sigma_{a,i}^{\text{nom}} < X_{e,i}^{\text{nom}} | \theta)^{1-\delta_i^{\text{ref}}} \\ &= \prod_{i=1}^r P_{f,i}^{\delta_i^{\text{ref}}}(\theta) P_{s,i}^{1-\delta_i^{\text{ref}}}(\theta)\end{aligned}\quad (5.16)$$

where the failure and survival probability $P_{f,i}$ and $P_{s,i} = 1 - P_{f,i}$ are evaluated using Eq. (5.7). In practice, $\ell(\theta | N_{\text{ref}})$ will have to be maximized using numerical means. As typical in this context, not the likelihood function itself, but its logarithm – the log-likelihood function \mathcal{L} – will be considered for optimization purposes. Hence, in order to fit the four parameters of the unit Haigh diagram one will have to maximize

$$\begin{aligned}\mathcal{L}(\theta | N_{\text{ref}}) &:= \log \ell(\theta | N_{\text{ref}}) \\ &= \sum_{i=1}^r \log \left(P_{f,i}^{\delta_i^{\text{ref}}}(\theta) P_{s,i}^{1-\delta_i^{\text{ref}}}(\theta) \right).\end{aligned}\quad (5.17)$$

The corresponding model parameter vector will be denoted as θ_{opt} . Note that θ_{opt} will generally change for different values of N_{ref} as well as with the choice of Ω_1 . Both values should therefore be provided alongside with θ_{opt} .

5.2 Model discussion

In this section, the probabilistic Haigh diagram, as it was introduced above, should be discussed from several rather general perspectives. At first, in Section 5.2.1 the underlying model is compared with other existing methods that have been proposed in the past. The goal is to emphasize both differences as well as similarities among the approaches. Afterwards, in Section 5.2.2 the central subject of the used equivalent local stress models is addressed. Since the probabilistic Haigh diagram does not rely on specific models for the stress amplitude and mean stress respectively, there needs to be some guidance on which ones to choose in practice. Another open question is the choice of the integration domain. This problem is addressed in Section 5.2.3. Finally, in Section 5.2.4 the model scope and the corresponding limits are summarized.

5.2.1 Comparison with other approaches

The probabilistic Haigh diagram is based on a parameterized model describing some unit or reference domain. However, it is not the first model proposed in this scope. Over the past decades, other approaches have been used in a weakest-link framework in order to describe the mean stress effect. Many of them can be interpreted as alternative formulations of a unit fatigue strength diagram. In this section, it should be discussed how these formulations differ from the proposed model, and what their similarities are.

Particularly in multiaxial high-cycle fatigue applications, weakest-link models are often used in combination with mean stress corrections that are based on a linear stress amplitude adjustment as it was discussed in Sections 2.8.1 and 2.8.3. Those approaches include the models of Sines [125], Crossland [127], Findely [130], Mataka [131] and others [128].

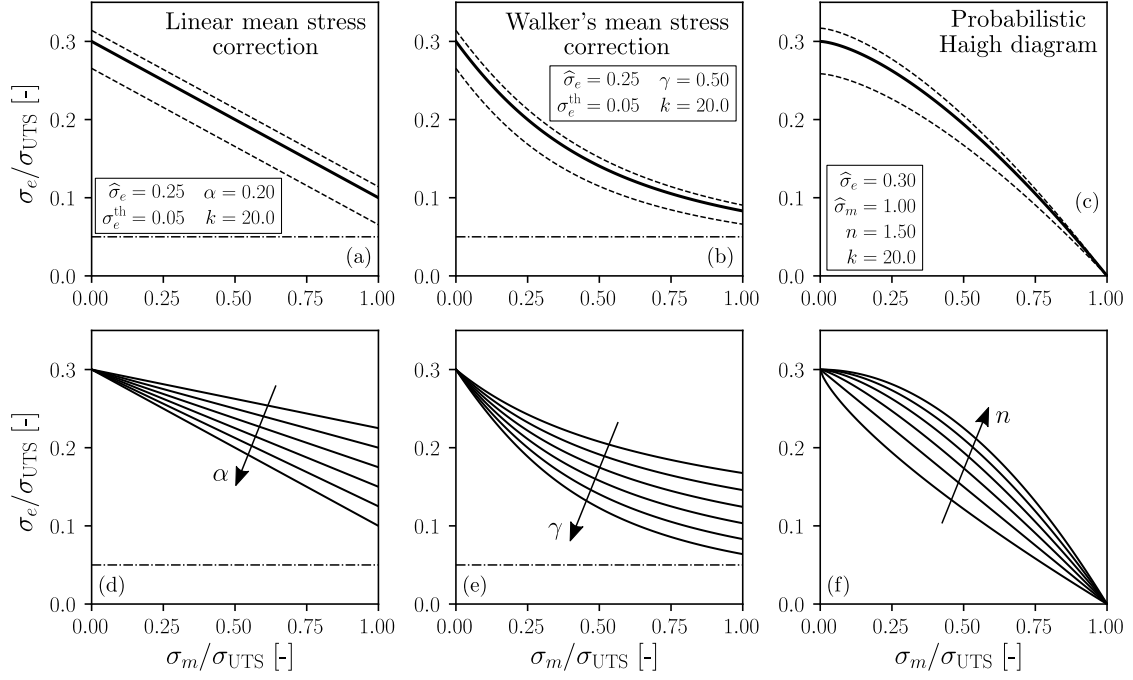


Figure 5.3: On the comparison between the probabilistic unit Haigh diagram and other mean stress models in a weakest-link context. The solid lines represent scale functions ($P_f \approx 63\%$), while the dashed lines in (a)-(c) depict the $P_f = 0.05$ and $P_f = 0.95$ quantile lines respectively. The diagrams in (d)-(e) illustrate the influence of central parameters on the respective scales.

When used in combination with a three-parameter Weibull distribution Eq. (2.28) in order to describe the fatigue strength scatter, as often done in the literature [41, 96, 163], the corresponding failure probability P_f^1 for a unit domain – compare Eq. (5.5) – homogeneously loaded with mean stress σ_m and stress amplitude σ_a , is described by

$$P_f^1(\sigma_m, \sigma_a | \theta_\alpha) = 1 - \exp \left\{ - \left(\frac{\langle \sigma_a + \alpha \sigma_m - \sigma_e^{th} \rangle}{\hat{\sigma}_e} \right)^k \right\}. \quad (5.18)$$

Here, the model vector is given by $\theta_\alpha = (\hat{\sigma}_e, \sigma_e^{th}, \alpha, k)$. Note that Eq. (5.18) describes a Weibull fatigue strength distribution with a mean stress dependent threshold parameter $\hat{\sigma}_e^{th}(\sigma_m) = \sigma_e^{th} - \alpha \sigma_m$. The corresponding unit fatigue strength diagram is depicted in terms of three quantile lines in Fig. 5.3a for a generic set of parameters. The influence of the mean stress parameter α on the scale function is shown in Fig. 5.3d. Characteristic for this type of mean stress model is the restriction to a linear trend, as well as the parallel quantile lines. The latter implies an increase of the relative scatter with mean stress. Both properties are not found in the proposed model shown in Fig. 5.3c and f, which allows for different curvatures via the parameter n , and exhibits non-parallel quantile lines reflecting a decreasing absolute scatter with increasing mean stress. Note that the proposed model is capable of describing linear trends of different slopes by means of varying the parameter $\hat{\sigma}_m$ while setting $n = 1$. On the other hand, in the case where the mean stress effect is well captured by a linear fatigue strength decrease, both models appear to be – except for the description of scatter – rather similar.

Another stress amplitude correction that should be addressed here is Walker's mean stress model [52], which was already discussed in Section 2.8.1. As it was pointed out before, this model contains the popular Smith-Watson-Topper [123] model as a special case ($\gamma = 0.5$), cf. [124]. When used within a weakest-link framework in order to describe the fatigue strength [161], Walker's model can also be interpreted as a corresponding unit fatigue strength diagram. In combination with a three-parameter Weibull distribution, that is by employing Eqs. (2.23) or (2.36) together with Eqs. (2.17) and (2.54) the failure probability of the unit domain when homogeneously loaded with mean stress σ_m and stress amplitude σ_a is expressed via

$$P_f^1(\sigma_m, \sigma_a | \theta_\gamma) = 1 - \exp \left\{ - \left(\frac{\langle \sigma_a \left(\frac{\sigma_m + \sigma_a}{\sigma_a} \right)^\gamma - \sigma_e^{\text{th}} \rangle}{\hat{\sigma}_e} \right)^k \right\}. \quad (5.19)$$

In this case the model parameter vector is defined by $\theta_\gamma = (\hat{\sigma}_e, \sigma_e^{\text{th}}, \gamma, k)$. When the threshold parameter σ_e^{th} is set to zero, the model can be interpreted as describing a Weibull fatigue strength distribution with a stress ratio dependent scale parameter. The corresponding unit diagram is shown in Fig. 5.3b for a generic set of parameters in form of three different quantile lines. Note that the latter have to be determined numerically, since Eq. (5.19) cannot be solved for σ_a analytically. The influence of the central model parameter γ on the scale function is illustrated in Fig. 5.3e. Characteristic for this model is the convex shape of its graph, where the slope is steep at $\sigma_m = 0$, and then flattens with increasing mean stress. Note that the vertical distance between two different quantile lines is not constant over the mean stress. In comparison with the proposed model shown in Fig. 5.3, one finds that the restriction of Walker's model to convex scale functions is not shared by the unit Haigh diagram. Also the scatter description varies between the two models. However, in a case where the fatigue strength can be described by a convex function over mean stress, the differences between both approaches appears to be small.

In summary, one finds that the considered approaches primarily exhibit differences with respect to the curvature of the quantile lines in the underlying unit fatigue strength diagram. While the linear stress amplitude correction is limited to a constant slope, Walker's model corresponds to an increasing one resulting in a convex graph. The proposed model on the other hand allows for convex ($n < 1$), straight ($n = 1$) or concave ($n > 1$) quantile lines. Additionally, the fatigue strength scatter dynamic over mean stress is modeled with subtle differences between the three model types. In the same context, one has to point out that the proposed model does not consider a fatigue strength threshold parameter, in contrast to the other two models.

As a final remark, it should be pointed out, that while both of the models presented in this section are known and used for several decades (Walker's model, for example, was introduced in 1970), they have – to the knowledge of the author – not been calibrated to test data using the procedure presented in Section 5.1.3 yet.

5.2.2 On the equivalent stress models

The computation of the probabilistic design Haigh diagram via Eq. (5.7) or Eq. (5.11) requires the definition of two equivalent local stress models, cf. Section 2.2. One for the stress amplitude σ_a^{eq} and one for the mean stress σ_m^{eq} . The purpose of this section is to discuss the choice for each of these two models.

The decision on which stress models to use essentially reflects a specific understanding of the fatigue process in the considered material. With respect to the stress amplitude, there is a broad consensus in the corresponding literature, see for example [129, 185, 186], that the crack initiation in metals associated with high-cycle fatigue is typically a process that is primarily driven by cyclic shear stresses, cf. Section 2.3. Before this background, the equivalent local stress amplitude in weakest-link models is often chosen as a critical-plane shear stress, cf. Ineqs. (2.40) and (2.41), or as the von Mises stress of the stress amplitude tensor given in Eq. (2.7), see Eqs. (2.38), (2.39). Compare also with [128, 129, 133]. In this context, it should be pointed out that shear stresses associated with critical planes are typically computationally more expensive to determine than the von Mises stress of the stress amplitude tensor, cf. [187].

With respect to the mean stress, it is often argued, that its detrimental influence is determined by its tensile contribution in normal direction with respect to the plane associated with the cyclic shear stress. This is essentially the perspective of critical plane approaches [20, 76]. Following this reasoning, the equivalent mean stress model in weakest-link approaches is often defined either as a static normal stress with respect to a critical plane, or as a related invariant of the mean stress tensor such as the hydrostatic mean stress. Compare also the local models discussed in Section 2.8.1, and the weakest-link study presented in [133]. Since they do not require the determination of a critical plane, invariant-based mean stresses such as the hydrostatic mean stress are computationally less expensive than critical plane mean stresses.

In this work, critical plane stresses have not been considered in the studies presented below. According to a study of Norberg and Olsson [133] the use of critical plane stresses in combination with weakest-link models has very little influence on the predicted failure probabilities compared to stress models based on tensor invariants. Due to their increased computational costs, they have therefore been forgone in this work. Instead, the equivalent stress amplitude σ_a^{eq} has been evaluated via von Mises' stress throughout this work, while three different equivalent mean stress models σ_m^{eq} based on the mean stress tensor's invariants have been considered – the von Mises, maximum principal and hydrostatic mean stress model. In this context, it must be pointed out, that the hydrostatic (octahedral) stress defined in Eq. (2.12) will always be used with a factor of three ($3\sigma^{\text{h}}$) in order to compare it with the two other models. Only in this way, all three models compute the same effective stress under uniaxial stress conditions, compare Eqs. (2.11), (2.12) and (2.14). Note however, that this additional factor does not change the model's failure predictions, but merely scales the model parameter $\hat{\sigma}_m$.

In order to get a first idea on the influence of the three considered mean stress models on the probabilistic design Haigh diagram, the latter was computed for two different notched specimens with respect to a common fixed model parameter vector θ . One cylindrical specimen (CN1, see Fig. 4.7), and one sheet specimen (NACA2B, see Fig. 4.2) have been modeled as finite element models under a nominal mean stress σ_m^{nom} in combination with a cyclic nominal stress amplitude σ_a^{nom} and evaluated using Eq. (5.11) in terms of their median lines ($P_f = 50\%$) for the three mean stress models. A more detailed description of this process, that is the numerical evaluation of Eq. (5.11) by means of finite element data, is provided in Section 5.3. Note that both specimens have a comparable stress concentration factor of $K_t = 1.99$ for the cylindrical one, and $K_t = 2.17$ for the sheet specimen. The results are presented in Fig. 5.4. Note that this figure also contains the results for different integration domains, which, however, will

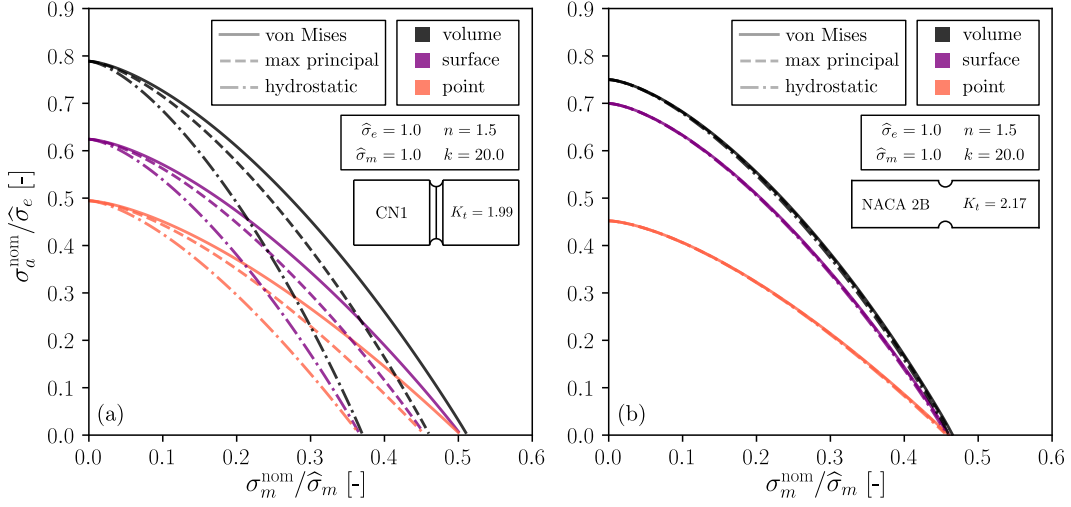


Figure 5.4: On the resulting median lines in the probabilistic design Haigh diagram for three different equivalent mean stress models and integration domains at a fixed model parameter vector θ . The equivalent stress amplitude is in all cases von Mises. Plot (a) shows the evaluation for a cylindrical and plot (b) for a sheet specimen. The unit domain was set to $\text{vol}(\Omega_1) = \text{vol}(\Omega_C)$.

not be discussed here, but in the next Section 5.2.3. On both diagrams, the used mean stress model is indicated by the line style of the median graphs. The color relates to the considered integration domain. In plot (a) the results for the cylindrical specimen CN1 are shown, while plot (b) depicts the median lines of the sheet specimen NACA2B.

The choice of the mean stress appears to affect mostly the mean stress intercept of the design Haigh diagram, independently of the considered integration domain. The von Mises mean stress model results in the greatest intercept, while the hydrostatic stress corresponds to the smallest intercept. The maximum principal lies in between. While this effect clearly shows in Fig. 5.4a for the cylindrical specimen, it is barely visible in Fig. 5.4b relating to the sheet specimen.

The difference between the two specimen types is related to the degree of multiaxiality encountered in the respective stress states. While the thin sheet specimen represents an example for close-to plane-stress conditions dominated by stress components in axial direction, the cylindrical specimen reflects plane-strain conditions with non-negligible stress components in circumferential direction.

In order to understand these differences from a more quantitative perspective, consider a general stress tensor $\boldsymbol{\sigma}$ in its principal axis system. When denoting the three principal stresses as σ_I , σ_{II} and σ_{III} , and expressing the two latter ones via $\sigma_{II} = \alpha_2 \sigma_I$ and $\sigma_{III} = \alpha_3 \sigma_I$ respectively, the three considered mean stress models can be expressed via

$$\sigma^{\text{mP}}(\boldsymbol{\sigma}) = \sigma_I \quad (5.20)$$

$$\sigma^{\text{vM}}(\boldsymbol{\sigma}) = \sigma_I \sqrt{\frac{1}{2} ((1 - \alpha_2)^2 + (1 - \alpha_3)^2 + (\alpha_2 - \alpha_3)^2)} \quad (5.21)$$

$$3\sigma^{\text{h}}(\boldsymbol{\sigma}) = \sigma_I (1 + \alpha_2 + \alpha_3). \quad (5.22)$$

One finds, that the two latter ones – the von Mises and hydrostatic stress – can be expressed in terms of the maximum principal stress and a factor depending on the degree multiaxiality, represented by α_2 and α_3 . A corresponding evaluation for $\alpha_2, \alpha_3 \in [0, 1]$,

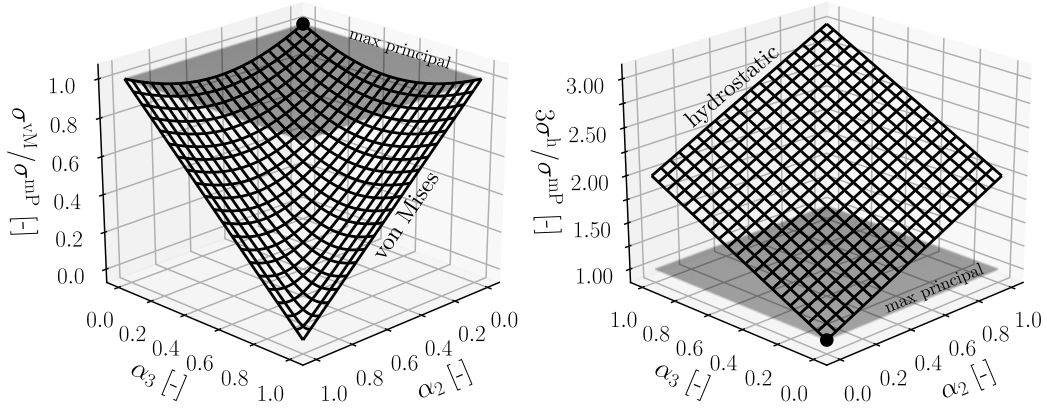


Figure 5.5: On the comparison between von Mises, maximum principal and hydrostatic stress models according to Eqs. (5.20)-(5.22). The black marker at (0,0,1) corresponds to uniaxial conditions, and is merely included for orientation. Note the different scales on the vertical axis.

that is for assuming that all principal stresses are positive (or negative), is presented in Fig. 5.5. In the left subplot one finds a comparison of the von Mises and the maximum principal stress, while the right subplot shows a respective comparison between the hydrostatic and the maximum principal stress. Note that the latter, which is independent of α_2 and α_3 , is visualized as a gray plane.

The results of this simple evaluation show that the von Mises model is always producing smaller effective stress values than the maximum principal stress. On the other hand, the hydrostatic stress model in form of $3\sigma^{\text{h}}$ is always producing greater effective stress values than the maximum principal stress. Hence, given $\sigma_I, \sigma_{II}, \sigma_{III} \geq 0$, one has

$$\sigma^{\text{vM}}(\boldsymbol{\sigma}) \leq \sigma^{\text{mP}}(\boldsymbol{\sigma}) \leq 3\sigma^{\text{h}}(\boldsymbol{\sigma}). \quad (5.23)$$

If the condition $\sigma_I, \sigma_{II}, \sigma_{III} \geq 0$ is not satisfied, Ineq. (5.23) does not hold in general. However, since hot-spot load conditions associated with high-cycle fatigue are often (but not always) associated with tensile stress states, the relation $\sigma_I, \sigma_{II}, \sigma_{III} \geq 0$ will be encountered in many applications.

In light of these results, one will expect that a probabilistic Haigh diagram based on the equivalent mean stress model utilizing the von Mises stress of the mean stress tensor corresponds to the most optimistic assessment. The hydrostatic model on the other hand is expected to produce the most conservative probabilistic Haigh diagrams with the maximum principal stress ending up in between. This is exactly the phenomenology that was found in the results reflected in Fig. 5.4. As a comparison: A look on the three principal stresses in the notch roots of the two specimen types in Fig. 5.4 reveals $(\alpha_2, \alpha_3) = (0.24, 0.006)$ for CN1 and $(\alpha_2, \alpha_3) = (0.003, 0.002)$ for NACA2B.

So far the discussion was focused on general, possibly triaxial, stress conditions. However, these stress conditions around a component's hot spot – which contribute the most to the resulting failure probability – are often dominated by only one or two principal stress components. This is due to the fact, that the hot-spot is almost always located on the component's surface, which is associated with plane stress conditions, since the stress component normal to the surface is zero ($\alpha_3 = 0$). The relations between the three considered effective stress models under these circumstances are visualized in Fig. 5.6 – this time also including the possibility of a negative second principal stress $\sigma_{II} = \alpha_2\sigma_I$.

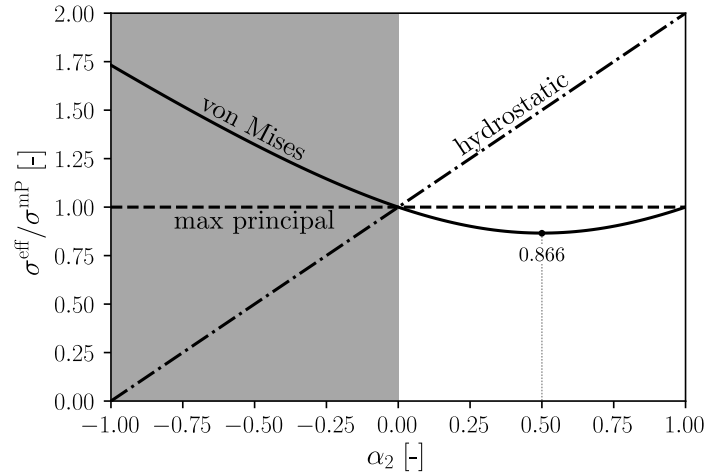


Figure 5.6: On the comparison between von Mises, maximum principal and hydrostatic stress models according to Eqs. (5.20)-(5.22) under plane-stress conditions ($\alpha_3 = 0$).

Considering the graphs corresponding to the three different models over the positive α_2 -axis, it is emphasized that the von Mises and maximum principal stress are typically very similar. The biggest difference for $\alpha_2 \geq 0$ is obtained when the second principal stress has half the magnitude of the first principal stress. In this case the von Mises stress drops to $\sqrt{3}/2 \approx 0.866$ of the corresponding value of the first principal stress. Under uniaxial stress conditions and under biaxial stress conditions with $\sigma_I = \sigma_{II}$, the von Mises and maximum principal stress are identical. The difference of the two aforementioned stress models with respect to the hydrostatic stress model is greater. This higher the degree of biaxiality, the greater the hydrostatic stress value. Note however that this trend flips when the second principal stress is negative ($\alpha_2 < 0$). In summary, one has to expect that under tension dominated hot-spot stress conditions ($\sigma_I, \sigma_{II} \geq 0$) with emphasized biaxiality, the use of the hydrostatic model for computing the effective mean stress field will produce considerably more conservative results than both the von Mises and maximum principal stress function when applied to the same model vector θ .

5.2.3 On the integration domain

During the formulation of the design Haigh diagram in Section 5.1.2, the integration domain that needs to be evaluated for the computation of the component's failure probability was denoted by the general entity Ω_C , see Eq. (5.7). In a practical application, this placeholder has to be specified. Frequently used integration domains for weakest-link models are the component volume $\Omega_C = V_C$ [36, 92, 163], and the component surface $\Omega_C = A_C$ [146]. As it was already discussed in Section 2.8.3 there are arguments for and against both of these choices which also apply in the context of the proposed model.

In order to get an impression on the effect of different integration domains in the design Haigh diagram's quantile lines, the example case described in the previous Section 5.2.2 will be considered. The median lines for the two specimen types CN1 and NACA2B have not only been computed for different mean stress models, but also for three different integration domains – the component volume, its surface and the critical location. Note that the latter can be interpreted as an integration domain consisting of a single point. In Fig. 5.4 the different domains are indicated by the three different colors.

In contrast to the effect of the mean stress model, the choice of the integration domain affects both specimen types. However, there are subtle differences. The primary effect of the integration domain appears to be the intercept of the median lines on the stress amplitude axis. While the volume model results in the greatest intercept, the point method corresponds to the lowest value. The surface domain remains in between. While this qualitative ranking is found in both specimen types, the difference between the volume and the surface domain is more pronounced for the cylindrical specimen. For the sheet specimen, on the other hand, the median lines of the surface and the volume method are very close together.

The small differences between the graphs corresponding to the surface and the volume domain of the sheet specimen are, again, explained by its geometry. Due to the sheet's flatness, the resulting stress fields have little variation in the thickness direction (plane stress). For a 2D-like stress field the surface and volume integrals from Eq. (5.7) are very similar, hence the small differences in the corresponding median lines in Fig. 5.4b.

5.2.4 Model scope and limits

The probabilistic Haigh diagram that was introduced over the last sections is intended as a means for estimating the failure probability of a metallic component with respect to high-cycle fatigue. As every model, it is based on several assumptions that translate into a certain applicability scope together with corresponding limitations. It is the purpose of this section to provide a respective summary.

Since the foundation of the model is established by a weakest-link framework, the assumptions associated with this type of approach are inherited by the probabilistic Haigh diagram. Most importantly, these assumptions include the statistical independence of the crack initiation process at any two locations on the considered component, i.e. no interaction between possible initiation sites, cf. [15]. Based on the typical HCF failure mechanism associated with sparsely distributed defects, this assumption is justified in most cases. Moreover it requires for the continuum hypothesis to be a reasonable approximation for the considered material. If the material exhibits large grains with pronounced elastic anisotropy, a continuum model may not be appropriate anymore.

Unrelated to the weakest-link model the following assumptions should be emphasized. Each of them should be checked before the model is applied to a specific problem.

- The component is subjected to cyclic constant-amplitude loads. While this will not be the case in most applications, the constant-amplitude assumptions has to be a reasonable approximation.
- The mean stress field is predominantly tensile and not compressive. This should hold at least for the considered domain around the relevant stress concentration.
- The temperature field is constant in space and time during the application of the cyclic loads. If this assumption does not hold for the entire component, it should at least be satisfied for the regions around the relevant stress concentration.
- The material properties are isotropic and remain constant over the considered component domain. Directional dependent or spatial fatigue strength variations are not captured by the model.
- The material properties remain constant over time. This restriction aims at creep and degradation processes. Effects like surface roughening, corrosion or the generation of creep voids are not accounted for by the model.

5.3 Numerical aspects

The computation of the failure probability expressed in Eq. (5.7) requires the evaluation of the weakest-link integral I , as defined in Eq. (5.24) below. Unfortunately, in almost all cases of practical relevance, no analytical solution will be available, which makes it necessary to provide an approximation in the form of

$$I := \int_{\Omega} \left(\frac{\sigma_a(\mathbf{x})}{\sigma_e(\sigma_m(\mathbf{x}))} \right)^k \frac{d\Omega(\mathbf{x})}{\text{vol}(\Omega_1)} = Q + E \quad (5.24)$$

where Q denotes the approximation of I and E represents the absolute error that goes along with it. Note that in Eq. (5.24) the equivalent local stress fields are denoted as $\sigma_m(\mathbf{x}) := \sigma_m^{\text{eq}}(\sigma_m(\mathbf{x}, [0, T]))$ and $\sigma_a(\mathbf{x}) := \sigma_a^{\text{eq}}(\sigma_a(\mathbf{x}, [0, T]))$ respectively. This abbreviated notation will be kept throughout this section in order to unburden the notation. The denominator $\sigma_e(\sigma_m(\mathbf{x}))$ is used with respect to Eq. (5.2). As discussed in Section 5.2.3, the integration domain Ω might represent the component volume ($\Omega = V$), its surface ($\Omega = A$) or subdomains or even combinations thereof, depending on the chosen approach. The corresponding failure probability P_f , which, after all, is the end result of the assessment, is consequently approximated via

$$P_f = 1 - \exp\{-I\} \approx 1 - \exp\{-Q\} =: \tilde{P}_f. \quad (5.25)$$

The approximative character is introduced by two sources. First, the equivalent local stress fields σ_a and σ_m appearing in the integrand of Eq. (5.24) are typically provided by means of a finite element analysis, which is essentially an approximate method to solve the underlying system of partial differential equations. Consequently, the available stress field values will deviate from the exact solution to some extent, depending on analysis settings like the mesh resolution. The second approximation is introduced by numerical integration (quadrature) itself. Quadrature becomes necessary, since in general, even if exact solutions for σ_m and σ_a were available, I could still not be evaluated analytically. The error of this second approximation is typically controllable by a resolution parameter describing the number of used integration points.

Questions arising in this context, especially with respect to practical applications in an engineering context, need to aim at the sensitivity of the computed failure probability with respect to the errors introduced by the two approximations, i.e. how important is a good approximation of the used stress fields with respect to the derived failure probability, and how many integration points are required in the applied quadrature rule to obtain a reasonable approximation? Those considerations are particularly important with regard to errors that might translate in non-conservative failure probabilities.

Before discussing these questions in detail, the applied numerical integration scheme based on Gaussian quadrature is presented in Section 5.3.1. This specific quadrature rule is rather common in weakest-link applications. However, some of the existing alternatives are briefly discussed. The respective quadrature error is considered in the following Section 5.3.2. Based on some theory-focused preparation, the quadrature error is analyzed in a numerical study for a parameterized element stress field. Finally, the role of deviations in the stress field approximation as well as their interaction with the quadrature error is studied in Section 5.3.3 by conducting different mesh convergence studies for notched members. The results are summarized in Section 5.3.4.

5.3.1 Quadrature rule

Considering the approximation of the weakest-link integral I in Eq. (5.24), it is assumed that the basis for the evaluation of I are stress fields obtained from a finite element analysis, which generally corresponds to the practical setup. The quadrature will therefore be applied to each element individually, resulting in

$$I = \sum_{i=1}^{n_e} I_i = \sum_{i=1}^{n_e} \int_{\Omega_i} \left(\frac{\sigma_a(\mathbf{x})}{\sigma_e(\sigma_m(\mathbf{x}))} \right)^k d\Omega_i(\mathbf{x}) = \sum_{i=1}^{n_e} (Q_i + E_{Q_i}). \quad (5.26)$$

where n_e denotes the number of finite elements. Analogous with Eq. (5.24), Q_i and E_{Q_i} correspond to the approximation of the element integral I_i and the associated absolute error respectively. Note that in Eq. (5.26) the notation of the unit domain Ω_1 was omitted in order to avoid confusion with the domain of the first element in the summation over all elements. Effectively, this means $\text{vol}(\Omega_1) = 1$, which will be assumed for the entire following discussion, since Ω_1 plays no role for the approximation error.

In order to approximate the element integral I_i in Eq. (5.26), Gauss-Legendre quadrature rules are used throughout this work, cf. [188]. With respect to the overall weakest-link integral I from Eq. (5.26), this translates into the expression

$$\begin{aligned} I &= \sum_{i=1}^{n_e} \left(\sum_{j=1}^{n_{g,i}} \left(\frac{\sigma_a(\mathbf{x}_{ij})}{\sigma_e(\sigma_m(\mathbf{x}_{ij}))} \right)^k |\det(D\Phi(\mathbf{x}_{ij}))| w_{ij} + E_{Q_i} \right) \\ &= \underbrace{\sum_{i=1}^{n_e} \sum_{j=1}^{n_{g,i}} \left(\frac{\sigma_a(\mathbf{x}_{ij})}{\sigma_e(\sigma_m(\mathbf{x}_{ij}))} \right)^k \tilde{w}_{ij}}_{=Q} + \underbrace{\sum_{i=1}^{n_e} E_{Q_i}}_{=E_Q} \end{aligned} \quad (5.27)$$

where $n_{g,i}$ denotes the number of Gaussian integration points on element i and \mathbf{x}_{ij} corresponds to the j^{th} integration point on the i^{th} element. Moreover $\Phi_i : \Omega_i^{\text{ref}} \rightarrow \Omega_i$ denotes the transformation between the generally skewed element geometry Ω_i and a corresponding reference geometry Ω_i^{ref} , see Fig. 5.7, while $D\Phi$ represents its Jacobi matrix. The integration weights w_{ij} of the Gauss-Legendre rule correspond to the reference geometry, whereas $\tilde{w}_{ij} := |\det(D\Phi(\mathbf{x}_{ij}))| w_{ij}$ simply combines the integration weights for the reference domain with the contribution $|\det(D\Phi(\mathbf{x}_{ij}))|$ accounting for the actual geometry. A more detailed description of the use of Gaussian quadrature in the context of a weakest-link integral based on finite element data can be found in [92].

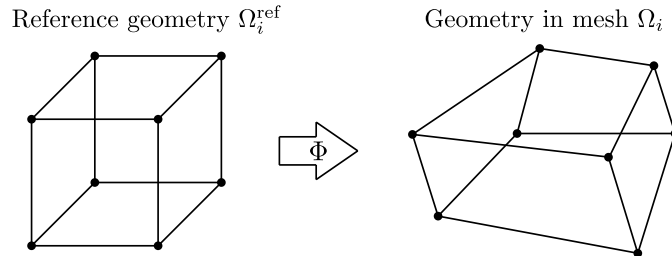


Figure 5.7: On the transformation Φ mapping between a brick element's reference geometry Ω_i^{ref} and the actual element geometry $\Omega_i = \Phi(\Omega_i^{\text{ref}})$ as it is found in the finite element mesh.

It should be pointed out, that Eq. (5.27) can be evaluated with standard output from finite element software as long as one is integrating over the entire volume ($\Omega = V$). Both, the stresses $\sigma_m(\mathbf{x}_{ij})$, $\sigma_a(\mathbf{x}_{ij})$ at the element integration points \mathbf{x}_{ij} , together with the corresponding integration weights \tilde{w}_{ij} can be printed to a file by setting corresponding output flags. In Abaqus, for example, one can trigger the output of the integration weights \tilde{w}_{ij} , which correspond to volume increments, by setting the IVOL flag. However, in this approach the number of integration points is limited to those used by the respective element type. For brick elements, for example, this typically allows the use of no more than three integration points per dimension, i.e. 27 per element. In order to overcome this boundary, a finite element post-processor was developed in the course of this work (based on already existing routines provided by Siemens), which allows the use of up to 16 integration points per dimension for both surface and volume integration. Note that the surface weakest-link integral ($\Omega = A$) cannot be evaluated based on standard finite element data, since it requires surface identification and the definition of additional integration points on this surface, cf. [92].

Other approaches for approximating weakest-link integrals have been considered in the literature – although in the context of different models than the one introduced here. In [167] the utilized volumetric weakest-link integration scheme only used one equivalent stress value per element, evaluated at its centroid. On the other hand, in [36] the element stress fields were assumed vary linearly over the element volume bounded by the element minimum and maximum stress. Under this assumption the element integrals could be solved analytically for the considered model in [36]. Both methods were aiming to allow an easy use of the weakest-link approach in engineering practice by only using standard output from finite element software. However, as pointed out before, this also holds for the method presented here, with respect to the volumetric weakest-link integral.

5.3.2 On the quadrature error

In this section, the error between the weakest-link integral I and its approximation Q is investigated, cf. Eq.(5.24). This error does not include the stress field error introduced by the finite element approximation, which will be treated in the following Section 5.3.3. From this perspective, the considered quadrature error refers to a given stress field, irrespective of the approximation errors reflected by it.

Before going into detail, a brief comment on the role of rounding errors on the quadrature error should be added. Since the expression for the overall approximation Q as stated in Eq. (5.27), is a well-conditioned sum over strictly positive summands – the Gaussian integration weights w_{ij} are always positive – no particularly error contributions are to be expected from rounding errors. It is for this reason, that rounding errors are not further considered in the remainder of this section.

When discussing the quadrature error, one has to keep in mind that the end result of any probabilistic analysis, such as the weakest-link assessment considered here, is the computed probability of failure P_f . Consequently, the severity of the quadrature error has to be evaluated with respect to its influence on P_f , cf. Eq. (5.25). In order to study this effect, the following relative errors are introduced.

$$\varepsilon_I := \left| \frac{I - Q}{I} \right| \quad \varepsilon_{P_s} := \left| \frac{P_s - \tilde{P}_s}{P_s} \right| \quad \varepsilon_{P_f} := \left| \frac{P_f - \tilde{P}_f}{P_f} \right| \quad (5.28)$$

They quantify the relative quadrature error, cf. Eq. (5.24), the relative error with respect to the probability of survival $P_s = 1 - P_f$ and finally the relative error with respect to the failure probability P_f . As mentioned above, the last error ε_{P_f} is of primary concern here. Therefore, before discussing the quadrature error ε_I itself in more detail, the first intermediate goal is to link the quadrature error ε_I to ε_{P_f} .

As a first step in this direction, using Eq. (5.25) one may reformulate ε_{P_f} in terms of the relative error in the survival probability ε_{P_s} . This results in

$$\varepsilon_{P_f} = \varepsilon_{P_s} \frac{P_s}{P_f}. \quad (5.29)$$

Consequently, for a fixed P_f – and therefore a fixed P_s – the relative error ε_{P_f} is proportional to ε_{P_s} . However, if P_f is small, as it should be the case in design applications, the second factor in Eq. (5.29) becomes large. Hence, in most cases, the relative error in the failure probability ε_{P_f} will be considerably greater than the relative error ε_{P_s} .

As a next step, the relative error of the survival probability ε_{P_s} is expressed in terms of the relative quadrature error ε_I . By combining Eq. (5.25) with Eq. (5.28) one deduces

$$\varepsilon_{P_s} = |1 - \exp\{I - Q\}| = |1 - \exp\{\pm\varepsilon_I I\}| = |1 - P_s^{\mp\varepsilon_I}| \quad (5.30)$$

where the sign of ε_I depends on the sign of $I - Q$. By combining Eqs. (5.29) and (5.30) one arrives at an expression which describes ε_{P_f} as a function of ε_I and P_s , that is

$$\varepsilon_{P_f} = |1 - P_s^{\pm\varepsilon_I}| \frac{P_s}{1 - P_s}. \quad (5.31)$$

In this formulation, it is still unclear how the relative quadrature error ε_I generally translates into ε_{P_f} . In order to provide an estimate of ε_{P_f} solely in terms of ε_I the following two lemmata will be of help. Note that the first one, Lemma 5.1 is merely a means to show the following Lemma 5.2.

Lemma 5.1. *Let $p, q \in \mathbb{R}$ with $p \in (0, 1)$ and $q > 0$ then*

$$p^q \leq 1 + q(p - 1) \quad \text{if } 0 < q < 1 \quad (5.32)$$

$$p^q \geq 1 + q(p - 1) \quad \text{if } q > 1 \quad (5.33)$$

Proof. The stated inequalities follow immediately from the generalization of Bernoulli's inequality for real exponents [189]. Indeed, let $x > -1$ and $0 < q < 1$ then the generalization reads $(1 + x)^q \leq 1 + qx$. With $x = p - 1 > -1$ one obtains (5.32). In case of $x > -1$ and $q > 1$ the generalization reads $(1 + x)^q \geq 1 + qx$. Defining again $x = p - 1 > -1$ one obtains the second inequality (5.33) stated above. \square

Lemma 5.2. *Let $p, r \in \mathbb{R}$ with $p \in (0, 1)$ and $r \in [-1, 1]$ then*

$$|1 - p^r| \frac{p}{1 - p} \leq |r|. \quad (5.34)$$

Proof. If $r \in \{-1, 0, 1\}$ the stated inequality (5.34) obviously holds. Now, consider $r \in (0, 1)$. In this case, $0 < p^r < 1$, hence $1 - p^r > 0$. Together with (5.33) from the

previous Lemma 5.1 one obtains

$$\begin{aligned}
|1 - p^r| \frac{p}{1-p} &= (1 - p^r) \frac{p}{1-p} \\
&= \frac{p}{1-p} - \frac{p^{r+1}}{1-p} \\
&\leq \frac{p}{1-p} - \frac{1 + (1+r)(p-1)}{1-p} \\
&= \frac{p-1}{1-p} + 1 + r \\
&= |r|
\end{aligned}$$

confirming the claim. Now, consider the remaining case of $r \in (-1, 0)$ corresponding to $p^r > 1$. Using again Lemma 5.1, this time inequality (5.32), one derives

$$\begin{aligned}
|1 - p^r| \frac{p}{1-p} &= (p^r - 1) \frac{p}{1-p} \\
&= \frac{p^{r+1}}{1-p} - \frac{p}{1-p} \\
&\leq \frac{1 + (1+r)(p-1)}{1-p} - \frac{p}{1-p} \\
&= \frac{1}{1-p} - 1 - r - \frac{p}{1-p} \\
&= |r|
\end{aligned}$$

consistent with (5.34) and concluding the proof. \square

The result stated in the last Lemma 5.2 provides a means to give an estimation of the relative error ε_{P_f} solely in terms of ε_I . Assuming $\varepsilon_I \leq 1$ – which is an assumption that should always hold in a serious design effort – one obtains with respect to Eq. (5.31)

$$\boxed{\varepsilon_{P_f} = |1 - P_s^{\pm\varepsilon_I}| \frac{P_s}{1 - P_s} \leq \varepsilon_I.} \quad (5.35)$$

This important intermediate result shows that the relative error in the failure probability ε_{P_f} cannot be greater than the relative quadrature error ε_I , when the latter is not exceptionally large ($\varepsilon_I \leq 1$). Consequently, by establishing an upper bound for the relative error in I , one simultaneously obtains an upper bound for the relative error in P_f . Therefore, in the remainder of this section, the estimation of ε_I will be discussed.

In this context, a first trivial result is obtained when expressing the overall weakest-link integral I as the sum of the element weakest-link integrals as stated in Eq. (5.26). Using that $I_i > 0$ for all $i \in \{1, \dots, n_e\}$, cf. Eq. (5.26), and consequently $I > 0$ one finds

$$\varepsilon_I = \left| \frac{I - Q}{I} \right| = \left| \frac{\sum_{i=1}^{n_e} \frac{I_i - Q_i}{I_i} I_i}{I} \right| \leq \frac{\sum_{i=1}^{n_e} \varepsilon_{I_i} I_i}{I} \leq \frac{\varepsilon_{I_{\max}} \sum_{i=1}^{n_e} I_i}{I} = \varepsilon_{I_{\max}}. \quad (5.36)$$

Here, $\varepsilon_{I_i} := |(I_i - Q_i)/I_i|$ denotes the relative quadrature error for element $i \in \{1, \dots, n_e\}$, while the subscript “max” refers to maximum value of I_i over all elements. Consequently,

by taking into account the two previous Ineqs. (5.35) and (5.36), one obtains

$$\varepsilon_{P_f} \leq \varepsilon_{I_{i_{\max}}}. \quad (5.37)$$

Hence, an upper bound for the relative error in the failure probability can be established by the largest relative quadrature error on element level.

In order to study the quadrature error for individual elements, some simplifying assumptions will have to be made. In this context, it should be pointed out, that it is not goal of this investigation is to obtain a quantitative a-priori error estimate for all possible situations and element types, since the number of relevant parameters is too high. Instead, a qualitative understanding of different influence parameters in a characteristic setting should be discussed in order to raise awareness with respect to which parameters amplify the error and which ones are less critical. Due to Ineq. (5.37) these influences can be directly related to the relative error in the computed failure probability P_f .

For the generic case to be discussed, a (volumetric) brick element $i \in \{1, \dots, n_e\}$ in a given finite element model is considered. This element type is the most frequently used type with respect to the considered finite element models in this work. As pointed out in Section 5.3.1, the element geometry V_i will generally be skewed to some degree in the mesh. Before the Gaussian quadrature rule is applied, this skewed geometry is transformed into a unit cube $V_i^{\text{ref}} = [0, 1]^3$ by means of the transformation Φ_i . The weakest-link element integral is then expressed as an integral over the unit cube via

$$I_i := \int_{V_i} \left(\frac{\sigma_a(\mathbf{x})}{\sigma_e(\mathbf{x})} \right)^k dV_i(\mathbf{x}) = \int_{V_i^{\text{ref}}} \left(\frac{\sigma_a(\Phi_i(\mathbf{x}))}{\sigma_e(\sigma_m(\Phi_i(\mathbf{x})))} \right)^k |\det(D\Phi_i(\mathbf{x}))| dV_i^{\text{ref}}(\mathbf{x}). \quad (5.38)$$

In this context, the first simplification concerns the influence of the skewed element geometry, as it appears in the mesh. This influence is reflected by the term $|\det(D\Phi_i(\mathbf{x}))|$ appearing in the integrand above. In the following discussion, this term will not be considered, so that effectively the quadrature error over the reference geometry will be studied. This simplification is justified by argument that in an appropriate finite element mesh the elements should generally not be excessively distorted. In these cases, the term $|\det(D\Phi_i(\mathbf{x}))|$ will be of small variation over the element, especially compared with the first term of the integrand, where the exponent k may assume values up until $k = 40$. The corresponding contribution to the quadrature error will be small as well.

The second simplification is introduced by an explicit description of the equivalent local stresses $\sigma_a(\Phi_i(\mathbf{x}))$ and $\sigma_m(\Phi_i(\mathbf{x}))$. Since a general description is not feasible, both due to the variety of equivalent local stress models, and the number of required parameters, a simple linear variation for both stress fields will be assumed, that is

$$\sigma_m(\Phi_i(\mathbf{x})) = \sigma_m^{\max} \left(1 - \frac{\rho_m}{3} \sum_{j=1}^3 x_j \right). \quad (5.39)$$

$$\sigma_a(\Phi_i(\mathbf{x})) = \sigma_a^{\max} \left(1 - \frac{\rho_a}{3} \sum_{j=1}^3 x_j \right) \quad (5.40)$$

Here, σ_a^{\max} and σ_m^{\max} represent the maximum stresses attained in the considered element, while $0 < \rho_a, \rho_m < 1$ describe the relative stress variation over the element with respect to σ_a^{\max} and σ_m^{\max} respectively. Moreover, $x_j \in [0, 1]$ for $j \in \{1, 2, 3\}$, see also Fig. 5.8.

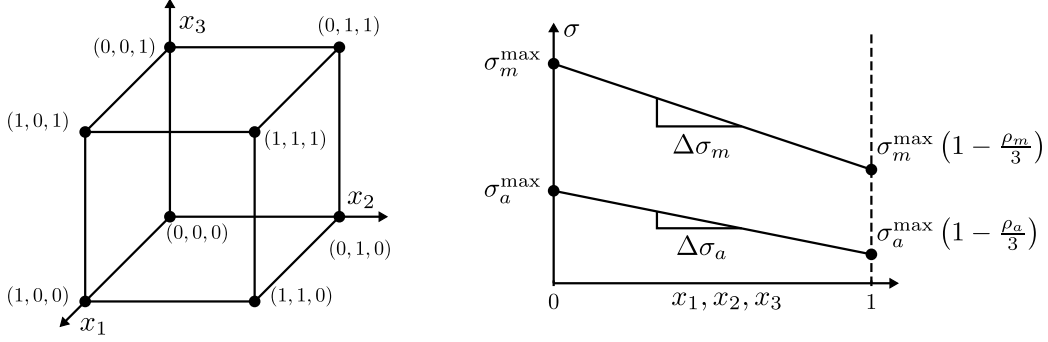


Figure 5.8: On the stress fields considered in the analysis of the quadrature error.

At this point, it is possible to specifically formulate the considered integral I_i together with the approximation Q_i . Denoting the number of integration points in one dimension as n_{ip} , using Eqs. (5.38), (5.40), (5.39) and (5.27) one ends up at

$$I_i = \int_{[0,1]^3} f(\mathbf{x}) \, d\mathbf{x} \approx \sum_{h,l,m=1}^{n_{ip}} f(x_{1,h}, x_{2,l}, x_{3,m}) w_{1,h} w_{2,l} w_{3,m} = Q_i \quad (5.41)$$

with $f(x_1, x_2, x_3) = \left(\frac{\sigma_a^{\max}}{\hat{\sigma}_e} \right)^k \left(\frac{1 - \frac{\rho_a}{3} \sum_{j=1}^3 x_j}{1 - \left(\frac{\sigma_m^{\max}}{\hat{\sigma}_m} \right)^n \left(1 - \frac{\rho_m}{3} \sum_{j=1}^3 x_j \right)^n} \right)^k$.

The first observation with respect to Eq. (5.41) is that neither σ_a^{\max} nor $\hat{\sigma}_e$ influence the relative quadrature error ε_{I_i} , since they cancel out in the fraction

$$\varepsilon_{I_i} = \left| \frac{I_i - Q_i}{I_i} \right|. \quad (5.42)$$

For the same reason, also the presence of a constant nonzero mean stress ($\rho_m = 0 < \sigma_m^{\max}$) does not influence the quadrature error. If, on the other hand, the mean stress is not constant ($\sigma_m^{\max}, \rho_m > 0$) the ρ_m - and σ_m^{\max} -terms do not generally cancel out in Eq. (5.42) and one finds an influence on the quadrature error. Note that these results remain to hold for the general case, when the above simplifications are dropped. Hence, the parameters that affect ε_{I_i} are ρ_a, ρ_m as well as the ratio $\sigma_m^{\max}/\hat{\sigma}_m$ the Weibull shape k , the curvature n and of course the number of integration points per dimension n_{ip} . In order to study these influences, a concise numerical study was conducted. For several combinations of $\rho_a, \rho_m, \sigma_m^{\max}/\hat{\sigma}_m, n$ and k , the relative error ε_{I_i} was evaluated over the number of used integration points n_{ip} . Since, even with the considered simplifications, I_i could not be evaluated analytically, it was approximated using the Gaussian quadrature rule with a high number of integration points, specifically $n_{ip}^{\text{ref}} = 15$. The results of this study, which were generated using a Python-script, are presented in Fig. 5.9.

All diagrams contained in this figure show the relative quadrature error on a logarithmic scale as a function of the number of integration points in one dimension n_{ip} for several parameter combinations. In the two upper diagrams (a) and (b) the mean stress was set to zero, i.e. $\sigma_m^{\max} = \rho_m = 0$, while ρ_a, n and k are varied. One observes, that for all analyzed parameter combinations ε_{I_i} decreases with an increase in n_{ip} . Due to the use of floating point numbers, the relative error can only be evaluated to values as low as approximately machine precision, which was $\text{eps} = 2.22 \cdot 10^{-16}$ on the used machine with

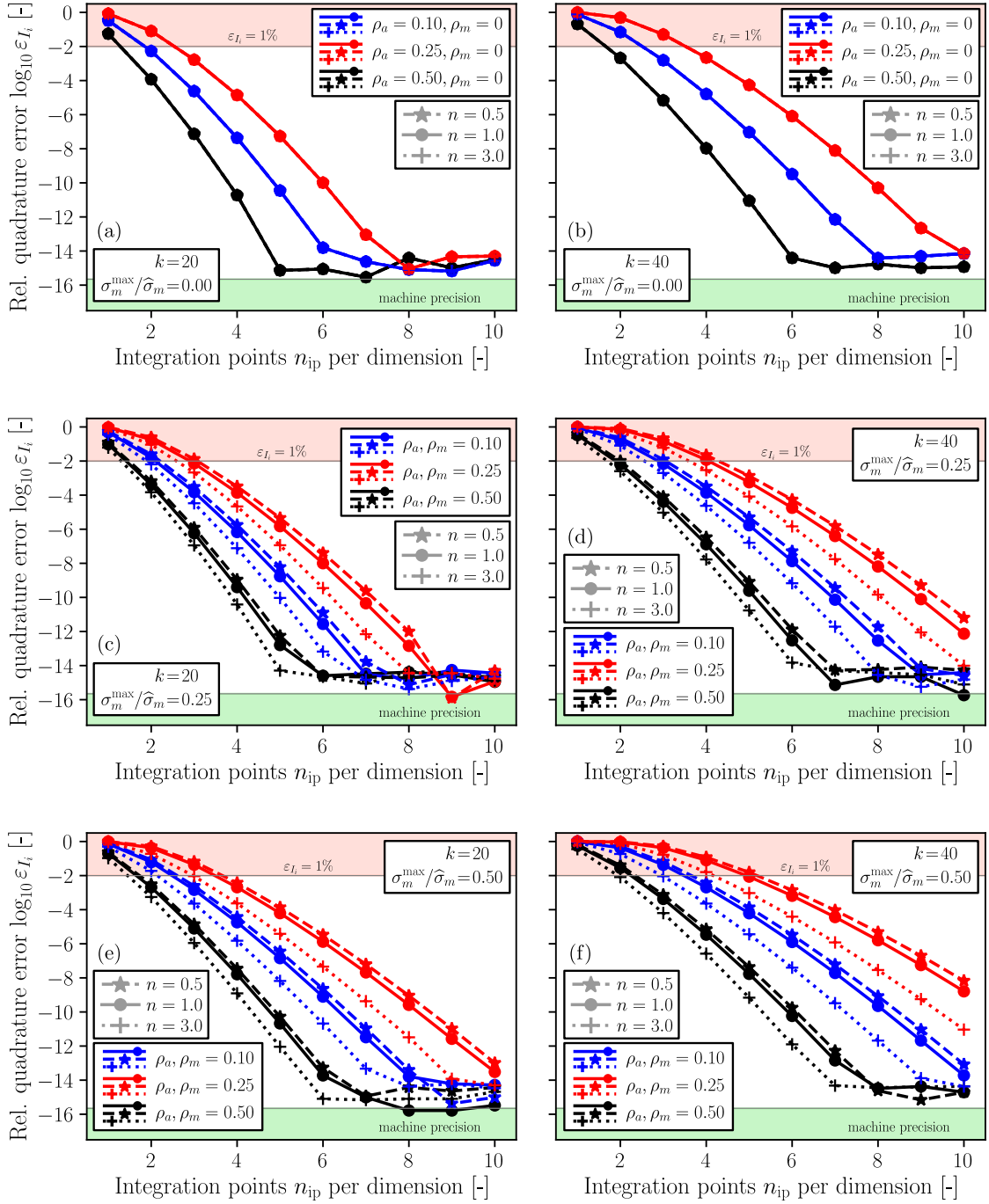


Figure 5.9: The relative quadrature error ε_{I_i} of the weakest-link integral I_i for a single brick element $[0, 1]^3$ over the number of Gaussian integration points n_{ip} in one dimension (hence, n_{ip}^3 integration points per element), cf. Eq. (5.41). The two columns refer to the scatter parameter $k \in \{20, 40\}$, while the rows correspond to different mean stress levels in the notch root. The green area indicates errors below machine precision, which was $\text{eps} = 2.22 \cdot 10^{-16}$, while the red area represents relative errors above 1%.

the considered data type. This is the reason why the the shown graphs are trailing off horizontally as soon as the error approaches eps. The respective values in these horizontally trending branches correspond to relative errors below machine precision, indicated by the green shaded area at the bottom of each diagram. With respect to the other influence parameters, one observes an increase in the relative error due to an increase in both k and ρ_a . Due the absence of mean stress, the curvature parameter n has no influence, so that all respective graphs coincide.

In the second row of diagrams, containing plot (c) and (d), a non-constant mean stress field is present. The ratio $\sigma_m^{\max}/\hat{\sigma}_m$ was set to 0.25, while the mean stress variation ρ_m was set to the same values as $\rho_a \in \{0.1, 0.25, 0.5\}$. The only difference between the two diagrams is the Weibull shape k , which was $k = 20$ in plot (c), and $k = 40$ in plot (d), similar as in the other two rows. Looking from left to right, one again observes the error-increasing effect of larger k values. Comparing the second row of plots with the one above, one additionally notices an increase in ε_{I_i} with the presence of a non-constant mean stress field. The curvature n , which was set to values of $n \in \{0.5, 1, 3\}$, shows an error decreasing effect when n itself is increased.

Finally, in the last row of diagrams, containing plot (e) and (f), one encounters the same selection of parameters as in the second row, with the only difference being the increased value of the ratio $\sigma_m^{\max}/\hat{\sigma}_m$ to 0.5 compared to 0.25 in the middle row. As a result, one finds a further increase in the quadrature error. Moreover, the qualitative influence of the curvature parameter n is the same as for the diagrams in the row above.

If one defined a relative quadrature error of $\varepsilon_{I_i} \leq 1\%$ as acceptable – resulting in $\varepsilon_{P_f} \leq 1\%$ due to Ineq. (5.37) – one can look up the required number of integration points in one dimension for the Gaussian quadrature rule in order to achieve this accuracy. In the shown diagrams in Fig. 5.9 this number corresponds to the first point on a considered line below the red shaded area at the top of each diagram. In this context, note that the relative error bound of $\varepsilon_{P_f} \leq 1\%$ is a rather strict tolerance with respect to the absolute error $|P_f - \tilde{P}_f|$, if P_f is small. For example, if the exact failure probability is $P_f = 0.1\%$ an approximated value of $\tilde{P}_f = 0.102\%$ would not be acceptable since the corresponding relative error would be $\varepsilon_{P_f} = 2\%$, cf. Eq. (5.28), exceeding the threshold of 1%.

While in the absence of mean stress, or the presence of a constant mean stress, two or three integration points per dimension are sufficient in most cases, this changes when a non-constant mean stress is present. The greater the mean stress variation ρ_m and the peak mean stress σ_m^{\max} with respect to $\hat{\sigma}_m$ the more integration points are required to meet the goal of $\varepsilon_{I_i} \leq 1\%$. A qualitatively similar effect holds for the Weibull shape k . The higher the shape k , the more integration points will be required. For the curvature parameter n on the other hand, the influence appears reversed. Higher values of n lead to a reduction of the quadrature error in the considered case, although this influence seems smaller than the influence of k . Consequently, the most challenging situation from a numerical perspective is encountered in an element that exhibits large stress variations ρ_m, ρ_a and a high peak mean stress σ_m^{\max} with respect to $\hat{\sigma}_m$ in combination with a high Weibull shape k and a low curvature parameter n .

It must be pointed out again that these results have been derived from a generic example case under several simplifying assumptions, especially with respect to the stress fields σ_m and σ_a . However, they reflect qualitative trends that are also encountered in many practical applications of the method. This will be demonstrated by the examples provided in the next section, where the influence of the mesh resolution is discussed.

5.3.3 On the role of the mesh resolution

Next to the error introduced by numerical integration as discussed in the previous section, a second major error source emerges when the evaluated stress fields are merely approximations of their exact solutions. This situation is encountered in almost all design applications, where the stress fields are obtained by means of finite element analyses. When denoting the exact values of the equivalent stress fields by $\sigma_m(\mathbf{x})$ and $\sigma_a(\mathbf{x})$, while the approximations are written as $\tilde{\sigma}_m(\mathbf{x})$ and $\tilde{\sigma}_a(\mathbf{x})$ this error can be expressed via

$$I = \int_D \left(\frac{\sigma_a(\mathbf{x})}{\sigma_e(\sigma_m(\mathbf{x}))} \right)^k \frac{d\Omega(\mathbf{x})}{\text{vol}(\Omega_1)} = \underbrace{\int_\Omega \left(\frac{\tilde{\sigma}_a(\mathbf{x})}{\sigma_e(\tilde{\sigma}_m(\mathbf{x}))} \right)^k \frac{d\Omega(\mathbf{x})}{\text{vol}(\Omega_1)}}_{=: \tilde{I}} + E_I. \quad (5.43)$$

Here, \tilde{I} represents the exact evaluation of the weakest-link integral using the approximative stress fields, while E_I denotes the corresponding absolute error. As discussed in the last section, \tilde{I} typically cannot be evaluated exactly. Instead, an approximative quadrature rule is used $\tilde{I} = Q + E_Q$, cf. Eq. (5.27), resulting in a respective error E_Q . In the obtained overall approximation, stated in Eq. (5.24), both errors are combined as to

$$I = Q + \underbrace{E_Q + E_I}_{=: E}. \quad (5.44)$$

Assuming that a finite element analysis is used to obtain the required stress field approximation, the purpose of this section is to study the influence of the used finite element model on the error in the computed failure probability P_f that results from the combined integral error E . The focus will be solely on the mesh resolution, meaning the fineness of the used grid. Note that the choice of the mesh indeed influences both error sources stated in Eq. (5.44). It specifically also influences the quadrature error, since finer meshes typically result in smaller stress variations per element, which reduces the quadrature error, as discussed in the last section.

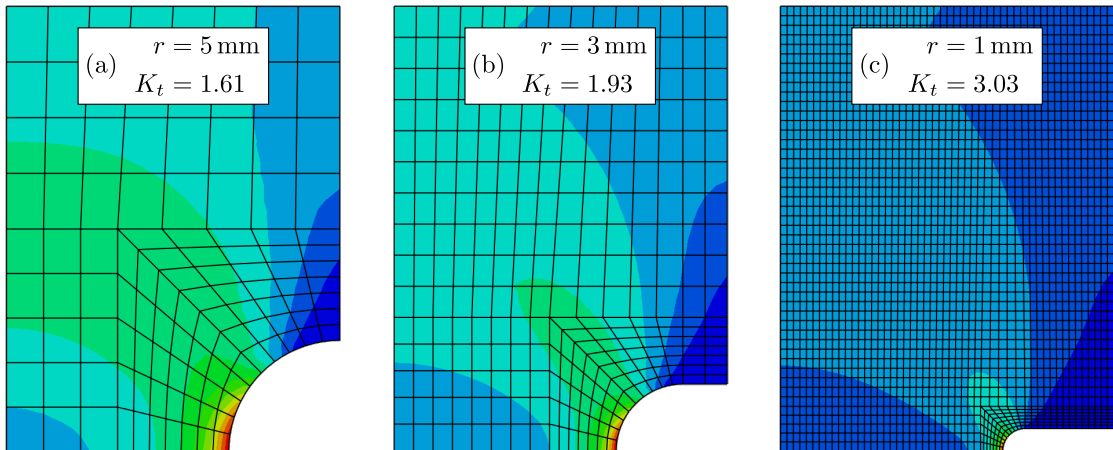


Figure 5.10: The three notched cylindrical coupons used in the analysis with $n_{\text{res}} = 10$ elements on the half-notch arc. Due to symmetry reasons, only the upper half section was modeled. The coupon radius was set to 15 mm while the shown half-length was defined as 20 mm.

In order to examine the mesh influence, a finite element model of an axially loaded cylindrical coupon containing a semicircle shaped notch was set up, see Fig. 5.10. Three different notch radii r were considered with $r \in \{1 \text{ mm}, 3 \text{ mm}, 5 \text{ mm}\}$, while the notch root cross section was kept constant. The resulting stress concentration factors are stated in Fig. 5.10. Due to planar symmetry, only the upper half of the coupon was modeled, which was setup as a 2D-model with rotational symmetry. The used element type was CAX8, which is a quadratic axisymmetric element with eight nodes. The material model was defined to be linear-elastic. The mesh resolution of all models was parameterized using the number of elements of the half-notch arc n_{res} , see Fig. 5.10. The remaining mesh was adjusted based on the choice of n_{res} . The setup of these models was automated using a script that expected the geometry parameters and the mesh resolution n_{res} as input values. The axial loading of each coupon was defined by the nominal mean stress σ_m^{nom} and the nominal stress amplitude σ_a^{nom} , see also Eq. (5.12). Both of these stresses refer to the respective average stress in the notch root cross section.

In a first analysis, the influence of the mesh resolution was studied in the context of different Weibull shape parameter k and different mean stresses. Since both of these quantities showed a strong influence on the quadrature error, as discussed in Section 5.3.2, their effect was studied for different mesh resolutions. In order to so, the failure probability P_f was computed for several combinations of r , k , σ_m^{nom} and n_{res} using

$$P_f = 1 - \exp \left\{ - \underbrace{\left(\frac{\sigma_a^{\text{nom}}}{\hat{\sigma}_e} \right)^k}_{=: \alpha} \int_V \underbrace{\left(\frac{\tilde{\sigma}_{a,1}^{\text{nom}}(\mathbf{x}; n_{\text{res}})}{\left\langle 1 - \left\langle \frac{\sigma_m^{\text{nom}} \tilde{\sigma}_{m,1}^{\text{nom}}(\mathbf{x}; n_{\text{res}})}{\hat{\sigma}_m} \right\rangle^n \right\rangle} \right)^k}_{=: q(n_{\text{res}})} dV \right\}. \quad (5.45)$$

Here, $\tilde{\sigma}_{m,1}^{\text{nom}}(\mathbf{x}; n_{\text{res}})$ and $\tilde{\sigma}_{a,1}^{\text{nom}}(\mathbf{x}; n_{\text{res}})$ refer to the von Mises mean stress and stress amplitude fields taken from the finite element solution for a nominal unit stress, cf. Eq. (5.12), corresponding to a mesh resolution of n_{res} . The two model parameters $\hat{\sigma}_m$ and n were set to one, $\hat{\sigma}_m = n = 1$ in all analyses. Note that the nominal stress amplitude σ_a^{nom} and the remaining parameter $\hat{\sigma}_e$ can be combined to a factor before the integral, denoted as α in Eq. (5.45). For a given combination of r , k and σ_m^{nom} its value was defined via

$$\alpha = \frac{-\log(1 - P_f)}{q(n_{\text{res}}^{\text{max}})} \quad (5.46)$$

where $n_{\text{res}}^{\text{max}}$ denotes the mesh resolution parameter with respect to the finest grid used in the study, while P_f was defined as 1%. This definition of P_f normalizes the computed failure probability P_f among different parameter combinations in a sense that may be expressed as $P_f(r, k, \sigma_m^{\text{nom}}, n_{\text{res}}) \rightarrow 1\%$ for $n_{\text{res}} \rightarrow n_{\text{res}}^{\text{max}}$. In this way, it is easier to compare the graphs corresponding to the different parameter settings.

Next to using the nominal stresses σ_m^{nom} and σ_a^{nom} as load references, one can also use the stresses at the component's hot spot σ_m^{crit} and σ_a^{crit} for expressing the components load state, see Eq. (5.8). In this framework, where the peak stresses are identical for each mesh resolution by definition, one obtains the same equations as stated in Eqs. (5.45) and (5.46), with the only difference that all superscript ‘‘nom’’ are replaced by ‘‘crit’’. Here, σ_m^{crit} is defined via $\sigma_m^{\text{crit}} = \sigma_m^{\text{crit}}(n_{\text{res}}^{\text{max}})$. In the following analysis, both types of stress references will be considered, since the obtained error phenomenology is different.

Finally, before discussing the first results, it should be commented on the used quadrature rule. Since the resulting error in P_f was supposed to reflect the error introduced by the stress field approximation only, excluding the quadrature error, an adaptive quadrature routine was used. For each element i , the number of used integration points was increased until Q_i converged. Note that this approach is valid for obtaining a converged value for P_f due to Ineq. (5.37). As a consequence, the approximation errors discussed in this first analysis are solely due to the deviations in the stress fields.

The results of this study are presented in Fig. 5.11. Each pair of plots shown in the three rows of Fig. 5.11 contains the results with respect to a fixed notch radius r , beginning with the largest notch radius $r = 5$ mm at the top, and ending with the smallest notch radius $r = 1$ mm at the bottom. The three diagrams in the left column correspond to loads with zero mean stress, while the right column refers to results with $\sigma_m^{\text{nom}}/\hat{\sigma}_m = 0.25$. For each stress references, each plot contains three graphs depicting the computed failure probability P_f over n_{res} for different values of k , while an additional graph was added showing the computed value of the stress concentration factor K_t .

One generally finds, that with increasing values of the parameters k , σ_m^{nom} and K_t , higher mesh resolutions are required in order to obtain a converged value of P_f . This was expected based on the results of Section 5.3.2. Moreover, if the mesh resolution is not sufficiently high, lower failure probabilities than the converged value are computed in all considered cases when using the nominal stress reference. This corresponds to a non-conservative error. On the other hand, when using the hot-spot stresses as a reference, the computed error is higher when the mesh resolution is too low. This corresponds to a conservative error. One also finds, that the effect of an increasing K_t on the resulting error is rather small in the absence of mean stress (left column), while it is much greater for a nonzero mean stress level (right column). This phenomenon appears to be more pronounced when using nominal compared to hot-spot stresses.

The explanation for the different error signs when using nominal and hot-spot stresses respectively is related to the evolution of the equivalent stress fields $\tilde{\sigma}_{a,1}^{\text{nom}}$ and $\tilde{\sigma}_{a,1}^{\text{crit}}$ in the vicinity of the notch root with increasing mesh resolution. The increase of the computed failure probability P_f with n_{res} when using nominal stresses is explained by the increase of the peak stresses reflected in $\tilde{\sigma}_{a,1}^{\text{nom}}$ and $\tilde{\sigma}_{m,1}^{\text{nom}}$, cf. Eq. (5.45). This trend is visualized in the upper plot in Fig. 5.12. Due to the large exponents k the failure probability P_f is very sensitive to peak stress variations, and increases as a result of the aforementioned peak stress increase. On the other hand, when using hot-spot stresses as a load reference in Eq. (5.45), the peak stresses in the stress fields $\tilde{\sigma}_{a,1}^{\text{crit}}$ and $\tilde{\sigma}_{m,1}^{\text{crit}}$ do not increase with n_{res} since these fields are normalized with σ_m^{crit} and σ_a^{crit} . Instead, merely the shape of these functions around the notch root changes. What this means is shown in the bottom plot of Fig. 5.12. While the peak stresses for the three considered mesh resolutions are identical, the stresses just below the notch root are increasing with decreasing n_{res} . This translates into higher failure probabilities, when a coarse mesh is used in comparison with the obtained P_f for a converged mesh.

Another observation can be made with respect to the computed stress concentration factor K_t , depicted in form of the gray graphs in Fig. 5.11. In all shown cases K_t was already approximated with a relative error of less than 1% for the lowest considered mesh resolution of $n_{\text{res}} = 10$ compared with the highest one, that is $K_t(n_{\text{res}}^{\text{max}})$. However, the corresponding approximation of P_f was in all cases much worse – especially for the nominal reference. One therefore concludes that the suitability of a finite element mesh

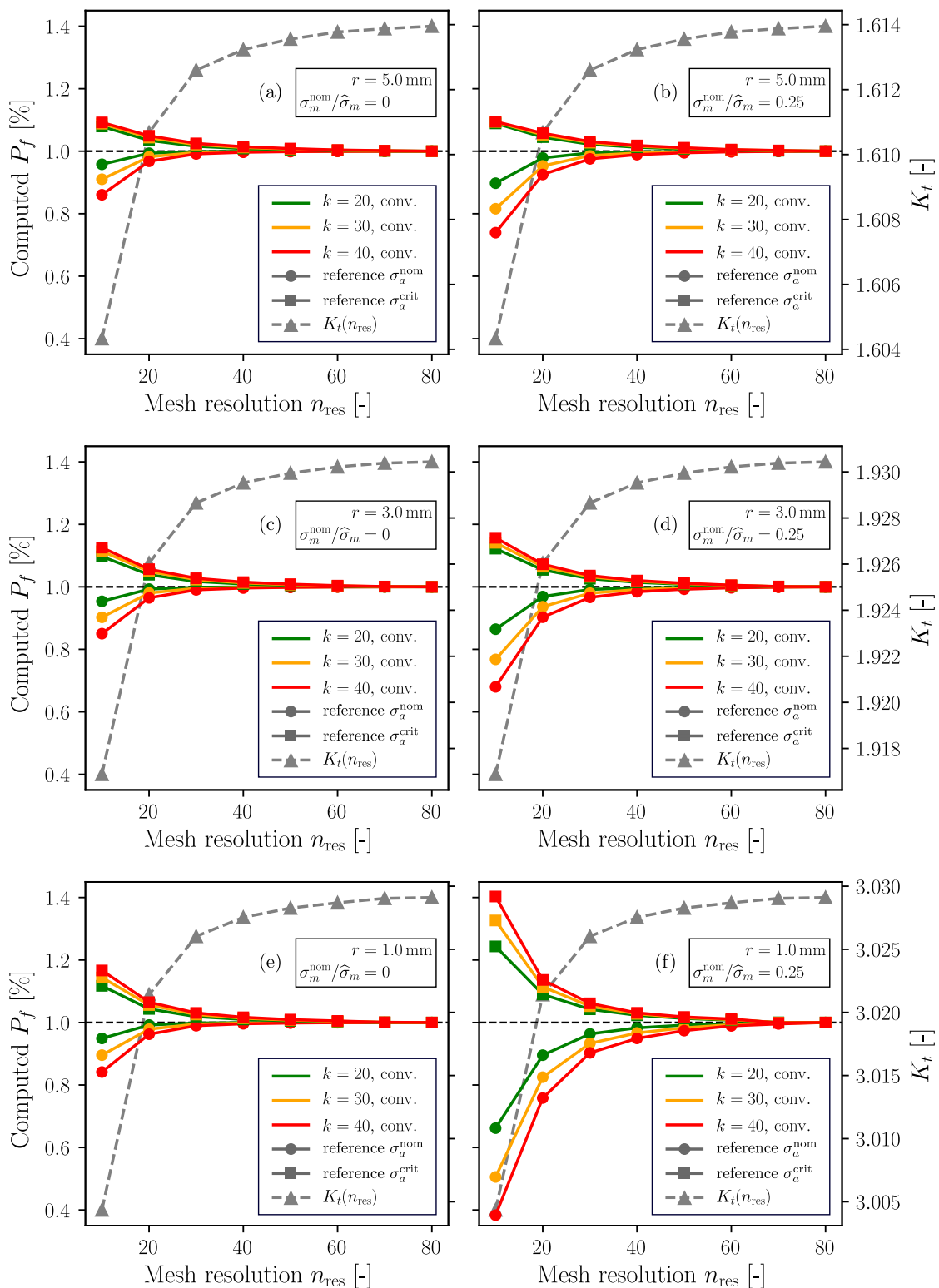


Figure 5.11: On the influence of the mesh resolution n_{res} on the computed failure probability P_f . All results were computed using an adaptive quadrature scheme, eliminating quadrature errors. Compare with Fig. 5.10 for the considered coupon geometries in each row of subplots.

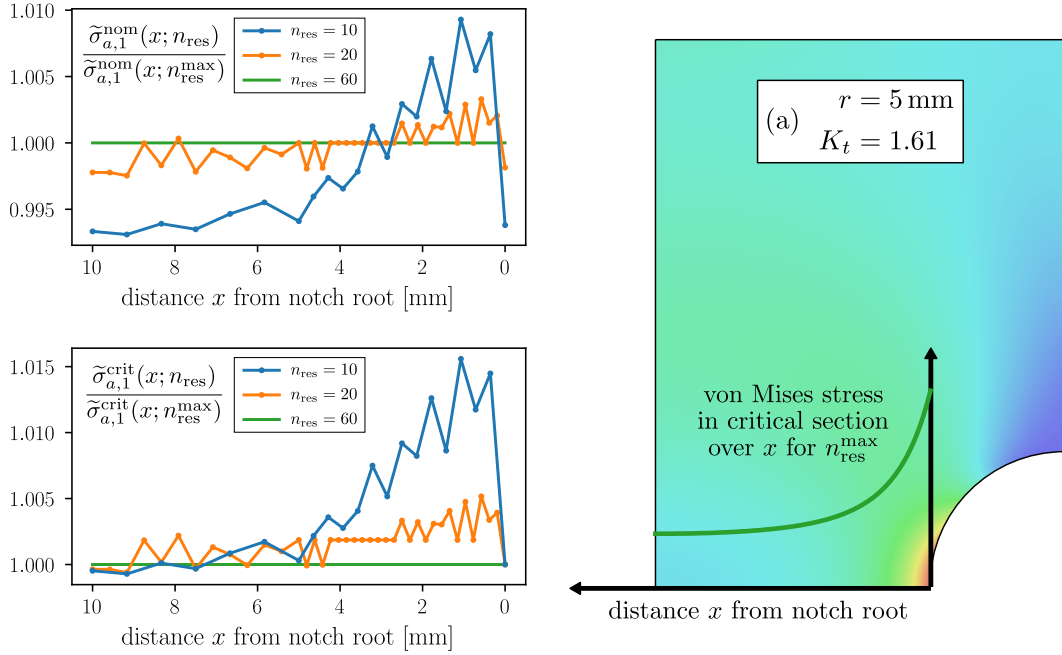


Figure 5.12: On the difference between $\tilde{\sigma}_{a,1}^{\text{nom}}$ and $\tilde{\sigma}_{a,1}^{\text{crit}}$. The shown case refers to the averaged nodal von Mises stresses in the notch root section for specimen type (a) from Fig. 5.10. Note that $n_{\text{res}}^{\text{max}}$ refers to $n_{\text{res}} = 60$ in this analysis.

with respect to a good approximation of the weakest-link based failure probability P_f cannot be judged in terms of its capability to provide a good peak stresses approximation.

As it was already mentioned in Section 5.3.1, the volumetric weakest-link integral I can also be evaluated using standard output from finite element software. One does not necessarily need a specific post-processing routine. However, when using standard finite element output, one cannot define an arbitrary number of integration points for the quadrature rule. Instead one is limited to the number of integration points used by the considered element types. In the case of brick elements, this typically does not allow for more than three integration points per dimension. In order to study how the resulting quadrature error interacts with the stress field error introduced by the finite element model, a second study was conducted comparing the converged results shown in Fig. 5.11 with evaluations using only two or three integration points per dimension respectively. The corresponding results, focusing on the numerically most demanding case of $k = 40$, are presented in Fig. 5.13.

The result format used in Fig. 5.13 is identical to the one from Fig. 5.11. The two black graphs appearing in each of the six subplots depict the converged results from Fig. 5.11 for the case $k = 40$ using nominal and hot-spot stresses respectively. The red and blue graphs on the other hand show the results of the same analyses using two and three integration points. Each combination was evaluated using nominal or hot-spot stresses as the load reference. Considering the graphs, for each stress reference, one finds large deviations between the converged results in comparison to the ones corresponding to two and three integration points. This indicates a considerable contribution of the quadrature error when low numbers of integration points are used. Note that the quadrature error is visible as the distance between the black and a red/blue graph for

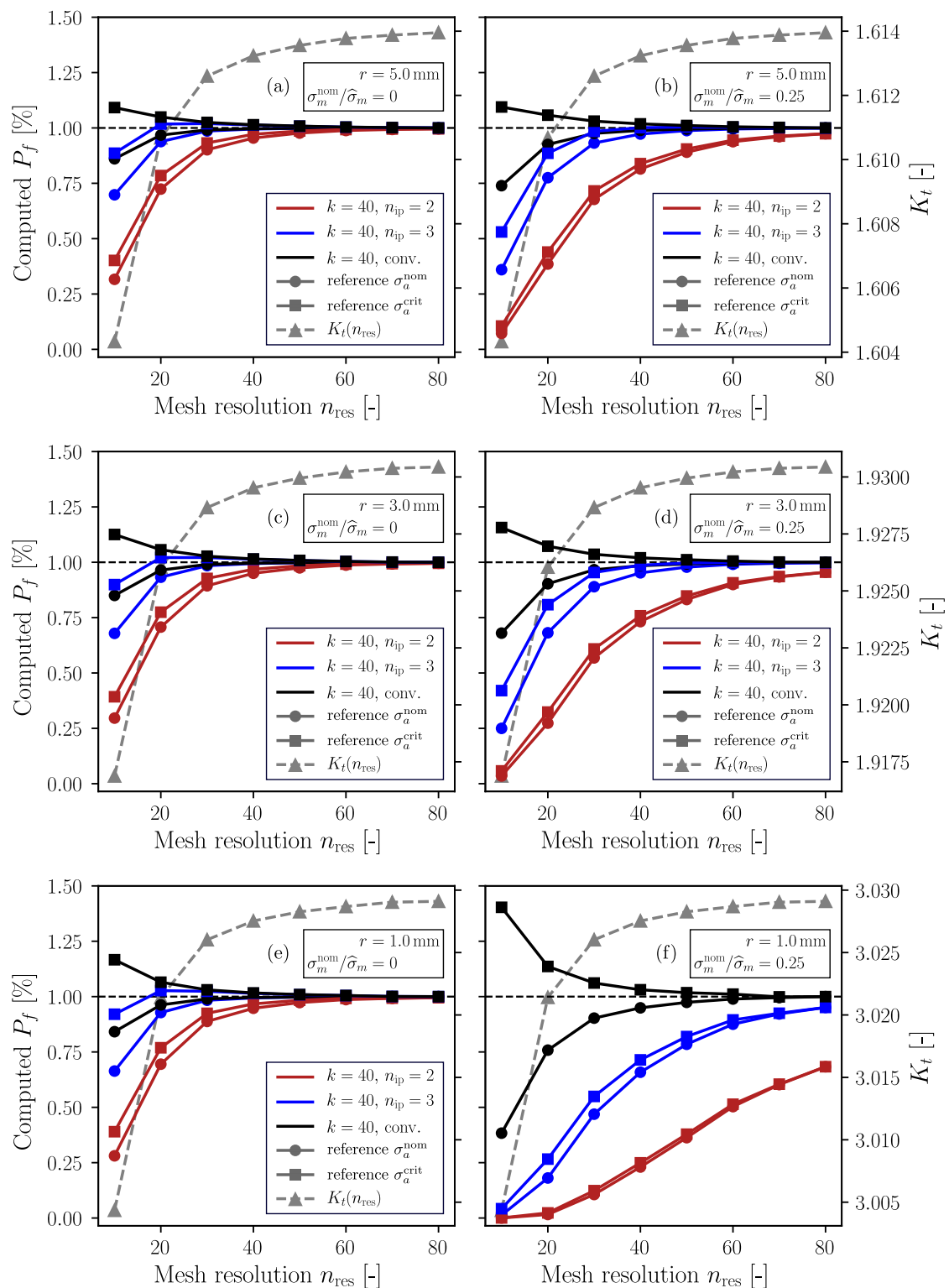


Figure 5.13: On the combined influence of the mesh resolution n_{res} and the number of integration points n_{ip} on the computed failure probability P_f .

a considered stress reference. It must be pointed out that in each analyzed case – also when the hot-spot stress reference was used – the quadrature error led to a reduction of the computed failure probability. It therefore represents a non-conservative error source for both stress references. Based on the shown graphs, the quadrature error can be reduced with a refinement of the mesh, but the required mesh resolution for convergence appears to be quite high in most cases, particularly if $n_{\text{ip}} = 2$ integration points per dimension are used. An extreme case is provided by subplot (f), where large deviations still exist at the highest mesh resolution of $n_{\text{res}} = 80$. This finding applies to the results corresponding to both the nominal and the hot-spot stress reference. It should not be overlooked, however, that the graphs of the hot-spot stress reference for $n_{\text{ip}} = 2, 3$ show slightly smaller absolute errors with respect to the converged failure probability of $P_f = 1\%$ than the graphs of the nominal reference. This phenomenon is attributed to the different absolute error signs of the converged failure probabilities with respect to the number of integration points computed for a nominal or hot-spot stress reference respectively (black graphs). This was discussed in more detail in the context of Fig. 5.12. Nonetheless, considering these results, one concludes that caution is advised when applying the weakest-link methodology in combination with standard output from finite element analyses, corresponding to low numbers of integration points per element. A mesh-convergence study with respect to the computed failure risk is essential in these cases. As a final remark, it should be pointed out, that the considered case of $k = 40$ in the last analysis represents an extreme case. The values for k encountered in the model calibrations presented later in this work are typically considerably smaller, which translates into less pronounced error contributions from the quadrature error.

5.3.4 Summary and conclusion

The influence of two error sources on the failure probability computed with the volumetric version of the proposed model have been discussed – the quadrature error with respect to Gauss-Legendre rules, and the error introduced by a finite element stress field approximation in terms of the mesh resolution.

Concerning the quadrature error, the fatigue strength scatter parameter k as well as the stress field variability ρ_m, ρ_a over an element, and the magnitude of the peak mean stress with respect to $\hat{\sigma}_m$ have been identified as having the greatest influence on this type of error. The greater their value, the greater the quadrature error.

With respect to the role of the mesh resolution, similar trends have been found. When the quadrature error was excluded by using a sufficiently high number of integration points, it was found that the more severe the stress concentrations encountered in the analyzed notched coupons in combination with a non-zero mean stress level, and the greater the scatter parameter k , the higher the mesh resolution that was required to obtain a converged value of the computed failure probability. When the mesh resolution was not sufficiently high, different phenomenologies with respect to the resulting absolute error have been encountered depending on the used load reference. In the case where nominal stresses were used for expressing the considered load case, the obtained error was always non-conservative, i.e. lower failure probabilities than the converged value were computed. On the other hand, when expressing the load case via hot-spot stresses, the obtained error for low-resolution meshes was always conservative, i.e. the computed failure probabilities were higher than the one computed with a high-resolution mesh. This last property is very attractive for practical applications, since it is often not

feasible to use finite element meshes with a very high resolution due to the associated computational costs. It should be pointed out however, that this trend of a decreasing computed failure probability with an increasing mesh resolution at a sufficient number of integration points was shown for a specific structure under a specific load type. There might be situations where this trend is not encountered. One should therefore always check this property with a mesh resolution study in practice.

In an additional study, it was found that the mesh resolution also had a considerable impact on the quadrature error when the number of integration points per element was fixed. The higher the mesh resolution, the smaller the quadrature error. This effect was most emphasized when the number of integration points was low. It is generally possible to eliminate the quadrature error when the mesh is fine enough – even if the required resolutions might be unfeasibly high. It is however not possible to eliminate the error introduced through a coarse mesh by a high number of integration points.

With respect to the practical application of the proposed method it is recommended to always conduct a mesh convergence study with respect to the computed failure probability. This is particularly important when a low number of integration points per element is used, as provided by the standard finite element output. In this context, it should also be pointed out that a mesh associated with a good approximation of the component's peak stresses is not necessarily sufficient for computing a converged failure probability, as it was shown by the analyses in this section.

5.4 Model fits assuming elastic material behavior

After having discussed the numerical aspects of the proposed weakest-link approach, in order to prepare an appropriate use in combination with finite element data, the model is going to be fitted to actual fatigue test data. In this section, the focus of these fits will be put on fatigue tests, conducted with smooth and notched tests specimens, at low to moderate static loads so that the corresponding stress response can be modeled as predominantly linear-elastic. An exact definition of this constraint will be given below. The application to low-amplitude fatigue tests on notched members with high static loads associated with notch root plasticity will be the subject of Section 5.6.

At first, in Sections 5.4.1 and 5.4.2 the considered test data together with the used finite element models will be discussed. In the following Section 5.4.3, the details of the used methodology in order to derive the model fits is described. The results of the fits are then presented in Section 5.4.4 and discussed in Section 5.4.5. Finally, the results are summarized in Section 5.4.6. Note that most of the presented results from this section have been published in [179].

5.4.1 Used test data

The test data used for the model fits considered in this study was taken from the NACA data sets presented in Sections 4.1, 4.2 and 4.3, corresponding to the normalized steel SAE-4130, and the two aluminum alloys AL2024-T3 and AL7075-T6. Three different test specimen types were considered. The dogbone shaped, almost smooth NACA1 type with $K_t \approx 1.03$, the NACA2(A) type, containing a mild notch of $K_t \approx 1.6$, as well as the NACA3(B) type which contains a sharp notch with $K_t \approx 5.8$, see Fig. 5.14. However, not all of the corresponding test data provided in the NACA reports was used, but rather a subset. Three criteria, stated below, were applied in order to select the test data.

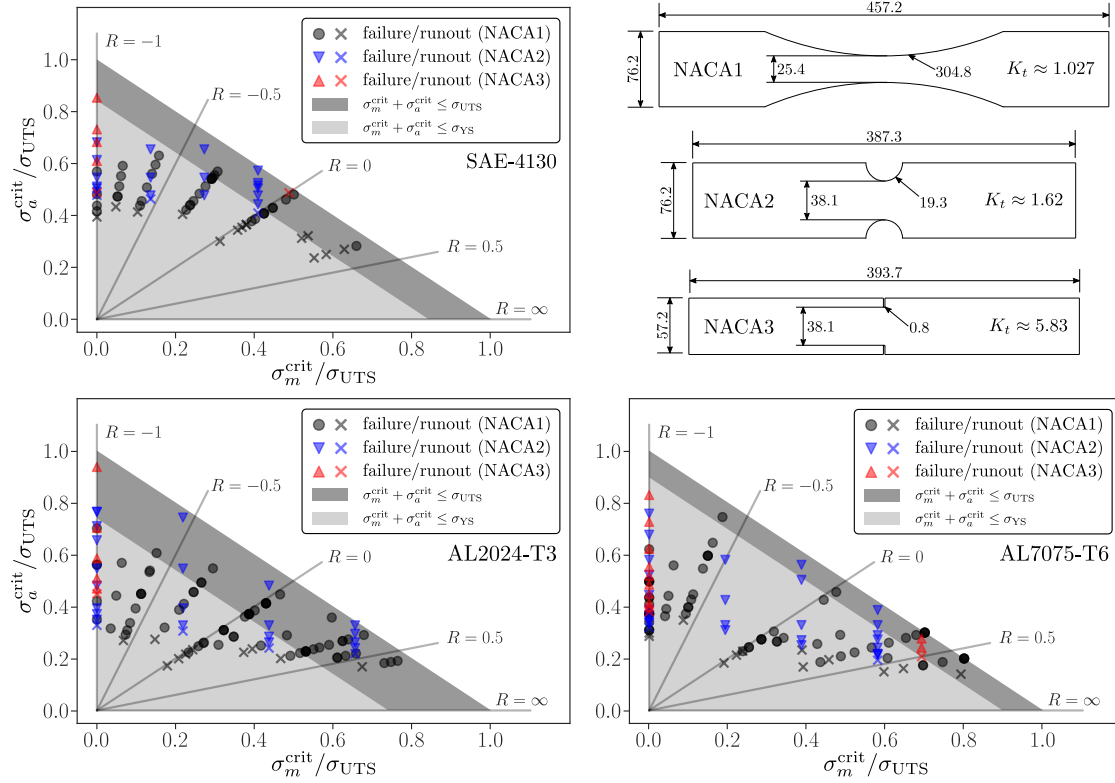


Figure 5.14: Used test data for all three specimen types of all three materials from NACA reports, cf. [170–172]. The stresses σ_m^{crit} and σ_a^{crit} refer to the von Mises mean stress and stress amplitude in the notch root respectively.

1. **Predominantly elastic material behavior** Since the proposed model as it was introduced in Section 5.1 does not explicitly account for plastic material behavior (due to high mean stresses) it would make sense to consider only data points with fully elastic material behavior. However, since such a restriction is reducing the data set considerably, especially with respect to the notched specimens in the higher mean stress region, it was decided – as a compromise – to take into account all data points with $\sigma^{\text{vM}}(\sigma_m(\mathbf{x})) + \sigma^{\text{vM}}(\sigma_a(\mathbf{x})) < \sigma_{\text{UTS}}$ for all $\mathbf{x} \in \Omega$. The influence of the hereby allowed plasticity is checked later in Section 5.4.4.4.
2. **No test irregularities** The NACA reports provided a short comment on the test execution of each data point. This allowed for filtering out all test points with irregularities either during testing or with respect to the failure behavior, such as specimen buckling or failure in the grips.
3. **No low-cycle tests** The NACA data set contains many tests that were conducted at rather high stress amplitudes, resulting in short lives (low-cycle fatigue). Since these data points do not contribute information to the model fits, test points were excluded which were corresponding to specimens that collected less than 10^4 cycles. All of the affected tests corresponded to high amplitude tests. Note that it was checked that the resulting fits from Section 5.4.4 do not change when these omitted data points were included in the fitting data.

	SAE-4130	AL2024-T3	AL7075-T6
NACA1	51 (14)	80 (10)	74 (12)
NACA2(A)	21 (3)	25 (4)	29 (2)
NACA3(B)	6 (2)	6 (1)	13 (2)
total	78 (19)	111 (15)	116 (16)

Table 5.1: Overview of used test data for each material and specimen type. The numbers in parentheses state the number of runouts as stated in the NACA reports. For example: 51 data points of the NACA1 type for SAE-4130 were analyzed, 14 of which were runouts.

Applying these three criteria on the provided data pool still resulted in a large number of test points for each material. The exact numbers are summarized in Table 5.1, distinguishing between failures and runouts as reported in the NACA documents. Note that due to the extremely sharp notch in the NACA3(B) specimen type, most test points of this kind were excluded as a consequence of the very high stresses in the notch root. A visual overview of the test data sets with respect to the corresponding mean stress and stress amplitude assumed in the notch root is provided in Fig. 5.14.

5.4.2 Finite element models

In order to obtain the equivalent local stress fields σ_m^{eq} and σ_a^{eq} of the loaded specimens, which are required for the evaluation of the weakest-link integral in Eq. (5.7), the three considered sheet specimens were modeled as finite element models using the commercial finite element software Abaqus 2017. As pointed out before, cf. Sections 4 and 5.2.2, most of the sheet specimens were rather thin compared to the radius of their notches, so that the stress fields resulting from axial tension are almost constant in direction of the thickness. While this 2D-perspective is an appropriate approximation for the NACA1 and NACA2(A) specimen – compare also with [143] – 3D-characteristics were found in the stress field around the very sharp notch of the NACA3(B) geometry, cf. Fig. 5.15. Due to this situation, all specimens were represented as 3D solid models.

Exploiting the two symmetry planes in each geometry, all specimens were modeled as one eighth of the full model, cf. Fig. 5.15. The only used element type was C3D20, which is a brick element with 20 nodes that uses quadratic shape function resulting in three integration points per dimension, thus 27 integration points per element. All meshes were structured and the resolution was initially chosen based on a mesh convergence study with respect to the peak stress attained on the surface in the notch root and then checked if this mesh resolution in combination with the use of 27 integration points per element was sufficient for the convergence of the results of the model fits shown below. In this context, see also the results and discussions from Section 5.3.3.

For all considered tests, linear-elastic material behavior was assumed. No difference was made for tests during which the corresponding maximum stresses exceeded the yield strength, i.e. with $\mathbf{x} \in \Omega$ such that $\sigma^{\text{vM}}(\boldsymbol{\sigma}_m(\mathbf{x})) + \sigma^{\text{vM}}(\boldsymbol{\sigma}_a(\mathbf{x})) > \sigma_{\text{YS}}$. With this approach it was not necessary to reevaluate the stress field for each test point again. Using the linearity of the problem with respect to the stress field solution, the stress field only had to be evaluated once for each specimen geometry with a nominal unit tensile stress. To obtain the stress fields for the different test loads one merely had to scale the unit stress fields with the considered test stresses. The combined stress fields of mean stress and stress amplitude were then obtained by linear superposition.

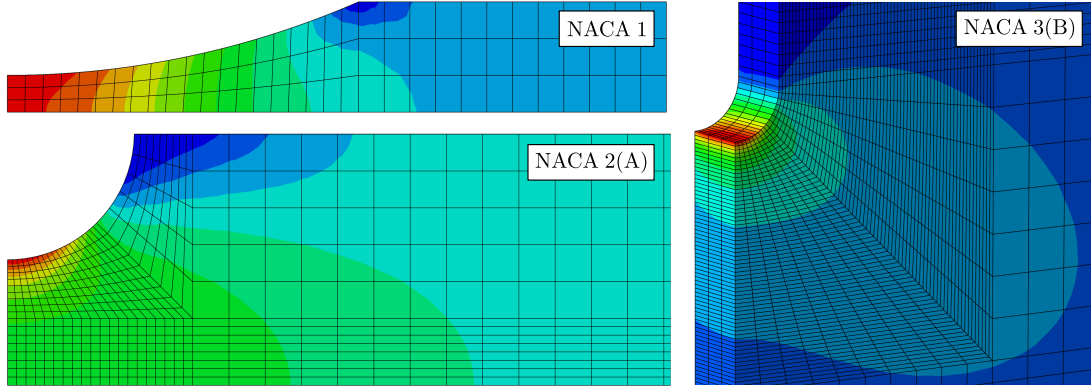


Figure 5.15: Used finite element meshes for the fitting procedure including a contour plot of the von Mises stress field resulting from a tensile stress applied at the specimen top.

5.4.3 Evaluation method

The test data and the corresponding finite element models presented in the previous sections will be used in a two-step approach, consisting of a calibration step and a following prediction step, in order to study the potential of the proposed probabilistic Haigh diagram. This approach will be applied on each of the three materials separately. The reference number of cycles for all diagrams was defined as $N_{\text{ref}} = 5 \cdot 10^6$ although most tests were not aborted before reaching 10^7 cycles. This choice was made in order to increase the number of runouts, which in this context refers to specimens that survive N_{ref} load cycles. As it will be discussed in Section 5.7, a low number either of runouts or failures, translates into higher model uncertainties.

In the first step, the parameters of the unit Haigh diagram for $N_{\text{ref}} = 5 \cdot 10^6$ are calibrated with a subset of the available test data for the considered material. This subset will comprise all data points from two out of the three specimen geometries, for example all NACA1 and all NACA2(A) data points. The calibration is obtained by numerically maximizing the log-likelihood function $\mathcal{L}(\theta)$, cf. Eq. (5.17) as described in Section 5.1.3. The corresponding model parameter vector θ_{opt} is the result of the calibration step. To further illustrate this result, also the design Haigh diagrams of the specimens which were used in the calibration will be computed and visualized.

In the second step, the previously calibrated unit Haigh diagram defined by θ_{opt} is used to compute the design Haigh diagram for the specimen geometry that was not considered for the calibration. For example, if all NACA1 and NACA2(A) data points are used for the calibration, one would compute the design Haigh diagram for the NACA3(B) geometry in this second step. Since no data points of this geometry were contributing to the calibration, the computed design Haigh diagram is a pure prediction and can be compared to the corresponding test data.

All evaluations in this study are based on the volumetric formulation of the probabilistic Haigh diagram. Gaussian quadrature rules were used to evaluate the corresponding weakest-link integral, as discussed in Section 5.3.1. With respect to the notation used in Section 5.3.3, this leads to the approximation

$$I = \int_V \left(\frac{\sigma_a(\mathbf{x})}{\sigma_e(\sigma_m(\mathbf{x}))} \right)^k \frac{dV(\mathbf{x})}{V_1} \approx \alpha_{\text{sym}} \sum_i^{n_e} \sum_j^{n_{g,i}} \left(\frac{\tilde{\sigma}_a(\mathbf{x}_{ij})}{\sigma_e(\tilde{\sigma}_m(\mathbf{x}_{ij}))} \right)^k \frac{\tilde{w}_{ij}}{V_1} \quad (5.47)$$

where n_e and $n_{g,i}$ are the number of elements and the number of integration points in the i^{th} element respectively. The factor α_{sym} takes possible symmetries into account. In this case one has $\alpha_{\text{sym}} = 8$ since only one eighth of the specimens was modeled. The stresses $\tilde{\sigma}_m(\mathbf{x}_{ij})$ and $\tilde{\sigma}_a(\mathbf{x}_{ij})$ refer to the von Mises stress field approximations taken from the finite element solutions. The unit volume V_1 was set to 1 in^3 due to the use of imperial units in the NACA reports. This corresponds to $V_1 \approx 16.4 \text{ cm}^3$. It should be pointed out that all stresses in this study, and therefore also the stress related parameters $\hat{\sigma}_e$ and $\hat{\sigma}_m$ are normalized to the ultimate tensile strengths σ_{UTS} of the corresponding materials, as they are summarized in Table 4.3. The von Mises stress fields together with the integration weights were written in three integration table files that were then used during the optimization loops.

The script that was used to compute the model fits was written in Python, using the Nelder-Mead algorithm of the “minimize” function from the `scipy.optimize` package as its optimizer. Before beginning with an optimization run, an initial guess θ_0 had to be provided. A good choice for such an initial guess was obtained by evaluating the log-likelihood function $\mathcal{L}(\theta_0^*)$, cf. Eq. (5.17), at randomly sampled realizations of the model parameter $\theta_0^* \in \Theta := [0.1, 0.6] \times [0.8, 1.5] \times [0.8, 5] \times [1, 40]$. Afterwards, the actual optimization run was started, beginning with the best initial guess θ_0 without prescribing any parameter bounds. All optimizations terminated quickly without showing any numerical problems. Repeated optimization runs of the same problem but different start vectors θ_0 resulted in identical estimates.

5.4.4 Results

The results of the calibration and prediction step will be presented for each material separately, beginning with SAE-4130 in Paragraph 5.4.4.1, followed by AL2024-T3 in Paragraph 5.4.4.2 and ending with AL7075-T6 in Paragraph 5.4.4.3. The influence of test results outside of the elastic region on these fits is analyzed in Section 5.4.4.4.

5.4.4.1 SAE-4130 In order to calibrate the model vector for SAE-4130, all NACA1 and NACA2(A) data points were used. The NACA3(B) data points were consequently not included in this step. The resulting model vector θ_{opt} (representing the unit Haigh diagram) is presented in the upper right corners of the two plots shown in Fig. 5.16. The corresponding probabilistic design Haigh diagrams for the specimen geometries NACA1 and NACA2(A) are presented, together with the respective test data, in the left plot of Fig. 5.16. The comparison of these design Haigh diagrams with the NACA1 and NACA2(A) test data allows a visual assessment of the fit’s plausibility. Apparently both of the design Haigh diagrams are in good agreement with the respective test data. Most of the test points corresponding to specimens that failed (filled symbols) are above or slightly below the respective median lines. On the other hand, most runouts (unfilled symbols), which in this context refers to all specimens that collected more than $5 \cdot 10^6$ cycles, turn out to be below or slightly above the corresponding 50%-percentile.

After the model was calibrated, it was used to predict the design Haigh diagram for the NACA3(B) specimen. The result of this prediction, together with the NACA3(B) test data, is shown in the right plot of Fig. 5.16. One finds that the prediction is consistent with the test data. However, it should be emphasized that the number of tests that can be compared with the obtained prediction is rather limited in this case.

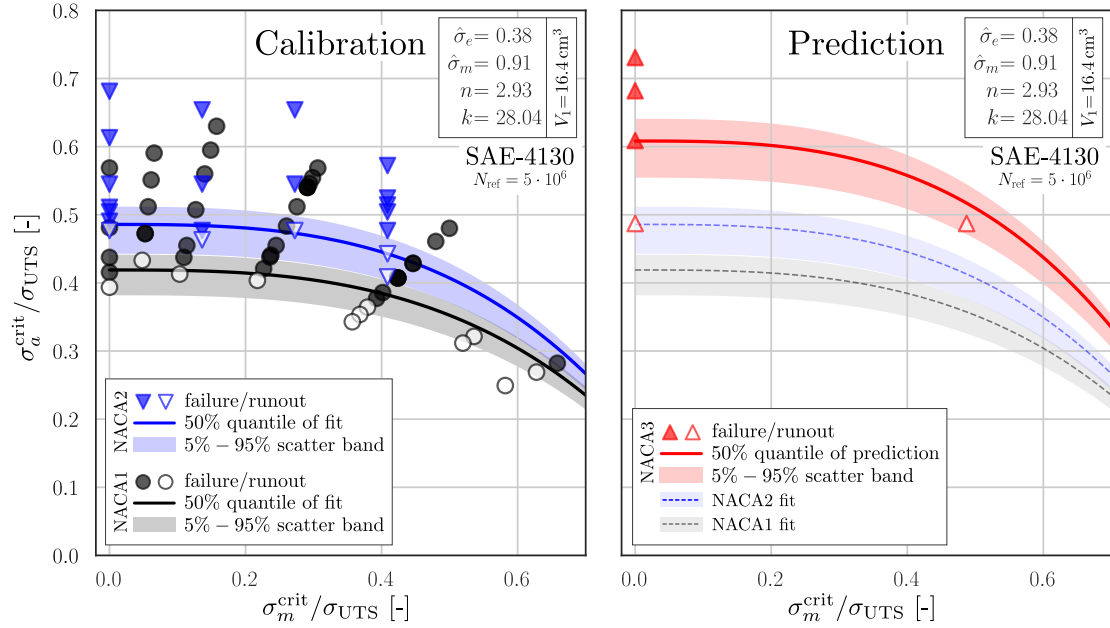


Figure 5.16: Calibration and prediction results for low-alloy steel SAE-4130 at $N_{\text{ref}} = 5 \cdot 10^6$ together with test data. The values on both axes refer to normalized von Mises stresses.

SAE-4130 (NACA1 + NACA2 → NACA3)						
Linear corr.	$\mathcal{L}(\theta_{\text{opt}}, \mathcal{T}_{\text{cal}})$	$\hat{\sigma}_e$	σ_{th}	α	k	$\mathcal{L}(\theta_{\text{opt}}, \mathcal{T}_{\text{pred}})$
hydrostatic	-15.90	0.38	0.0	0.14	24.9	-2.14
max principal	-15.88	0.39	0.0	0.14	24.9	-2.12
von Mises	-15.87	0.39	0.0	0.14	24.9	-2.11
Walker corr.	$\mathcal{L}(\theta_{\text{opt}}, \mathcal{T}_{\text{cal}})$	$\hat{\sigma}_e$	σ_{th}	γ	k	$\mathcal{L}(\theta_{\text{opt}}, \mathcal{T}_{\text{pred}})$
hydrostatic	-17.80	0.38	0.0	0.18	23.2	-2.78
max principal	-17.77	0.38	0.0	0.18	23.3	-2.76
von Mises	-17.76	0.38	0.0	0.18	23.3	-2.75
Prob. Haigh	$\mathcal{L}(\theta_{\text{opt}}, \mathcal{T}_{\text{cal}})$	$\hat{\sigma}_e$	$\hat{\sigma}_m$	n	k	$\mathcal{L}(\theta_{\text{opt}}, \mathcal{T}_{\text{pred}})$
hydrostatic	-10.57	0.38	0.91	2.96	28.0	-2.20
max principal	-10.55	0.38	0.91	2.94	28.0	-0.93
von Mises	-10.54	0.38	0.91	2.93	28.0	-0.80

Table 5.2: Comparison between different mean stress models and effective mean stress functions with respect to the calibration/prediction results for SAE-4130 shown in Fig. 5.16.

In order to put these fitting results in perspective, they were compared with fits using the mean stress models and effective mean stress functions discussed in Section 5.2.2. The corresponding results are presented in Table 5.2. Next to the model parameters of the respective θ_{opt} , the table contain the values of the log-likelihood function evaluated at θ_{opt} for the calibration data set \mathcal{T}_{cal} – NACA1 and NACA2(A) tests – and the prediction data set $\mathcal{T}_{\text{pred}}$ – NACA3(B) tests. While almost no differences are observed between the different effective mean stress functions for each model, considerable differences are found between the three models in terms of the log-likelihood values. These $\mathcal{L}(\theta_{\text{opt}})$ -values are greatest for the proposed model, and considerable smaller for the other two models.

5.4.4.2 AL2024-T3 The calibration of the unit Haigh diagram for the aluminum alloy AL2024-T3 was performed using all NACA1 and NACA3(B) test results. Hence, in this case, the NACA2(A) data points were not considered for the first step. The resulting model parameter vector θ_{opt} describing the unit Haigh diagram is presented in the upper right corners of the two plots shown in Fig. 5.17. The corresponding probabilistic design Haigh diagrams for the specimen geometries NACA1 and NACA3(B) are presented, together with the respective test data, in the left plot of Fig. 5.17. Again, the fit shows good agreement with the test data of both specimen types. Note, that in this case the failure/runout scatter of the NACA1 data points appears to be larger than in the previously discussed case for SAE-4130, cf. Fig. 5.16.

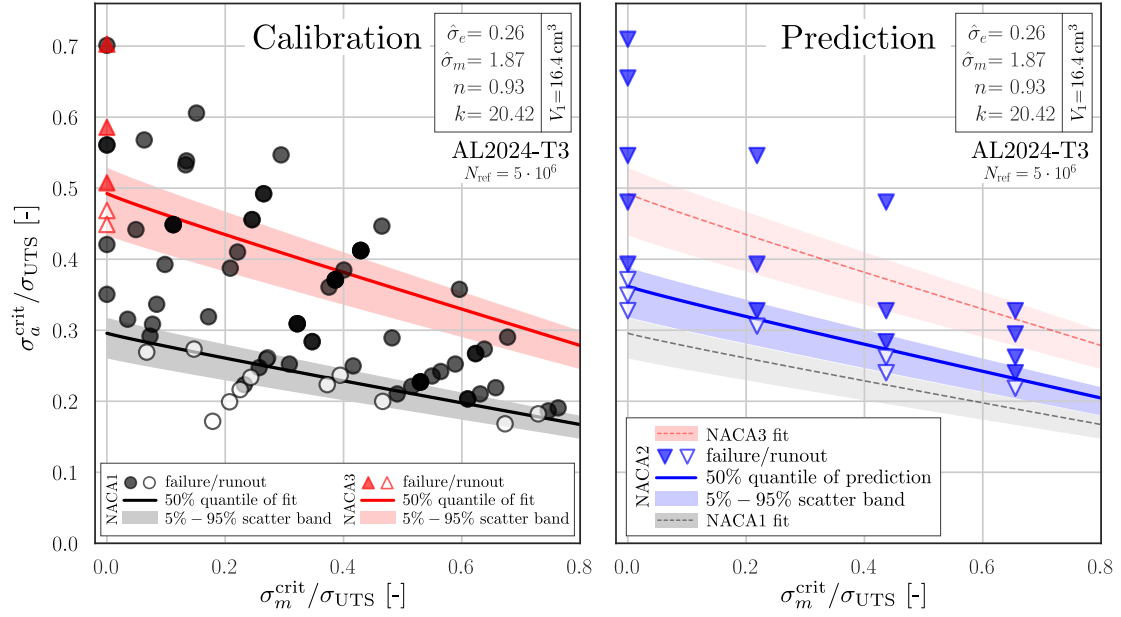


Figure 5.17: Calibration and prediction results for aluminum alloy AL2024-T3 at $N_{\text{ref}} = 5 \cdot 10^6$ together with test data. The values on both axes refer to normalized von Mises stresses.

AL2024-T3 (NACA1 + NACA3 \rightarrow NACA2)						
Linear corr.	$\mathcal{L}(\theta_{\text{opt}}, \mathcal{T}_{\text{cal}})$	$\hat{\sigma}_e$	σ_{th}	α	k	$\mathcal{L}(\theta_{\text{opt}}, \mathcal{T}_{\text{pred}})$
hydrostatic	-13.62	0.26	0.0	0.16	20.6	-4.96
max principal	-13.62	0.26	0.0	0.17	20.7	-5.07
von Mises	-13.62	0.26	0.0	0.17	20.7	-5.12
Walker corr.	$\mathcal{L}(\theta_{\text{opt}}, \mathcal{T}_{\text{cal}})$	$\hat{\sigma}_e$	σ_{th}	γ	k	$\mathcal{L}(\theta_{\text{opt}}, \mathcal{T}_{\text{pred}})$
hydrostatic	-14.35	0.29	0.0	0.34	23.4	-2.95
max principal	-14.33	0.29	0.0	0.34	23.4	-3.00
von Mises	-14.32	0.29	0.0	0.34	23.4	-3.02
Prob. Haigh	$\mathcal{L}(\theta_{\text{opt}}, \mathcal{T}_{\text{cal}})$	$\hat{\sigma}_e$	$\hat{\sigma}_m$	n	k	$\mathcal{L}(\theta_{\text{opt}}, \mathcal{T}_{\text{pred}})$
hydrostatic	-13.53	0.26	1.90	0.94	20.4	-3.30
max principal	-13.53	0.26	1.88	0.93	20.4	-3.31
von Mises	-13.54	0.26	1.87	0.93	20.4	-3.31

Table 5.3: Comparison between different mean stress models and effective mean stress functions with respect to the calibration/prediction results for AL2024-T3 shown in Fig. 5.17.

The prediction of the design Haigh diagram for the NACA2(A) specimen geometry together with the corresponding test data is presented in the right diagram of Fig. 5.17. Again, one finds that the prediction is consistent with the test data. In this case the result is emphasized by the higher number of test points compared with the situation for the prediction step with SAE-4130 discussed before.

The comparison of the fitting results with the other mean stress models and effective mean stress functions is summarized in Table 5.3. In general, one finds the same characteristics as in the fits for SAE-4130 discussed above. However, the differences between the three models in terms of the log-likelihood values are smaller than for SAE-4130.

5.4.4.3 AL7075-T6 The last data set considered here is from the second aluminum alloy AL7075-T6. In this case, the data sets of the two notched specimen geometries NACA2(A) and NACA3(B) were used for the calibration of the unit Haigh diagram. Consequently, the NACA1 data points were not taken into account for this step. The resulting model parameter vector θ_{opt} describing the unit Haigh diagram is presented in the upper right corners of the two plots shown in Fig. 5.18. The corresponding probabilistic design Haigh diagrams for the specimen geometries NACA2(A) and NACA3(B) are presented, together with the respective test data, in the left plot of Fig. 5.18. As for the two previous cases one observes good agreement between the design Haigh diagrams of the two specimens used for calibration and the respective test data.

In the right plot of Fig. 5.18 the results of the prediction for the design Haigh diagram for the NACA1 specimen geometry based on the previously calibrated unit Haigh diagram is presented. As before one finds a median prediction that is consistent with the test data. However, in this case the failure/runout scatter of the test points around the 50%-percentile seems to be larger than predicted. Especially one test point is standing

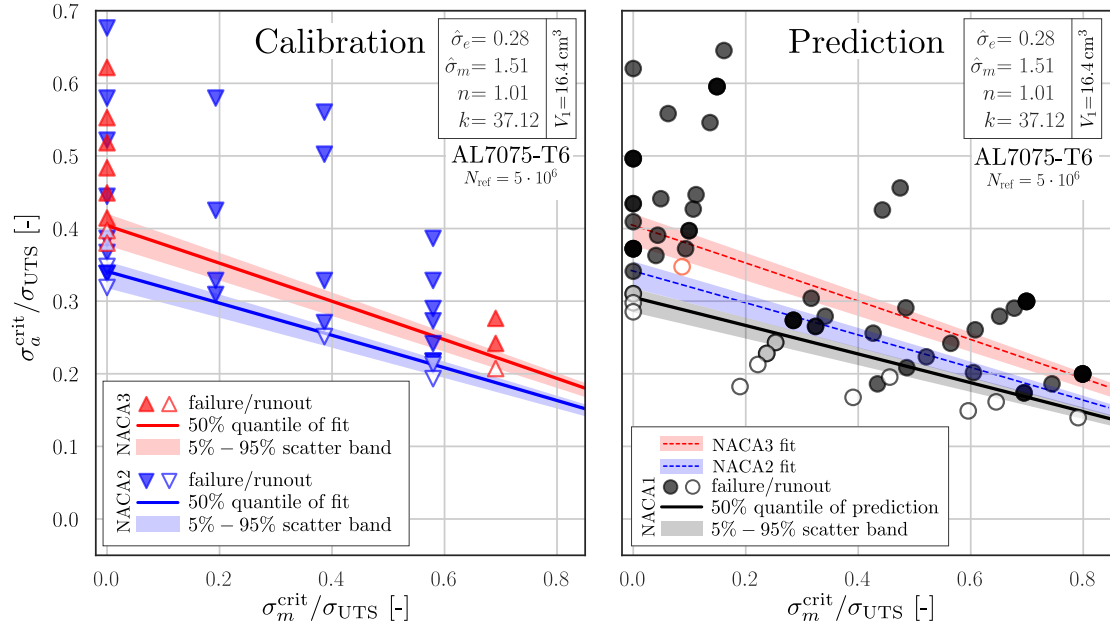


Figure 5.18: Calibration and prediction results for aluminum alloy AL7075-T6 at $N_{\text{ref}} = 5 \cdot 10^6$ together with test data. The values on both axes refer to normalized von Mises stresses. The red-marked test in the right plot was not included in the computation of $\mathcal{L}(\theta_{\text{opt}}, \mathcal{T}_{\text{pred}})$ in Table 5.4.

AL7075-T6 (NACA2 + NACA3 → NACA1)						
Linear corr.	$\mathcal{L}(\theta_{\text{opt}}, \mathcal{T}_{\text{cal}})$	$\hat{\sigma}_e$	σ_{th}	α	k	$\mathcal{L}(\theta_{\text{opt}}, \mathcal{T}_{\text{pred}})$
hydrostatic	-6.24	0.29	0.0	0.22	38.8	-13.88
max. principal	-6.54	0.29	0.0	0.23	41.5	-15.22
von Mises	-6.88	0.29	0.0	0.23	42.7	-15.91
Walker corr.	$\mathcal{L}(\theta_{\text{opt}}, \mathcal{T}_{\text{cal}})$	$\hat{\sigma}_e$	σ_{th}	γ	k	$\mathcal{L}(\theta_{\text{opt}}, \mathcal{T}_{\text{pred}})$
hydrostatic	-7.71	0.29	0.0	0.36	41.6	-11.80
max. principal	-8.23	0.29	0.0	0.37	42.9	-12.07
von Mises	-8.56	0.29	0.0	0.37	43.1	-12.05
Prob. Haigh	$\mathcal{L}(\theta_{\text{opt}}, \mathcal{T}_{\text{cal}})$	$\hat{\sigma}_e$	$\hat{\sigma}_m$	n	k	$\mathcal{L}(\theta_{\text{opt}}, \mathcal{T}_{\text{pred}})$
hydrostatic	-6.24	0.28	1.83	0.87	34.3	-15.37
max. principal	-5.73	0.28	1.57	0.98	36.5	-16.88
von Mises	-5.62	0.28	1.51	1.01	37.1	-17.46

Table 5.4: Comparison between different mean stress models and effective mean stress functions with respect to the calibration/prediction results for AL7075-T6 shown in Fig. 5.18.

out – the runout that is marked in red in the right plot of Fig. 5.18. The predicted probability for this test to be a runout is extremely small. However, no irregularities are reported on this test (tagged as B18M4) in the corresponding NACA report [170].

A corresponding comparison between the different mean stress models and effective mean stress functions is presented in Table 5.4. Note that for the computation of the values stated in the $\mathcal{L}(\theta_{\text{opt}}, \mathcal{T}_{\text{pred}})$ -column, the red-marked runout in the right plot of Fig. 5.18 has not been included, since it drives the corresponding log-likelihood values to extremely large negative values. This obscures the impact of all the other test points. With that being said, one finds again that the effective mean stress function has little influence within the framework of a fixed mean stress model. However, the differences are larger in this case compared with the two previous ones. The differences between the three general models in terms of the log-likelihood values is comparable with those for AL2024-T3, i.e. rather small, as it pertains to the calibration fit. The values corresponding to the prediction data set, on the other hand, show differences that are larger than the ones encountered in the two other cases.

5.4.4.4 Influence of plasticity In order to check the influence of the test points that were associated with elasto-plastic material behavior due to high mean stresses on the obtained model fits for the probabilistic Haigh diagram, a comparison was made between the calibration fits presented in the previous paragraphs and the corresponding fits that were obtained when only tests with $\sigma_m^{\text{vM}}(\boldsymbol{\sigma}_m(\mathbf{x})) + \sigma_a^{\text{vM}}(\boldsymbol{\sigma}_m(\mathbf{x})) < \sigma_{\text{YS}}$ for all $\mathbf{x} \in V$ were considered. The results are summarized in Table 5.5. For each material two columns are given which compare the original fits from the previous subsections (column σ_{UTS}) with the fits based on tests corresponding to elastic material behavior (column σ_{YS}). The numbers in the third row (#) state how many test points were contained in the respective data sets. One finds that the more test points outside of the purely elastic region were used for the model calibration, the greater was their influence on the obtained fit. Indeed, for SAE-4130 and AL7075-T6 which had a comparably low number of test points outside of the elastic region contained in their data set, the differences between both model vectors is rather small. However, for AL2024-T3 whose test data set contains a rather large number of tests associated with elasto-plastic material behavior, the two model vectors are quite different.

	SAE-4130		AL2024-T3		AL7075-T6	
	σ_{UTS}	σ_{YS}	σ_{UTS}	σ_{YS}	σ_{UTS}	σ_{YS}
#	72	56	86	50	42	36
$\hat{\sigma}_e$	0.38	0.39	0.26	0.24	0.28	0.28
$\hat{\sigma}_m$	0.91	0.87	1.87	0.9	1.51	1.48
n	2.93	2.77	0.93	2.09	1.01	1.02
k	28.04	29.64	20.42	17.74	37.12	37.35

Table 5.5: Comparison of model fits for the original data set (column σ_{UTS}) with fits based on test data corresponding to fully elastic material behavior (column σ_{YS}). The third row (#) states the total number of data points in the corresponding data set.

5.4.5 Discussion

The proposed model showed good results for all three considered materials. Not only was it capable of describing the failure behavior of different types of specimen geometries out of one common model, when fitted to the pooled data as shown in the combined fits of the calibration steps. It was also able to predict the failure behavior of geometries, that were not used to calibrate the model, as shown in the prediction steps. Compared with other mean stress models such as the linear stress amplitude correction or Walker's model it showed a better overall-compatibility with the test data over the three considered materials. This is a result of the greater model flexibility pointed out in Section 5.2.1. The advantage of the proposed model over the other two was most emphasized for SAE-4130 which exhibited a concave unit Haigh diagram, that cannot be adequately described by the linear stress amplitude correction or Walker's model. On the other hand, the differences between the models were considerably smaller for the two aluminum alloys. The choice of the effective mean stress function had almost no influence on the fitting results for all three considered mean stress models. This observation is well in line with the results obtained for the sheet specimen in the brief study on the effective mean stresses conducted in Section 5.2.2.

Even though the predictions were in good agreement with the respective test data, it should not be overlooked that these predictions were not based on the test results of a single specimen geometry. Instead, two geometries were used to predict a third one. If one tries to make predictions based on the test results of a single specimen geometry, one will find that the results are less good, especially for the two aluminum alloys. The reason for this trend is the difficulty to obtain a good estimate for the fatigue strength scatter parameter k when using the data set of only one geometry. In this context two different phenomena were encountered. The first of these appeared when it was attempted to predict the NACA2(A) and NACA3(B) design Haigh diagrams for SAE-4130 solely based on a calibration with the NACA1 data. This calibration resulted in an estimate of $k \approx 53$, which is a rather high value and indicates a very small scatter of the fatigue strength. The reason for this high estimate is the comparably good separability of failures and runouts by a fitted 50%-percentile line of the corresponding design Haigh diagram. This means that almost all failures are above and almost all runouts are below this line. In Fig. 5.19 an extreme case of test point separability is shown. In such a case the optimizer will chose the model parameters $\hat{\sigma}_e$, $\hat{\sigma}_m$ and n such that the scale function ends up in the white space between the failure and the runout front, while the

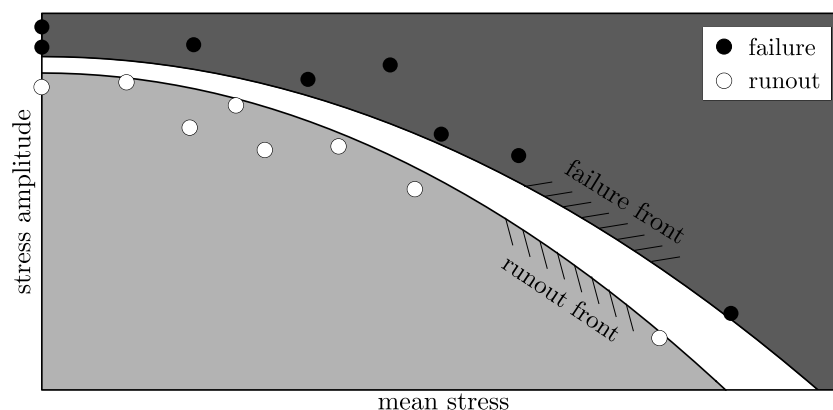


Figure 5.19: On the separability of test data in the Haigh plane.

last parameter k will be chosen as large as the optimizer is allowed to. In this way, the log-likelihood function, which can only assume non-positive values, will approach zero, the maximum possible value. However, note that an overestimation of the scatter k introduces a conservative error, as it shifts the assessment closer to the (conservative) point method, where only the peak stress in the notch is used to assess the failure probability. More problematic is an underestimation of k , which was encountered for both of the aluminum alloys when trying to predict the NACA2(A) and NACA3(B) design Haigh diagrams merely on a calibration with NACA1 data. Here, estimates of $k \approx 16$ for AL2024-T3 and $k \approx 8$ for AL7075-T6 were obtained. The latter was mostly driven by the outlier B18M4 discussed before. These low shape values, corresponding to a large fatigue strength scatter in the unit Haigh diagram, lead to an overestimation of the notched geometries as they translate into non-negligible probabilities of very high values for their fatigue strength.

Another observation in this context is the rather low scatter observed in the test data for the notched specimens – NACA2(A) and NACA3(B) – of all materials, while the unnotched test data – NACA1 – exhibits a low scatter only for the steel SAE-4130, but not for the two aluminum alloys. This phenomenology might be associated with the fact that steels with a body-centered cubic lattice structure are typical representatives for materials with a distinct conventional fatigue limit, while aluminum alloys on the other hand, exhibiting a face-centered cubic lattice structure, are typical representatives for materials that show a continuous descent in their SN -curves throughout the HCF region, compare also Section 2.3.

In summary, the findings of these analyses raise awareness of the importance of the scatter parameter k , and the pitfalls in estimating it. When applying the method to predict a design Haigh diagram for a component, it is therefore strongly recommended to use test results of more than one test specimen geometry, including notched geometries, in the calibration process. One should be particularly careful when encountering low values for k (as they likely result in non-conservative predictions), which – for the examples analyzed here – would be values considerably below $k = 20$.

The influence of test points associated with partially plastic material behavior due to high mean stresses on the resulting fits was found to be considerable for AL2024-T3 where 36 out of the 86 data points of the analyzed data set were outside the elastic range. The effect was less emphasized for SAE-4130 where 16 out of 72 data points were not purely elastic, and almost non-existent for AL7075-T6 where only 6 out of 42 tests were

partially plastic test points, cf. Table 5.5. Most affected by the inclusion of elasto-plastic data points were the two parameters $\hat{\sigma}_m$ and n , which mostly control the unit Haigh diagram's shape in the high mean stress range. Based on these findings one concludes, that one should not calibrate the model with purely elastic data points and then use it to predict the failure probability for loads outside of the elastic region. On the other hand, if one calibrates the model with data sets consisting of a mix of purely elastic and elasto-plastic data points, its failure predictions outside the elastic region seem to be consistent with corresponding test data as it was shown for example for AL2024-T3 in Paragraph 5.4.4.2. However, this does not have to be the case for other materials.

5.4.6 Summary and conclusion

The proposed model has been applied in a two-step calibration/prediction methodology to constant-amplitude fatigue test data with respect to three materials – the normalized steel SAE-4130, and the two aluminum alloys AL2024-T3 and AL7075-T6. For each material, three kinds of sheet specimens were considered. One almost smooth dogbone-type and two different notched specimens including a mild and a sharp notch. Each calibration was based on test results with respect to two specimen types, while the remaining third type was the subject of the following prediction step. Linear-elastic material behavior was assumed in all analyses, although not the entire test data set corresponded to this assumption. Some of the test points referred to specimens which experienced peak stresses greater than the material's yield strength.

The model was able to consistently describe the majority of the test data it was fitted to, while showing mostly good predictive capabilities with respect to test results that were not included in the calibration process. In comparison with the linear stress amplitude correction and Walker's mean stress model, the proposed model showed a better overall-consistency considering the different test data sets over the three materials. The choice of the equivalent local mean stress in terms of the three effective stress models von Mises, maximum principal and hydrostatic mean stress, turned out to have almost no impact on the resulting model fits or predictions. What did have an impact on the calibration was the number of test points associated with elasto-plastic material behavior due to high mean stresses that were included in the data sets the calibration was based on. The higher the number of test points that were associated with partially plastic material behavior, the greater their influence on the model parameters compared to the case where these data points were removed from the calibration set.

In summary, looking on the obtained results, two major questions have emerged in the context of applying the proposed model. The first one concerns the used test data. Which kind of test data should be used for the calibration of the unit Haigh diagram: Several combinations with respect to the specimen types were considered in this study, but which one should be preferred? Is it even necessary to combine test data from different specimen types in order to obtain a reliable fit, or is it also possible to just use a single type when the number of available test results is high enough? This question is addressed in the following Section 5.5. The second question concerns the issue of plasticity. Is it possible to extend the model in order to account for macroscopic plasticity effects, that are present in the notch roots when the considered mean stresses are high? This question is addressed later in Section 5.6 where the model is applied in the context of stress fields that are derived from non-linear elasto-plastic finite element simulations.

5.5 On the selection of test data for the model fit

The model fits considered in the previous Section 5.4 were based on different test data sets. All of these sets had in common that they contained test data from two specimen geometries. As it was discussed, fits to data sets that contained tests on exclusively one specimen type led to worse fits, mostly related to problems in estimating the scatter parameter k . In the current section, this fitting property is investigated in more detail.

The underlying question is approached from an experimental point of view, in order to emphasize its practical relevance. If it was the goal to experimentally determine the model parameters of the unit Haigh diagram for some new material, how would a corresponding test program look like? Would it be a good idea to use the full test budget to exclusively conduct tests with one specimen type, like a smooth or some type of notched specimen? Or should one rather distribute the given budget on tests with more than one specimen type, as the results of Section 5.4 indicated? The answers to these questions will also be helpful in the context of fitting the model to existing data sets. If one knows what kind of test data is required for a reliable model calibration, it is possible to assess the available test data from that perspective.

The subject will be addressed by statistically evaluating different test programs based on Monte Carlo simulations. Starting with the definition of a “true” model vector, each test program configuration is simulated for a large number of times, while the resulting model vector estimates are collected, allowing for their statistical analysis.

Each program will have the format of a staircase scheme applied at a number of different mean stresses, while the number of tests per test program will be fixed. This fixed number of tests can be used for tests on a single specimen type, or distributed on tests for two specimen types. This setup reduces the number of test program parameter to an overseeable amount, as it will be discussed below.

The presented material of this study is structured as follows. The definition of the assumed “true” model will be introduced in the Section 5.5.1, while the details on the conducted simulations and statistical analyses are explained afterwards in Section 5.5.2. The results obtained from these analyses are presented in Section 5.5.3, discussed in Section 5.5.4 and summarized in the last Section 5.5.5. Note that most of the material presented in this section was published in [180].

5.5.1 True model definition

In order to judge whether or not a certain test program is appropriate for providing test data which can be used to derive a reliable estimate of the model parameters describing the physical reality which led to the specific outcome of the tests, one has to know these “true” underlying model parameters in advance. If this is the case, one can repeatedly conduct the test program – either physically or by means of simulations – use the results of each test program to estimate the model parameters, and then compare the statistics of the estimated parameters with the true model parameters. This will be the general approach of the current study, using simulations for repeatedly running the programs. However, the essential requirement to begin with this type of analysis is the definition of a “true” model. In the context considered here, such a model corresponds to a model parameter vector θ_{true} for the unit Haigh diagram, cf. Eq. (5.4), that has to be defined in advance. Pretending that this true model vector was unknown, it will then be estimated based on simulated staircase test programs whose outcomes are governed by θ_{true} .

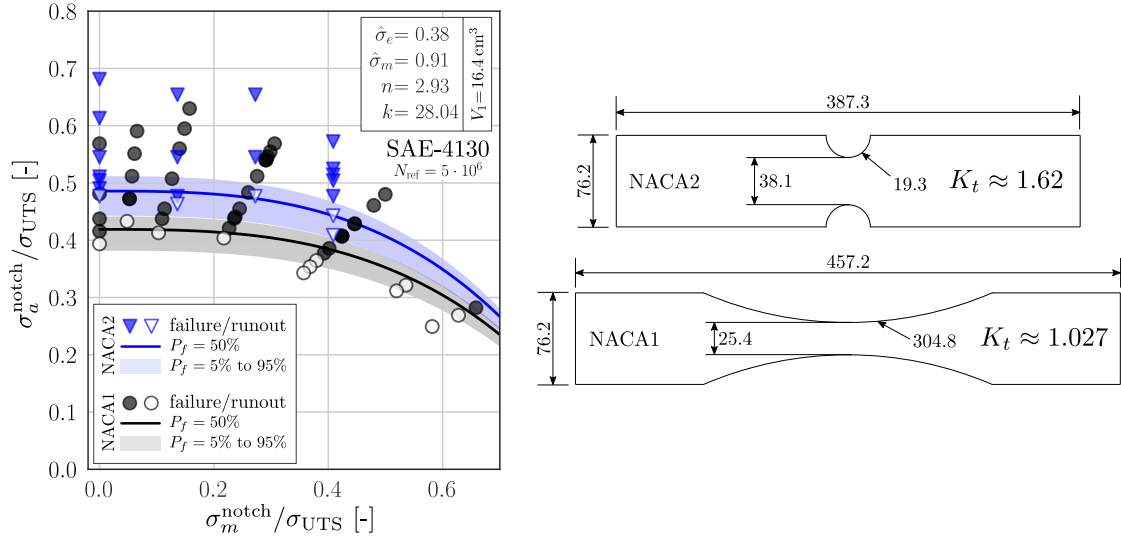


Figure 5.20: Test data for the NACA1 and NACA2(A) specimen geometry [170, 171] together with median lines and scatter band of the two probabilistic design Haigh diagrams. The respective model fit, which is defined as the true model in this study, is stated in the upper right corner.

	smooth	NACA1	NACA2
$V [\text{cm}^3]$	16.39	50.52	54.0
$K_t [-]$	1.0	1.027	1.62

Table 5.6: Total specimen volumes V based on the dimensions given in Fig. 5.20 and stress concentration factors K_t (based on finite element analyses of the considered specimen geometries).

In order to link the true model to a real example it will be defined as one of the model fits from the analyses given in Section 5.4. In this case, the NACA test data with respect to SAE-4130 and the two specimen types NACA1 and NACA2(A) were used. The selected test data was the same as in the previous study from Section 5.4. This corresponds to 51 data points for NACA1, 14 of which were runouts and 21 NACA2(A) data points containing 3 runouts. The test data is depicted in Fig. 5.20 with respect to the corresponding peak stresses σ_m^{notch} and σ_a^{notch} which are normalized with the ultimate tensile strength σ_{UTS} . The NACA1 specimen had a dogbone geometry with a very mild notch of $K_t \approx 1.027$, while the NACA2(A) specimen geometry had a moderate notch with $K_t \approx 1.62$. Both specimen types, which are shown in Fig. 5.20, had a thickness of 1.9 mm and were modeled as linear-elastic finite element models in Abaqus 2017 for the analyses. The mesh convergence with respect to the results presented in Section 5.5.3 was checked. The corresponding specimen volumes and K_t factors – based on finite element analyses – are summarized in Table 5.6. Note that this table also contains an entirely smooth specimen geometry with a gauge volume of $V = 1 \text{ in}^3 \approx 16.4 \text{ cm}^3$. It should be emphasized that this specimen type was not included in the NACA test campaigns, hence there exists no test data on it. However, once the model vector θ_{true} , cf. Eq. (5.4) is defined, one can simulate the failure behavior of this smooth specimen using Eq. (5.7). In this function it will serve as a smooth reference geometry in the simulated staircase programs considered in the statistical analyses in Section 5.5.2.

If the parameters of the unit Haigh diagram, as presented in Section 5.1 are fitted to this data set, using $V_1 = 1 \text{ in}^3 \approx 16.4 \text{ cm}^3$ and $N_{\text{ref}} = 5 \cdot 10^6$, as described in Section 5.1.3, one obtains a model parameter vector θ as presented in the right upper corner of Fig. 5.20. Since this vector will be used as the true model vector for the staircase analyses presented in Section 5.5.2 it shall be repeated here by defining

$$\theta_{\text{true}} := \begin{pmatrix} \hat{\sigma}_e \\ \hat{\sigma}_m \\ n \\ k \end{pmatrix} = \begin{pmatrix} 0.38 \\ 0.91 \\ 2.93 \\ 28.04 \end{pmatrix}. \quad (5.48)$$

Next to the shown test data and the fitted values for the elements of θ , two lines and two shaded areas are shown in Fig. 5.20. The black line represents a function of the normalized stress amplitude $\sigma_a^{\text{notch}}/\sigma_{\text{UTS}}$ over the normalized mean stress $\sigma_m^{\text{notch}}/\sigma_{\text{UTS}}$ in the notch root of the NACA1 geometry that results in a 50% global failure probability for this specimen. The gray shaded area fills the area between a corresponding line for a 5% and 95% failure probability respectively. The blue line and the blue shaded area, which refer to the NACA2(A) geometry give an analogous representation. Both lines and areas are derived based on θ_{true} by means of Eq. (5.7) and Eq. (5.8). As explained in Section 5.1.2 these lines will be referred to as quantile lines from the probabilistic design Haigh diagrams for the NACA1 and NACA2(A) specimen respectively.

5.5.2 Statistical analyses

The goal of the analyses described in this section is to examine the statistical characteristics of parameter estimates with respect to the true model given in Eq. (5.48) for Monte Carlo simulations of different test programs based on the staircase method. To that end, a concise definition on what is understood under a staircase test program and how it can be described using certain test program parameter is presented in Paragraph 5.5.2.1. In the following Paragraph 5.5.2.2 it will then be defined which of these parameter combinations will be considered in the analyses. Finally, in Paragraph 5.5.2.3 the details of a test program's simulation will be explained.

5.5.2.1 Test program definition The general approach of how the staircase tests are set up in this study is to define a fixed number $v \in \mathbb{N}$ of mean stress levels and a fixed number $w \in \mathbb{N}$ of test points per mean stress level, resulting in a total of $N := vw$ tests per program. Since each test program will contain tests of either one or two specimen geometries $G \in \mathcal{G} := \{\text{smooth}, \text{NACA1}, \text{NACA2}\}$, the number of test points per mean stress level $w := w_1 + w_2$ is expressed as the sum of the number w_1 of test points per mean stress level with specimen geometry $G_1 \in \mathcal{G}$ and the number w_2 of test points per mean stress level with specimen geometry $G_2 \in \mathcal{G}$. Note that in the case when two specimen geometries are used in one test program, they are never mixed in one staircase sequence. Instead, the $w = w_1 + w_2$ test points per mean stress level are used to first conduct a staircase with geometry G_1 over w_1 test points, after which a second staircase is conducted testing geometry G_2 in w_2 tests, cf. Fig. 5.21.

The v mean stress levels are denoted as $\bar{\sigma}_{m,i}^{\text{notch}}$ where $i \in \{1, \dots, v\}$ and the tested stress amplitudes on mean stress level i with geometry $G_k \in \mathcal{G}$, $k \in \{1, 2\}$ as $\sigma_{a,i,j_k}^{\text{notch}}$ for $j_k \in \{1, \dots, w_k\}$. cf. Fig. 5.22. If only one geometry is used the index k will be omitted.

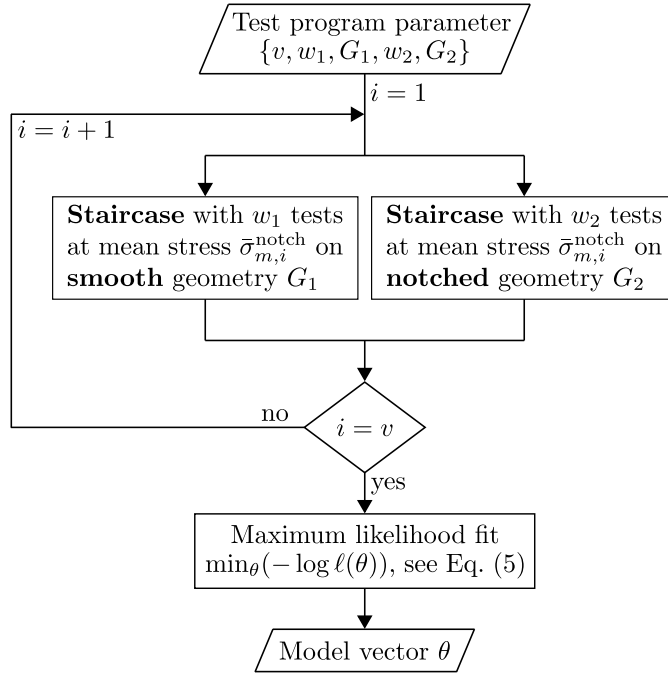


Figure 5.21: Flowchart of a staircase test program using a combination of smooth and notched specimen geometries, cf. Alg. 1. After the test program is finished the results can be used to fit the model vector θ , see Section 5.1.1.

For easier reference the j_k^{th} test point on the i^{th} mean stress level will be referred to as test point (i, j_k) or simply (i, j) if only one geometry is used.

For each mean stress level $\bar{\sigma}_{m,i}^{\text{notch}}$, $i \in \{1, \dots, v\}$ and each geometry $G_k \in \mathcal{G}$, $k \in \{1, 2\}$, a start point $\sigma_{a,i,1k}^{\text{notch}}$ with respect to the stress amplitude and a step size $s \in \mathbb{R}_+$ has to be defined. The step size s , which will be identical for all mean stress levels and geometries, defines the next stress amplitude to be tested, after a test has finished. Beginning with the first stress amplitude $\sigma_{a,i,1k}^{\text{notch}}$ the following stress amplitudes are given recursively by

$$\sigma_{a,i,j_k+1}^{\text{notch}} = \begin{cases} (1+s)\sigma_{a,i,j_k}^{\text{notch}} & \text{if specimen } (i, j_k) \text{ survived} \\ (1-s)\sigma_{a,i,j_k}^{\text{notch}} & \text{if specimen } (i, j_k) \text{ failed.} \end{cases} \quad (5.49)$$

Note that the definition given in Eq. (5.49) results in varying stress amplitude levels. This means that a test sequence beginning with a failure/runout followed by the opposite result does not return to the original stress level since $(1+s)(1-s) \neq 1$ for $s > 0$. This constitutes a difference to many staircase schemes analyzed in the literature, where the step size is typically chosen constant on the linear or log scale. It turned out that test programs featuring only one specimen geometry, i.e. $G_1 = G_2$, resulted in better fits when they were generated by Eq. (5.49) compared to the case where they would be generated using a recursion with constant stress amplitude levels. For all combined test programs however, it did not matter if constant or varying stress amplitude levels were used. Both fits quantitatively showed very similar characteristics. It was therefore decided to conduct all test programs presented in this study using the variable step definition given in Eq. (5.49).

In summary, a staircase test program is defined by the geometries $G_1, G_2 \in \mathcal{G}$, the v mean stress levels $\bar{\sigma}_{m,1}^{\text{notch}}, \dots, \bar{\sigma}_{m,v}^{\text{notch}}$, two numbers of tests $w_1, w_2 \in \mathbb{N}$ per mean stress level and geometry, v initial stress amplitudes $\sigma_{a,1,1_k}^{\text{notch}}, \dots, \sigma_{a,v,1_k}^{\text{notch}}$ for each considered geometry $G_k \in \mathcal{G}$, $k \in \{1, 2\}$, and finally a step size $s > 0$ defining the steps via Eq. (5.49).

5.5.2.2 Analyzed test programs All test programs considered in this work contain a total of $N = 45$ test points. To some extent, this number was defined based on recommendations from staircase-testing literature, which range from 10 to 50 test points for a fixed mean stress, cf. [43, 99]. But mostly it was chosen because this number can be factorized in different ways, which is convenient when studying the influence of the number of considered mean stress levels v at a fixed total number of tests N . Specifically, test programs with $(v, w_1, w_2) \in \{(3, 8, 7), (5, 5, 4), (9, 3, 2)\}$ will be considered here.

In order to specify the mean stress levels $\bar{\sigma}_{m,i}^{\text{notch}}$, $i \in \{1, \dots, v\}$ one may introduce a maximum normalized mean stress in the notch root of $\sigma_{m,\text{max}}^{\text{notch}}/\sigma_{\text{UTS}} = 0.8$ and define the v mean stress levels in an equidistant manner, that is

$$\bar{\sigma}_{m,i}^{\text{notch}} = \frac{i-1}{v-1} \sigma_{m,\text{max}}^{\text{notch}}, \quad i \in \{1, \dots, v\}. \quad (5.50)$$

With respect to the staircase step $s \in \mathbb{R}_+$ the three different sizes $s \in \{3\%, 8\%, 12\%\}$ were chosen, cf. Eq. (5.49). While $s = 3\%$ represents a rather small step size, $s = 12\%$ reflects a relatively large increment, leaving $s = 8\%$ as a medium choice.

Considering the start values for the stress amplitudes $\sigma_{a,i,1_k}^{\text{notch}}$ with respect to mean stress level $i \in \{1, \dots, v\}$ and geometry $G_k \in \mathcal{G}$ two cases are distinguished. Most analyses that were conducted use an initial value of $\sigma_{a,i,1_k}^{\text{notch}}$ with $P_f(\sigma_{m,i}, \sigma_{a,i,1_k}, G_k \mid \theta_{\text{true}}) = 50\%$. Hence, the staircase starts on its true median stress amplitude on the respective mean stress for the considered specimen geometry. This is of course an unrealistic scenario with respect to practical test campaigns, since the true median stress amplitude is unknown before testing. However, this choice has the advantage that it removes the influence of the staircase start points on the parameter estimates, and emphasizes the effects of other test program parameters, such as the geometry or the number of mean stress levels.

In order to study the influence of the choice of the start values $\sigma_{a,i,1_k}^{\text{notch}}$ a uniformly distributed perturbation factor Y is applied as in

$$\tilde{\sigma}_{a,i,1_k}^{\text{notch}} := Y \cdot \sigma_{a,i,1_k}^{\text{notch}}, \quad Y \sim \mathcal{U}_a^b \quad (5.51)$$

where \mathcal{U}_a^b denotes a uniform distribution over $I := [a, b]$ where $a := 1/(1+s) < 1$ and $b := 1/(1-s) > 1$ with s being the chosen step size. The choice of I was motivated by the idea that the staircase step after the first test on a given mean stress level i should be able to cross the median stress $\sigma_{a,50\%}^{\text{notch}}(\bar{\sigma}_{m,i}^{\text{notch}})$ of the considered specimen geometry G_k , cf. Eq. (5.49). This means that either $\sigma_{a,i,1_k}^{\text{notch}} \leq \sigma_{a,50\%}^{\text{notch}}(\bar{\sigma}_{m,i}^{\text{notch}}) \leq \sigma_{a,i,2_k}^{\text{notch}}$ when starting below the median or $\sigma_{a,i,1_k}^{\text{notch}} \geq \sigma_{a,50\%}^{\text{notch}}(\bar{\sigma}_{m,i}^{\text{notch}}) \geq \sigma_{a,i,2_k}^{\text{notch}}$ when starting above should be possible outcomes after the first two tests on mean stress level i . This *crossing condition* is supposed to reflect (to some extent) the role of expert knowledge in staircase testing. Small step sizes will only be chosen when the median stress $\sigma_{a,50\%}^{\text{notch}}$ can be guessed (for example based on information on comparable materials) fairly well. If on the other hand little is known about $\sigma_{a,50\%}^{\text{notch}}$ the step size will be chosen larger in order to avoid a long ascent/decent to the median stress. Both scenarios tend to satisfy the crossing condition.

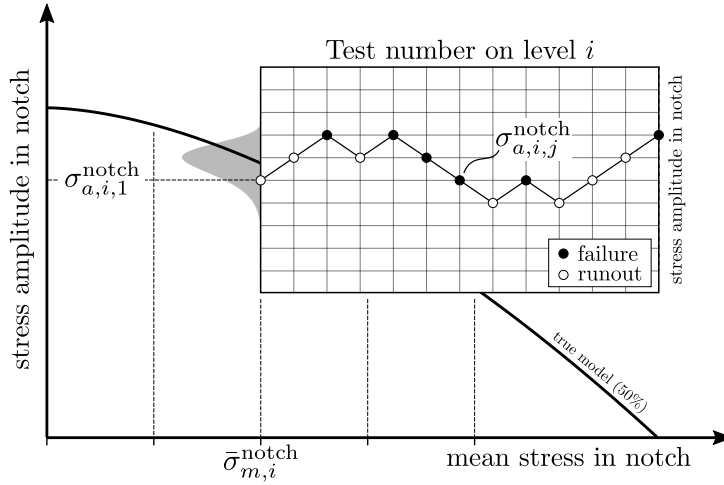


Figure 5.22: On the setup of the simulated staircase tests. The plot schematically shows a staircase test scheme conducted for one of the considered mean stress levels and one geometry. All shown tests refer to the same mean stress. Note that the depicted staircase steps have constant step size, while in the simulations a variable step size was used, cf. Eq. (5.49).

5.5.2.3 Simulation procedure All test programs considered in this study are simulated, hence one has to define how to model the failure/survival of a specimen in a single simulated test. To that end, the failure probability expressed in Eq. (5.7) was used in combination with the true model model vector given in Eq. (5.48). Consequently, a fatigue test with specimen geometry $G_k \in \mathcal{G}$, mean stress field $\bar{\sigma}_{m,i}$ and stress amplitude field $\sigma_{a,i,j,k}$ is modeled as a Bernoulli trial given by

$$\{0, 1\} \ni X \sim \mathcal{B}(P_f(\sigma_{m,i}, \sigma_{a,i,j}, G_k \mid \theta_{\text{true}})). \quad (5.52)$$

Consistent with the flag δ_i^{ref} defined in Eq. (5.15), one associates $X = 0$ with a test specimen that survived, while $X = 1$ corresponds to a test that results in failure.

In a simulated test program, one is given a predefined set of mean stress levels $\bar{\sigma}_{m,i}^{\text{notch}}$, $i \in \{1, \dots, v\}$ as defined in Eq. (5.50) and a corresponding initial stress amplitude $\sigma_{a,i,1,k}^{\text{notch}}$ for each geometry and each mean stress level. The test program is now conducted by simulating one or two staircase schemes (one for each considered geometry) on each mean stress level, see Fig. 5.22. These staircase schemes are independent from each other. For a fixed mean stress level $i \in \{1, \dots, v\}$ it begins with sampling from Eq. (5.52). Depending on the outcome, either $X = 0$ indicating that the specimen survived, or $X = 1$ indicating failure, the stress amplitude for the next Bernoulli trial is determined by Eq. (5.49). Once all $N = 45$ tests have been simulated, the test program has finished and the results are used to estimate the model vector θ using Eq. (5.16).

Since the statistics of these estimates are of primary concern, this process is repeated for a large number of times. In this work $N_s = 10000$ test programs were simulated for each test program setup. The whole process is summarized using pseudo code in Alg. 1.

After its termination, Alg. 1 results in a set of N_s model parameter vector estimates $\Theta := \{\theta_1, \dots, \theta_{N_s}\}$ which will be evaluated by computing the 5%, 50% and 90% percentiles of each of the four containing parameters $\hat{\sigma}_e$, $\hat{\sigma}_m$, n and k .

Algorithm 1 Statistical Evaluation of staircase test program

```

1: for  $r = 1$  to  $N_s$  do
2:   for  $k = 1$  to 2 do
3:     for  $i = 1$  to  $v$  do
4:       for  $j_k = 1$  to  $w_k$  do
5:         Sample  $X$  via Eq. (5.52)
6:         Determine next stress amplitude via Eq. (5.49)
7:       Perform maximum likelihood fit for  $\theta_r$  using Eq. (5.16)

```

5.5.3 Results

Three different analyses have been conducted in order to study the influence of the different test program parameters. In Paragraph 5.5.3.1 the influence of the used test specimen geometry is investigated. In the following Paragraph 5.5.3.2 the effect of distributing the given $N = 45$ test points on different numbers of mean stress levels is analyzed. Finally, in the last Paragraph 5.5.3.3 the influence of both the step size and the chosen initial stress amplitudes is considered.

5.5.3.1 Influence of test specimen geometry The first analysis is intended to study the influence of the specimen geometry $G \in \mathcal{G} = \{\text{smooth}, \text{NACA1}, \text{NACA2}\}$ that is used for testing, cf. Table 5.6. For each geometry three mean stress levels are considered, that is $v = 3$ and consequently $w = 15$ test points per mean stress level. In the tables and figures below this setup will be abbreviated as 3×15 . The initial stress amplitudes were placed on the true median stress amplitude for the corresponding specimen type, as explained in Paragraph 5.5.2.2. The step size s was set to the medium choice of 8%.

Additionally to these single geometry test programs, also two combinations were considered. The smooth geometry was combined with the NACA1 and the NACA2 geometry respectively. In both of these settings again $v = 3$ and $w = 15$ were chosen, now with $w_1 = 8$, that is 8 tests with the smooth geometry and $w_2 = 7$, that is 7 tests with the notched geometry (NACA1 or NACA2) per mean stress level. This setup will be abbreviated as $3 \times (8 + 7)$ in the following tables and figures.

The results of the statistical evaluations of the $N_s = 10000$ parameter vector estimates for the considered programs are presented in Fig. 5.23 and in Table 5.7. While the figure shows the four parameter histograms for each test program setup, the table presents numerical values on the 5%, 50% and 90% percentiles of these histograms. Note that the median values are given as absolute numbers, whereas both the 5% and the 95% percentiles are given in terms of their relative deviation from the 50% percentiles. The difference between the 95% and the 5% percentile ($Q_{.95} - Q_{.05}$) reflects the 90% confidence interval of the respective parameter estimation.

One finds that the standard approach, using only smooth test specimens results in an unbiased estimation for $\hat{\sigma}_e$ with a small confidence interval. Also the two other form parameters $\hat{\sigma}_m$ and n are estimated without bias. However, while $\hat{\sigma}_m$ is associated with a small confidence interval, the scatter of the n estimates is considerable larger. Finally, the estimates on the fatigue strength scatter parameter k are dramatically worse than the three other ones. The estimation shows a considerable bias, in combination with an extremely large confidence interval. When substituting the smooth specimen geometry with the NACA1 or NACA2 geometry throughout the entire test program, the resulting

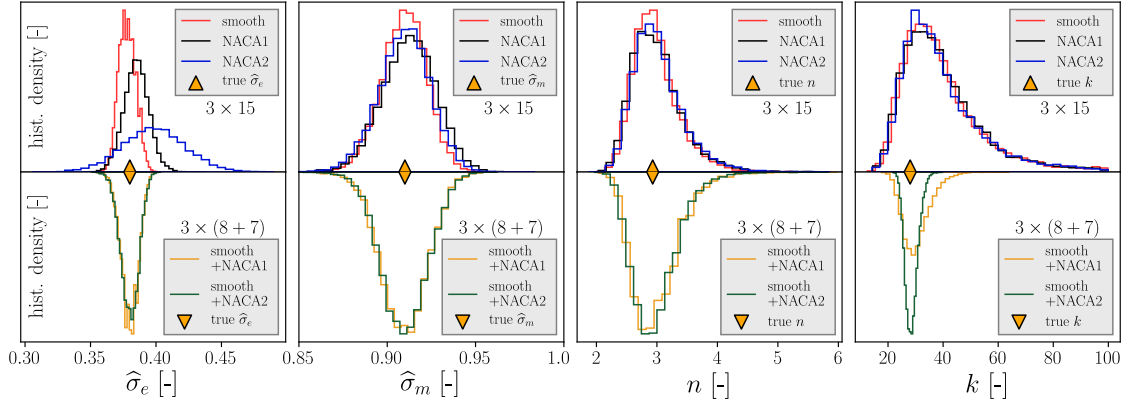


Figure 5.23: Influence of specimen geometry on parameter estimates. True median initial stresses and a medium step size of $s = 8\%$ have been used. A corresponding numerical representation in terms of different percentiles can be found in Table 5.7.

50% start 8% step		3 × 15 (solo)			3 × (8 + 7) (combined)	
		smooth	NACA1	NACA2	smooth+NACA1	smooth+NACA2
$\hat{\sigma}_e$ (0.38)	$Q_{.95}$	+2.9%	+4.0%	+10.0%	+2.7%	+2.8%
	$Q_{.50}$	0.38	0.39	0.40	0.38	0.38
	$Q_{.05}$	-2.7%	-4.1%	-9.9%	-2.9%	-3.0%
$\hat{\sigma}_m$ (0.91)	$Q_{.95}$	+2.2%	+2.7%	+2.6%	+2.3%	+2.3%
	$Q_{.50}$	0.91	0.91	0.91	0.91	0.91
	$Q_{.05}$	-2.4%	-2.7%	-2.7%	-2.3%	-2.3%
\mathbf{n} (2.93)	$Q_{.95}$	+24.0%	+25.9%	+25.8%	+22.3%	+21.8%
	$Q_{.50}$	2.93	2.95	2.96	2.94	2.93
	$Q_{.05}$	-17.3%	-18.8%	-18.6%	-17.7%	-17.2%
\mathbf{k} (28.04)	$Q_{.95}$	+57.8%	+59.8%	+57.8%	+29.2%	+13.8%
	$Q_{.50}$	36.5	36.8	36.2	29.7	28.4
	$Q_{.05}$	-52.6%	-52.3%	-53.1%	-22.4%	-11.9%

Table 5.7: Influence of specimen geometry on parameter estimates. The given quantiles refer to the histograms presented in Fig. 5.23. The relative numbers in the $Q_{.05}$ and $Q_{.95}$ columns correspond to the respective $Q_{.5}$ value, while the numbers in parenthesis in the first column denote the true parameter values, cf. Eq. (5.48).

estimates of $\hat{\sigma}_m$, n and k do not change much. However, the estimation of the $\hat{\sigma}_e$ parameter becomes worse, in terms of bias and confidence interval.

On the other hand, if one combines tests with smooth and notched specimen geometries, one gets the following picture. The estimation statistics of $\hat{\sigma}_e$ is in both cases that have been considered here comparable with the smooth-solo scenario – unbiased and with a small confidence interval. Also the estimates of the two form parameters $\hat{\sigma}_m$ and n have essentially the same characteristics as encountered in the three uncombined test program setups. However, when considering the estimation of the fatigue strength scatter parameter k one finds a substantial improvement compared to the uncombined scenarios. Both the bias and the confidence interval of the estimations are considerably reduced. Comparing the two combined cases one finds that the estimates from the smooth plus NACA2 combination have better properties than the corresponding estimates from the smooth plus NACA1 combination.

5.5.3.2 Influence of the number of mean stress levels In order to study the influence of how to distribute the given $N = 45$ test points on different mean stress levels three different partitions were considered. These were 3, 5 and 9 equidistantly spaced mean stress levels, cf. Eq. (5.50), with 15, 9 and 5 tests per level respectively. In formal notation $(v, w) = (3, 15)$, $(v, w) = (5, 9)$ and $(v, w) = (9, 5)$. Since the previous analysis on the influence of the specimen geometry revealed, that the best fits are obtained for the combined test programs, the analysis of the effects resulting from the test point partition will focus on these combined programs only. That means that one has to define how to split up the number of test points per mean stress level on the smooth and the notched (NACA1, NACA2) geometry. This was done again in a half-and-half manner, meaning that it was tried to assign each geometry in the combination the same number of test points per mean stress level. As this was not possible due to odd numbers, one ended up with the partitions $(w_1, w_2) = (8, 7)$ for $w = 15$, as already considered in the previous

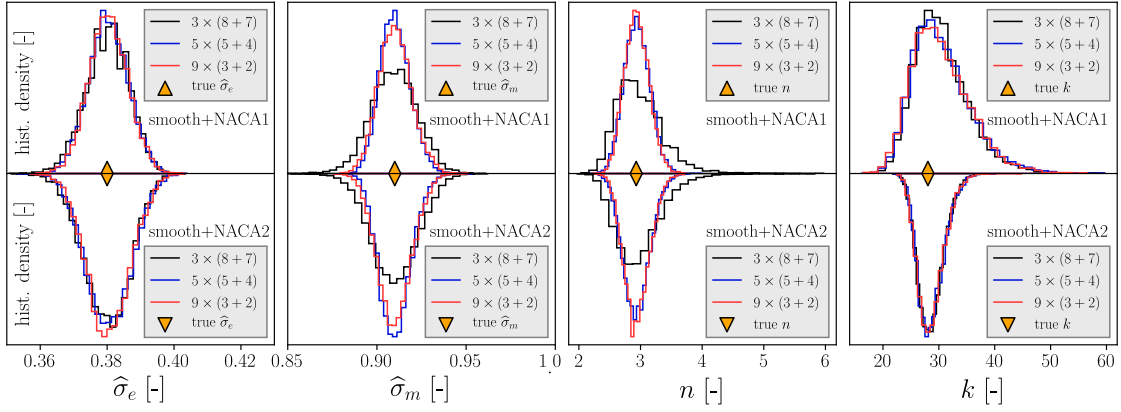


Figure 5.24: Influence of number of mean stress levels on parameter estimates. True median initial stresses and a medium step size of $s = 8\%$ have been used. A corresponding numerical representation in terms of different percentiles can be found in Table 5.8.

50% start 8% step		smooth + NACA1			smooth + NACA2		
		$3 \times (8+7)$	$5 \times (5+4)$	$9 \times (3+2)$	$3 \times (8+7)$	$5 \times (5+4)$	$9 \times (3+2)$
$\hat{\sigma}_e$ (0.38)	$Q_{.95}$	+2.7%	+2.6%	+2.6%	+2.8%	+2.8%	+2.8%
	$Q_{.50}$	0.38	0.38	0.38	0.38	0.38	0.38
	$Q_{.05}$	-2.9%	-2.6%	-2.5%	-3.0%	-2.8%	-2.7%
$\hat{\sigma}_m$ (0.91)	$Q_{.95}$	+2.3%	+1.6%	+1.7%	+2.3%	+1.6%	+1.7%
	$Q_{.50}$	0.91	0.91	0.91	0.91	0.91	0.91
	$Q_{.05}$	-2.3%	-1.4%	-1.6%	-2.3%	-1.5%	-1.6%
\mathbf{n} (2.93)	$Q_{.95}$	+22.3%	+11.8%	+11.4%	+21.8%	+12.3%	+11.8%
	$Q_{.50}$	2.94	2.94	2.94	2.93	2.93	2.93
	$Q_{.05}$	-17.7%	-11.4%	-10.8%	-17.2%	-11.5%	-10.8%
\mathbf{k} (28.04)	$Q_{.95}$	+29.2%	+31.7%	+31.2%	+13.8%	+14.2%	+14.1%
	$Q_{.50}$	29.7	29.8	29.7	28.4	28.5	28.4
	$Q_{.05}$	-22.4%	-23.5%	-24.2%	-11.9%	-11.8%	-12.0%

Table 5.8: Influence of number of mean stress levels on parameter estimates. The given quantiles refer to the histograms presented in Fig. 5.24. The relative numbers in the $Q_{.05}$ and $Q_{.95}$ columns correspond to the respective $Q_{.5}$ value, while the numbers in parenthesis in the top row denote the true parameter values, cf. Eq. (5.48).

analysis, $(w_1, w_2) = (5, 4)$ for $w = 9$ and $(w_1, w_2) = (3, 2)$ for $w = 5$. In the same way as in the previous study the initial stress amplitudes of the staircase schemes were placed at each mean stress level and each geometry at their true median value in order to exclude effects stemming from bad start points. The step size s was again fixed to 8%.

In the same manner as in the previous evaluation, the results are presented in Fig. 5.24 and Table 5.8. The general finding of this analysis can be expressed as follows. With an increasing number of mean stress levels one obtains better estimation properties of the three form parameters $\hat{\sigma}_e$, $\hat{\sigma}_m$ and n (excluding the trend of the $\hat{\sigma}_m$ estimates from the $5 \times (5 + 4)$ to the $9 \times (3 + 2)$ programs), while the confidence interval of the fatigue strength scatter parameter k tends to widen. In this context one also notes that the differences between the $3 \times (8 + 7)$ and the $5 \times (5 + 4)$ programs are more pronounced than the differences between the $5 \times (5 + 4)$ and the $9 \times (3 + 2)$ programs. Comparing both combinations, the test programs including NACA2 test points again show better estimate properties than the test programs with NACA1 contribution.

5.5.3.3 Influence of start points and step size So far only test programs were considered with initial stress amplitudes on the corresponding true median and a fixed step size of $s = 8\%$. In this analysis, the focus will be on the effects of different step sizes and deviations of the initial stress amplitude from the median values. Since the previous analysis revealed that choosing more than three mean stress levels is mostly beneficial for the resulting estimation properties, the focus was put on the case of the $5 \times (5 + 4)$ test point partition. This means that $w = 5$ mean stress levels were considered at which $w_1 = 5$ smooth and $w_2 = 4$ notched specimens (NACA1, NACA2) are tested. The case $9 \times (3 + 2)$ was not chosen since the differences in the estimation properties compared to the $5 \times (5 + 4)$ case were small and of different signs as pointed out in Paragraph 5.5.3.2.

The initial stress amplitudes and the chosen step size have been considered together in the manner that was explained in Paragraph 5.5.2.3. Three different step sizes $s \in \{3\%, 8\%, 12\%\}$ have been studied in combination with a random s -dependent perturbation of the initial stresses according to the crossing condition introduced in the context of Eq. (5.51).

The results of this analysis, which are presented analogously to the previous results

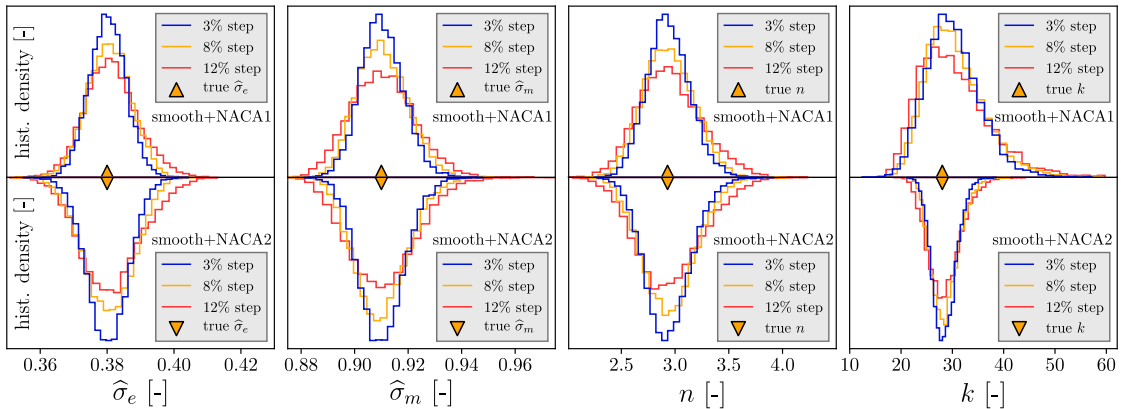


Figure 5.25: Influence of initial stresses and step size on parameter estimates. In all cases, 5 mean stress levels, i.e. $5 \times (5 + 4)$ have been used. The initial stress amplitudes were derived with Eq. (5.51). A corresponding numerical evaluation can be found in Table 5.9.

$5 \times (5 + 4)$		smooth + NACA1			smooth + NACA2		
		3% step	8% step	12% step	3% step	8% step	12% step
$\hat{\sigma}_e$ (0.38)	$Q_{.95}$	+2.4%	+2.8%	+3.6%	+2.5%	+3.0%	+4.0%
	$Q_{.50}$	0.38	0.38	0.38	0.38	0.38	0.38
	$Q_{.05}$	-2.4%	-2.8%	-3.2%	-2.6%	-3.2%	-3.6%
$\hat{\sigma}_m$ (0.91)	$Q_{.95}$	+1.5%	+1.8%	+2.2%	+1.5%	+1.8%	+2.2%
	$Q_{.50}$	0.91	0.91	0.91	0.91	0.91	0.91
	$Q_{.05}$	-1.4%	-1.6%	-2.1%	-1.4%	-1.6%	-2.1%
\mathbf{n} (2.93)	$Q_{.95}$	+11.6%	+13.3%	+17.8%	+12.0%	+13.8%	+17.8%
	$Q_{.50}$	2.93	2.93	2.93	2.93	2.94	2.93
	$Q_{.05}$	-10.8%	-12.6%	-15.1%	-11.0%	-13.0%	-15.6%
\mathbf{k} (28.04)	$Q_{.95}$	+29.9%	+34.3%	+42.2%	+13.3%	+16.2%	+19.4%
	$Q_{.50}$	29.7	29.8	29.3	28.3	28.4	28.3
	$Q_{.05}$	-25.7%	-26.2%	-30.5%	-12.1%	-13.6%	-16.8%

Table 5.9: Influence of initial stresses and step size on parameter estimates. The given quantiles refer to the histograms presented in Fig. 5.25. The relative numbers in the $Q_{.05}$ and $Q_{.95}$ columns correspond to the respective $Q_{.5}$ value, while the numbers in parenthesis in the top row denote the true parameter values, cf. Eq. (5.48).

in Fig. 5.25 and Table 5.9, show that the smallest step size of $s = 3\%$ yields the best estimation characteristics for all four model parameters, while the largest one of $s = 12\%$ results in the worst estimations among the considered cases. However, the differences are only small to moderate. Again, the combined programs including NACA2 specimens show better estimates for the fatigue strength scatter parameter k than the programs with NACA1 specimens, while the estimation properties of the three remaining model parameters show no significant difference between the two combined cases.

5.5.4 Discussion

The results presented in Section 5.5.3 will be discussed in two parts. First, in Paragraph 5.5.4.1 the findings from the previous analyses will be interpreted, and their significance for the practical application of staircase test programs is assessed. In the following Paragraph 5.5.4.2 an explanation for the most significant outcome of the analyses is presented, which is the improvement of the fatigue strength scatter estimate by including tests with both smooth and notched test specimens in a staircase test program.

5.5.4.1 Interpretation of results As already mentioned above, the most significant finding of the results presented in Section 5.5.3 is the effect of a combination of test specimen geometries in a staircase test program on the properties of the resulting parameter estimation of the probabilistic unit Haigh diagram. While neither a test program using exclusively N smooth or N notched specimens is capable of providing reliable estimates for the fatigue strength scatter, their half-and-half combination (i.e. using approximately $N/2$ smooth and $N/2$ notched specimens) results in a substantial improvement of the estimation properties. Note that also other test point partitions were studied among the two combined specimen types than the presented half-and-half combination, for example $3 \times (10 + 5)$ or $3 \times (5 + 10)$. However, an asymmetric partition emphasizing either the smooth or the notched specimens in a test program resulted in worse estimation properties. While the combination effect was demonstrated for the model of a probabilistic

Haigh diagram, it also holds for the conventional determination of the fatigue strength at a fixed mean stress. This result is particularly interesting since the bad performance of staircase test schemes with respect to the estimation of the fatigue strength scatter of a material is considered its major drawback, cf. Section 2.6. A detailed explanation for this improvement will be given in the following Paragraph 5.5.4.2.

The second outcome of the conducted analyses is concerning the number of mean stress levels. A partition of the given test points on more than three mean stress levels (three levels is the minimum, because with fewer levels one cannot determine the curvature n anymore, cf. Fig. 5.1) seems to be advantageous in order to determine the three form parameters $\hat{\sigma}_e$, $\hat{\sigma}_m$ and n at the cost of a slight widening of the confidence interval of the estimated fatigue strength scatter k . In this context, one has to mention that this result corresponds to a single θ_{true} , cf. Eq. (5.48), that has been analyzed here. In this particular example, the curvature of the true unit Haigh diagram $n = 2.93$ is rather emphasized. If one analyzes the influence of the number of mean stress levels on the estimation of the three form parameters for models with smaller n values one finds the effect to be less pronounced. Due to the slight worsening of the k estimation with an increase in mean stress levels, in these cases it might be better to use only three mean stress levels. Another practical problem with a greater number of mean stress levels is the need for more initial stress values, which can be hard to estimate when little is known about the shape of the Haigh diagram.

The problem of the influence of the initial stresses at the different mean stress levels and the step size on the estimation properties was addressed in the third and last analysis presented in Paragraph 5.5.3.3. The results can be interpreted as follows. As long as the initial stresses satisfy the crossing condition, cf. Paragraph 5.5.2.1, a larger step size does not worsen the estimations in an unacceptable way. This holds true in particular for the estimates of the fatigue strength scatter k . Hence, when satisfying the crossing condition, the improvement of the k -estimation resulting from the combination of different specimen geometries in a test program is not exceptionally sensitive against the step size.

5.5.4.2 Explanation of the combination effect The explanation for the improvement of the fatigue strength scatter estimate resulting from the combination of smooth and notched specimens in a common staircase test program leads back to the different sensitivities of the fatigue strength median $\sigma_{a,50\%}^{\text{notch}}$ line, cf. Eq. (5.11), of each specimen type to a variation in the three form parameters $\hat{\sigma}_e$, $\hat{\sigma}_m$, n on one hand, and the fatigue strength scatter parameter k on the other.

To understand this phenomenon, it suffices to focus on the fatigue strength distribution at a fixed mean stress. Here, for the sake of simplicity, $\sigma_m \equiv 0$ was chosen. This choice has the advantage, that only one of the three form parameters, that is $\hat{\sigma}_e$, has to be considered, since the other two, $\hat{\sigma}_m$ and n , do not influence the probabilistic Haigh diagram at zero mean stress. In order to study the sensitivities, the median derivatives $\partial\sigma_{a,50\%}^{\text{notch}}/\partial\hat{\sigma}_e$ and $\partial\sigma_{a,50\%}^{\text{notch}}/\partial k$ were determined numerically at θ_{true} for all three specimen geometries using Eq. (5.11). The results are visualized in Fig. 5.26.

One finds that the median fatigue strength at zero mean stress of all three geometries have almost the same sensitivity against variations in $\hat{\sigma}_e$, while the sensitivities against k -variations are very different. The fatigue strength median of the smooth specimen is almost unaffected by small changes in k , while the NACA1 and NACA2 geometry exhibit much greater sensitivities, which additionally have a different sign.

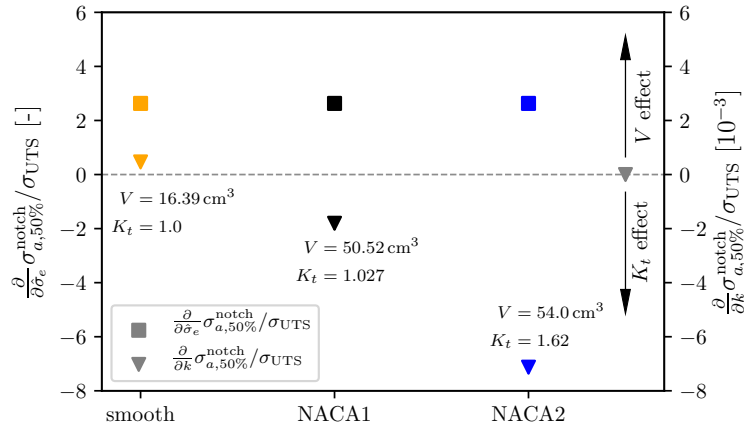


Figure 5.26: On the sensitivity of the median component fatigue strength $\sigma_{a,50\%}^{\text{notch}}$ at zero mean stress with respect to a perturbation in the fatigue strength scale parameter $\hat{\sigma}_e$ and shape parameter k respectively.

Now, one has to recall that a staircase test scheme is essentially a method to approximately determine the median of a distribution, i.e. in this case $\sigma_{a,50\%}^{\text{notch}}(\sigma_m \equiv 0)$. For a staircase sequence testing exclusively smooth specimen this means that the results will determine $\hat{\sigma}_e$ to a much smaller confidence interval than k because the median sensitivity against $\hat{\sigma}_e$ is much greater than the k -sensitivity. This property is reflected in the results of the test programs using only smooth specimens in Fig. 5.23 and Table 5.7. For the notched specimens NACA1 and NACA2 on the other hand, the influence of k on the median fatigue strength is greater due to a higher absolute sensitivity – especially for the NACA2 geometry, cf. Fig. 5.26. This means that if one determines the median fatigue strength for a notched geometry, none of the two parameters $\hat{\sigma}_e$ and k will be estimable with high confidence because both parameters considerably affect the median. This is the reason why the test programs containing only notched specimens showed worse $\hat{\sigma}_e$ estimation properties in Fig. 5.23 and Table 5.7 compared to the test programs with only smooth specimens.

However, if one combines tests with smooth and notched specimens in a common test program, one obtains the following qualitative effect: The test with smooth specimens allow a good estimate of $\hat{\sigma}_e$, as explained above, while the scatter parameter k is mostly undetermined (large confidence interval). With already one of the two parameters $\hat{\sigma}_e$ and k , which influence the median fatigue strength of the notched specimen, determined to a small confidence interval (i.e. $\hat{\sigma}_e$), the estimation of the median fatigue strength of the notched specimen essentially corresponds to an estimation of k – the only remaining mostly undetermined parameter.

Among the two considered combinations the improvement of the k -estimation is best for the combination of smooth and NACA2 specimens, due to the higher k -sensitivity of the NACA2 fatigue strength median compared with the NACA1 geometry, cf. Fig. 5.26. This increased sensitivity is a result of the sharper notch of the NACA2 type. Further sensitivity studies on other specimen geometries showed the general trends of the k -sensitivity as indicated by the arrows on the right side in Fig. 5.26. A higher stress concentration factor K_t (i.e. a sharper notch) results in a sensitivity shift in negative

Specimen type G_1	Specimen type G_2	κ_{12}
smooth	NACA1	$+8.4 \cdot 10^{-7}$
smooth	NACA2	$+3.3 \cdot 10^{-6}$
NACA1	NACA2	$-1.3 \cdot 10^{-5}$

Table 5.10: Numerical evaluation of the sensitivity parameter κ_{12} for different combinations of specimen geometries, cf. Eq. (5.53).

direction, while an increase in specimen volume (by scaling the entire geometry) leads to a sensitivity shift in positive direction. Moreover, these additional investigations indicated that the k -estimation properties of a combined test program with geometries G_1, G_2 can be further improved by increasing

$$\kappa_{12} := -\frac{\partial}{\partial k} \sigma_{a,50\%}^{\text{notch}}(G_1 | \theta_{\text{true}}) \frac{\partial}{\partial k} \sigma_{a,50\%}^{\text{notch}}(G_2 | \theta_{\text{true}}). \quad (5.53)$$

The sensitivity parameter κ_{12} becomes large when the k -sensitivities of the two specimen types are high and of different sign, cf. Table 5.10. This can be achieved by using a smooth specimen (minimal K_t) with large volume, and a notched specimen, with a sharp notch (high K_t) and small volume. However, especially with respect to the design of the notched geometry one has to be careful to stay within the boundaries of the model applicability. These boundaries comprise applications, where fatigue failure can be attributed to the occurrence of a local defect within the grain structure of the considered metal or alloy, which can be described statistically. With increasing K_t however, the highly stressed volume around the notch root which is generating the computed failure risk by Eq. (5.7), will eventually become smaller than a single grain or even smaller than a possible defect. It is very likely that in these cases other effects than a defect distribution will become critical for the resulting failure behavior.

Fortunately, the improvement of the fatigue strength scatter estimate resulting from a combination of smooth and notched test specimens in a test program does not require notched geometries with sharp notches to become relevant. As it was demonstrated in the results for the combination with NACA1 specimens ($K_t \approx 1.027$), already the inclusion of a very mildly notched specimen results in a considerable improvement of the fatigue strength scatter estimation properties compared to uncombined test programs.

5.5.5 Summary and conclusion

In three simulation studies of staircase test programs with different configurations, the influence of several test program parameters on the resulting model estimates was investigated. The considered parameters covered the choice of the test specimen geometry, the number of mean stress levels tests were conducted at, as well as the staircase step size in combination with the required initial stress amplitudes.

The most significant finding concerns the choice of the test specimen geometry. It was shown, that by combining results from specimen tests of two different geometries, the confidence interval of the fatigue strength scatter estimate was significantly reduced in comparison to the cases where exclusively results from one specimen type were used. The effect was most pronounced when test data for smooth specimens was combined with test data with respect to a notched specimen type.

Considering the calibration of the proposed model, this finding translates into the recommendation to always use test data from different specimen types for determining the model parameters. A calibration using the same number of test points from exclusively one specimen type results in much greater model uncertainties with respect to the fatigue strength scatter parameter, which is a crucial parameter for assessing notched components. Hence, test programs which are aiming to determine the model parameters of the probabilistic unit Haigh diagram should always distribute the test budget on tests with a smooth specimen type and a notched specimen type in a way where each type receives about the same number of tests.

5.6 Model fits accounting for high mean stress plasticity

The second major question, that emerged during the analysis of the model fits assuming elastic material behavior in Section 5.4 was the following. How to deal with loading conditions, under which the material would not behave fully elastically anymore at each location on the considered component? In a high-cycle fatigue typically setting, where the stress amplitudes are low compared to the material's yield strength, this situation might be encountered when dealing with high mean stresses in combination with structural discontinuities, such as notches or fillets. In these cases, the superposition even with low stress amplitudes might result in peak stresses that exceed the material's yield strength. As a result, the stress field around the notch root will undergo a plasticity induced redistribution over the first few load cycles, quickly converging to a state that might differ considerably from the stress field obtained from a linear-elastic analysis. Due to the introduction of compressive residual stresses around the notch root, the redistributed stress field is often characterized by a reduced notch root mean stress compared to an elastic estimate, compare Section 7.3 in [14].

High-cycle fatigue design methodologies have to take this stress redistribution into account to avoid overly conservative designs under such conditions. One example for how this situation is dealt with is provided by the German FKM (Forschungskuratorium Maschinenbau) guideline [59]. Here, the fatigue strength in the constructed Haigh diagram eventually assumes a constant value in the high mean stress range.

In weakest-link applications to LCF problems, where elasto-plastic material behavior is introduced by high load amplitudes, cyclic plasticity is frequently accounted for by shakedown models, cf. [15, 16]. In these approaches the strain amplitude fields from linear-elastic finite element calculations are corrected using a cyclic stress-strain relationship. However, in almost all publications related to the weakest-link approach with respect to HCF applications, elasto-plastic material behavior, which in these cases can only be introduced by high mean stresses, is not accounted for. One of the few examples, where this topic is discussed is given by a study of Lanning et Al. [146]. In their work, the authors state that localized plastic straining at high stress ratios led to difficulties with the weakest-link method that were not adequately addressed in their study.

The investigation presented here aims to provide a further step in this direction. It focuses on the applicability of the weakest-link concept with respect to notched components under low-amplitude loading in combination with mean stresses that are high enough to trigger an elasto-plastic stress redistribution in the notch roots. To that end, the test data of the two aluminum alloys AL2024-T3 and AL7075-T6, as presented in Sections 4.2 and 4.3, will be analyzed. The corresponding stress fields accounting for

elasto-plastic material behavior will be generated using fully non-linear finite element simulations based on quasi-static stress-strain curves for the considered materials. Test results and stress fields will then be analyzed in the framework of the probabilistic Haigh diagram, presented in Section 5.1. Similar to the approach in Section 5.4, for each material a subset of the corresponding test data will be used to calibrate the four model parameters. After calibration, the failure behavior of all remaining tests will be predicted, the data of which has not been used in the model calibration.

Before going over the structure of the following sections, a brief comment on the role of cyclic creep or ratcheting effects in the considered context seems to be in order. Since, throughout this study, test data provided from relatively short fatigue experiments at room temperature is considered, cyclic creep influences are expected to be limited to a stress field redistribution converging over the first few cycles of the load application. Any additional creep effects such as the generation of creep voids are assumed to be absent or at least insignificant for the failure behavior. However, in high-cycle fatigue relevant applications where elevated mean stresses act over a longer period of time in combination with high temperatures – the classic example is a turbine blade in a gas turbine – additional creep effects are likely to play a non-negligible role, cf. [190–192]. In these kinds of situations the proposed method should not be applied without extending it with respect to the relevant creep mechanisms.

The material presented in this study, major parts of which were published in [181], is structured as follows. In Sections 5.6.1 and 5.6.2 an overview of the considered test data sets, the used elasto-plastic material model as well as the finite element models of the notched specimens is provided. In Section 5.6.3 the details of the calibration/prediction methodology that was applied to generate the results are elaborated. These results will afterwards be presented and discussed in Section 5.6.4. The study closes with a summarizing conclusion presented in Section 5.6.5.

5.6.1 Material and test data

The two aluminum alloys AL2024-T3 and AL7075-T6, see Sections 4.2 and 4.3, are considered in this study. Basis for the respective material properties presented in this section were the NACA reports [170–173], which also contain the information on the conducted fatigue tests. Unfortunately these reports do not include stress-strain curves for the two materials, so that it became necessary to search for an additional source, which was found in [175]. It would have been very interesting to also include the test data on the steel SAE-4130 in this analysis. However, the corresponding stress-strain curves were not included in the reports. Moreover, stress-strain curves from other sources always had the problem that the reported material strength parameter were too different from the stated values in the NACA reports. The SAE-4130 data was therefore excluded from this analysis due to the lack of an appropriate quasi-static stress-strain curve.

The aluminum alloy's yield strengths σ_{YS} , the ultimate tensile strengths σ_{UTS} as well as Young's modulus E are summarized in Table 5.11. The values provided in [170] were used for the yield and tensile strength, while the Young's moduli were taken from [175], since they were not provided in [170]. Note that the values for σ_{YS} and σ_{UTS} provided in the test reports [170–173] were slightly different from those provided in the material report [175]. However, since these differences were smaller than three percent they were interpreted as the typical scatter with respect to a material parameter.

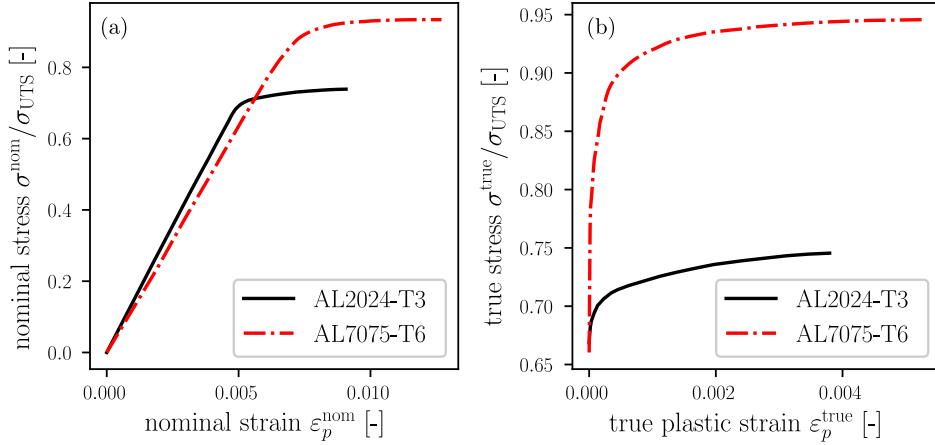


Figure 5.27: (a) Static nominal stress-strain curves at room temperature for both considered materials taken from page 31 in [175] (b) The derived relationship of true stress over true plastic strain. Note that all stresses are normalized to the respective value of σ_{UTS} , see Table 5.11.

	E [MPa]	σ_{YS} [MPa]	σ_{UTS} [MPa]
AL2024-T3	70326	372.3	503.3
AL7075-T6	70326	524.0	568.8

Table 5.11: Relevant material parameters for the two aluminum alloys, cf. [170, 175].

In order to describe the elasto-plastic material behavior, information on the stress-strain relationship outside of the elastic regime was required. Ideally, this relationship should correspond to the cyclic nature of the considered high-cycle fatigue loads. Given a (high) static mean stress σ_m and a (small) cyclic stress amplitude σ_a with $\sigma_m + \sigma_a > \sigma_{YS}$ one is interested in the resulting (true) mean strain ε_m and strain amplitude ε_a . Since this information was not available for the two considered aluminum alloys, it was decided to use quasi-static stress-strain relationships instead.

As mentioned above, the test reports [170–173] did not include quasi-static stress-strain curves for AL2024-T3 and AL7075-T6. However, such curves were provided in yet another NACA report [175] on page 31, although merely in graphical form. By means of a vector graphics program the provided graphs were traced and converted into numerical data. The corresponding stress-strain curves, stating nominal stresses σ^{nom} and nominal strains ε^{nom} , are shown in the left plot of Fig. 5.27. These nominal curves were then used as input to derive the relationship of true stress σ^{true} over true plastic strain $\varepsilon_p^{\text{true}}$, cf. Chapter 1 in [193], via

$$\sigma^{\text{true}} = (1 + \varepsilon^{\text{nom}})\sigma^{\text{nom}} \quad (5.54)$$

$$\varepsilon_p^{\text{true}} = \log(1 + \varepsilon^{\text{nom}}) - E^{-1}\sigma^{\text{true}}. \quad (5.55)$$

Here, E denotes the Young's modulus, cf. Table 5.11. The resulting relationships $\sigma^{\text{true}}(\varepsilon_p^{\text{true}})$ for both materials are shown in Fig. 5.27a. They will be used in the setup of the elasto-plastic finite element simulations, as they will be discussed in Section 5.6.2.

The fatigue test data of the two aluminum alloys AL2024-T3 and AL7075-T6 was taken from the NACA reports [170–173], as it was already presented in Section 4.2 and 4.3. Similar to the previous studies, only those test results were used for which no irregularities had been reported during test execution. Additionally all test points were excluded representing fatigue failure in less than 10^4 cycles. These tests corresponded to high stress amplitudes which were irrelevant for the fit of the fatigue strength with respect to $N_{\text{ref}} = 5 \cdot 10^6$. Finally, it should be pointed out that one valid test result for AL7075-T6, labeled B18M4 in [170], was excluded. This test on a NACA1 specimen was conducted using a high stress amplitude and resulted unexpectedly in a runout, see the red marker in the right plot of Fig. 5.18. The predicted probability for such an event was so remote, that this test point had a large influence on the resulting model parameters. Since the next closest test point had an approximately 50 times shorter life it was decided to exclude this point from the used data pool even though no irregularities had been reported for this test. Note that this unexpected event is on the safe side. It would have been more alarming if one had encountered a totally unexpected failure among the test data which was fortunately not the case. An overview of the resulting numbers of test points for each specimen geometry is provided in Tables 4.5 and 4.6 and visualized in Figs. 4.3 and 4.4.

5.6.2 Finite element models

In order to evaluate the weakest-link integral given in Eq. (5.7) elasto-plastic finite element simulations have been conducted to obtain stress fields and corresponding volume increments. In this section it should be explained how the corresponding models have been set up and evaluated. First, in Paragraph 5.6.2.1 details on the used meshes and elements are provided, followed by a brief description of the plasticity settings in Paragraph 5.6.2.2. The methodology of obtaining mean stress and stress amplitude fields is explained in Paragraph 5.6.2.3, while, finally, in Paragraph 5.6.2.4 details are provided on how the stress fields have been processed in order to numerically evaluate the weakest-link integral.

5.6.2.1 Meshes and elements The finite element analyses in this study have been conducted using the commercial finite element software Abaqus 2017. Each specimen geometry has been modeled exploiting all possible symmetries using a structured volume mesh of brick elements using quadratic shape functions. An example for specimen type NACA2A is shown in Fig. 5.28. The sufficiency of the mesh resolution was checked in a convergence study with respect to the results presented in Section 5.6.4. The corresponding elastic stress concentration factors are summarized in Table 4.5 and 4.6.

5.6.2.2 Plasticity model Material plasticity was incorporated into the finite element models by defining a plastic material behavior with isotropic hardening. A plasticity model using kinematic hardening, accounting for the cyclic nature of the loading, especially in the context of larger cyclic plasticity, could not be defined based on the quasi-static stress-strain curves. However, in the load conditions considered in this work, high mean stresses and low stress amplitudes, the cyclic plasticity is limited to the first few cycles, followed by mostly elastic cycling. Therefore, it was assumed that an isotropic hardening model was sufficient to capture the major plasticity influences in this context.

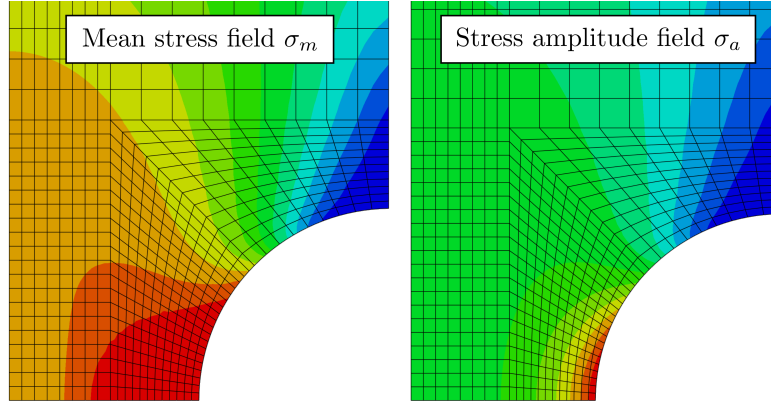


Figure 5.28: Top view on the used finite element mesh for specimen NACA2A. Additionally the von Mises contour plots for both the mean stress and stress amplitude field, cf. Eqs. (5.56) and (5.57), resulting from a high σ_m^{nom} low σ_a^{nom} loading are shown.

The required lookup table stating true stress over true plastic strain was shown in graphical form on the right plot of Fig. 4.5. The corresponding numerical data was defined within the Abaqus material definition.

5.6.2.3 Mean stress and stress amplitude fields In contrast to stress field solutions for linear-elastic problems, where different load magnitudes result in scaled versions of the same stress field, the solution space has different properties when considering non-linear elasto-plastic problems. Neither can stress fields be generally scaled nor can they be superimposed anymore without leaving the solution space. In a practical context, this means that for each combination of σ_m^{nom} and σ_a^{nom} an individual finite element simulation has to be conducted in order to obtain the mean stress field and the stress amplitude field. Considering a specimen geometry G at a given nominal mean stress σ_m^{nom} and a given nominal stress amplitude σ_a^{nom} two load steps were evaluated in the corresponding finite element analysis. In the first step the specimen G was loaded with an axial load resulting in a nominal stress of $\sigma_m^{\text{nom}} + \sigma_a^{\text{nom}}$. The resulting six component stress tensor field solution will be referred to as $\boldsymbol{\sigma}^{(+)} : V_G \rightarrow \mathbb{R}^6$. In a second step the nominal stress amplitude was applied in the opposite direction, resulting in a total nominal stress of $\sigma_m^{\text{nom}} - \sigma_a^{\text{nom}}$. Consequently, the associated stress tensor field will be referred to as $\boldsymbol{\sigma}^{(-)} : V_G \rightarrow \mathbb{R}^6$. The mean stress field $\sigma_m : V_G \rightarrow \mathbb{R}_+$ and the stress amplitude field $\sigma_a : V_G \rightarrow \mathbb{R}_+$ are then defined via

$$\sigma_m(\mathbf{x}) = \sigma^{\text{eff}} \left(\frac{1}{2} \left[\boldsymbol{\sigma}^{(+)}(\mathbf{x}) + \boldsymbol{\sigma}^{(-)}(\mathbf{x}) \right] \right) \quad (5.56)$$

$$\sigma_a(\mathbf{x}) = \sigma^{\text{eff}} \left(\frac{1}{2} \left[\boldsymbol{\sigma}^{(+)}(\mathbf{x}) - \boldsymbol{\sigma}^{(-)}(\mathbf{x}) \right] \right) \quad (5.57)$$

where $\sigma^{\text{eff}} : \mathbb{R}^6 \rightarrow \mathbb{R}_+$ denotes an effective stress function, mapping the six component stress tensor to a scalar value, cf. Section 2.2. In the original publication [181] only the results of the von Mises model, i.e. $\sigma^{\text{eff}} = \sigma^{\text{vM}}$ were presented. Here, additionally the maximum principal $\sigma^{\text{eff}} = \sigma^{\text{mP}}$ as well as the (scaled) hydrostatic stress function $\sigma^{\text{eff}} = 3\sigma^{\text{h}}$ (for an explanation of the factor 3, see Section 5.2.2) will be discussed.

5.6.2.4 Numerical integration Similar to the study presented in Sections 5.4 Gauss-Legendre quadrature, see Section 5.3, has been applied to approximate the volume-version of the weakest-link integral based on the stress fields derived from the finite element simulations. This corresponds to the approximation

$$I = \int_V \left(\frac{\sigma_a(\mathbf{x})}{\sigma_e(\sigma_m(\mathbf{x}))} \right)^k \frac{dV(\mathbf{x})}{V_1} \approx \alpha_{\text{sym}} \sum_i^{n_e} \sum_j^{n_{g,i}} \left(\frac{\tilde{\sigma}_a(\mathbf{x}_{ij})}{\sigma_e(\tilde{\sigma}_m(\mathbf{x}_{ij}))} \right)^k \frac{\tilde{w}_{ij}}{V_1} \quad (5.58)$$

where n_e denotes the number of elements in the considered finite element model, while $n_{g,i}$ represents the number of Gaussian integration points in element i . The integration weight $\tilde{w}_{i,j}$ can be interpreted as the volume increment corresponding to the j^{th} integration point in element i . Finally, the factor α_{sym} accounts for symmetries used in the setup of the finite element model. If for example only half of the specimen is modeled due to symmetry, one would have $\alpha_{\text{sym}} = 2$.

The stress values $\tilde{\sigma}_m(\mathbf{x}_{ij})$, $\tilde{\sigma}_a(\mathbf{x}_{ij})$ and integration weights $\tilde{w}_{i,j}$ were taken directly from Abaqus without further post-processing. The sufficiency of the integration point resolution was checked by an integration point study using an in-house post-processor that allows to define the number of used integration points for evaluating Eq. (5.58). It turned out that, for the considered mesh resolutions in combination with the number of integration points provided by Abaqus was sufficient to obtain good approximations by using the above quadrature rule.

5.6.3 Evaluation method

The probabilistic model described in Section 5.1 will be applied to the experimental test data presented in Section 5.6.1 utilizing the finite element models and stress fields discussed in Section 5.6.2 by means of a calibration/prediction approach that was also applied in the study from Section 5.4. It is the purpose of this section to explain the evaluation method that was used to generate the results presented in Section 5.6.4.

In a first step, the calibration part, the four parameters of the unit Haigh diagram, cf. Eq. (5.4), will be calibrated using test data from two out of the eight specimen types in combination with the maximum likelihood approach outlined in Section 5.1.3. Note that two instead of one specimen type was used for calibration since it was shown in Section 5.5 that this combined approach results in significantly more reliable fits compared with calibrations based on test data from only one specimen type. The calibration step results in numerical values for the four model parameters.

In a second step, the prediction part, the calibrated model will be used to compute the probability of failure for all tests that have not been used in the previous calibration, using Eq. (5.7). In this way one predicts the failure behavior for all test points with respect to six out the eight specimen types. One can then, for each test point, compare the predicted failure probability with the actual test outcome observed in the experiment. A good model should predict high risks for specimens that failed, while runouts should be associated with comparably low risks.

After this brief recapitulation of the calibration/prediction methodology, the remainder of this section focuses on how the corresponding results are derived and how they will be presented in Section 5.6.4. Once the model vector θ is determined by applying the fitting strategy described in Section 5.1.3 it is possible to compute the probability of

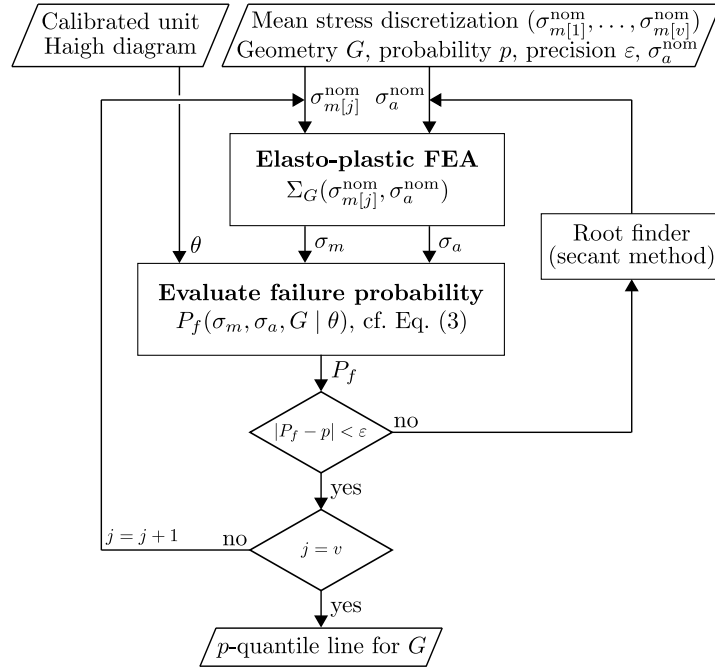


Figure 5.29: On the determination of a p -quantile line in the nominal Haigh plane for a considered specimen geometry G based on a given model vector θ . Here, $\varepsilon = 5 \cdot 10^{-3}$ was used.

failure P_f for any specimen geometry G at any nominal mean stress σ_m^{nom} and any nominal stress amplitude σ_a^{nom} . To do so, one first would have to evaluate the resulting stress fields σ_m and σ_a from the given nominal values by means of Eq. (5.13). In practice, this means that one will have to conduct a finite element analysis applying the evaluation described in Section 5.6.2.3. Then, Eqs. (5.7) and (5.58) can be used to compute the failure probability.

In the result presentation of Section 5.6.4 this relationship will be used to compute different quantile lines in the nominal Haigh plane, i.e. the $\sigma_m^{\text{nom}}\sigma_a^{\text{nom}}$ plane. More specifically, the p -quantile lines for $p \in \{0.05, 0.5, 0.95\}$ will be computed. Note that each geometry has its own quantile lines. Such a line contains all $(\sigma_m^{\text{nom}}, \sigma_a^{\text{nom}})$ combinations that results in the respective failure probability $P_f = p$ for the considered specimen geometry. For example, the 0.5-quantile line for specimen type NACA1 contains all $(\sigma_m^{\text{nom}}, \sigma_a^{\text{nom}})$ points that result in a failure probability of $P_f = 50\%$ for this geometry.

In order to compute the p -quantile line for a specific specimen geometry G in the nonlinear context considered in this study, the σ_m^{nom} axis was discretized in a sequence of $v \in \mathbb{N}$ values $\sigma_m^{\text{nom}} [j]$, $j = 1, \dots, v$. Afterwards, for each nominal mean stress $\sigma_m^{\text{nom}} [j]$ the nominal stress amplitude σ_a^{nom} was determined such that

$$P_f\left(\Sigma_G(\sigma_m^{\text{nom}} [j], \sigma_a^{\text{nom}}), G \mid \theta\right) - p = 0 \quad (5.59)$$

using a simple secant method. This root finding algorithm has the advantage that no derivatives have to be evaluated (which is computationally expensive in this case), while converging faster than a basic bisection method. Nonetheless, the use of an other root finding algorithm is of course possible. A flowchart describing the procedure of determining the p -quantile lines is provided in Fig. 5.29.

5.6.4 Results and discussion

Following the procedure explained in the previous section, the results were produced in a calibration/prediction methodology. In order to calibrate the four parameters of the unit Haigh diagram, test data from the two specimen types NACA1 and NACA2A was used. The failure behavior of the six remaining specimen types (see Fig. 4.2) was predicted based on these calibrations. The results of this study will be presented and discussed for each material separately in Paragraphs 5.6.4.1 (AL7075-T6) and 5.6.4.2 (AL2024-T3). In the following two Paragraphs 5.6.4.3 and 5.6.4.4, these results will be discussed further in terms of the used effective mean stress function, and compared with fits based on two other mean stress models – the linear stress amplitude correction and Walker’s model. Finally, in the last Paragraph 5.6.4.5, the influence of the elasto-plastic material model is demonstrated by comparing the obtained results against a similar approach where a linear-elastic material model is used in the finite element simulations.

5.6.4.1 AL7075-T6 The results for the first aluminum alloy AL7075-T6 are presented in Fig. 5.30. This figure contains eight subplots where each one corresponds to a distinct specimen type. This correspondence is graphically indicated by a schematic sketch of the specimen (not true to scale) which contains the name of the specimen type, see Table 4.5 and 4.6, together with the elastic (von Mises) stress concentration factor K_t .

Each subplot shows a nominal Haigh plane with the nominal mean stress σ_m^{nom} on the horizontal and the nominal stress amplitude σ_a^{nom} on the vertical axis. Note that both of these stresses are normalized with the ultimate tensile strength σ_{UTS} of AL7075-T6, see Table 4.3. Each one of these Haigh planes shows the test data for the corresponding specimen type which is presented either as failures (filled symbols) or survivors (un-filled symbols) with respect to $N_{\text{ref}} = 5 \cdot 10^6$, cf. Eq. (5.15). Multiple tests at similar stress conditions with different outcomes are indicated by half-filled symbols together with a tag denoting their outcomes. In this context, an ‘f’ indicates a failure and an ‘s’ a survivor. A tag ‘fs’, for example, represents two tests, one of which resulted in failure and the other one in a survivor. Note that not all of the test data is shown. Each plot is zoomed into the region of interest, i.e. where the predicted quantile lines are located. Tests with higher stress amplitudes (all of which were failures) are therefore not shown.

Each Haigh plane contains a straight dashed line. This line separates all nominal stress conditions that result in a purely elastic material response (left side) from those which will trigger elasto-plastic material behavior (right side). The line is drawn based on the peak stress $K_t(\sigma_m^{\text{nom}} + \sigma_a^{\text{nom}})$ encountered in a specimen test. If this peak stress remained below the minimum stress for which the stress-stain relationship shown in Fig. 4.5 states non-zero plastic strain, the material behavior will be elastic. If not, local plasticity will occur. This line allows to visually distinguish tests associated with notch root plasticity from those where the whole specimen remains in the elastic regime.

Next to the test data, each subplot contains three quantile lines of the specimen’s design Haigh diagram for each of the three considered effective mean stress functions. The $p = 0.5$ quantile line ($P_f = 50\%$) is shown as a thick line. This line is surrounded by a shaded area which is bordered at its bottom by the $p = 0.05$ quantile line ($P_f = 5\%$) and at its top by the $p = 0.95$ quantile line ($P_f = 95\%$). All three quantile lines for each geometry and each effective mean stress function were computed using the procedure explained in Section 5.6.3 based on the parameters stated at the top of Fig. 5.30.

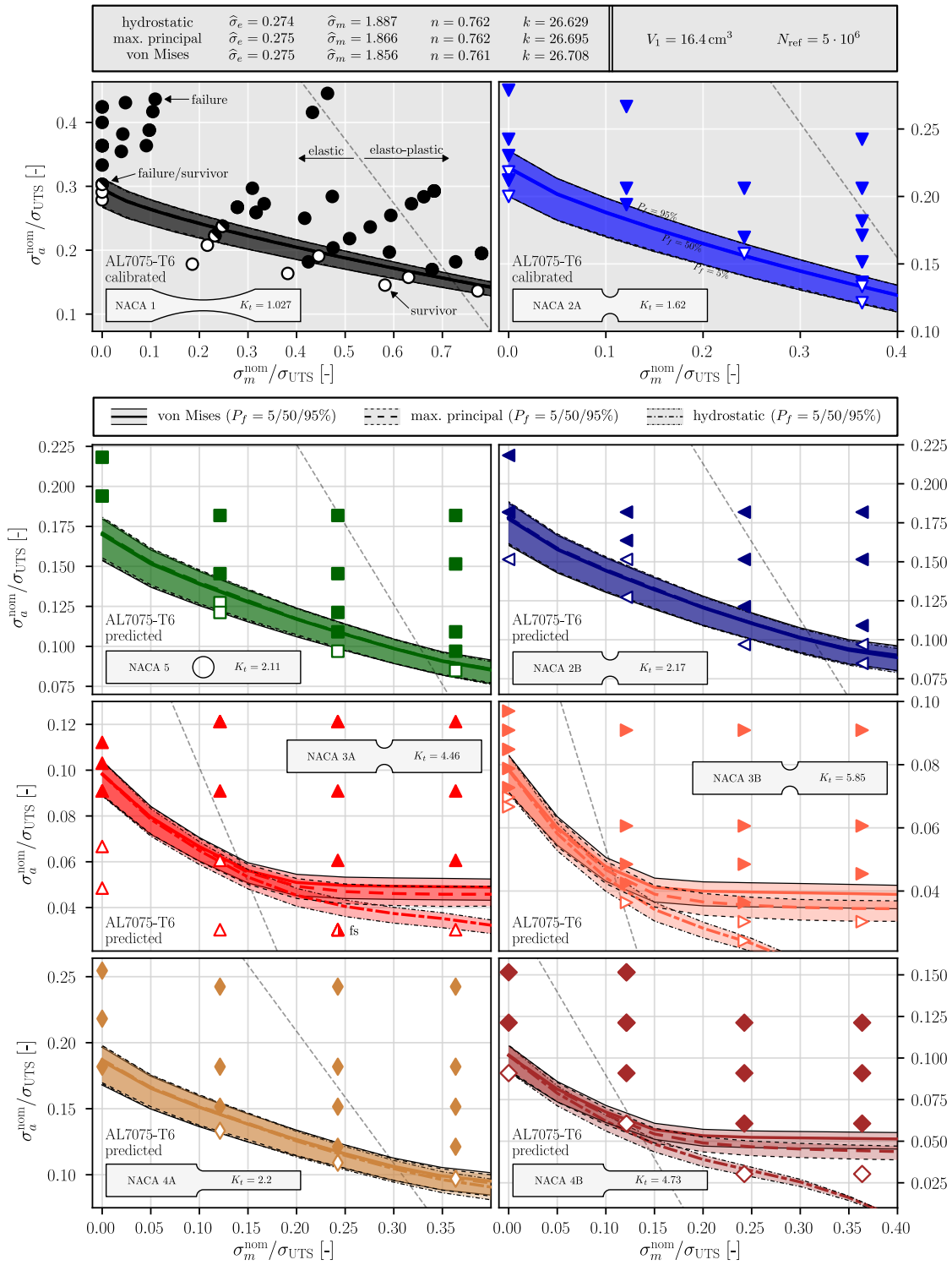


Figure 5.30: Calibration and prediction results for AL7075-T6 at $N_{\text{ref}} = 5 \cdot 10^6$ with respect to three different effective mean stress functions. The test data from the first two plots (gray background) was used for the model calibration with $V_1 = 16.4 \text{ cm}^3$ resulting in the parameter values given at the top. The remaining plots show pure predictions based on these calibrations.

The stated parameters were derived in the calibration step based on the test data of the two specimen types NACA1 and NACA2A. Both are presented in the first row of the subplots in Fig. 5.30. In order to visually indicate that these geometries were used for calibration the corresponding subplots are shown with a gray background. The probabilistic Haigh diagrams of the six remaining specimen types, shown in the subplots with a white background, are pure predictions based on the calibrated parameter values. Note that each effective mean stress function corresponds to an own calibration step, which is the reason for the three different parameter vectors shown at the top of Fig. 5.30.

The presentation of the results – test data vs. quantile lines – allows for a visual comparison between the predicted failure behavior, illustrated by the computed quantile lines, with the actual test outcomes, reflected in the test data. A first look on the calibration plots (gray background) shows good agreement between test data and the calibrated quantile lines. Note that no difference is found with respect to the three effective mean stress models as the corresponding quantile lines essentially overlap. This phenomenology is well in line with the results of the study presented in Section 5.4 assuming elastic material behavior, where almost no differences were found between the quantile lines computed with different effective mean stress functions. Since the test data for NACA1 and NACA2A shown in Fig. 5.30 is almost entirely in the elastic domain of the Haigh plane (left of the dashed line), a comparable situation is encountered here.

If one now takes a look at the six prediction subplots (white background) several observations can be made. Considering the predictions with respect to the mildly notched specimen types NACA2A, NACA4A and NACA5 good agreement with the test data is found. Similar as for the two specimen types used for calibration, NACA1 and NACA2A, almost no difference is found between the quantile lines for the different effective mean stress functions. On the other hand, when considering the results for the specimen types with sharp notches, NACA3A, NACA3B and NACA4B, one does find differences between the predictions based on the different effective mean stress functions. While the quantile lines corresponding to the von Mises and the maximum principal stress functions are generally close together, a greater difference is found between the two aforementioned models and the quantile lines of the hydrostatic mean stress function. Note that these differences are most emphasized in the elasto-plastic domain of the Haigh plane. The von Mises model results in the most optimistic prediction while the hydrostatic model corresponds to the most conservative quantile lines. The respective graphs of the maximum principal mean stress function end up in between those two, however closer to the von Mises predictions. The explanation for this phenomenon will be discussed in Paragraph 5.6.4.4. When comparing these different predictions for NACA3A, NACA3B and NACA4B with the failure behavior reflected in the test data, one finds that the hydrostatic model appears to correspond to an underestimation for the two sharpest notches found in NACA3B and NACA4B. For NACA3A however, no underestimation of the hydrostatic model can be identified. The von Mises and maximum principal models on the other hand are mostly in good agreement with the available test data. The only test result that does not agree with any of the three predictions is an unexpected failure encountered for the lowest tested stress amplitude at $\sigma_m^{\text{nom}}/\sigma_{\text{UTS}} \approx 0.25$ (B6S3B). Even if no irregularities were reported for this test, it might represent an outlier whose failure was caused by some anomaly with respect to the material, the specimen geometry or its surface. However, if this data point is not an outlier – which cannot be ruled out – none of the models can explain it.

An interesting phenomenon with respect to the computed predictions is the flattening of the quantile lines in the high mean stress regime. This trend is most emphasized in the von Mises and maximum principal predictions for the specimen types with sharp notches. The reason for this behavior is the notch root plasticity which has the following effect. As soon as it occurs, an increase in the nominal mean stress decreasingly raises the local mean stress in the notch root, and instead leads to a mean stress redistribution in its vicinity, cf. Fig. 5.28. As a result, the volume surrounding the notch root where high mean stresses are attained is growing, but the mean stress in the notch root itself, where the highest local stress amplitudes occurs, does not change so much, see also Fig. 5.28. A similar trend can be suspected in the high mean stress range for the mild-notched specimen types NACA2B, NACA4A and NACA5, however much less emphasized.

5.6.4.2 AL2024-T3 The results corresponding to the evaluation of the second aluminum alloy AL2024-T3 are presented in Fig. 5.31. Since the result presentation is identical to the previously discussed AL7075-T6 counterpart, general explanations with respect to how the material is presented will be skipped in this paragraph.

When considering the two calibration subplots shown in the first row of Fig. 5.31 (gray backgrounds), the first thing that stands out is that much more test points are now located in the elasto-plastic domain, compared with the calibration test data of AL7075-T6, cf. Fig. 5.30. This is due to the fact that, based on the stress-strain curve for AL2024-T3 shown in Fig. 5.27, this material is more ductile than AL7075-T6. As a consequence, the purely elastic part of the Haigh domain (left of the dashed line) is smaller in comparison. However, despite the higher content of test data associated with notch root plasticity, the calibrated quantile lines still show satisfactory agreement with the test data, irrespective of the used effective mean stress function.

The six predictions, i.e. the computed quantile lines for the different specimen geometries, shown in the remaining three rows of Fig. 5.31 (white background), look in some ways similar to those shown in Fig. 5.30 and in some ways different. The most apparent general difference is that for AL2024-T3 also the quantile lines of the mildly notched specimens geometries NACA2B, NACA4A and NACA5 exhibit a horizontal trend in the high mean stress range. This behavior, which can be attributed to the increased ductility of this material compared to AL7075-T6, is predicted almost similarly over all three effective mean stress functions. Note, that the horizontal trending of the quantile lines for these three specimen types is in good agreement with the respective test data.

When considering the three specimen types with sharp notches, NACA3A, NACA3B and NACA4B, one finds the same horizontal trends of the quantile lines as for the mildly notched types discussed before. However, in contrast to the mildly notched types, the quantile lines of the specimens with sharp notches differ between the different effective mean stress functions. This behavior was already observed for AL7075-T6 discussed in the previous section. Again, the hydrostatic model corresponds to the most conservative quantile lines, while the von Mises model results in the most optimistic predictions. The maximum principal model ends up, again, in between, closer to the von Mises predictions. When comparing these quantile lines with the test data of the sharp-notched types, one finds that the hydrostatic and the maximum principal models correspond to the most consistent predictions, even if the quantile lines of the hydrostatic model show an unusual slight increase in the high mean stress domain for NACA3A. The von Mises model on the other hand appears to result in slightly too optimistic predictions for these types.

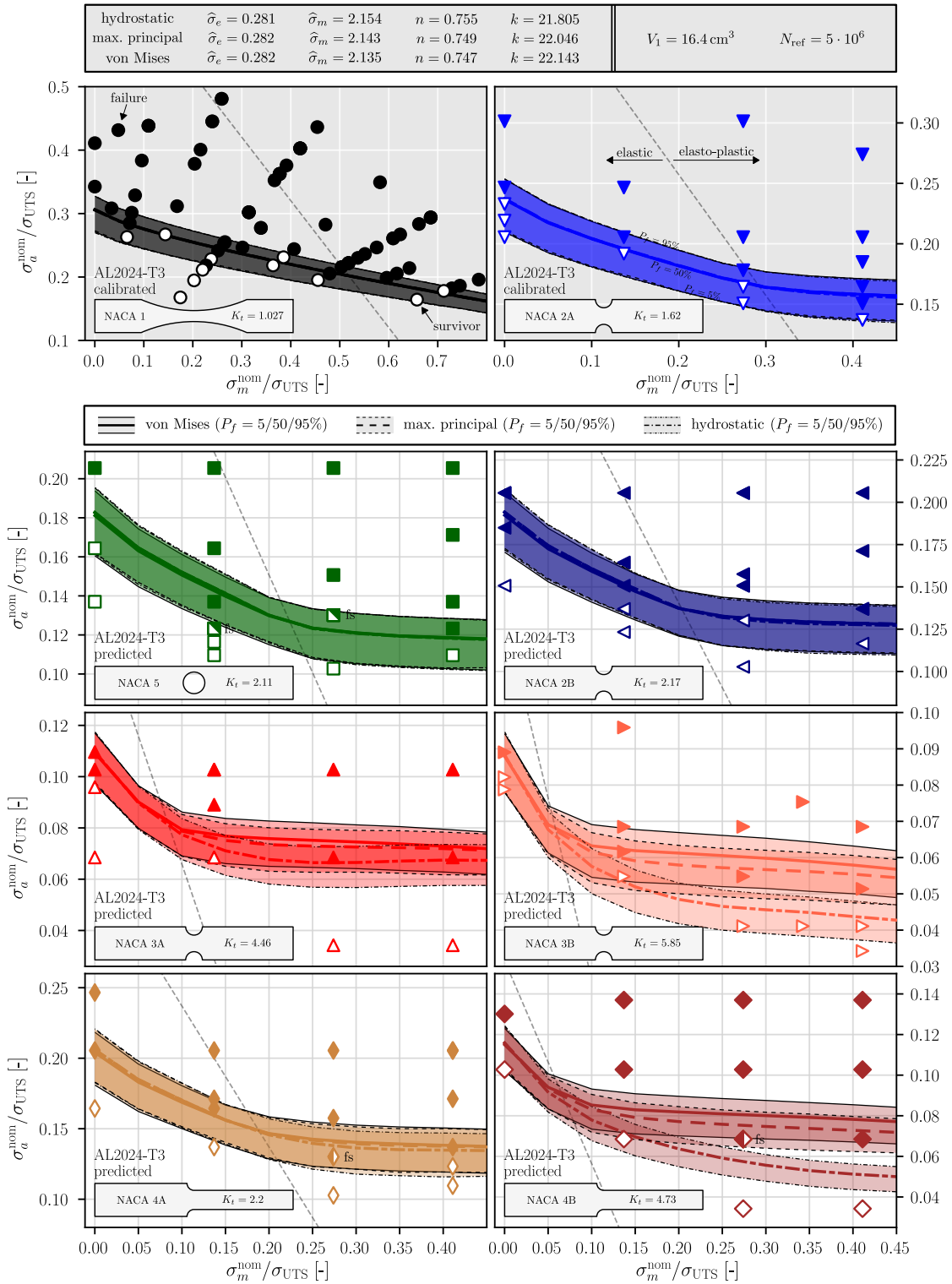


Figure 5.31: Calibration and prediction results for AL2024-T3 at $N_{\text{ref}} = 5 \cdot 10^6$ with respect to three different effective mean stress functions. The test data from the first two plots (gray background) was used for the model calibration with $V_1 = 16.4 \text{ cm}^3$ resulting in the parameter values given at the top. The remaining plots show pure predictions based on these calibrations.

5.6.4.3 On the influence of the effective mean stress function The results presented in the two previous sections revealed an influence of the effective mean stress function on the computed quantile lines that can be summarized as follows. While no significant effect was encountered for sheet specimen types with mild notches, a considerable influence was found for sheet specimen types with sharp notches – most emphasized in the high mean stress range. This influence always resulted in the hydrostatic model providing the most conservative quantile lines, while the von Mises model showed the most optimistic predictions. The quantile lines derived using the maximum principal mean stress function ended up in between the two aforementioned models.

This phenomenology can be understood by looking back on the results from Section 5.2.2 presented in Fig. 5.4, where the influence of the effective mean stress function was analyzed for a fixed model parameter vector comparing a cylindrical specimen with a sheet specimen, both containing a mild notch. In this setup, it was shown that the choice of the effective mean stress function had almost no influence on the design Haigh diagram of the sheet specimen exhibiting a plane-stress-like stress field, see Fig. 5.4b. This situation is encountered in the calibration step based on the NACA1 and NACA2A test data conducted in the analysis considered here, see Figs. 5.30 and 5.31. As a consequence, the calibration for all three effective mean stress functions resulted in almost similar model parameter vectors, as stated at the top of Figs. 5.30 and 5.31. Also the predictions for the mildly notched specimen types NACA2B, NACA4A and NACA5 reflect evaluations of plane-stress-like stress fields – irrespective of the encountered notch root plasticity – resulting in no major difference between the effective mean stress models.

However, the specimen types with sharp notches, NACA3A, NACA3B and NACA4B, exhibit 3D-features in their stress fields around the notch root, which corresponds to an increased influence of the effective mean stress model as demonstrated in Fig. 5.4a. The magnitude of the second principal stress in the notch root's center of the corresponding linear-elastic models was 6% (NACA3A), 11% (NACA3B) and 14% (NACA4B) of the first principal stress, while the third principal stress was approximately zero (surface node), compare with the role of α_2 in Fig. 5.6. Note that due to the almost similar model parameter vectors obtained in the calibration step for the different effective mean stress functions, the situation encountered in the predictions for NACA3A, NACA3B and NACA4B is almost similar to the example case shown in Fig. 5.4a where the model parameter vector was fixed. As a consequence, the same relation between the quantile lines corresponding to the different effective mean stress functions is found for NACA3A, NACA3B and NACA4B as already encountered in Fig. 5.4a. The hydrostatic model provides the most conservative prediction followed by the maximum principal model, while the von Mises model corresponds to the most optimistic one.

In order to conclude this paragraph, a correction with respect to a statement corresponding to the influence of the effective mean stress function on the quantile lines of the probabilistic Haigh diagram mentioned in [181] has to be made. In the aforementioned paper it was stated by the author in a side note (without showing the specific results) that the use of the maximum principal effective mean stress model resulted in considerable worse predictions with respect to the study presented above, compared with those obtained by means of the von Mises or hydrostatic stress model. This incorrect statement was based on an analysis with a script that contained a bug, as it was discovered after the paper was already published. The actual influence of the used effective mean stress function was discussed above and is reflected in Figs. 5.30 and 5.31.

5.6.4.4 Comparison with other mean stress models In a similar fashion as it was done in Section 5.4, when discussing the model fits assuming linear-elastic material behavior, the obtained results from the Paragraphs 5.6.4.1 and 5.6.4.2 should be compared to fits using different general mean stress models. To that end, the same calibration/prediction methodology has been conducted using either a linear stress amplitude correction model, cf. Eq. (5.18), or Walker’s approach, cf. Eq. (5.19), in combination with either a hydrostatic, maximum principle or von Mises effective mean stress function. The results for both aluminum alloys are summarized in Tables 5.12 and 5.13.

Both tables have the same structure. They contain the respective model parameters based on a fit with NACA1 and NACA2A test data, together with different evaluations of the negative log-likelihood function. In the column labeled $-\mathcal{L}(\theta_{\text{opt}}, \mathcal{T}_{\text{cal}})$ the negative log-likelihood function is evaluated for the calibration test data, containing the NACA1 and NACA2A test results. The two major right columns, on the other hand, contain the evaluation of the negative log-likelihood function for two subsets of the prediction test data using the calibrated model vector θ_{opt} . The column $-\mathcal{L}(\theta_{\text{opt}}, \mathcal{T}_{\text{pred}}^{\text{mild}})$ refers to the test data of the mild-notched types NACA2B, NACA4A and NACA5. The column on the right next to it, labeled $-\mathcal{L}(\theta_{\text{opt}}, \mathcal{T}_{\text{pred}}^{\text{sharp}})$ refers to the remaining sharp-notched types NACA3A (excluding the possible outlier B6S3B), NACA3B and NACA4B. Note that each of these columns contains several sub-columns containing the individual contributions of the different specimen types contained in the respective group. The sub-columns with the Σ -symbol refer to the respective sum of all contribution within one group. Generally, the smaller the stated negative log-likelihood values, the greater the value of the likelihood function, and hence the better the agreement between test data and model.

Looking at both of these tables, several observations can be made. At first, one notices the very similar model parameters when comparing the fits for different effective mean stress functions for a fixed general mean stress model. This characteristic, which can be found for both materials and all three models, has already been explained in the previ-

AL7075-T6	NACA1 + NACA2A \rightarrow $\begin{cases} \text{NACA 2B, 4A, 5} & \text{(mild notches)} \\ \text{NACA 3A, 3B, 4B} & \text{(sharp notches)} \end{cases}$														
	Calibration							Prediction							
Linear corr.	$\hat{\sigma}_e$	σ_{th}	α	k	$-\mathcal{L}(\theta_{\text{opt}}, \mathcal{T}_{\text{cal}})$			$-\mathcal{L}(\theta_{\text{opt}}, \mathcal{T}_{\text{pred}}^{\text{mild}})$				$-\mathcal{L}(\theta_{\text{opt}}, \mathcal{T}_{\text{pred}}^{\text{sharp}})$			
					1	2A	Σ	2B	4A	5	Σ	3A	3B	4B	Σ
hydrostatic	.28	0	.21	33.5	12.5	5.9	18.3	4.5	2.0	1.8	8.3	2.0	∞	9.6	∞
max principal	.28	0	.21	33.8	12.5	5.9	18.3	4.5	1.9	1.8	8.2	1.6	5.6	0.5	7.7
von Mises	.28	0	.21	34.0	12.4	5.9	18.3	4.5	1.9	1.8	8.2	1.5	7.6	1.1	10.2
Walker	$\hat{\sigma}_e$	σ_{th}	γ	k	$-\mathcal{L}(\theta_{\text{opt}}, \mathcal{T}_{\text{cal}})$			$-\mathcal{L}(\theta_{\text{opt}}, \mathcal{T}_{\text{pred}}^{\text{mild}})$				$-\mathcal{L}(\theta_{\text{opt}}, \mathcal{T}_{\text{pred}}^{\text{sharp}})$			
					1	2A	Σ	2B	4A	5	Σ	3A	3B	4B	Σ
hydrostatic	.28	0	.37	31.7	8.9	6.8	15.7	9.0	1.5	1.4	11.9	3.8	5.6	0.7	10.1
max principal	.28	0	.38	31.9	8.9	6.7	15.6	9.1	1.5	1.4	12.0	3.7	7.8	0.4	11.9
von Mises	.28	0	.38	32.0	8.9	6.7	15.6	9.1	1.5	1.4	12.0	3.6	9.7	1.0	14.2
Prob. Haigh	$\hat{\sigma}_e$	$\hat{\sigma}_m$	n	k	$-\mathcal{L}(\theta_{\text{opt}}, \mathcal{T}_{\text{cal}})$			$-\mathcal{L}(\theta_{\text{opt}}, \mathcal{T}_{\text{pred}}^{\text{mild}})$				$-\mathcal{L}(\theta_{\text{opt}}, \mathcal{T}_{\text{pred}}^{\text{sharp}})$			
					1	2A	Σ	2B	4A	5	Σ	3A	3B	4B	Σ
hydrostatic	.27	1.9	.76	26.7	9.7	6.3	15.9	9.9	3.1	1.1	14.1	6.1	∞	∞	∞
max principal	.28	1.9	.76	26.7	9.7	6.2	15.9	9.5	2.6	1.1	13.2	5.5	9.7	0.8	16.6
von Mises	.28	1.9	.76	26.7	9.7	6.2	15.9	9.4	2.4	1.1	12.9	5.4	6.8	0.4	12.7

Table 5.12: Comparison between different general mean stress models and effective mean stress functions with respect to the calibration/prediction results for AL7075-T6, cf. Fig. 5.30.

ous Paragraph 5.6.4.3. Also the small differences of $-\mathcal{L}(\theta_{\text{opt}}, \mathcal{T}_{\text{cal}})$ and $-\mathcal{L}(\theta_{\text{opt}}, \mathcal{T}_{\text{pred}}^{\text{mild}})$ respectively between the three effective mean stress functions for a given general mean stress model can be explained along these lines. Considerably larger differences between the effective mean stress functions for a given general mean stress model are found in the $-\mathcal{L}(\theta_{\text{opt}}, \mathcal{T}_{\text{pred}}^{\text{sharp}})$ group – a phenomenon that was also discussed in the previous paragraph. In this context, note that the ∞ -values appearing in the two tables denote evaluations where the negative log-likelihood function assumes very large values, indicating predictions which are not consistent with the respective test data.

Comparing the three general mean stress models with respect to their results reflected in the two tables, one finds that for both materials the probabilistic Haigh diagram and Walker’s model correspond to better calibration results in terms of $-\mathcal{L}(\theta_{\text{opt}}, \mathcal{T}_{\text{cal}})$ compared with the linear stress amplitude correction, irrespective of the used effective mean stress function. However, the differences are only small. On the other hand, when considering the evaluations of the log-likelihood function for the different predictions, one finds a more mixed picture. Not only vary the values $-\mathcal{L}(\theta_{\text{opt}}, \mathcal{T}_{\text{pred}}^{\text{mild}})$ and $-\mathcal{L}(\theta_{\text{opt}}, \mathcal{T}_{\text{pred}}^{\text{sharp}})$ for a given material with both the general mean stress model and the effective mean stress function. Most of the found trends also seem to differ between both materials. The linear stress amplitude correction, for example, provides the lowest $-\mathcal{L}(\theta_{\text{opt}}, \mathcal{T}_{\text{pred}}^{\text{mild}})$ value for AL7075-T6 but the highest one for AL2024-T3. Considering the probabilistic Haigh diagram, the von Mises model results in the lowest value of $-\mathcal{L}(\theta_{\text{opt}}, \mathcal{T}_{\text{pred}}^{\text{sharp}})$ for AL7075-T6, while it corresponds to a comparably high value for AL2024-T3. On the other hand, a trend reflected in both tables is the good prediction results of Walker’s model in combination with the hydrostatic mean stress function. Finally, it should not be overlooked that the probabilistic Haigh diagram often performs (slightly) worse in terms of the values for $-\mathcal{L}(\theta_{\text{opt}}, \mathcal{T}_{\text{pred}}^{\text{mild}})$ and $-\mathcal{L}(\theta_{\text{opt}}, \mathcal{T}_{\text{pred}}^{\text{sharp}})$ compared to the other two general mean stress models, when the effective stress function is fixed. Therefore, no advantage over the other two general mean stress models can be claimed here.

AL2024-T3	NACA1 + NACA2A → $\begin{cases} \text{NACA 2B, 4A, 5} & \text{(mild notches)} \\ \text{NACA 3A, 3B, 4B} & \text{(sharp notches)} \end{cases}$														
	Calibration						Prediction								
Linear corr.	$\hat{\sigma}_e$	σ_{th}	α	k	$-\mathcal{L}(\theta_{\text{opt}}, \mathcal{T}_{\text{cal}})$			$-\mathcal{L}(\theta_{\text{opt}}, \mathcal{T}_{\text{pred}}^{\text{mild}})$				$-\mathcal{L}(\theta_{\text{opt}}, \mathcal{T}_{\text{pred}}^{\text{sharp}})$			
					1	2A	Σ	2B	4A	5	Σ	3A	3B	4B	Σ
hydrostatic	.27	0	.18	21.8	13.4	5.7	19.1	5.6	7.4	8.8	22.0	6.1	5.5	3.6	15.2
max principal	.27	0	.18	22.0	13.4	6.0	19.4	5.7	8.1	8.8	22.7	8.0	11.9	8.5	28.4
von Mises	.27	0	.18	22.1	13.5	6.1	19.6	5.8	8.3	8.8	23.0	8.7	14.6	10.4	33.6
Walker	$\hat{\sigma}_e$	σ_{th}	γ	k	$-\mathcal{L}(\theta_{\text{opt}}, \mathcal{T}_{\text{cal}})$			$-\mathcal{L}(\theta_{\text{opt}}, \mathcal{T}_{\text{pred}}^{\text{mild}})$				$-\mathcal{L}(\theta_{\text{opt}}, \mathcal{T}_{\text{pred}}^{\text{sharp}})$			
					1	2A	Σ	2B	4A	5	Σ	3A	3B	4B	Σ
hydrostatic	.29	0	.35	24.9	14.1	3.8	17.8	3.7	4.3	5.8	15.8	5.1	3.7	2.7	11.5
max principal	.29	0	.35	25.1	14.1	3.9	18.0	3.6	4.6	7.8	16.0	6.1	6.6	6.0	18.7
von Mises	.29	0	.36	25.2	14.1	3.9	18.0	3.6	4.8	7.8	16.1	6.5	8.3	7.5	22.3
Prob. Haigh	$\hat{\sigma}_e$	$\hat{\sigma}_m$	n	k	$-\mathcal{L}(\theta_{\text{opt}}, \mathcal{T}_{\text{cal}})$			$-\mathcal{L}(\theta_{\text{opt}}, \mathcal{T}_{\text{pred}}^{\text{mild}})$				$-\mathcal{L}(\theta_{\text{opt}}, \mathcal{T}_{\text{pred}}^{\text{sharp}})$			
					1	2A	Σ	2B	4A	5	Σ	3A	3B	4B	Σ
hydrostatic	.28	2.2	0.76	21.8	13.2	3.7	16.9	3.7	3.7	8.4	15.6	4.1	2.5	13.2	19.7
max principal	.28	2.1	0.75	22.0	13.3	3.7	17.0	3.6	4.1	8.3	16.0	5.7	4.2	3.8	13.6
von Mises	.28	2.1	0.75	22.1	13.3	3.8	17.0	3.6	4.2	8.3	16.1	6.3	6.3	6.0	18.6

Table 5.13: Comparison between different general mean stress models and effective mean stress functions with respect to the calibration/prediction results for AL2024-T3, cf. Fig. 5.31.

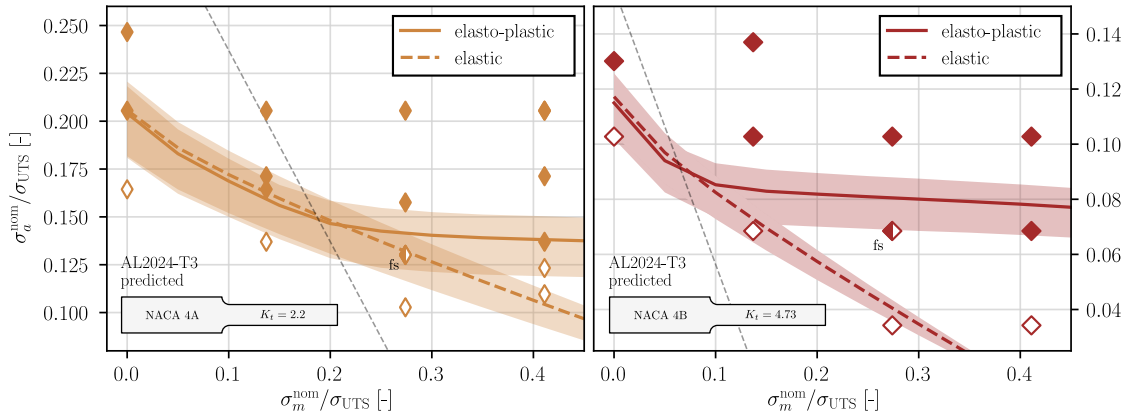


Figure 5.32: Comparison of linear-elastic and elasto-plastic failure predictions for NACA4A and NACA4B of AL2024-T3 using the von Mises effective mean stress function. The quantile lines of the elasto-plastic predictions are the same as those shown in Fig. 5.31. The quantile lines referring to the elastic model resulted from a fit to NACA1 and NACA2A test data while only using linear-elastic stress field solutions (no plasticity model). The linear-elastic fit resulted in the model parameters $\hat{\sigma}_e = 0.278$, $\hat{\sigma}_m = 2.123$, $n = 0.772$ and $k = 20.919$.

5.6.4.5 Comparison with elastic model In order to show the importance of modeling the stress redistribution triggered by elasto-plastic material behavior in the notch root for avoiding overly conservative designs, a comparison between an elasto-plastic and a linear-elastic model is provided in Fig. 5.32. Here, two failure predictions for the specimen types NACA4A and NACA4B of AL2024-T3 are compared in this regard. The presented quantile lines have been computed using von Mises mean stresses.

In both subplots, the prediction labeled as “elasto-plastic”, is similar to the von Mises results provided in the bottom row of Fig. 5.31. It is based on a model fit to test data of NACA1 and NACA2A using stress fields from elasto-plastic finite element simulations. The second prediction, labeled “elastic”, results from a fit to the same test data, but using stress fields from linear-elastic models. While this means that the corresponding finite element models which provided the stress fields did not contain the material plasticity model, the parameter values resulting from this fit were only slightly different from those obtained in the elasto-plastic case as stated in the caption of Fig. 5.32. However, the resulting predictions for NACA4A and NACA4B, represented by the quantile lines shown in Fig. 5.32 differ considerably in the high mean stress domain. It is obvious that the linear-elastic model results in much more conservative predictions than the elasto-plastic model and is much less consistent with the test data.

The reason for this phenomenon is that the linear-elastic model allows the local mean stress in the notch root to increase proportionally to the nominal mean stress without any restrictions. As a consequence the local fatigue strength will decrease accordingly. In the elasto-plastic model on the other hand, the mean stress level close to the notch root will eventually begin to stagnate when increasing the nominal mean stress due to the plasticity induced stress redistribution. Instead the mean stress will increase in regions that are further away from the notch root. These regions however will be subjected to stress amplitudes that are too low to significantly contribute to the total failure probability, cf. Fig. 5.28. The fatigue strength will consequently decrease much slower with increasing nominal mean stress compared to the linear-elastic model.

5.6.5 Summary and conclusion

The applicability of the proposed model for failure prediction of notched members subjected to high-cycle fatigue relevant constant-amplitude loads under high mean stresses was studied for two aluminum alloys AL7075-T6 and AL2024-T3. For large parts of the test data, the considered mean stresses were high enough that in combination with the superimposed stress amplitude, the material's yield strength in the notch root of the considered sheet specimens was exceeded. In contrast to the study presented in Section 5.4 where linear-elastic material behavior was assumed, in this investigation the employed material model accounted for plastic effects by means of a quasi-static stress-strain relationship in combination with non-linear finite element analyses.

In a calibration/prediction methodology, which was already applied in Section 5.4, the model parameters were first fitted based on test data from two out of eight considered specimen types. In a second step, the calibrated model was used to predict the failure behavior of the remaining specimen types by computing their design Haigh diagrams based on the stress fields obtained from the elasto-plastic finite element analyses.

It was found that this approach using the proposed weakest-link model in combination with stress fields obtained from elasto-plastic finite element simulations was able to predict the failure behavior of the mildly notched sheet specimen types ($K_t = 1 \dots 2.2$) quite well. Particularly the decelerated decrease of the fatigue strength in the high mean stress domain was captured accordingly. The influence of the effective mean stress function, considering a von Mises, maximum principal and hydrostatic model, was shown to be very small for all mildly notched specimens corresponding to plane-stress-like load conditions. Additionally, in comparison with two other general mean stress models – the linear stress amplitude correction and Walker's model – only small differences with respect to the corresponding predictions were found.

Considering the results for the sharp-notched specimen types ($K_t = 4 \dots 6$) on the other hand, one had to differentiate. While the predictions of the probabilistic Haigh diagram for these specimen types generally showed satisfactory agreement with the failure behavior reflected in the test data, the predictions revealed a considerable influence of the effective mean stress function. Using a hydrostatic mean stress consistently resulted in the most conservative predictions, while the use of a von Mises mean stress corresponded to the most optimistic one. The maximum principal mean stress resulted in quantile lines that were in between the predictions of the two aforementioned models. Also the comparison with the two other general mean stress models resulted in a mixed picture, which in several cases did not favor the probabilistic Haigh diagram.

In view of the results presented in this study, the following conclusion is drawn. The considered approach based on stress fields obtained from elasto-plastic finite element simulations appears to be capable of describing the fatigue strength of notched sheet specimens under high mean stress notch root plasticity, as long as the stress state encountered in the test data of the calibration step is comparable with those in the loaded specimen whose failure probability should be assessed. If this is not the case, caution is advised, especially with respect to the used equivalent (effective) mean stress function.

As a final remark, it should be pointed out that caution is also advised when applying the model in the context of non-negligible additional creep influences – for example under considerably elevated temperatures. Since the approach merely accounts for the effect of elasto-plastic stress redistributions, but not for any additional creep effects, a model extension will be required when applied in the context of those kinds of load conditions.

5.7 On the model uncertainty

Until this point, the general approach of most of the conducted analyses in the previous sections was to calibrate the four parameters of the probabilistic unit Haigh diagram with a given set of test data, and validate if this fitted model was capable of predicting the failure behavior reflected in test data for specimen types that were not included in the calibration step. This two-step procedure was intended to reflect the situation encountered in design practice, where some sort of fatigue model, which is typically calibrated with laboratory test data, is used to predict the failure behavior of an engineering component with a very different geometry compared to the test specimens. The difference of the design application case compared to the two-step approach described in the analyses before is that the second step of the analyses, where the validity of the failure prediction is checked with test data, is typically missing in the design case. Due to high costs of component fatigue tests and practical problems of applying operation-typical loads in a laboratory environment no real feedback on whether or not the model predictions are consistent with the actual component behavior is obtained until the component is in use.

The lacking validation of the model predictions – whether it is in the context of the unit Haigh diagram considered here or any other fatigue model – emphasizes the importance of avoiding to derive non-conservative model parameters from the available test data. The phenomenon this consideration is aiming at is the momentum of randomness reflected in the obtained test data. While the conducted tests had a specific outcome – one may think of a constant-amplitude fatigue test, that resulted in a certain number of cycles to failure – the results could also have been different, taking into account the typical scatter encountered in fatigue tests. However, the derived model parameters are often based merely on the specific outcome, not considering the uncertainty of this model with respect to randomness behind the realization of the test data. The potentially unsafe scenario that might be encountered is where the obtained test data, as a result of its randomness, has a bias towards higher fatigue resistance, for example longer lives, than it actually has on average. Consequently, a model derived on such a data set will tend to be non-conservative. This problem is particularly pronounced when the available test data set is small – a situation which is not uncommon in engineering practice.

If the used fatigue model is a deterministic one, it is unclear how to account for this problem, since it requires a stochastic interpretation of the test data. In a probabilistic model on the other hand, methods exist that can quantify the described model uncertainty, cf. [194]. It is the purpose of this section to explain how the model uncertainty of the probabilistic Haigh diagram can be determined after it was calibrated to a given test data set. Based on a model fit to the test data of PH12-10Mo, see Section 4.4, two approaches will be discussed. Parametric bootstrapping on the one hand, and Markov chain Monte Carlo (MCMC) sampling on the other. Both methods are associated with specific advantages and disadvantages, which will be addressed.

The presented material is structured as follows. The model fit to the available test data will be presented and discussed in Section 5.7.1. Afterwards, the general approach of deriving the model uncertainty will be explained in Section 5.7.2. This methodology will be applied using parametric bootstrapping and Markov chain Monte Carlo sampling respectively. The results of the former approach will be presented in Section 5.7.3 while the results of the MCMC methodology will be addressed in Section 5.7.4. Afterwards, a corresponding discussion is provided in Section 5.7.5. Finally, the results are summarized and contextualized in Section 5.7.6.

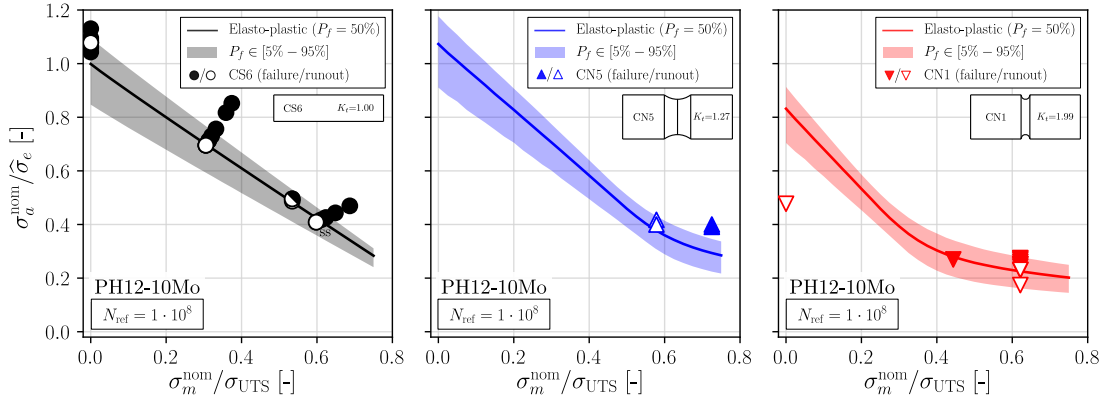


Figure 5.33: Design Haigh diagrams for cylindrical specimens CS6, CN5 and CN1 of material PH12-10Mo, see Section 4.4. The underlying unit Haigh diagram for $V_1 = 1 \text{ cm}^3$ was fitted to the combined test data for $N_{\text{ref}} = 1 \cdot 10^8$, see Eq. (5.60). The annotation “ss” in the left subplot refers to two specimens that survived N_{ref} cycles under similar nominal stress conditions.

5.7.1 Model fit

The model parameter vector θ of the unit Haigh diagram, see Eq. (5.4), was calibrated with the available test data on PH12-10Mo, which was presented in Section 4.4. In contrast to the test data considered in the fits over the last sections, this data set is the first one referring to tests on cylindrical instead of sheet specimens. Three types of specimen geometries were described by the data set. One smooth (CS6), and two types of notched specimens (CN5 and CN1). Since most of the tests on the notched types were conducted using mean stresses that were high enough to trigger notch root plasticity, a quasi-static elasto-plastic stress-strain relationship was required to describe the corresponding stress redistributions as it was done in Section 5.6. Such a model was taken from the Siemens material database, describing the stress-strain relationship with a Ramberg-Osgood fit. After modeling the two notched specimens in Abaqus 2017, using an axisymmetric model, and deriving the stress fields using the same procedure as described in Paragraph 5.6.2.3, the model parameter vector θ was fitted using the combined data set of all 41 data points on the three specimen types for $V_1 = 1 \text{ cm}^3$ and $N_{\text{ref}} = 1 \cdot 10^8$. When using the von Mises stress as the effective mean stress function, the maximum likelihood estimation (mle) resulted in

$$\theta_{\text{mle}} = \begin{pmatrix} \hat{\sigma}_e \\ \hat{\sigma}_m \\ n \\ k \end{pmatrix} = \begin{pmatrix} * \\ 1.06 \\ 0.97 \\ 15.84 \end{pmatrix}. \quad (5.60)$$

where the asterisk refers to a value that had to be censored, due to the use of Siemens data. The corresponding design Haigh diagrams for the three specimen types are presented in Fig. 5.33. Note that due to the censoring of the data, the vertical axis is normalized with the value of $\hat{\sigma}_e$ taken from the maximum likelihood fit.

Considering the results shown in Fig. 5.33 one generally finds satisfactory agreement between the quantile lines of the probabilistic Haigh diagrams and the failure behavior reflected in the test data. Only the two runouts of CN5, which appear above the 0.5-quantile line reflect a feature trending against the fit. It certainly would have been interesting to have more data points on CN5 from this region.

PH12-10Mo (CS6 + CN5 + CN1)									
Linear corr.	$\hat{\sigma}_e$	σ_{th}	α	k	$-\mathcal{L}(\theta_{opt}, \mathcal{T}_{cal})$				
					CS6	CN5	CN1	Σ	$\bar{\Sigma}$
hydrostatic	*	0.12	0.40	9.0	11.2	1.3	5.2	17.7	18.7
max. principal	*	0.00	0.44	24.0	11.4	1.8	4.1	17.2	
von Mises	*	0.00	0.46	38.0	12.4	4.2	5.1	21.2	
Walker	$\hat{\sigma}_e$	σ_{th}	γ	k	$-\mathcal{L}(\theta_{opt}, \mathcal{T}_{cal})$				
					CS6	CN5	CN1	Σ	$\bar{\Sigma}$
hydrostatic	*	0.0	0.59	20.7	10.2	2.1	2.8	15.0	19.2
max. principal	*	0.0	0.62	35.3	10.2	4.0	3.7	18.0	
von Mises	*	0.0	0.62	47.4	10.7	5.5	8.3	24.5	
Prob. Haigh	$\hat{\sigma}_e$	$\hat{\sigma}_m$	n	k	$-\mathcal{L}(\theta_{opt}, \mathcal{T}_{cal})$				
					CS6	CN5	CN1	Σ	$\bar{\Sigma}$
hydrostatic	*	2.0	0.52	9.5	11.3	1.3	3.8	16.5	16.0
max. principal	*	1.3	0.73	13.7	9.8	1.5	3.1	14.4	
von Mises	*	1.1	0.97	15.8	10.0	3.5	3.6	17.1	

Table 5.14: Comparison between different mean stress models in combination with different effective mean stress functions with respect to the calibration for PH12-10Mo shown in Fig. 5.33. The asterisk symbol * refers to values that had to be censored due to the use of Siemens data.

The value of the scatter parameter $k = 15.84$ is rather low compared with the fits considered over the last sections. As it was discussed before, a low value of k translates to more optimistic quantile lines. It turns out that this low value is mostly introduced by the two CN5 runouts pointed out before. When removing the CN5 data from the fit, the estimated value of the scatter parameter is increased to the more conservative value of $k = 24.51$. With respect to the discussion of the model uncertainty in the introduction to this study, the two CN5 runouts might therefore reflect a random feature in the test data, pushing the resulting fit to a more optimistic model. It is the purpose of a model uncertainty analysis to alleviate the influence of such non-conservative artifacts.

However, before analyzing the model uncertainty, the fit presented in Fig. 5.33 should be compared with fits that use a different effective mean stress function and/or a different general mean stress model. As it was already done in previous analyses, the linear stress amplitude correction and Walker's model have been considered in combination with the von Mises, maximum principal and hydrostatic mean stress function. The results of this comparison are presented in Table 5.14 and in Fig. 5.34 in a similar fashion as it was done in Section 5.6.4. For each combination of the three mean stress models and effective mean stress functions a maximum likelihood fit using the entire test data has been conducted. The corresponding parameters and log-likelihood values are summarized in Table 5.14 while Fig. 5.34 shows the corresponding 0.05-, 0.5- and 0.95-quantile lines.

Based on the calibrated model parameters stated in Table 5.14 one finds a non-negligible influence of the effective mean stress function for each general mean stress model, especially on the fatigue strength scatter parameter k . It appears that in all three cases the von Mises model results in the highest value for k , followed by the maximum principal and hydrostatic mean stress. In this regard, considering the fitted model parameters for the probabilistic Haigh diagram, all three values for k are rather low in comparison to the model fits derived in the previous sections. Moreover, the two parameters $\hat{\sigma}_m$ and n vary considerable between the three mean stress models.

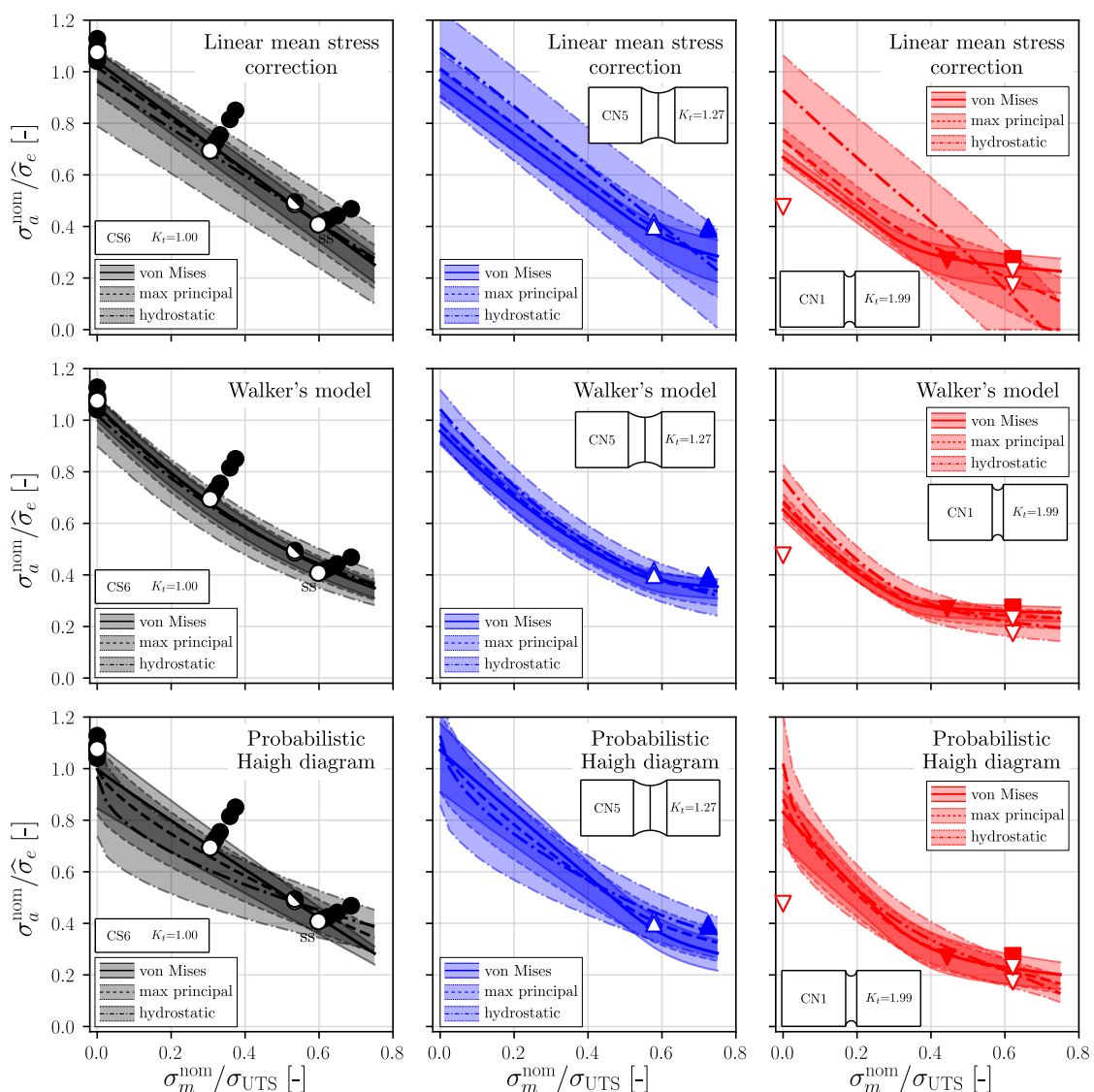


Figure 5.34: Visual comparison of the model fits between with $N_{\text{ref}} = 10^8$ for different mean stress models and effective mean stress functions, see also Table 5.14. The shaded areas always correspond to the area between the 0.05- and 0.95-quantile lines.

Also with respect to the log-likelihood values one finds differences between the general models. Looking on the average values over the three effective mean stress functions in the $\bar{\Sigma}$ -column of Table 5.14 shows a small advantage for the probabilistic Haigh diagram. However, the differences are only small. Also note, that these differences are mostly caused by the contributions of the notched specimen types – the test data of which is very limited and therefore susceptible to bias phenomena. It is therefore questionable if the log-likelihood values are a good measure to identify the most suitable model.

For the further discussion of the model uncertainty of the probabilistic Haigh diagram, the von Mises mean stress model was chosen because it resulted in the highest, and therefore most conservative scatter parameter k and showed the best fit of the 0.5-quantile line to the test data of CS6, on which the most test data was available.

5.7.2 General approach

In this study, the general approach to analyzing the model uncertainty is based on a methodology that produces a number of θ -samples, representing possible alternative model parameter vectors of the unit Haigh diagram, cf. Section 5.1.1. If $N_s \in \mathbb{N}$ denotes the number of generated samples, one may summarize them in the sample vector

$$\Theta_s := (\theta_1, \dots, \theta_{N_s}) \quad \text{with} \quad \theta_i = (\hat{\sigma}_{e,i}, \hat{\sigma}_{m,i}, n_i, k_i) \quad \text{for} \quad i = 1, \dots, N_s. \quad (5.61)$$

Two methods for generating such sample vectors Θ_s will be discussed in the subsequent sections. The first method is parametric bootstrapping [195], which is a frequentist approach, while the second method is called Markov chain Monte Carlo sampling [196], and typically represents a Bayesian approach. However, note that both methods merely result in a sample vector Θ_s , which cannot be directly interpreted as a model uncertainty. Therefore, it is the purpose of this section to describe how Θ_s can be post-processed to assess the model uncertainty of a component's design Haigh diagram.

In order to discuss the model uncertainty, one has to agree on a common definition. In the context considered here, the model uncertainty will be understood as follows. Based on a given set Θ_s of possible model vectors for the probabilistic unit Haigh diagram, a model uncertainty analysis will produce an adjusted unit Haigh diagram, comprising a scale function σ_e^{mu} and a scatter parameter k^{mu} , which – when used for design – will result in more conservative results (meaning higher predicted failure probabilities) than p^* of the model vectors contained in Θ_s . As it will be shown below $p^* = 1 - p^2$ for some $p \in [0, 1]$ that needs to be defined before the analysis. In the study conducted here, $p = 0.95$ and hence $p^* \approx 0.90$ was used, meaning that the adjusted model results in more conservative failure predictions than approximately 90% of the generated model samples would have produced. Note that the choice of p is arbitrary, and could for example be defined in a respective design procedure. The higher the chosen value of p , the more conservative the adjusted unit Haigh diagram.

Before discussing the two approaches for obtaining such an adjusted unit Haigh diagram, it makes sense to introduce some terminology. At first, it should be emphasized that each sample $\theta_i = (\hat{\sigma}_{e,i}, \hat{\sigma}_{m,i}, n_i, k_i) \in \Theta_s$ is understood as a corresponding scale function $\sigma_e^{\theta_i}$ of the unit Haigh diagram, see Section 5.1.1, with

$$\sigma_e^{\theta_i}(\sigma_m) = \hat{\sigma}_{e,i} \left\langle 1 - \left\langle \frac{\sigma_m}{\hat{\sigma}_{m,i}} \right\rangle^{n_i} \right\rangle \quad (5.62)$$

and a respective scatter parameter k_i . To some extent, both of these quantities $\sigma_e^{\theta_i}$ and k_i will be considered separately in the following discussion as it will become more clear in the following definitions. With respect to the scale functions given in Eq. (5.62), one obtains N_s values $[\sigma_e^{\theta_i}(\sigma_m)]_{i=1}^{N_s}$ for any fixed mean stress σ_m . Also for the scatter parameter one obtains N_s sampled values $[k_i]_{i=1}^{N_s}$. It is possible to analyze such sample vectors using the empirical quantile function Q_p , which is defined as the inverse of the empirical distribution function. If, for the sake of generality, $X := [x_i]_{i=1}^{N_s}$ denotes the considered sample vector, possibly containing values with multiple occurrences, and $pN_s \geq 1$ then Q_p can be expressed as

$$Q_p(X) := x_j \quad \text{with} \quad j = \pi_X^{-1}(\lfloor pN_s \rfloor). \quad (5.63)$$

Here, $\lfloor x \rfloor$ denotes the floor function, rounding to the closest integer smaller than or equal to x and $\pi_X : \{i\}_{i=1}^{N_s} \rightarrow \{i\}_{i=1}^{N_s}$ is a sorting function on index level with respect to X , which satisfies $x_{j^*} \leq x_{k^*}$ with $j^* = \pi_X^{-1}(j)$ and $k^* = \pi_X^{-1}(k)$ for all $j, k \in \{1, \dots, N_s\}$ with $j \leq k$. In other words, $\pi_X(i)$ is the position of x_i in a vector X^* that would result from sorting X ascendingly. Note that in the programming language Python the function π_X is implemented in the numpy package under the name “argsort”.

The first method, that comes to mind in order to compute the scale function of the adjusted unit Haigh diagram, is the definition with mean-stress specific quantiles as in $\sigma_e^{\text{mu}}(\sigma_m) := Q_q([\sigma_e^{\theta_i}(\sigma_m)]_{i=1}^{N_s})$ with $q = 1 - p$. In this way, at each mean stress p of the scale functions are greater or equal to $\sigma_e^{\text{mu}}(\sigma_m)$. If the unit Haigh diagram was evaluated only for a single mean stress in order to compute a failure probability, this would be a valid approach. However, due to the weakest-link methodology in combination with typically non-constant mean stress fields in an engineering component, the unit Haigh diagram is evaluated for a range of mean stresses in the computation of the failure probability, cf. Eq. (5.7). Therefore, it is necessary to derive an adjusted scale function which underestimates the sampled scale functions $\sigma_e^{\theta_i}$ not only pointwise, but over the entire mean stress range.

In order to implement such a non-local definition, the applied approach in this study is based on a minimum envelope established by a subset of the scale functions $\sigma_e^{\theta_i}$ identified with the sampled $\theta_i \in \Theta_s$ derived from the index set

$$I_p := \pi_{\Sigma_e}^{-1} \left(\lfloor [i]_{\lfloor qN_s \rfloor + 1}^{N_s} \rfloor \right) \quad \text{where} \quad \Sigma_e := [\hat{\sigma}_{e,i}]_{i=1}^{N_s} \quad (5.64)$$

and again $q = 1 - p$. In less formal terms, the index set I_p contains all $\lfloor pN_s \rfloor$ indices, that correspond to scale functions σ_e^{θ} whose value at zero mean stress $\sigma_e^{\theta}(\sigma_m = 0) = \hat{\sigma}_e$ is greater than the q -quantile of all sampled $[\hat{\sigma}_{e,i}]_{i=1}^{N_s}$ contained in Θ_s . By utilizing the index set I_p , the modified scale function $\sigma_{e,p}^{\text{mu}}$ and the adjusted scatter parameter k_p^{mu} of the unit Haigh diagram accounting for the model uncertainty, in the sense explained above, are defined as

$$\sigma_{e,p}^{\text{mu}}(\sigma_m) := \min_{i \in I_p} \left\{ \sigma_e^{\theta_i}(\sigma_m) \right\} \quad (5.65)$$

$$k_p^{\text{mu}} := Q_p([k_i]_{i \in I_p}). \quad (5.66)$$

The scale function $\sigma_{e,p}^{\text{mu}}$ describes the minimum envelope established by all scale functions represented by I_p while k_p^{mu} expresses the p -quantile of all k_i associated with I_p . By using this definition, the obtained unit Haigh diagram given by Eqs. (5.65) and (5.66) is more conservative than $p^* = (1 - p)^2$ of all models represented by Θ_s . Indeed, with respect to the scale function, only $(1 - p)$ of all samples represent possibly less conservative models. Consequently, from the p samples that exhibit a more conservative scale function, only those can (but do not have to) result in less conservative models which have a greater scatter parameter k than k_p^{mu} . However, with respect to the definition of k_p^{mu} this is only possible for $(1 - p)$ of these samples, hence

$$p^* = (1 - p) + p(1 - p) = 1 - p^2 \quad (5.67)$$

It should be pointed out, that other definitions for I_p from Eq. (5.64) are possible. Generally, one could remove any subset of $\lfloor qN_s \rfloor$ elements from Θ_s and use the remaining

$[pN_s]$ samples to define I_p . However, it is unclear which criterion should be used in order to determine which subset should be removed. Indeed, all of these selections result in identical model uncertainties, even though their scale functions and shape parameters will slightly differ from one another. The definition used here, expressed in Eq. (5.64) was chosen due to its simplicity.

In the following two Sections, the model uncertainty adjusted unit Haigh diagram defined by Eqs. (5.65) and (5.66) for PH12-10Mo with respect to the test data shown in Fig. 5.33 will be derived based on Θ_s vectors obtained by two different approaches. In the next Section 5.7.3 parametric bootstrapping will be used, while Markov chain Monte Carlo sampling is considered in Section 5.7.4.

5.7.3 Parametric bootstrapping

Parametric bootstrapping [195] is a resampling technique where one assumes that the available test data was sampled from a known stochastic model that can be described by certain parameters, for example a parametric distribution. Typically, the known (or true) model is an estimate based on the observed outcome reflected in the test data. One then proceeds to conduct a resampling of the test data based on the true model. The simulated test results, which will generally deviate from the original results, will then be used to re-fit the model. Since the simulated test results are usually different than the original results, the fitted model parameters will typically deviate from the model parameters described by the true model. By repeating this process for a number of times, one obtains a number of estimates for the underlying model.

In this study, it will be assumed that the true model parameter vector of the unit Haigh diagram is given by θ_{mle} which resulted from the maximum likelihood fit presented in Eq. (5.60). Using θ_{mle} in combination with the formula for the failure probability stated in Eq. (5.7) and repeated below

$$P_f(\sigma_m^{\text{nom}}, \sigma_a^{\text{nom}}, G \mid \theta_{\text{mle}}) = 1 - \exp \left\{ - \int_{V_G} \left(\frac{\sigma_a^{\text{vM}}(\mathbf{x})}{\hat{\sigma}_e \left\langle 1 - \left\langle \frac{\sigma_m^{\text{vM}}(\mathbf{x})}{\sigma_m} \right\rangle^n \right\rangle} \right)^k \frac{dV_G(\mathbf{x})}{V_1} \right\} \quad (5.68)$$

one can simulate the test outcome of each test i with the nominal test stresses $\sigma_{m,i}^{\text{nom}}$, $\sigma_{a,i}^{\text{nom}}$ and specimen geometry $G_i \in \{\text{CS6}, \text{CN5}, \text{CN1}\}$ contained in the considered test data of PH12-10Mo as a Bernoulli trial defined via

$$\{0, 1\} \ni \delta_i^{\text{ref}} \sim \mathcal{B} \left(P_f(\sigma_{m,i}^{\text{nom}}, \sigma_{a,i}^{\text{nom}}, G_i \mid \theta_{\text{mle}}) \right) \quad (5.69)$$

where $\delta_i^{\text{ref}} = 0$ corresponds to a runout, and $\delta_i^{\text{ref}} = 1$ to a failure, cf. Eq. (5.15). Since there are only two possible outcomes of a simulated trial there is only a finite set of possible test results for the entire data set. If $r \in \mathbb{N}$ denotes the number of available test results one has 2^r possible test outcomes for the data set as a whole. For cases where r is small, say $r \leq 10$, it is therefore feasible to analytically compute the resampling distribution of each parameter after the 2^r fits are computed. However, in the case considered here, the sample size of $r = 41$ prevents the analytical approach.

The generation of a single θ_i consists of the actual resampling of the test data using the true model, and a consecutive maximum likelihood fit to the resampled test data, see Section 5.1.3. In the study considered here, a total of $N_s = 10000$ samples were

created. Using a Python script on a regular desktop computer, each sample took two to five seconds to compute, mostly due to the handling of the stress field data. In total, the serial evaluation amounts to approximately ten hours of computing time.

It should be emphasized that it is an inherent property of the unit Haigh diagram, that it cannot be fitted to arbitrary test outcomes. If for example all considered tests were sampled as failures, the model cannot be fitted based on such an outcome. Other constellations, typically rather unlikely ones, will result in peculiar model estimates, than would not have been accepted for use in a practical context. The resulting samples, were therefore filtered with the following conditions, which were based on the authors experience with the model. In a Bayesian context, these conditions would be interpreted as prior information. In order for a sample $\theta_i = (\hat{\sigma}_{e,i}, \hat{\sigma}_{m,i}, n_i, k_i) \in \Theta_s$ to be accepted as a possible model fit, the respective parameters had to satisfy

$$\hat{\sigma}_{m,i}/\hat{\sigma}_m \in [0.8, 5] \quad n_i \in [0.6, 5] \quad k_i \in [5, 50]. \quad (5.70)$$

No restrictions were used for $\hat{\sigma}_{e,i}$. The corresponding histograms for each of the four model parameters are presented in Fig. 5.35. The plots also contain the parameter estimates from the original maximum likelihood fit, as well as the histograms with respect to the samples from the MCMC approach which will be described in the next section. Also the respective mean values of each parameter sample vector have been indicated in the four subplots. Note that the first parameter is normalized with the (censored) true model parameter from Eq. (5.60) due to confidentiality reasons (Siemens data).

Looking on the results, one finds that both the $\hat{\sigma}_m$ -samples and the k -samples correspond to histograms with a low to moderate positive skewness, centering around values of the original model fit (orange triangles). The amount of scatter in these two histograms appears to be moderate with respect to the corresponding histograms obtained in Section 5.5. The histograms for the $\hat{\sigma}_e$ -samples and the n -samples on the other hand show a much higher degree of skewness. While the $\hat{\sigma}_e$ -histogram shows a long tail towards lower values, the n -histogram exhibits a tail towards higher values. Both of these histograms have in common that the respective other tail is rather short. Finally, one notices that the mean values of the parameter vectors – with the exception of the $\hat{\sigma}_m$ -samples – seem to have an offset with respect to the values estimated by the maximum likelihood fit.

The bootstrapping samples – which may be referred to as Θ_s^{BS} – visualized in Fig. 5.35 were translated into a model uncertainty adjusted unit Haigh diagram using the approach described in Section 5.7.2 with $p = 0.95$ and hence $p^* \approx 0.9$. The resulting scale function together with the adjusted scatter parameter are presented in Fig. 5.36. One finds a considerable reduction of the scale function, particularly in the low and high mean stress range, and an increase of the scatter estimate from 15.84 to 24.09.

When translating this model uncertainty adjusted unit Haigh diagram into the design Haigh diagrams for the three used specimen types in the considered data set, one obtains the quantile lines presented in Fig. 5.37. Most striking about these results are the design Haigh diagrams of the two notched specimen geometries. While the quantile lines using the original maximum likelihood fit exhibit a decreasing slope in the high mean stress region as a result of the notch root plasticity, this trend has entirely vanished in the quantile lines corresponding to the model uncertainty adjustment.

A discussion of these results will be presented in Section 5.7.5 after the MCMC approach was described, which is the content of the following section.

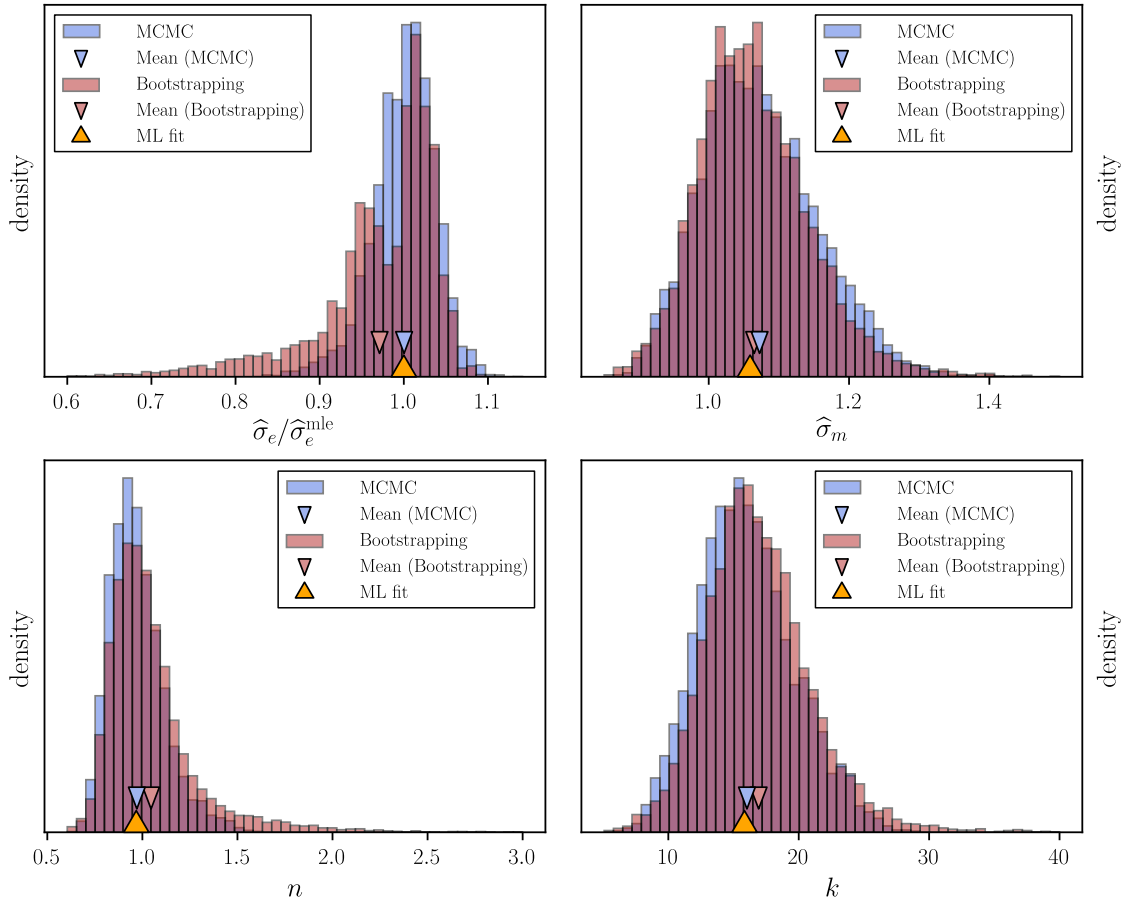


Figure 5.35: Parameter histograms of Θ_s^{BS} and Θ_s^{MCMC} generated using parametric bootstrapping (BS) and Markov chain Monte Carlo sampling (MCMC) respectively.

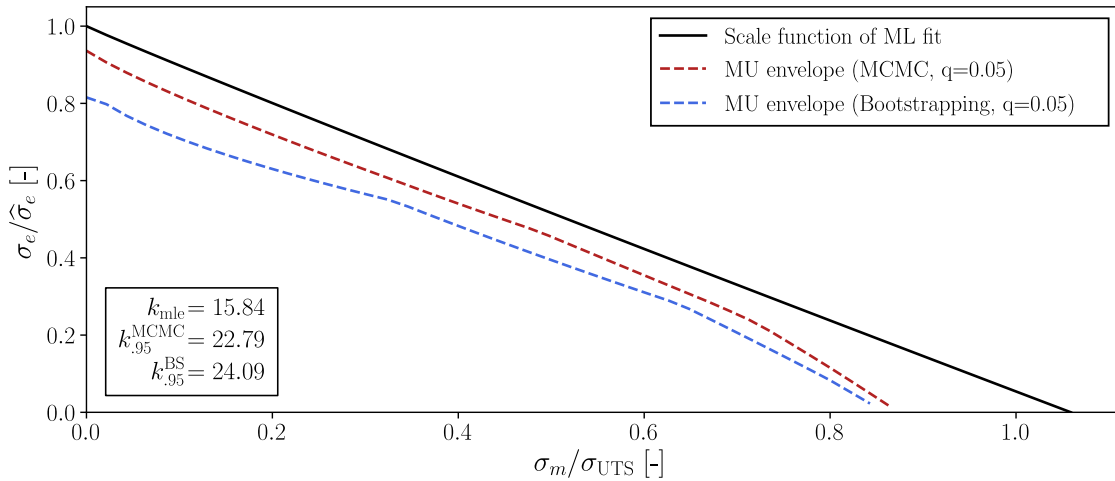


Figure 5.36: Unit Haigh diagram based on the original maximum likelihood fit (mle), compared with the model uncertainty adjusted unit Haigh diagrams based on parametric bootstrapping (BS) and Markov chain Monte Carlo sampling (MCMC) respectively. Each model is represented by a scale function and a corresponding scatter parameter given in the box on the bottom-left.

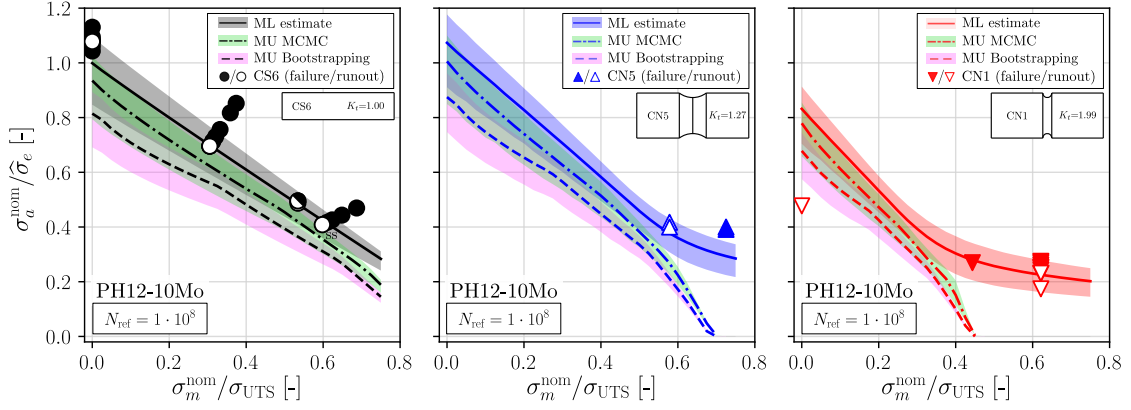


Figure 5.37: Design Haigh diagrams for CS6, CN5 and CN1 based on the original maximum likelihood fit and model uncertainty adjustments based on Markov chain Monte Carlo sampling (MCMC) and bootstrapping.

5.7.4 Markov chain Monte Carlo

In contrast to the parametric bootstrapping approach discussed in the previous section, Markov chain Monte Carlo (MCMC) sampling [102] takes an entirely different approach to generate Θ_s . In a way, this alternative approach can be seen as inverse or dual to the one represented by parametric bootstrapping described in Section 5.7.3. Instead of resampling the test data based on fixed model parameters, in MCMC sampling the test data is fixed and the model parameters are resampled.

In the analysis conducted here, the Metropolis-Hastings algorithm [196] with uniform priors according to the conditions stated in Eq. (5.70) and normal proposal distributions was used to generate Θ_s . Beginning with an initial sample θ_0 , which in this case was set to θ_{mle} as stated in Eq. (5.60), the algorithm successively creates new θ -samples, where each sample merely depends on the previous one (Markov property). Given a sample θ_i , a proposal for the next sample $\theta_{p,i+1}$ is created by sampling from the proposal distributions

$$\hat{\sigma}_{e,p}^{[i+1]} \sim \mathcal{N}(\hat{\sigma}_e^{[i]}, sd_e) \quad (5.71)$$

$$\hat{\sigma}_{m,p}^{[i+1]} \sim \mathcal{N}(\hat{\sigma}_m^{[i]}, sd_m) \quad (5.72)$$

$$n_p^{[i+1]} \sim \mathcal{N}(n^{[i]}, sd_n) \quad (5.73)$$

$$k_p^{[i+1]} \sim \mathcal{N}(k^{[i]}, sd_k). \quad (5.74)$$

Here, $\mathcal{N}(\mu, sd)$ represents a normal distribution with location μ and standard deviation sd . As expressed in Eqs. (5.71) to (5.74) each parameter proposal is sampled from a normal distribution that is centered at the parameter value of the previous sample, and has a parameter-specific standard deviation. The values for the standard deviations sd_e , sd_m , sd_n and sd_k are tuning parameters of the algorithm, which, in this study, were chosen as 5% of the respective parameter values of the maximum likelihood fit given in Eq. (5.60). It is however not claimed that this setting produces the best results. Especially when analyzing different sets of test data, other settings might be required. Note that the optimal definition of the proposal distribution for a given problem, which corresponds to the fastest convergence of the generated (a-posteriori) distributions is a research subject in its own right, see for example [197].

Once the proposal vector $\theta_{p,i+1} = (\hat{\sigma}_{e,p}^{[i+1]}, \hat{\sigma}_{m,p}^{[i+1]}, n_p^{[i+1]}, k_p^{[i+1]})$ is sampled, it is used to evaluate the corresponding likelihood $\ell(\theta_{p,i+1})$ with Eq. (5.16), which is then compared with the likelihood of the previous sample $\ell(\theta_i)$ by computing

$$\alpha = \min \left(1, \frac{\ell(\theta_{p,i+1})\pi(\theta_{p,i+1})}{\ell(\theta_i)\pi(\theta_i)} \right). \quad (5.75)$$

Here, π corresponds to the prior distribution according to the conditions stated in Eq. (5.70). Note that $\pi(\theta_{p,i+1})/\pi(\theta_i) = 1$ if both parameter vectors satisfy Eq. (5.70), and $\pi(\theta_{p,i+1})/\pi(\theta_i) = 0$ if the proposed vector $\theta_{p,i+1}$ is outside of these bounds. If the proposed sample $\theta_{p,i+1}$ is valid and does not reduce the likelihood, i.e. $\ell(\theta_{p,i+1}) \geq \ell(\theta_i)$ then $\alpha = 1$, otherwise $\alpha \in [0, 1)$. Based on α , the next sample θ_{i+1} is now determined by sampling $u \sim \mathcal{U}_0^1$ with \mathcal{U}_0^1 being a uniform distribution on $[0, 1]$ and setting

$$\theta_{i+1} = \begin{cases} \theta_{p,i+1} & \text{if } u \leq \alpha \text{ (accepted)} \\ \theta_i & \text{if } u > \alpha \text{ (rejected)}. \end{cases} \quad (5.76)$$

Consequently, when the proposed vector $\theta_{p,i+1}$ is valid and increases the likelihood, it will always be accepted. However, if the proposed vector is valid and decreases the likelihood, it will be accepted with a probability of α . If a proposal vector $\theta_{p,i+1}$ is rejected, the last sample θ_i will be repeated in Θ_s^{MCMC} and a new proposal will be drawn. This procedure is repeated until enough samples have been obtained for the generated (a-posteriori) histograms to have sufficiently converged. Here, convergence was assessed based on the visual impression of the generated histograms. In this study, around 10^5 samples were generated using the outlines Metropolis algorithm. Note that the MCMC procedure is much faster than the one for parametric bootstrapping, since no optimization loops are required. The generation of the 10^5 samples only took several minutes of computation time. The individual parameter histograms resulting from this approach are shown in Fig. 5.35 next to the histograms obtained from parametric bootstrapping.

Considering these results, one finds a qualitative resemblance of each histogram comparing MCMC and bootstrapping. In the cases of $\hat{\sigma}_m$ and k one even finds a notable quantitative similarity. For the remaining two parameters, $\hat{\sigma}_e$ and n on the other hand, one observes that the qualitatively similar tails are now less emphasized compared to the bootstrapping samples. Finally, one has point out that the offsets between the mean values of the parameter sample vectors and the respective maximum likelihood estimates are reduced compared to the bootstrapping samples.

When translating these results into the corresponding adjusted unit Haigh diagram, as it was done for bootstrapping in the previous section, one obtains a scale function that is plotted in Fig. 5.36 and a scatter parameter of $k = 22.79$. Comparing these results to the ones obtained from bootstrapping, which are also shown in Fig. 5.36 one finds a qualitatively similar looking, but less conservative adjustment resulting from MCMC with respect to both the scale function and the scatter parameter.

The less conservative adjustment is also reflected in Fig. 5.37, where the model uncertainty adjusted design Haigh diagram is compared with the corresponding adjustment resulting from bootstrapping and the original maximum likelihood fit. However, while the MCMC quantile lines are in between the bootstrapping quantile lines and the original quantile lines in the lower mean stress range, only a minor difference is observed between the two adjustments in higher mean stress range.

5.7.5 Discussion

When considering the individual parameter histograms in Fig. 5.35 obtained from bootstrapping and MCMC, it becomes apparent, that both methods qualitatively indicate the same shortcomings of the provided data set. There exists a risk that the first parameter $\hat{\sigma}_e$ is overestimated (emphasized left tail), while the curvature parameter n might be underestimated (emphasized right tail). In this context, note that the underestimation of n corresponds to a risk of being too conservative, since a greater n at fixed $\hat{\sigma}_e$ and $\hat{\sigma}_m$ corresponds to greater fatigue strengths for non-zero mean stresses, cf. Fig. 5.3f. The possible overestimation of $\hat{\sigma}_e$ on the other hand corresponds to a risk of being too optimistic. The difference between both methods with respect to these histograms is that the bootstrapping approach is highlighting these apparent shortcomings in a more pronounced way, since the corresponding tails have more weight compared to the MCMC histograms. With respect to this result, one has to note that the model fits generated by the bootstrapping approach appear to allow for a greater model flexibility in terms of the possible parameter ranges than the MCMC procedure.

The resulting unit Haigh diagrams shown in Fig. 5.36 are consistent with the findings from analyzing the parameter histograms. The strikingly lower values in the low mean stress range of the bootstrapping scale function compared to the one generated by MCMC can be explained by the θ -samples generated in the bootstrapping procedure that contained low $\hat{\sigma}_e$ - and high n -values. With increasing mean stress, the more similar form and values of the two scale functions is due to the increasing influence of $\hat{\sigma}_m$ on the fatigue strength, whose histograms in Fig. 5.35 are very similar. Generally, the model uncertainty adjustment of the scale function is considerable, especially in the high mean stress range for both methods and in the lower mean stress range for the bootstrapping approach. The reason for this significant reduction is the low number of runouts contained in the test data. As a consequence, quantile lines of lower failure probabilities are associated with rather high uncertainty, because only few of tests support their location. With respect to testing practice, one should therefore aim to provide approximately similar numbers of failures and runouts when fitting the model, in order to avoid a high debit (the reduction of the scale function) due to model uncertainty. The last comment concerning Fig. 5.36 refers to the resulting k values. The increase of k from the value obtained from the maximum likelihood fit to the adjustments from bootstrapping and MCMC respectively, is moderate. Also the difference between the two adjusted values is not large. Considering the rather low value of $k = 15.84$ given by the maximum likelihood fit, both corrections seem reasonable.

Considering the quantile lines of the design Haigh diagrams for CS6, CN5 and CN1 that resulted from the adjusted unit Haigh diagrams discussed before, one essentially finds the same trends. The only feature that needs to be looked upon in more detail is the totally different behavior in the high mean stress range. The complete vanishing of the plasticity induced flattening of the quantile lines associated with the two model uncertainty adjustments is a result of the considerable reductions of the unit Haigh diagram scale functions in the high mean stress range as discussed before. Due to this heavy debit, combinations of high mean stresses with stress amplitudes that would result in an elasto-plastic material response are associated with very high failure probabilities, so that loads with notch root plasticity become unacceptable. This phenomenon, which essentially inhibits the exploitation of the plasticity effect for design additionally emphasizes the need for more runouts in the considered test data set.

5.7.6 Summary and conclusion

Based on a given fatigue test data set of the high strength steel PH12-10Mo, containing test results on one type of smooth and two types of notched cylindrical specimens, the model uncertainty associated with the probabilistic Haigh diagram was investigated.

After discussing the model fit to the full data set comparing it to alternative fits using different general mean stress models and effective mean stress function, a fit for the probabilistic unit Haigh diagram based on the von Mises mean stress was selected for the following analysis of the model uncertainty.

The model uncertainty analysis itself was conducted introducing an approach where an adjusted unit Haigh diagram would be derived from a set of possible model vector alternatives Θ_s , which corresponds to a more conservative failure assessment for any design application than a defined percentage of the provided model vector alternatives in Θ_s would have produced. The set of the model parameter alternatives Θ_s was generated by two different approaches, parametric bootstrapping on the one hand, and Markov chain Monte Carlo (MCMC) sampling on the other. The resulting adjusted unit Haigh diagrams, as well as the resulting design Haigh diagrams for the three considered specimen types were compared with respect to the two considered approaches.

Both methods, parametric bootstrapping and MCMC, produced sets of model vector alternatives Θ_s^{BS} and Θ_s^{MCMC} corresponding to qualitatively similar marginal parameter histograms. They revealed the risk associated with the provided test data set of overestimating $\hat{\sigma}_e$ and underestimating n . However, the tails of these histograms, which indicated these shortcomings, were more pronounced for the bootstrapping approach.

The adjusted unit Haigh diagrams which were derived from Θ_s^{BS} and Θ_s^{MCMC} using the proposed methodology, as well as the corresponding design Haigh diagrams for the three considered specimen types showed a considerable reduction of the fatigue strength for both approaches, especially in the low and high mean stress range. Due to the more pronounced tails in the marginal parameter histograms encountered for the bootstrapping approach, the corresponding adjustment resulted in more conservative quantile lines in the probabilistic Haigh diagrams compared to the MCMC-based adjustment.

When comparing both approaches in the context of a practical application, the MCMC approach has the clear advantage of having a considerably reduced computation time. On the other hand, the need to define several tuning parameters of the underlying Metropolis-Hastings algorithm make the method more difficult use and interpret for users that have no experience with Markov chain Monte Carlo sampling. Parametric bootstrapping, on the other hand is easy to use and to interpret. Unfortunately, the computational costs are considerably higher compared with the MCMC procedure.

In view of the different pros and cons of the two approaches, in combination with the more conservative tendency of the bootstrapping method, it seems to be reasonable to apply Markov chain Monte Carlo sampling for quickly obtaining qualitative insights in the model uncertainty of a given data set – for example to identify general shortcomings. However, even in that context it is important that the method is applied by an experienced user. On the other hand, when it comes to the definition of an adjusted unit Haigh diagram for design purposes, it is recommended to apply parametric bootstrapping. This method is easy to use, straightforward to interpret and showed – at least in this study – a conservative trend in the produced quantile lines.

6 Application

In the final section of this work, it will be demonstrated how the weakest-link based probabilistic Haigh diagram can be used in a design context. The specific application considered here is the assessment of a compressor blade – as part of a gas or steam turbine compressor – with respect to the probability of vibration-induced high-cycle fatigue, cf. Section 2.1. Note however, that the described methods are not intended to reflect an entire design process. Due to the many interdisciplinary aspects, and the resulting iterative nature of the procedure, this is not possible in this format. It is merely presented, how central steps in the assessment of high-cycle fatigue can be treated in a probabilistic framework using the methodologies developed in Section 5.

The discussion of this design case is presented in two subsections. First, in the following Section 6.1 the focus is put on the individual compressor blade, its eigenmodes the mean stress influence and the resulting failure probabilities. However, after all, a compressor does not contain only one but many blades, distributed over several stages. This setup corresponds to a different failure probability than the one obtained for a single blade. Therefore, in Section 6.2 the failure probability of a full compressor stage due to vibration-induced high-cycle fatigue is assessed.

6.1 Probabilistic design of a compressor blade

The compressor blade model discussed in this section is derived from the respective component used in the fourth compressor stage in a large Siemens gas turbine. However, due to confidentiality the used model in this study is not identical with the original. In particular, it is analyzed in combination with a generic material model, that is not used for the manufactured compressor blade. Consequently, the derived eigenfrequencies, mean stresses and in the end also the computed failure probabilities and Haigh diagrams, are not representative for the respective components in operation.

The rotating part of the considered compressor stage contains 48 airfoils, also referred to as blades, mounted onto a disk. With respect to the corresponding finite element model – due to the resulting nominal symmetry – it is therefore sufficient to model only one 48th of the entire row, i.e. a section that contains one airfoil. The respective finite element model, which was set up in Abaqus 2017, is shown in Fig. 6.1. The indicated blade component of the assembly was prepared using three different meshes in order to analyze the effects of the used mesh resolution on the computed failure probabilities. These three meshes are shown in Fig. 6.2. Note that the mesh of the bottom fixture remains constant. With respect to the airfoil part, the coarse mesh contains 1860 elements, the intermediate mesh 7560 and the fine mesh 18000 elements. Almost all of the elements were 20-node brick elements (C3D20), while several 15-node prism elements (C3D15) were used at the rounded leading edge.

The loads acting on the compressor blade consist of a vibratory and a stationary part. The latter is typically dominated by the centrifugal loads, superimposed with the mean pressure of the airflow passing through the stage. The vibratory loads, typically introduced by the changes in the airflow pressure field while the blade is passing the stationary vanes, excite vibrations of the blade. These vibrations can be described using the eigenmodes of the blade-disk assembly under the influence of the mean stresses. Each of these eigenmodes is associated with a corresponding eigenfrequency. If the excitation frequency introduced by the vibratory loads is very different from all eigenfrequencies of

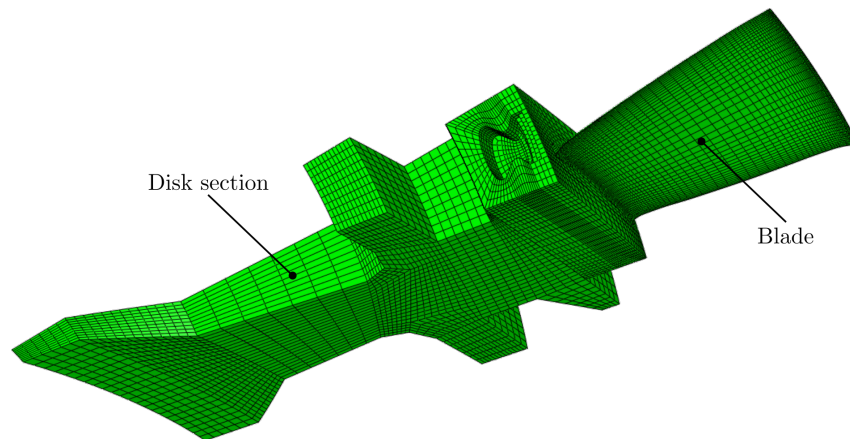


Figure 6.1: The full finite element section model including the disk and the blade.

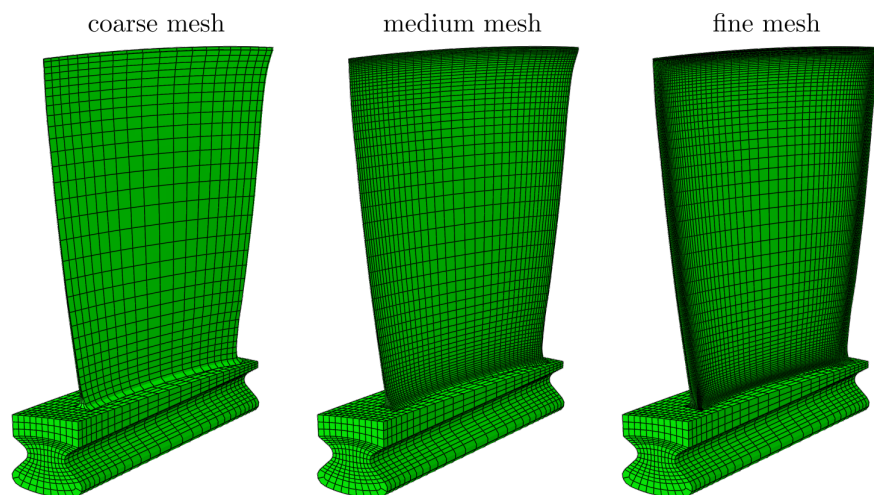


Figure 6.2: The three considered finite element meshes of the analyzed compressor blade.

the assembly, only small amounts of the energy contained in the airflow can be transferred into kinetic energy represented by blade vibrations. Consequently, the resulting stresses in the blade will be low. If however the excitation frequency comes close to an eigenfrequency (resonance), the energy transfer is much greater and the blade will start to vibrate considerably, see also Section 2.1. This is the load case considered here.

In order to describe the vibratory stresses, it is necessary to determine the eigenmodes of the disk-blade assembly for any mean stress field of interest. Note that due to stiffening effect of the stationary centrifugal loads, the eigenmodes and frequencies will differ between different rotor speeds, i.e. different mean stress fields. In the analysis conducted here, only eigenmodes with respect to the maximum nodal diameter of 24, corresponding to single blade vibrations, have been considered. The first three corresponding modes for a mean stress field resulting from a rotor speed of 30 Hz are shown in Fig. 6.3. The figure also contains the corresponding eigenfrequencies. Note that the comparably small contribution to the stationary stress field stemming from the mean pressure of the airflow was neglected in this analysis. A corresponding stress field based on a CFD (compu-

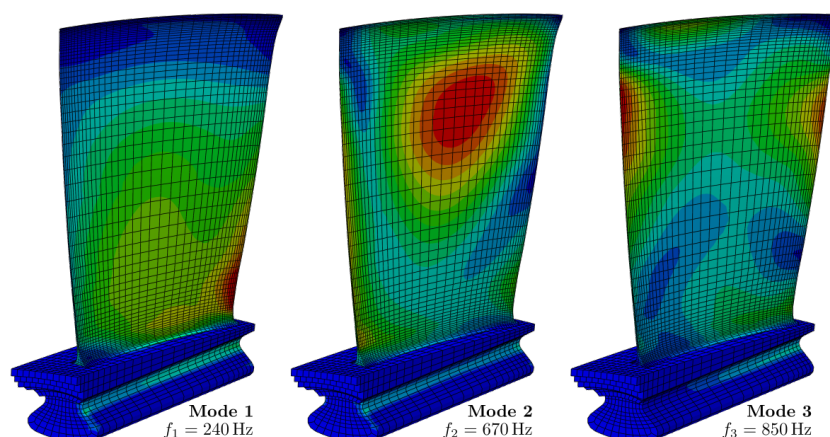


Figure 6.3: The first three compressor blade eigenmodes at $f = 30$ Hz.

tational fluid dynamics) analysis was available only for the rotor speed of $f = 60$ Hz (baseload) and showed negligible influence on the corresponding failure probabilities. It was therefore decided to omit additional efforts to describe this small contributions for other rotor speeds by scaling the 60 Hz-field or even more CFD simulations. However, if the blades are larger than the one considered here, the contribution of the stationary airflow might not be negligible anymore due to the higher resulting bending moment.

In the design process of a compressor blade, one typically focuses on certain critical eigenmodes in combination with critical engine orders with respect to certain operation conditions. The latter are often transient events, like starts or shutdowns, where due to the change in rotor speed, a range of excitation frequencies is realized over a rather short period of time. The derivation of such critical conditions shall not be the subject of the discussion presented here. However, the important outcome of such an analysis for this study, is a set of critical modes, meaning eigenmodes that are prone to vibrations during operation. In the following, it is assumed that the three first modes shown in Fig. 6.3 represent such critical modes. The methodology does not change, if other modes than those three are the actual critical ones.

As the major design tool for this application, the probabilistic design Haigh diagram should be derived for each of the three considered eigenmodes, cf. Section 5.1.2. To that end, one needs a scalar parameterization of the vibratory and the mean stress field, denoted as L_a and L_m in Section 5.1.2 respectively. Considering the vibratory part of the loading, the von Mises stress σ_a^{crit} at the critical location of the respective mode will be used. Note that the use of this local value does not mean that the failure probability is assessed locally at the critical location, but only that this value is used as a scaling factor for the vibratory stress field, compare the elaborations in Section 5.1.2. With respect to the mean stress field, the natural choice for a scalar parameterization is the rotor speed f , since it defines the centrifugal loads and to some extent the mean gas pressure. Note that for a detailed account of the latter, several CFD computations, optimally one for each considered rotor speed f , will be required. In the example case considered here, the contribution of the mean gas pressure to the mean stress field was so small compared to the contribution from the centrifugal loads that it was neglected, as already mentioned above. Consequently, the only source of the mean stress field in this analysis is the centrifugal force, resulting from the rotor's rotation.

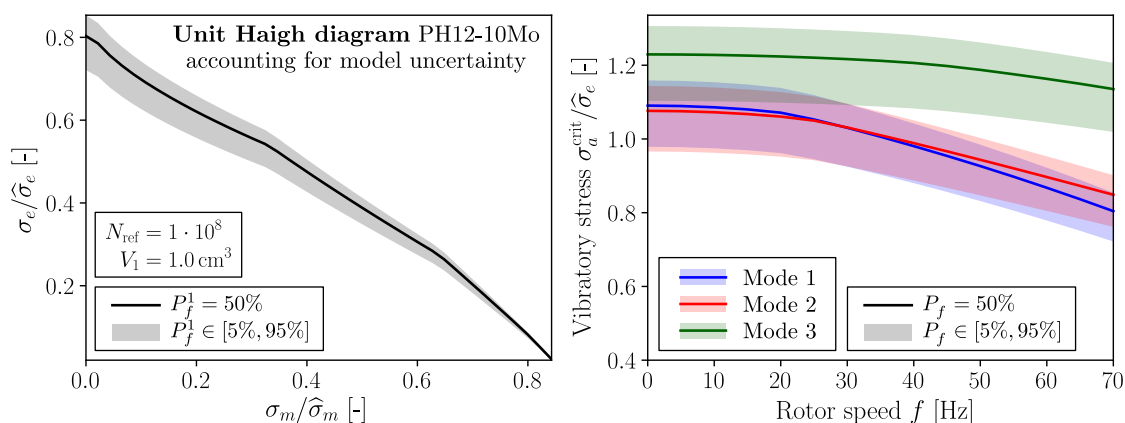


Figure 6.4: Model uncertainty adjusted unit Haigh diagram (bootstrapping) of PH12-10Mo, see Section 5.7, and the translation to the design Haigh diagrams for the three compressor blade modes shown in Fig. 6.3. Note that the mean stress axis is parameterized with the rotor speed.

In order to compute the design Haigh diagram for each considered mode, one needs to provide the unit Haigh diagram for the considered material. In this case, the model uncertainty adjusted (bootstrapping) unit Haigh diagram of PH12-10Mo, calculated by the methods described in Section 5.7 was used, see the left plot in Fig. 6.4. For the translation of this unit Haigh diagram to the design Haigh diagrams for each mode, the following procedure was applied. The relevant rotor speed range was defined for zero to 70 Hz, and discretized in 5 Hz steps. For each of the resulting speeds an own finite element simulation was conducted. Each single analysis contained two steps. At first the mean stress field was applied using the considered rotor speed. Afterwards, under the acting mean stress field, an eigenanalysis was performed, and the stress fields of the first three eigenmodes were extracted. Note that only the stress fields on the airfoil were extracted, since the vibratory part of the stress field on the disk were essentially zero. Finally, both mean stress and stress amplitude field were used to compute the 5%, 50% and 95% percentiles of the component fatigue strength using Eq. (5.11) with the full compressor blade volume as the integration domain. This equation was applicable since no plasticity occurred on the blade itself. An element-adaptive number of integration points was used – bringing the quadrature error close to zero – in combination with the fine mesh shown in Fig. 6.2. After repeating this analysis for each rotor speed, the design Haigh diagram is obtained by connecting the respective quantiles to quantile lines. The results for each of the three modes are shown in the right plot in Fig. 6.4.

Considering the obtained quantile lines, one finds that over the first half of the considered rotor speed range the second eigenmode is the most critical one, while in the second half the first eigenmode becomes more critical. However, the encountered differences are very small. The third mode on the other hand shows a considerably higher fatigue strength than the two other. Also, it seems to be rather unaffected by the acting mean stress fields. Note that $\sigma_{a,50\%}^{\text{crit}}/\hat{\sigma}_e > 1$ for all three modes at low rotor speeds because the highly stressed volume around the hot spots is smaller than $V_1 = 1 \text{ cm}^3$ which was used to calibrate $\hat{\sigma}_e$. Moreover, one has to note, that the mean stress effect for all three considered modes is small to moderate. The reason for this phenomenon is the small size of the considered blade in combination with the location of the peak stress being rather close to the blade tip – at least for mode two and three. The bigger the blade, and the closer the location of the peak stress regions to the blade fixture, the higher the

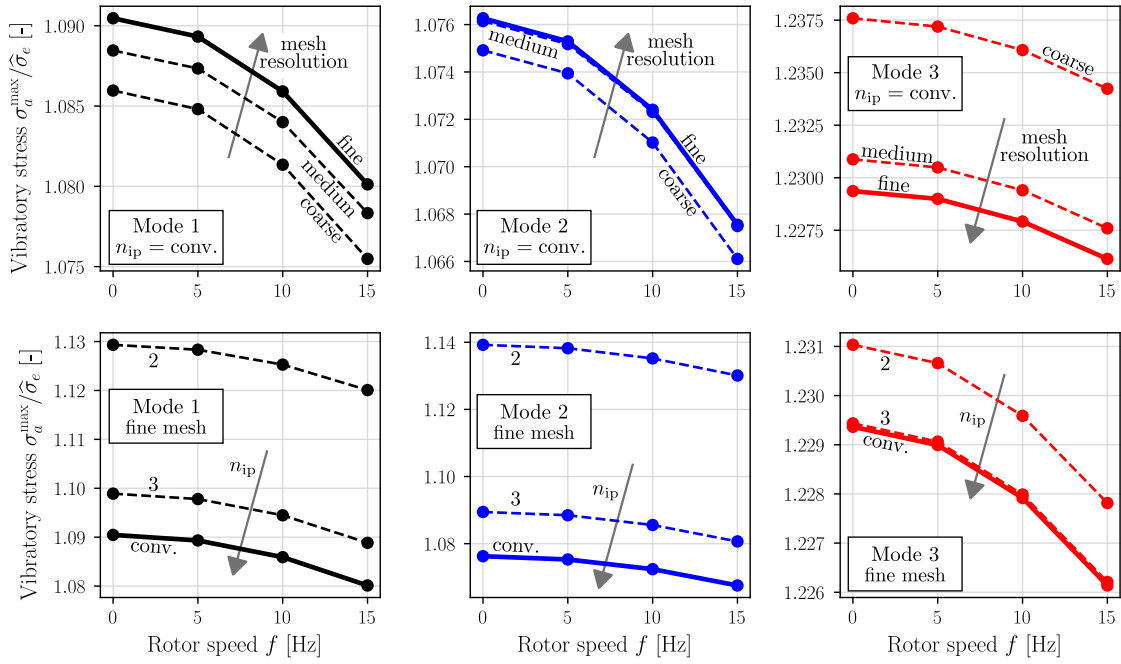


Figure 6.5: On the influence of the mesh resolution and the number of integration points on the median lines ($P_f = 50\%$) of the probabilistic Haigh diagram for each of the three modes.

mean stress effect. This trend may explain why the quantile lines of the first mode are showing a steeper slope in the higher mean stress range than the other two modes.

In order to get an impression on the role of the quadrature error and the mesh resolution on the results in this application case, the probabilistic Haigh diagrams discussed before were also computed using different mesh resolutions and different numbers of integration points respectively.

In a first analysis, the median lines of each mode for the three meshes shown in Fig. 6.2 were computed using the adaptive quadrature routine with respect to the number of integration points. This study exploits the influence of the mesh resolution when the quadrature error is close to zero. The results are shown in the upper row of Fig. 6.5. Note that only the rotor speed range up to 15 Hz is shown in order to visualize the small differences between the obtained graphs. One generally finds that the differences between the three median lines for each mode are very small, indicating a small influence of the finite element mesh when the quadrature error is small by using a sufficient number of integration points. Moreover, for the first two modes the error introduced by a coarse mesh is conservative – reducing the median fatigue strength. This is in line with the results presented in Section 5.3.3, since the vibratory load reference is the hot-spot stress. For the third mode on the other hand, the mesh error is non-conservative, as it leads to an increase of the median fatigue strength. This phenomenon is attributed to the fact that the hot-spot stress found in the stress field of the normalized third eigenmode is decreasing with a refinement of the mesh, while the inverse, more common trend – an increasing peak stress with an increased mesh resolution – is found for the first two eigenmodes.

In a second analysis, the influence of the number of integration points was studied considering the fine mesh. More specifically, two and three integration points per dimension (8 and 27 integration points per brick element) were compared against the adaptive

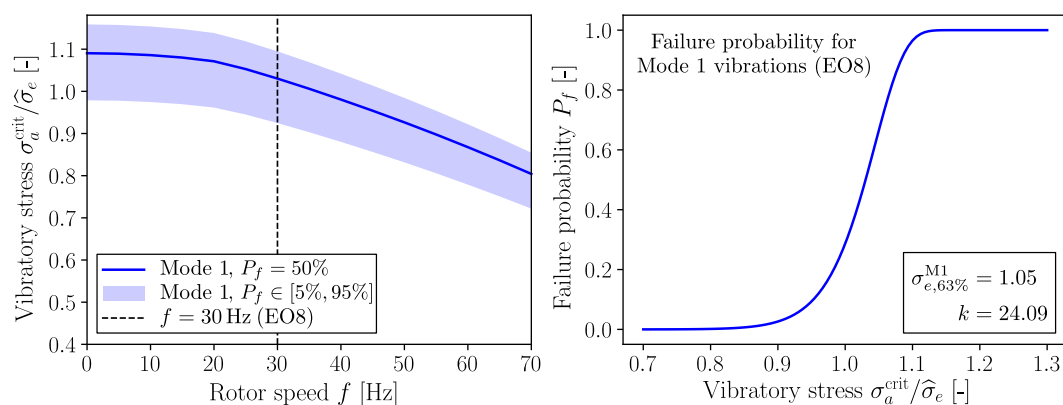


Figure 6.6: The failure probability of a single compressor blade for mode 1 vibrations, occurring at $f = 30$ Hz for engine order 8 (EO8). The cumulative distribution function shown in the right diagram is a Weibull distribution with the stated scale and shape. It corresponds to the distribution associated with the dashed black line from the left plot.

scheme, where the number of integration points for a given element is increased until the element integral converges. The results are presented in the second row of Fig. 6.5. In this case, one finds the same trend for each mode. The lower the number of used integration points per element, the greater the influence of the quadrature error on the computed failure probabilities. Note that this error is non-conservative, which is in line with the findings of Section 5.3.3. It should also be emphasized that the absolute error resulting from a low number of integration points is much greater than the one stemming from the finite element mesh in this case.

As it was already discussed in Section 2.1, it is typical for the compressor blade design procedure to associate the excitation of the critical eigenmodes with certain engine orders and operation conditions. In order to give an example which can serve as a starting point for the analysis given in the following Section 6.2, it should be assumed here, that mode 1 causes a vibration problem during the standard startup program when crossing a rotor speed around 30 Hz due to an EO8 excitation. Whether or not this is a realistic scenario depends mostly on the used vane numbers before and after the considered airfoil row, which might change during the design phase. Under the given conditions the excitation frequency is identical with the nominal eigenfrequency of the first mode from Fig. 6.3 at $f = 30$ Hz ($8 \cdot 30 \text{ Hz} = 240 \text{ Hz} = f_1$). As shown in Fig. 6.6 one can now use the design Haigh diagram of the first mode and look up the fatigue strength of the compressor blade with respect to this kind of loading at $f = 30$ Hz. The result is the Weibull distribution shown in the right plot of Fig. 6.6. Depending on the vibratory stresses, quantified by the respective value at the critical location σ_a^{crit} , one can now look up the corresponding failure probability for the single blade.

At this point one encounters a problem which is also relevant for the deterministic design approach. One has to provide an estimate for the expected stress amplitudes that occur during operation for the considered resonance event. This stress might be obtained from forced response simulation coupling the finite element model with a CFD model describing the conditions under which resonance occurs. However, these results are always computationally costly and often associated with large errors when compared against measured data. Another possibility is to use stress values based on experience. Independent from the method, once this value is defined, the single blade failure probability can be assessed by means of the distribution shown in the right plot of Fig. 6.6.

6.2 Probabilistic assessment of a compressor stage

The failure probability of a single compressor blade can only be an intermediate result of a corresponding probabilistic assessment. Since a compressor typically contains several stages which contain many compressor blade themselves, the natural follow up question is how to translate the failure probability of a single blade to the failure probability of a complete stage or the entire compressor. In this section the focus will be put on the failure probability for a single stage, sometimes also referred to as the stage risk.

The failure probability of a single compressor blade is determined by two major sources of stochastic variability. The dispersion of the component fatigue strength as it is expressed in the probabilistic design Haigh diagram on the one hand, and the scatter in the vibratory stress amplitude as a response to the resonance excitation on the other, see also Fig. 1.1. Since both sources influence the failure probability of a single blade, they also influence the stage risk. It is the purpose of this section to provide a methodology for computing the stage risk, taking into account both mentioned sources of variability.

As it was already explained in Section 2.1 one has to distinguish two types of scatter with respect to the blade resonance. First, the variability of the response of a single blade from one resonance event to another (event-to-event scatter), and secondly the scatter of the resonance response for a single resonance event between different blades (blade-to-blade scatter). While the event-to-event scatter is typically rather small, the blade-to-blade scatter is often much greater. Due to the small event-to-event scatter and the much greater blade-to-blade scatter one can interpret the resonance response of a single blade under specific operation conditions as characteristic for the considered blade with respect to these conditions. In the analysis conducted below, it will therefore be assumed that the resonance response of each blade $i \in \{1, \dots, N_s\}$, in terms of the resulting stress amplitude at the critical location $\sigma_{a,i}^{\text{crit}}$ of the considered mode, is drawn from an underlying distribution. In practice, this distribution will often be based on experience from previous measurement campaigns on comparable machine types. In the example shown here, a normal distribution $\mathcal{N}(\mu, \text{sd})$ will be assumed, since its two parameters, the mean value μ and the standard deviation sd , are easy to interpret. In formal terms, this may be expressed via

$$\sigma_{a,i}^{\text{crit}} \sim \mathcal{N}(\mu, \text{sd}). \quad (6.1)$$

Adapting the results of Section 6.1, it will be assumed that the considered event is resonance of the first mode at $f = 30$ Hz. According to the results shown in Fig. 6.6 this means that the survival probability of a single blade i , given $\sigma_{a,i}^{\text{crit}}$ can be computed via

$$P_{s,i}^{\text{blade}} = \exp \left\{ - \left(\frac{\sigma_{a,i}^{\text{crit}}}{\sigma_{e,63\%}^{\text{M1}}} \right)^k \right\} \quad (6.2)$$

with $\sigma_{e,63\%}^{\text{M1}} = 1.05$ and $k = 24.09$. The considered stage contains $N_b = 48$ airfoils, and it is assumed that the resonance response $\sigma_{a,i}^{\text{crit}}$ of each blade is independent from all other blades. With respect to the failure probability for the entire stage one therefore obtains

$$P_s^{\text{stage}} = \prod_{i=1}^{N_b} P_{s,i}^{\text{blade}} = \prod_{i=1}^{N_b} \exp \left\{ - \left(\frac{\sigma_{a,i}^{\text{crit}}}{\sigma_{e,63\%}^{\text{M1}}} \right)^k \right\} = \exp \left\{ - \sum_{i=1}^{N_b} \left(\frac{\sigma_{a,i}^{\text{crit}}}{\sigma_{e,63\%}^{\text{M1}}} \right)^k \right\}. \quad (6.3)$$

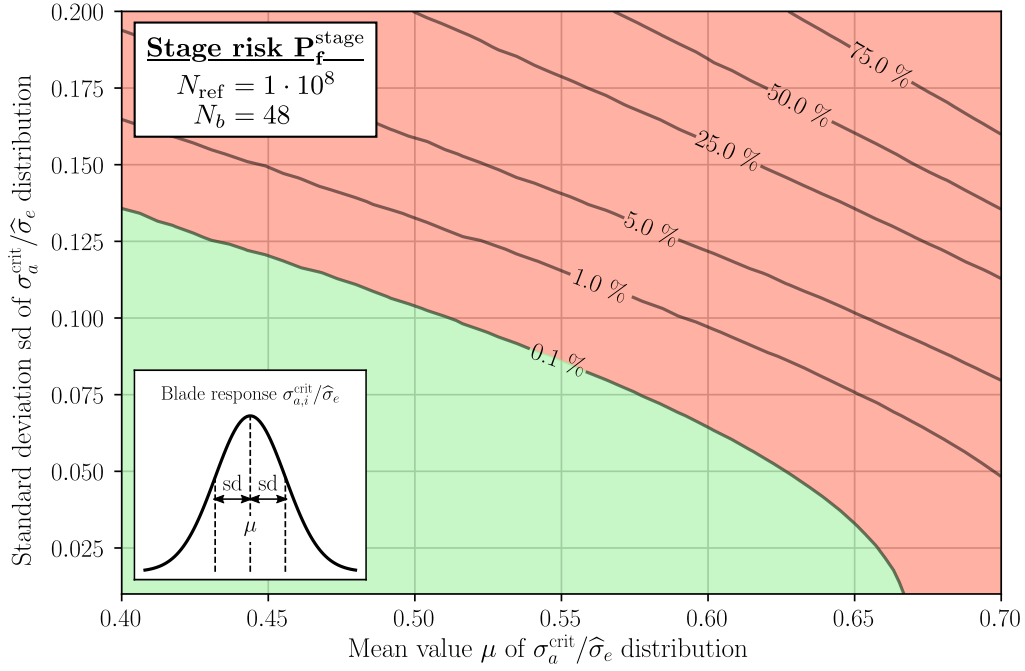


Figure 6.7: Probability of failure for a compressor row with $N_b = 48$ blades as a function of the resonance response distribution of the blades. In this plot it was assumed that $P_f = 0.1\%$ was the accepted stage risk.

In this definition, the stage reliability P_s^{stage} is a random variable itself, as it depends on the realizations of the individual blade responses. Unfortunately, it is not possible to state the corresponding distribution in analytical terms for arbitrary k . However, most relevant for the designer is the expected stage risk, which is the expected value of the distribution associated with $P_f^{\text{stage}} = 1 - P_s^{\text{stage}}$ for given μ and sd . In order to approximate this value, a simple Monte Carlo approach was utilized. With given μ and sd , in each run, the resonance response of the $N_b = 48$ blades are drawn from Expression (6.1). They are then used to evaluate the stage risk using Eq. (6.3). Repeating this procedure for N_s times results in N_s samples of P_f^{stage} , allowing to compute its mean value.

The results of such an analysis for the specific case considered here and a range of combinations of μ and sd are presented in Fig. 6.7. The shown intervals of μ and sd have been discretized using 50 steps on each axis. For every resulting combination a Monte Carlo simulation with $N_s = 5 \cdot 10^4$ samples was run. The results are shown in the format of a contour plot, where it was assumed that an expected stage risk of 0.1% was the maximum accepted risk. The domain in the $\mu - sd$ space where the expected stage risk is lower than 0.1% is colored in green, while the remaining domain, with a greater expected stage risk is colored in red.

In a design context, such a diagram can be used to quickly judge the stage risk of a current compressor design based on experience, expert knowledge or simulation results on the distribution of the resonance response. It additionally allows an estimation of the stage risk sensitivities with respect to the distribution parameters μ and sd . Last but not least, it can also be used during test campaigns in order to assess encountered vibration phenomena. In this application, the design is already realized and the blade response distribution can actually be measured.

7 Summary and conclusion

Motivated by the discrepancy of the inherent statistical properties of high cycle metal fatigue phenomena experienced by respectively loaded engineering components on the one hand, and the persistent hesitation of incorporating probabilistic methods into the industrial design process of such components on the other, a stochastic model has been developed in this work, aiming to contribute to filling this gap.

In order to achieve this goal, two major requirements have been emphasized during the model development. First, while providing a probabilistic framework, accounting for the statistical nature of the problem, the model was supposed to be conceptually related to current design procedures based on deterministic constant-life diagrams. This condition was aiming to allow for an easier transition from the established design practice to the proposed probabilistic one. The second prerequisite was the easy calibratability of the developed model in terms of required test data. Since novel design methods which necessitate expensive testing efforts before becoming applicable are less likely to be picked up in the first place, this second condition was aiming to avoid such a hurdle.

The model developed in this work satisfies both requirements. It was set up as a probabilistic constant-life diagram, which can be handled in a similar fashion as a conventional deterministic diagram. The only difference is that it no longer reflects a binary design boundary in terms of acceptable/unacceptable stress conditions, but instead expresses a continuous field of failure probabilities in the design plane. The model is described by four parameters which can be calibrated with conventional constant-amplitude fatigue test data. In contrast to other approaches which require calibration with test results that have been determined by following a certain systematic test scheme, like staircase or probit tests, the proposed model in this work can be calibrated with unsystematically obtained test results. This is particularly advantageous if the available test database for a considered material contains results from several unrelated test campaigns.

The probabilistic foundation of the proposed model is the weakest-link concept, which considers the volume of a loaded structure as an interconnected partition of smaller increments. In analogy with a loaded chain, failure is assumed as soon as at least one of these volume increments fails. The evaluation of the corresponding failure probability requires the numerical approximation of a volume integral based on stress solutions typically provided by finite element analyses. Since both quadrature errors, as well as inadequate finite element meshes translate into deviations in terms of the computed failure probability, the first part of the conducted analyses focused on the corresponding numerical properties of the proposed model. More specifically, it was investigated how the number of used integration points per element as well as the finite element mesh resolution related to the computed failure probability. It was found the most significant influence is exerted by the mesh resolution. Grids that are too coarse, especially in combination with pronounced stress concentrations, increase the required number of integration points, and lead in many cases – even with a sufficient number of integration points – to an underestimation of the failure probability. Additionally it was found, that the presence of elevated mean stresses as well as high values of the fatigue strength scatter parameter amplify the problem. For an application in a design context, it was recommended to always check the sensitivity of the computed failure probability with respect to the mesh resolution, as well as to use an adaptive quadrature scheme, which ensures a sufficient number of integration points per element.

After having studied its numerical properties, the proposed model was fitted to constant-amplitude fatigue test results. The data set of the first validation study was taken from several technical reports published by NACA in the 1950s and covered tests on three differently notched sheet specimen types made from steel and two types of aluminum alloys. Focus was put on predominantly elastic material behavior, excluding most tests on specimens where the nominal test stresses lead to macroscopic plasticity in the notch root. Some exceptions were made in order to prevent a too drastic reduction of the available test data and explore the scope-boundaries of the proposed model. The four model parameters were calibrated for each material using the corresponding test data from two out of the three specimen types. The resulting model fit was then used to predict the failure behavior of the test data with respect to the remaining specimen type that was not included in the calibration process. Each one of these three predictions was in good agreement with the respective test data. However, the produced results led to two major questions that immediately followed from the findings of this initial validation study. The first question referred to the data selection in order to calibrate the model. For each material, a different combination of two out of the three specimen types in terms of the considered test data for fitting the model was used. When test data exclusively from one specimen type was used for fitting, the failure predictions for the two remaining geometries were typically worse. Also, it was unclear which specimen type combination was most beneficial for fitting the model. The second question arose when comparing the obtained model fits, which were based on data sets, that contained a few test results associated with the occurrence of notch root plasticity, with corresponding fits where these test points had been removed. The parameters changed, indicating a need for treating stress fields associated with notch root plasticity in a different fashion than stress fields that remained completely in the elastic regime.

The following study was aiming to answer the first of the two aforementioned questions. Which test data should be used for fitting the model? This question was addressed from a practical point of view, assuming of having to specify a test program with a fixed total number of tests aiming to calibrate the four model parameter for a new material. In an extensive simulation study, different staircase based test programs have been analyzed. They differed in terms of the tested specimen types, the considered mean stresses, as well as step size and initial stresses. The most significant finding was that test programs that contained more than one specimen type resulted in considerably better fits in terms of the parameter confidence intervals, than test programs that contained tests on exclusively one specimen type. The most favorable mix was identified as the half-and-half combination of tests on a smooth and a notched specimen type in one test program. With respect to the data selection for fitting the model, these findings suggest to always use at least two specimen geometries for the model calibration including a smooth and a notched type. Model fitting based on test data on exclusively one test specimen geometry should be avoided since such fits correspond to higher model uncertainties.

The second question that resulted from the first validation study referred to the treatment of partially elasto-plastic material behavior in the considered model framework. Situations where this phenomenon might be encountered in the context of high-cycle fatigue are always associated with both stress concentrations and rather high mean stresses. In order to describe the failure probability for components under such loading conditions, it was attempted to use the weakest-link volume integral in combination with stress field data as it resulted from non-linear elasto-plastic finite element sim-

ulations. The required definition of plasticity was based on quasi-static stress-strain curves. With this setup, a second validation study with respect to the proposed model was conducted. The test database was again based on technical reports from NACA covering eight different types of notched sheet specimens. Using the same methodology as in the first validation study, the model parameters were fitted using a combination of test data from smooth and one type of notched specimens. The resulting calibrated model was then used to predict the failure behavior of the remaining specimen types. The obtained results showed again mostly satisfactory agreement with the respective test data, especially for those specimen types with mild notches.

In the last general analysis presented in this work, the focus was put on the statistical model uncertainty with respect to the test data that was used for its calibration. This subject is particularly relevant for the practical use of the model, in terms of preventing non-conservative parameter estimations due to random test data artifacts. Based on a data set for a high strength steel taken from the Siemens material test database, both of the investigated approaches, parametric bootstrapping and Markov chain Monte Carlo (MCMC) sampling, revealed the same shortcomings of the data set in terms of calibrating the proposed model. However, considering practical applications, it is recommended to use the bootstrapping approach, despite the higher computational costs. Next to providing more conservative adjustments, it is simple to use, as it does not require additional process parameters like MCMC, and the results are easy to interpret.

After the model had been analyzed and validated, its applicability in a design context was demonstrated for the example of a compressor blade in a gas turbine compressor. Based on a corresponding finite element model, a probabilistic design Haigh diagram was derived for the first three eigenmodes of the considered blade where the mean stress influence was parameterized with the rotor speed. This diagram, which essentially depicts the failure probability for a single blade when resonating at a specific rotor speed can be directly used for component design. In a second step it was shown how the failure assessment of a single blade can be extended to the entire compressor stage, by combining the single-blade fatigue strength distribution with a simple Monte Carlo analysis.

Several topics have not been covered in this work, and remain to be addressed in future research efforts. First and foremost should the model be applied to other materials and especially to different load cases (other than tension-compression), in order to further explore its scope. Emphasized focus should be put on the used mean stress model and the degree of multiaxiality. In this context, it might be worthwhile to compare the proposed probabilistic model with the deterministic approach of Susmel [76, 185, 186, 198], which uses a mean stress parameter that accounts for multiaxiality and non-proportional loads. Moreover it should be pointed out, that all test results which have been used throughout this work, were derived at room temperature. The influence of the material's temperature on the resulting model parameters has not been studied. A corresponding model, describing this temperature influence on the fatigue strength, would be interesting for several applications, like the high-cycle fatigue design of turbine blades. A related field of yet unaddressed issues are creep effects, that might occur at combinations of elevated temperatures and high mean stresses.

8 References

- [1] Schütz, W. A history of fatigue. *Engineering Fracture Mechanics*, 54(2):263–300, 1996.
- [2] Albert, W. A. J. Über Treibseile am Harz. *Archiv für Mineralogie, Geognosie. Bergbau und Hüttenkunde*, 10:215, 1837.
- [3] Braithwaite, F. On the fatigue and consequent fracture of metals. In *Minutes of the Proceedings of the Institution of Civil Engineers*, volume 13, pages 463–467. Thomas Telford-ICE Virtual Library, 1854.
- [4] Stopfl, P. Achsenbrüche an Lokomotiven, Tender und Wagen, ihre Erklärung und Beseitigung. *Org. Eisenbahnw.*, 3:55–67, 1848.
- [5] McConnell, J. On the deterioration of railway axles. *Proc. Inst. Mech. Engrs*, pages 5–19, 1850.
- [6] Smith, R. The Versailles railway accident of 1842 and the first research into metal fatigue (retroactive coverage). *Fatigue 90*, pages 2033–2041, 1990.
- [7] Zenner, H. and Hinkelmann, K. August Wöhler—founder of fatigue strength research: On the 200th anniversary of August Wöhler’s birth. *Steel Construction*, 12(2):156–162, 2019.
- [8] Wöhler, A. Versuche zur Ermittlung der auf die Eisenbahnwagenachsen einwirkenden Kräfte und die Widerstandsfähigkeit der Wagen-Achsen. *Zeitschrift für Bauwesen*, 10(1860):583–614, 1860.
- [9] Wöhler, A. Über Versuche zur Ermittlung der Festigkeit von Achsen, welche in den Werkstätten der Niederschlesisch-Märkischen Eisenbahn zu Frankfurt, angestellt sind. *Zeitschrift für Bauwesen*, pages 233–258, 1863.
- [10] Wöhler, A. Resultate der in der Central-Werkstatt der Niederschlesisch-Märkischen Eisenbahn zu Frankfurt a.d.O. angestellten Versuche für die relative Festigkeit von Eisen, Stahl und Kupfer. *Zeitschrift für Bauwesen*, pages 67–84, 1866.
- [11] Wöhler, A. *Über die Festigkeitsversuche mit Eisen und Stahl*. Ernst & Korn, 1870.
- [12] Manson, S. S. *Behavior of materials under conditions of thermal stress*, volume 2933. National Advisory Committee for Aeronautics, 1953.
- [13] Coffin, L. The problem of thermal stress fatigue in austenitic steels at elevated temperatures. In *Symposium on Effect of Cyclic Heating and Stressing on Metals at Elevated Temperatures*. ASTM International, 1954.
- [14] Schijve, J. *Fatigue of structures and materials*. Springer Science & Business Media, 2009.
- [15] Schmitz, S., Seibel, T., Beck, T., Rollmann, G., Krause, R., and Gottschalk, H. A probabilistic model for LCF. *Computational Materials Science*, 79:584–590, 2013.

-
- [16] Mäde, L., Schmitz, S., Gottschalk, H., and Beck, T. Combined notch and size effect modeling in a local probabilistic approach for LCF. *Computational Materials Science*, 142:377–388, 2018.
- [17] Azeez, A., Eriksson, R., Calmunger, M., Lindström, S. B., and Simonsson, K. Low cycle fatigue modelling of a steam turbine rotor steel. *Procedia Structural Integrity*, 23:149–154, 2019.
- [18] Borodii, M. and Adamchuk, M. Life assessment for metallic materials with the use of the strain criterion for low-cycle fatigue. *International Journal of Fatigue*, 31(10):1579–1587, 2009.
- [19] Nagata, N., Sato, S., and Katada, Y. Low cycle fatigue behavior of pressure vessel steels in high temperature pressurized water. *ISIJ International*, 31(1):106–114, 1991.
- [20] Papadopoulos, I. V. Long life fatigue under multiaxial loading. *International Journal of Fatigue*, 23(10):839–849, 2001.
- [21] Pyttel, B., Schwerdt, D., and Berger, C. Very high cycle fatigue – Is there a fatigue limit? *International Journal of Fatigue*, 33(1):49–58, 2011.
- [22] Mughrabi, H. On ‘multi-stage’ fatigue life diagrams and the relevant life-controlling mechanisms in ultrahigh-cycle fatigue. *Fatigue & Fracture of Engineering Materials & Structures*, 25(8-9):755–764, 2002.
- [23] Mughrabi, H. Specific features and mechanisms of fatigue in the ultrahigh-cycle regime. *International Journal of Fatigue*, 28(11):1501–1508, 2006.
- [24] Sendecyk, G. Constant life diagrams – a historical review. *International Journal of Fatigue*, 23(4):347–353, 2001.
- [25] Hanaki, S., Yamashita, M., Uchida, H., and Zako, M. On stochastic evaluation of S–N data based on fatigue strength distribution. *International Journal of Fatigue*, 32(3):605–609, 2010.
- [26] Bretl, N., Schurer, S., Tobie, T., Stahl, K., and Höhn, B.-R. Investigations on tooth root bending strength of case hardened gears in the range of high cycle fatigue. In *American Gear Manufacturers Association Fall Technical Meeting*, pages 103–118, 2013.
- [27] Liu, H., Liu, H., Zhu, C., and Tang, J. Study on gear contact fatigue failure competition mechanism considering tooth wear evolution. *Tribology International*, 147(106277), 2020.
- [28] Liu, Y., Stratman, B., and Mahadevan, S. Fatigue crack initiation life prediction of railroad wheels. *International Journal of Fatigue*, 28(7):747–756, 2006.
- [29] Roux, C., Lorang, X., Maitournam, H., and Nguyen-Tajan, M. Fatigue design of railway wheels: a probabilistic approach. *Fatigue & Fracture of Engineering Materials & Structures*, 37(10):1136–1145, 2014.

-
- [30] Leitner, M., Tuncali, Z., Steiner, R., and Grün, F. Multiaxial fatigue strength assessment of electroslag remelted 50CrMo4 steel crankshafts. *International Journal of Fatigue*, 100:159–175, 2017.
- [31] Nadot, Y. and Denier, V. Fatigue failure of suspension arm: experimental analysis and multiaxial criterion. *Engineering Failure Analysis*, 11(4):485–499, 2004.
- [32] Poursaeidi, E., Babaei, A., Behrouzshad, F., and Arhani, M. M. Failure analysis of an axial compressor first row rotating blades. *Engineering Failure Analysis*, 28:25–33, 2013.
- [33] Sandberg, D., Mansour, R., and Olsson, M. Fatigue probability assessment including aleatory and epistemic uncertainty with application to gas turbine compressor blades. *International Journal of Fatigue*, 95:132–142, 2017.
- [34] Sandberg, D., Sadek, S., Hagström, G., and Olsson, M. Fast multiaxial high cycle fatigue evaluation in the probabilistic fatigue post-processor AROMA-PF. In *ISABE-2015-20128*, 2015.
- [35] Heinze, K., Vogeler, K., and Friedl, W.-H. The impact of geometric scatter on high-cycle-fatigue of compressor blades. In *Turbo Expo: Power for Land, Sea, and Air*, volume 44014, pages 591–599, 2010.
- [36] Qvale, P. and Härkegård, G. A simplified method for weakest-link fatigue assessment based on finite element analysis. *International Journal of Fatigue*, 100:78–83, 2017.
- [37] Doorn, N. and Hansson, S. O. Should probabilistic design replace safety factors? *Philosophy & Technology*, 24(2):151–168, 2011.
- [38] Pascual, F. G. and Meeker, W. Q. Estimating fatigue curves with the random fatigue-limit model. *Technometrics*, 41(4):277–289, 1999.
- [39] Herman Shen, M.-H. and Nicholas, T. Reliability high cycle fatigue design of gas turbine blading system using probabilistic Goodman diagram. In *Key Engineering Materials*, volume 200, pages 139–162. Trans Tech Publ, 2001.
- [40] Wormsen, A. *A Fatigue Assessment Methodology for Notched Components Containing Defects*. PhD thesis, KTH, 2007.
- [41] Sadek, S. and Olsson, M. A probabilistic method for multiaxial HCF based on highly loaded regions below the threshold depth. *International Journal of Fatigue*, 87:91–101, 2016.
- [42] Sandberg, D. *Experiments, Computations and Models for Probabilistic HCF Design*. PhD thesis, KTH Royal Institute of Technology, 2016.
- [43] Dixon, W. J. and Mood, A. M. A method for obtaining and analyzing sensitivity data. *Journal of the American Statistical Association*, 43(241):109–126, 1948.
- [44] Boyce, M. P. *Gas turbine engineering handbook*. Elsevier, 2011.
- [45] Lechner, C. and Seume, J. *Stationäre Gasturbinen*. Springer-Verlag, 2018.

-
- [46] Williams, J. C. and Starke Jr, E. A. Progress in structural materials for aerospace systems. *Acta Materialia*, 51(19):5775–5799, 2003.
- [47] Breeze, P. *Gas-Turbine power generation*. Academic Press, 2016.
- [48] Nalla, R., Ritchie, R., Boyce, B., Campbell, J., and Peters, J. Influence of microstructure on high-cycle fatigue of Ti-6Al-4V: Bimodal vs. lamellar structures. *Metallurgical and Materials Transactions A*, 33(3):899–918, 2002.
- [49] Image of SGT-800. <https://new.siemens.com/global/en/products/energy/power-generation/gas-turbines/sgt-800.html>. Accessed: 2020-07-08.
- [50] Campbell, W. Protection of steam turbine disk wheels from axial vibration. In *Proceedings of the ASME Conference*, 1924.
- [51] Irgens, F. *Continuum mechanics*. Springer Science & Business Media, 2008.
- [52] Walker, K. *The effect of stress ratio during crack propagation and fatigue for 2024-T3 and 7075-T6 aluminum*. ASTM International, 1970.
- [53] Nicholas, T. *High cycle fatigue: a mechanics of materials perspective*. Elsevier, 2006.
- [54] Shiozawa, K., Morii, Y., Nishino, S., and Lu, L. Subsurface crack initiation and propagation mechanism in high-strength steel in a very high cycle fatigue regime. *International Journal of Fatigue*, 28(11):1521–1532, 2006.
- [55] Duan, Z., Shi, H., and Ma, X. Fish-eye shape prediction with gigacycle fatigue failure. *Fatigue & Fracture of Engineering Materials & Structures*, 34(10):832–837, 2011.
- [56] Ritz, F. and Beck, T. Influence of mean stress and notches on the very high cycle fatigue behaviour and crack initiation of a low-pressure steam turbine steel. *Fatigue & Fracture of Engineering Materials & Structures*, 40(11):1762–1771, 2017.
- [57] Bathias, C. There is no infinite fatigue life in metallic materials. *Fatigue & Fracture of Engineering Materials & Structures*, 22(7):559–565, 1999.
- [58] Radaj, D. and Vormwald, M. *Ermüdungsfestigkeit*. Springer, 2007.
- [59] FKM (Forschungskuratorium Maschinenbau). *Analytical Strength Assessment of Components*. VDMA, 6th revised edition edition, 2012.
- [60] Hertel, O. and Vormwald, M. Statistical and geometrical size effects in notched members based on weakest-link and short-crack modelling. *Engineering Fracture Mechanics*, 95:72–83, 2012.
- [61] Leitner, M., Vormwald, M., and Remes, H. Statistical size effect on multiaxial fatigue strength of notched steel components. *International Journal of Fatigue*, 104:322–333, 2017.
- [62] Papadopoulos, I. V. and Panoskaltsis, V. P. Invariant formulation of a gradient dependent multiaxial high-cycle fatigue criterion. *Engineering Fracture Mechanics*, 55(4):513–528, 1996.

-
- [63] Nicholas, T. Critical issues in high cycle fatigue. *International Journal of Fatigue*, 21:221–231, 1999.
- [64] Barat, K., Sivaprasad, S., Kar, S. K., and Tarafder, S. Low-cycle fatigue of IN718: Effect of waveform. *Fatigue & Fracture of Engineering Materials & Structures*, 42(12):2823–2843, 2019.
- [65] Morrissey, R., McDowell, D., and Nicholas, T. Frequency and stress ratio effects in high cycle fatigue of Ti-6Al-4V. *International Journal of Fatigue*, 21(7):679–685, 1999.
- [66] Beck, T., Kovacs, S. A., and Ritz, F. VHCF behavior and work hardening of a ferritic-martensitic steel at high mean stresses. In *Key Engineering Materials*, volume 664, pages 246–254. Trans Tech Publ, 2016.
- [67] Mall, S., Nicholas, T., and Park, T.-W. Effect of predamage from low cycle fatigue on high cycle fatigue strength of Ti-6Al-4V. *International journal of Fatigue*, 25(9-11):1109–1116, 2003.
- [68] Lanning, D., Haritos, G., Nicholas, T., and Maxwell, D. Low-cycle fatigue/high-cycle fatigue interactions in notched Ti-6Al-4V. *Fatigue & Fracture of Engineering Materials & Structures*, 24(9):565–577, 2001.
- [69] Petrucci, G. and Zuccarello, B. Fatigue life prediction under wide band random loading. *Fatigue & Fracture of Engineering Materials & Structures*, 27(12):1183–1195, 2004.
- [70] Wei, H., Carrion, P., Chen, J., Imanian, A., Shamsaei, N., Iyyer, N., and Liu, Y. Multiaxial high-cycle fatigue life prediction under random spectrum loadings. *International Journal of Fatigue*, 134:105462, 2020.
- [71] Vayssette, B., Saintier, N., Brugger, C., Elmay, M., and Pessard, E. Surface roughness of Ti-6Al-4V parts obtained by SLM and EBM: Effect on the High Cycle Fatigue life. *Procedia engineering*, 213:89–97, 2018.
- [72] Nicholas, T. and Zuiker, J. On the use of the Goodman diagram for high cycle fatigue design. *International Journal of Fracture*, 80(2-3):219–235, 1996.
- [73] Basquin, O. The exponential law of endurance tests. In *Proc Am Soc Test Mater*, volume 10, pages 625–630, 1910.
- [74] Dezecot, S. and Brochu, M. Microstructural characterization and high cycle fatigue behavior of investment cast A357 aluminum alloy. *International Journal of Fatigue*, 77:154–159, 2015.
- [75] Haigh, B. Experiments on the fatigue of brasses. *Journal of the Institute of Metals*, 18:55–86, 1917.
- [76] Susmel, L., Tovo, R., and Lazzarin, P. The mean stress effect on the high-cycle fatigue strength from a multiaxial fatigue point of view. *International Journal of Fatigue*, 27(8):928–943, 2005.

-
- [77] Goodman, J. *Mechanics applied to engineering*. Longmans, Green and Co., 1 edition, 1899.
- [78] Soderberg, C. R. Factor of safety and working stress. *Trans Am Soc Mech Eng*, 52:13–28, 1939.
- [79] Gerber, H. *Bestimmung der zulässigen Spannungen in Eisen-Constructionen*, volume 6. Z Bayer Archit Ing Ver, 1874.
- [80] Marsh, K. J. *Full-scale fatigue testing of components and structures*. Butterworth-Heinemann, 2013.
- [81] McGuigan Jr, M., Bryan, D., and Whaley, R. Fatigue investigation of full-scale transport-airplane wings: Summary of constant-amplitude tests through 1953. *NACA Technical Note 3190*, 1954.
- [82] Lee, H. G. and Park, J. Static test until structural collapse after fatigue testing of a full-scale wind turbine blade. *Composite Structures*, 136:251–257, 2016.
- [83] Morgan, J. M. and Milligan, W. W. A 1 kHz servohydraulic fatigue testing system. *High cycle fatigue of structural materials*. Warrendale, PA: TMS, pages 305–12, 1997.
- [84] George, T. J., Seidt, J., Shen, M.-H. H., Nicholas, T., and Cross, C. J. Development of a novel vibration-based fatigue testing methodology. *International Journal of Fatigue*, 26(5):477–486, 2004.
- [85] Marines, I., Dominguez, G., Baudry, G., Vittori, J.-F., Rathery, S., Doucet, J.-P., and Bathias, C. Ultrasonic fatigue tests on bearing steel AISI-SAE 52100 at frequency of 20 and 30 kHz. *International Journal of Fatigue*, 25(9-11):1037–1046, 2003.
- [86] Bellows, R. S., Muju, S., and Nicholas, T. Validation of the step test method for generating Haigh diagrams for Ti-6Al-4V. *International Journal of Fatigue*, 21(7):687–697, 1999.
- [87] Prot, M. Un nouveau type de machine d’essai des metaux a la fatigue par flexion rotative. *Revue de Métallurgie*, 34(7):440–442, 1937.
- [88] Maxwell, D. C. and Nicholas, T. A rapid method for generation of a Haigh diagram for high cycle fatigue. In *Fatigue and Fracture Mechanics: 29th Volume*. ASTM International, 1999.
- [89] Starke, P., Walther, F., and Eifler, D. “PHYBAL” a Short-Time Procedure for a Reliable Fatigue Life Calculation. *Advanced Engineering Materials*, 12(4):276–282, 2010.
- [90] Finney, D. The application of the probit method to toxicity test data adjusted for mortality in the controls. *Annals of Applied Biology*, 31(1):68–74, 1944.
- [91] Murty, A., Gupta, U., and Radha, A. A new approach to fatigue strength distribution for fatigue reliability evaluation. *International Journal of Fatigue*, 17(2):85–89, 1995.

-
- [92] Wormsen, A., Sjödin, B., Härkegård, G., and Fjeldstad, A. Non-local stress approach for fatigue assessment based on weakest-link theory and statistics of extremes. *Fatigue & Fracture of Engineering Materials & Structures*, 30(12):1214–1227, 2007.
- [93] Finney, D. J. Probit analysis, cambridge university press. *Cambridge, UK*, 1947.
- [94] Dorff, D. *Vergleich verschiedener statistischer Transformationsverfahren auf ihre Anwendbarkeit zur Ermittlung der Dauerschwingfestigkeit*. PhD thesis, TU Berlin, 1961.
- [95] Mauch, H. and Zenner, H. Statistische Methoden zur Beurteilung von Bauteillebensdauer und Zuverlässigkeit und ihre beispielhafte Anwendung auf Zahnräder, 1999.
- [96] Sandberg, D. and Olsson, M. An investigation of the prediction accuracy for volume based HCF models using scaled geometries and scaled loading. *International Journal of Fatigue*, 82:317–324, 2016.
- [97] Little, R. E. *Manual on statistical planning and analysis for fatigue experiments*. ASTM International, 1975.
- [98] Braam, J. and Van der Zwaag, S. A statistical evaluation of the staircase and the $\text{ArcSin}\sqrt{P}$ methods for determining the fatigue limit. *Journal of testing and evaluation*, 26(2):125–131, 1998.
- [99] Brownlee, K., Hodges Jr, J., and Rosenblatt, M. The up-and-down method with small samples. *Journal of the American Statistical Association*, 48(262):262–277, 1953.
- [100] Little, R. E. and Jebe, E. H. *Statistical design of fatigue experiments*. Applied Science Publishers, 1975.
- [101] Oron, A. P. *Up-and-down and the percentile-finding problem*. PhD thesis, University of Washington, 2007.
- [102] Müller-Gronbach, T., Novak, E., and Ritter, K. *Monte Carlo-Algorithmen*. Springer-Verlag, 2012.
- [103] Little, R. Estimating the median fatigue limit for very small up-and-down quantal response tests and for SN data with runouts. In *Probabilistic aspects of fatigue*. ASTM International, 1972.
- [104] Dixon, W. The up-and-down method for small samples. *Journal of the American Statistical Association*, 60(312):967–978, 1965.
- [105] Pollak, R. D. *Analysis of methods for determining high cycle fatigue strength of a material with investigation of titanium-aluminum-vanadium gigacycle fatigue behavior*. PhD thesis, Air Force Institute of Technology, 2005.
- [106] Müller, C., Wächter, M., Masendorf, R., and Esderts, A. Accuracy of fatigue limits estimated by the staircase method using different evaluation techniques. *International Journal of Fatigue*, 100:296–307, 2017.

-
- [107] Svensson, T., Loren, S., de Mare, J., and Wadman, B. Statistical models of the fatigue limit. *Project Paper, SP Sveriges Tekniska Forskningsinstitut*, 2000.
- [108] Fang, Q., Zhang, S. S., Zhao, M., and Liu, Y. A new method to deal with the staircase fatigue test. In *Key Engineering Materials*, volume 183, pages 951–956. Trans Tech Publ, 2000.
- [109] Rabb, B. R. Staircase testing-confidence and reliability. *WIT Transactions on Engineering Sciences*, 40, 2003.
- [110] Pollak, R., Palazotto, A., and Nicholas, T. A simulation-based investigation of the staircase method for fatigue strength testing. *Mechanics of Materials*, 38(12):1170–1181, 2006.
- [111] Wallin, K. R. Statistical uncertainty in the fatigue threshold staircase test method. *International Journal of Fatigue*, 33(3):354–362, 2011.
- [112] Deubelbeiss, E. Dauerfestigkeitsversuche mit einem modifizierten Treppenstufenverfahren. *Materialprüfung*, 16(8):240–244, 1974.
- [113] Hück, M. Ein verbessertes Verfahren für die Auswertung von Treppenstufenversuchen. *Materialwissenschaft und Werkstofftechnik*, 14(12):406–417, 1983.
- [114] Siddall, J. N. *Probabilistic engineering design*. CRC Press, 1983.
- [115] Aven, T. Perspectives on risk in a decision-making context—review and discussion. *Safety science*, 47(6):798–806, 2009.
- [116] Commission, U. N. R. *Reactor safety study: An assessment of accident risks in US commercial nuclear power plants*, volume 88. 1975.
- [117] Smith, N. and Mahadevan, S. Probabilistic methods for aerospace system conceptual design. *Journal of spacecraft and rockets*, 40(3):411–418, 2003.
- [118] D’Ovidio, A. and Pagano, M. Probabilistic multicriteria analyses for optimal biomass power plant design. *Electric power systems research*, 79(4):645–652, 2009.
- [119] McGuire, R. K. Deterministic vs. probabilistic earthquake hazards and risks. *Soil Dynamics and Earthquake Engineering*, 21(5):377–384, 2001.
- [120] Papazoglou, I. A., Nivolianitou, Z., Aneziris, O., and Christou, M. Probabilistic safety analysis in chemical installations. *Journal of Loss Prevention in the Process Industries*, 5(3):181–191, 1992.
- [121] Caruso, M. A., Cheok, M. C., Cunningham, M. A., Holahan, G. M., King, T. L., Parry, G. W., Ramey-Smith, A. M., Rubin, M. P., and Thadani, A. C. An approach for using risk assessment in risk-informed decisions on plant-specific changes to the licensing basis. *Reliability Engineering & System Safety*, 63(3):231–242, 1999.
- [122] Davoli, P. Principles of current methodologies in high-cycle fatigue design of metallic structures. In *High-Cycle Metal Fatigue*, pages 1–56. Springer, 1999.

-
- [123] Smith, K. N., Watson, P., and Topper, T. A stress-strain function for the fatigue of metals. *Journal of Materials*, 5:767–778, 1970.
- [124] Ince, A. and Glinka, G. A modification of Morrow and Smith–Watson–Topper mean stress correction models. *Fatigue & Fracture of Engineering Materials & Structures*, 34(11):854–867, 2011.
- [125] Sines, G. Failure of materials under combined repeated stresses with superimposed static stresses. Technical report, California. Univ., Los Angeles, 1955.
- [126] Sines, G. Behavior of metals under complex static and alternating stresses. *Metal Fatigue*, 1:145–169, 1959.
- [127] Crossland, B. Effect of large hydrostatic pressures on the torsional fatigue strength of an alloy steel. In *Proc. Int. Conf. on Fatigue of Metals*, volume 138, page 12. Institution of Mechanical Engineers London, 1956.
- [128] You, B.-R. and Lee, S.-B. A critical review on multiaxial fatigue assessments of metals. *International Journal of Fatigue*, 18(4):235–244, 1996.
- [129] Papadopoulos, I. V. Critical plane approaches in high-cycle fatigue: on the definition of the amplitude and mean value of the shear stress acting on the critical plane. *Fatigue & Fracture of Engineering Materials & Structures*, 21(3):269–285, 1998.
- [130] Findley, W., Coleman, J., and Hanley, B. Theory for combined bending and torsion fatigue with data for SAE 4340 steel. Technical report No. 1 on basic research on fatigue failures under combined stress. Technical report, Brown Univ., Providence. Engineering Materials Research Lab., 1956.
- [131] Mataka, T. An explanation on fatigue limit under combined stress. *Bulletin of JSME*, 20(141):257–263, 1977.
- [132] Siebel, E. and Stieler, M. Ungleichförmige Spannungsverteilung bei schwingender Beanspruchung. *VDI-Zeitschrift*, 97(5):121–126, 1955.
- [133] Norberg, S. and Olsson, M. The effect of loaded volume and stress gradient on the fatigue limit. *International Journal of Fatigue*, 29(12):2259–2272, 2007.
- [134] Neuber, H. *Theory of notch stresses: principles for exact calculation of strength with reference to structural form and material*, volume 4547. USAEC Office of Technical Information, 1961.
- [135] Taylor, D. Geometrical effects in fatigue: a unifying theoretical model. *International Journal of Fatigue*, 21(5):413–420, 1999.
- [136] Bellett, D., Taylor, D., Marco, S., Mazzeo, E., Guillois, J., and Pircher, T. The fatigue behaviour of three-dimensional stress concentrations. *International journal of Fatigue*, 27(3):207–221, 2005.
- [137] Peterson, R. E. Notch sensitivity. *Metal fatigue*, pages 293–306, 1959.

- [138] Kuguel, R. A relation between theoretical stress concentration factor and fatigue notch factor deduced from the concept of highly stressed volume. In *Proc. ASTM*, volume 61, pages 732–748, 1961.
- [139] Sonsino, C. Zur Bewertung des Schwingfestigkeitsverhaltens von Bauteilen mit Hilfe örtlicher Beanspruchungen. *Konstruktion (1981)*, 45(1):25–33, 1993.
- [140] Van Hooreweder, B., Moens, D., Boonen, R., and Sas, P. Fatigue strength analysis of notched aluminium specimens using the highly stressed volume method. *Fatigue & Fracture of Engineering Materials & Structures*, 35(2):154–159, 2012.
- [141] Ai, Y., Zhu, S., Liao, D., Correia, J., Souto, C., De Jesus, A., and Keshtegar, B. Probabilistic modeling of fatigue life distribution and size effect of components with random defects. *International Journal of Fatigue*, 126:165–173, 2019.
- [142] Baddeley, A., Gregori, P., Mateu, J., Stoica, R., and Stoyan, D. *Case studies in spatial point process modeling*, volume 185. Springer, 2006.
- [143] Babuška, I., Sawlan, Z., Scavino, M., Szabó, B., and Tempone, R. Spatial Poisson processes for fatigue crack initiation. *Computer Methods in Applied Mechanics and Engineering*, 345:454–475, 2019.
- [144] Zok, F. W. On weakest link theory and Weibull statistics. *Journal of the American Ceramic Society*, 100(4):1265–1268, 2017.
- [145] Sjödin, B. A non-local theory for the assessment of multiaxial high cycle fatigue failure. In *Proceedings of the 1998 International Gas Turbine & Aeroengine Congress & Exhibition, Stockholm, Sweden*. Citeseer, 1998.
- [146] Lanning, D. B., Nicholas, T., and Palazotto, A. HCF notch predictions based on weakest-link failure models. *International Journal of Fatigue*, 25(9-11):835–841, 2003.
- [147] Gaenser, H.-P. Some notes on gradient, volumetric and weakest link concepts in fatigue. *Computational materials science*, 44(2):230–239, 2008.
- [148] Bomas, H., Linkewitz, T., and Mayr, P. Application of a weakest-link concept to the fatigue limit of the bearing steel SAE 52100 in a bainitic condition. *Fatigue & Fracture of Engineering Materials & Structures*, 22(9):733–741, 1999.
- [149] Weibull, W. A statistical theory of strength of materials. *Swedish Inst Eng Res.*, 151:1–45, 1939.
- [150] Weibull, W. A Statistical Distribution Function of Wide Applicability. *Journal of applied mechanics*, 103(730):293–297, 1951.
- [151] Heckel, K., Köhler, J., and München, T. Experimentelle Untersuchung des statistischen Größeneinflusses im Dauerschwingversuch an ungekerbten Stahlproben. *Materialwissenschaft und Werkstofftechnik*, 6(2):52–54, 1975.
- [152] Böhm, J. and Heckel, K. Die Vorhersage der Dauerschwingfestigkeit unter Berücksichtigung des statistischen Größeneinflusses. *Materialwissenschaft und Werkstofftechnik*, 13(4):120–128, 1982.

-
- [153] Schweiger, G., Lowak, H., and Heckel, K. Über die Abschätzung des Größeneinflusses bei unregelmäßig beanspruchten Bauteilen. *Materialwissenschaft und Werkstofftechnik*, 16(2):39–44, 1985.
- [154] Krä, C. *Beschreibung des Lebensdauerverhaltens gekerbter Proben unter Betriebsbelastung auf der Basis des statistischen Größeneinflusses*. PhD thesis, Universität der Bundeswehr München, 1988.
- [155] Scholz, F. Untersuchungen zum statistischen Größeneinfluß bei mehrachsiger Schwingbeanspruchung. *VDI Reihe*, 18(50), 1988.
- [156] Liu, J. and Zenner, H. Berechnung von Bauteilwöhlerlinien unter Berücksichtigung der statistischen und spannungsmechanischen Stützziffer. *Materialwissenschaft und Werkstofftechnik*, 26(1):14–21, 1995.
- [157] Hudak Jr, S., Chell, G., Slavik, D., Nagy, A., and Feiger, J. Influence of notch geometry on high cycle fatigue threshold stresses in Ti-6Al-4V. In *Proceedings of the 6th National Turbine Engine High Cycle Fatigue (HCF) Conference, Jacksonville, Florida*, 2001.
- [158] Schnack, S. and Kienzler, R. Calculation of the fatigue limit of pulsed laser hardened specimen based on an engineering interpretation of the weakest-link concept. *Engineering Fracture Mechanics*, 71(4-6):779–787, 2004.
- [159] Wormsen, A. and Härkegård, G. A statistical investigation of fatigue behaviour according to Weibull’s weakest link theory. In *ECF15, Stockholm 2004*, 2004.
- [160] Wormsen, A. and Härkegård, G. Weibull fatigue analysis of notched components under constant and variable amplitude loading. In *Proceedings of the International Fatigue Congress 2006*. Elsevier Atlanta, Georgia, USA, 2006.
- [161] Wormsen, A., Härkegård, G., and Huth, H. Probabilistic fatigue assessment of a hydro-turbine blade model. In *Proceedings of the International Fatigue Congress Atlanta, USA*, 2006.
- [162] Norberg, S. Prediction of the fatigue limit: accuracy of post-processing methods. Licentiate thesis, KTH, 2006.
- [163] Karlén, K. and Olsson, M. Experimental and statistical investigation of the weakest link integral and the volume effect. *Procedia Engineering*, 2(1):1451–1457, 2010.
- [164] Karlén, K. and Olsson, M. A probabilistic model for the entire HCF domain based on equivalent stress-simulations and experiments. *International Journal of Fatigue*, 36(1):9–17, 2012.
- [165] Karlén, K., Olsson, M., Ahmadi, H., and Härkegård, G. On the effect of random defects on the fatigue notch factor at different stress ratios. *International Journal of Fatigue*, 41:179–187, 2012.
- [166] Karlén, K. *Probabilistic modeling of fatigue failures*. PhD thesis, KTH Royal Institute of Technology, 2012.

- [167] Sadek, S., Sandberg, D., and Olsson, M. FE-mesh effect of the volume based weakest-link fatigue probability applied to a compressor blade. In *ASME Turbo Expo 2012: Turbine Technical Conference and Exposition*, pages 427–438. American Society of Mechanical Engineers Digital Collection, 2012.
- [168] Sadek, S. and Olsson, M. New models for prediction of high cycle fatigue failure based on highly loaded regions. *International Journal of Fatigue*, 66:101–110, 2014.
- [169] Sandberg, D. and Olsson, M. On the optimal choice of experiments for determination of parameters in multiaxial HCF-criteria. *International Journal of Fatigue*, 61:315–324, 2014.
- [170] Grover, H. J., Bishop, S. M., and Jackson, L. R. Fatigue strengths of aircraft materials: axial-load fatigue tests on unnotched sheet specimens of 24S-T3 and 75S-T6 aluminum alloys and of SAE 4130 steel. *NACA Technical Note 2324*, 1951.
- [171] Grover, H. J., Hyler, W. S., and Jackson, L. R. Fatigue strengths of aircraft materials: axial-load fatigue tests on notched sheet specimens of 24S-T3 and 75S-T6 aluminum alloys and of SAE 4130 steel with stress-concentration factor of 1.5. *NACA Technical Note 2639*, 1952.
- [172] Grover, H. J., Bishop, S. M., and Jackson, L. R. Fatigue strengths of aircraft materials: axial-load fatigue tests on notched sheet specimens of 24S-T3 and 75S-T6 aluminum alloys and of SAE 4130 steel with stress-concentration factor of 5.0. *NACA Technical Note 2390*, 1951.
- [173] Grover, H. J., Bishop, S. M., and Jackson, L. R. Fatigue strengths of aircraft materials: axial-load fatigue tests on notched sheet specimens of 24S-T3 and 75S-T6 aluminum alloys and of SAE 4130 steel with stress-concentration factors of 2.0 and 4.0. *NACA Technical Note 2389*, 1951.
- [174] Chemical composition of SAE-4130. <https://www.astmsteel.com/product/4130-steel-aisi-25crmo4-7218-scm430/>. Accessed: 2020-07-01.
- [175] Heimerl, G. J. and Inge, J. E. Tensile properties of 7075-T6 and 2024-T3 aluminum-alloy sheet heated at uniform temperature rates under constant load. *NACA Technical Note 3462*, 1955.
- [176] Chemical composition of AL2024-T3. <http://asm.matweb.com/search/SpecificMaterial.asp?bassnum=MA2024T4>. Accessed: 2020-07-01.
- [177] Chemical composition of AL7075-T6. <http://asm.matweb.com/search/SpecificMaterial.asp?bassnum=MA7075T6>. Accessed: 2020-07-01.
- [178] Teuber, H., Barnikel, J., Dankert, M., David, W., Ghicov, A., and Voss, S. Development of a New High-Strength Steel for Low Pressure Steam Turbine End-Stage Blades. In *Turbo Expo: Power for Land, Sea, and Air*, volume 51173. American Society of Mechanical Engineers, 2018.
- [179] Klawonn, A., Hagenacker, A., and Beck, T. A probabilistic Haigh diagram based on a weakest link approach. *International Journal of Fatigue*, 133(105419), 2019.

-
- [180] Klawonn, A. and Beck, T. Efficient staircase testing of probabilistic Haigh diagrams. *International Journal of Fatigue*, 137(105627), 2020.
- [181] Klawonn, A. and Beck, T. A probabilistic haigh diagram for notched components considering notch root plasticity due to high mean stresses. *International Journal of Fatigue*, 140(105813), 2020.
- [182] Marin, J. Interpretation of fatigue strengths for combined stresses. In *Proceedings of International Conference on Fatigue of Metals*, pages 184–194, 1956.
- [183] Karlén, K. and Olsson, M. A study of the volume effect and scatter at the fatigue limit—experiments and computations for a new specimen with separated notches. *International Journal of Fatigue*, 33(3):363–371, 2011.
- [184] Meeker, W. Q. and Escobar, L. A. *Statistical methods for reliability data*. John Wiley & Sons, 2014.
- [185] Susmel, L. and Lazzarin, P. A bi-parametric Wöhler curve for high cycle multiaxial fatigue assessment. *Fatigue & Fracture of Engineering Materials & Structures*, 25(1):63–78, 2002.
- [186] Susmel, L. A unifying approach to estimate the high-cycle fatigue strength of notched components subjected to both uniaxial and multiaxial cyclic loadings. *Fatigue & Fracture of Engineering Materials & Structures*, 27(5):391–411, 2004.
- [187] Bernasconi, A. and Papadopoulos, I. Efficiency of algorithms for shear stress amplitude calculation in critical plane class fatigue criteria. *Computational Materials Science*, 34(4):355–368, 2005.
- [188] Golub, G. H. and Welsch, J. H. Calculation of Gauss quadrature rules. *Mathematics of computation*, 23(106):221–230, 1969.
- [189] Mitrinovic, D. S. and Vasic, P. M. *Analytic inequalities*, volume 61. Springer, 1970.
- [190] Lukáš, P., Kunz, L., and Svoboda, M. High cycle fatigue of superalloy single crystals at high mean stress. *Materials Science and Engineering: A*, 387:505–510, 2004.
- [191] Golub, V., Krizhanovskii, V., Pogrebnyak, A., and Romanov, A. A method of modeling the interaction of creep and high-cycle fatigue. *International Applied Mechanics*, 41(1):14–23, 2005.
- [192] Wright, J., Carroll, L., Sham, T.-L., Lybeck, N., and Wright, R. Determination of the creep-fatigue interaction diagram for Alloy 617. In *ASME 2016 Pressure Vessels and Piping Conference*. American Society of Mechanical Engineers Digital Collection, 2016.
- [193] Courtney, T. H. *Mechanical behavior of materials*. Waveland Press, 2005.
- [194] Draper, D. Assessment and propagation of model uncertainty. *Journal of the Royal Statistical Society: Series B (Methodological)*, 57(1):45–70, 1995.
- [195] Efron, B. and Tibshirani, R. J. *An introduction to the bootstrap*. CRC press, 1994.

-
- [196] Hastings, W. K. Monte Carlo sampling methods using Markov chains and their applications. *Biometrika*, 57:97–109, 1970.
- [197] Rosenthal, J. S. et al. Optimal proposal distributions and adaptive MCMC. *Handbook of Markov Chain Monte Carlo*, 4(10.1201), 2011.
- [198] Susmel, L. and Tovo, R. Estimating fatigue damage under variable amplitude multi-axial fatigue loading. *Fatigue & Fracture of Engineering Materials & Structures*, 34(12):1053–1077, 2011.

List of Figures

1.1	Schematic illustration emphasizing the statistical nature of the HCF-relevant compressor blade loading and its fatigue strength with respect to a given vibration mode.	2
1.2	Schematic illustration of a deterministic and a probabilistic Haigh diagram.	4
2.1	Gas turbine (SGT-800) containing a 15-stage compressor [49].	7
2.2	Generic Campbell diagram used for the design of compressor blades.	8
2.3	On the scatter in the blade response in terms of the hot-spot stress between different compressor blades of the same stage (blade-to-blade scatter) and repeated resonance events (event-to-event scatter). Typically the former is considerably greater than the latter.	9
2.4	On the used terminology in the context of cyclic stresses.	10
2.5	On the different phases of fatigue life in metals, taken from [14].	14
2.6	On the location of the critical fatigue crack for materials with a conventional fatigue limit (first plateau of the shown SN -curves), taken from [22].	15
2.7	On the initiation process of surface cracks due to cyclic loading, taken from [23]. The smooth surface in the initial state (a) is successively roughening (b) until the first persistent slip bands form (c).	16
2.8	Typical fracture surface of a fish-eye crack, which formed at a non-metallic inclusion within a cylindrical test specimen of steel SNCM439, taken from [55].	17
2.9	A typical SN -diagram (a) with Basquin fits for different aluminum alloys, taken from [74], and a Haigh diagram (b) for a titanium alloy, taken from [53].	22
2.10	Haigh diagram with graphs representing the empirical formulas of Goodman [77], Soderberg [78] and Gerber [79].	23
2.11	On the extrapolation method to derive a Haigh diagram from SN -curves.	25
2.12	On the test schemes used in the probit method [90] and the staircase method [43] in order to determine the fatigue strength distribution.	27
2.13	The concept of the local design approach using the hot-spot stresses in combination with a Haigh diagram. In this case, the design would be accepted since the hot-spot stresses indicated by the cross lie within the design bounds represented by the dashed line.	33
2.14	On the weakest-link concept.	38
4.1	Available fatigue test data on SAE-4130 in a nominal Haigh plane ($N_{\text{ref}} = 5 \cdot 10^6$).	44
4.2	Overview of used test sheet specimen geometries for NACA test data, cf. [170–173]. Dimensions are given in mm (original values are given in inches). R denotes the notch radius.	45
4.3	Available fatigue test data on AL2024-T3 in a nominal Haigh plane ($N_{\text{ref}} = 5 \cdot 10^6$).	46
4.4	Available fatigue test data on AL7075-T6 in a nominal Haigh plane ($N_{\text{ref}} = 5 \cdot 10^6$).	47

4.5	Plot (a) shows the static nominal stress-strain curves at room temperature for both considered materials taken from page 31 in [175]. Plot (b) shows the derived relationship of true stress over true plastic strain. Note that the stresses on the vertical axis are normalized to the respective value of σ_{UTS} , see Table 4.3.	48
4.6	Available fatigue test data on PH12-10Mo in a nominal Haigh plane ($N_{\text{ref}} = 10^8$).	49
4.7	Overview of cylindrical test specimen geometries for Siemens test data. Note that only the relevant test gauge is shown, i.e. no clamping structure. Dimensions are stated in mm.	49
5.1	Probabilistic unit Haigh diagram for unit domain Ω_1 . The function of the Weibull scale, representing the $1 - 1/e \approx 63\%$ percentile, is determined by the axis intercepts $\hat{\sigma}_e$, $\hat{\sigma}_m$ and the curvature n . The scatter, on the other hand, is defined by the constant shape parameter k	51
5.2	On the interpretation of specimens that failed (a) and specimens that survived (b) in a constant-amplitude fatigue test with respect to the censored fatigue strength information.	56
5.3	On the comparison between the probabilistic unit Haigh diagram and other mean stress models in a weakest-link context. The solid lines represent scale functions ($P_f \approx 63\%$), while the dashed lines in (a)-(c) depict the $P_f = 0.05$ and $P_f = 0.95$ quantile lines respectively. The diagrams in (d)-(e) illustrate the influence of central parameters on the respective scales.	58
5.4	On the resulting median lines in the probabilistic design Haigh diagram for three different equivalent mean stress models and integration domains at a fixed model parameter vector θ . The equivalent stress amplitude is in all cases von Mises. Plot (a) shows the evaluation for a cylindrical and plot (b) for a sheet specimen. The unit domain was set to $\text{vol}(\Omega_1) = \text{vol}(\Omega_C)$	61
5.5	On the comparison between von Mises, maximum principal and hydrostatic stress models according to Eqs. (5.20)-(5.22). The black marker at (0,0,1) corresponds to uniaxial conditions, and is merely included for orientation. Note the different scales on the vertical axis.	62
5.6	On the comparison between von Mises, maximum principal and hydrostatic stress models according to Eqs. (5.20)-(5.22) under plane-stress conditions ($\alpha_3 = 0$).	63
5.7	On the transformation Φ mapping between a brick element's reference geometry Ω_i^{ref} and the actual element geometry $\Omega_i = \Phi(\Omega_i^{\text{ref}})$ as it is found in the finite element mesh.	66
5.8	On the stress fields considered in the analysis of the quadrature error.	71
5.9	The relative quadrature error ε_{I_i} of the weakest-link integral I_i for a single brick element $[0, 1]^3$ over the number of Gaussian integration points n_{ip} in one dimension (hence, n_{ip}^3 integration points per element), cf. Eq. (5.41). The two columns refer to the scatter parameter $k \in \{20, 40\}$, while the rows correspond to different mean stress levels in the notch root. The green area indicates errors below machine precision, which was $\text{eps} = 2.22 \cdot 10^{-16}$, while the red area represents relative errors above 1%.	72

5.10	The three notched cylindrical coupons used in the analysis with $n_{\text{res}} = 10$ elements on the half-notch arc. Due to symmetry reasons, only the upper half section was modeled. The coupon radius was set to 15 mm while the shown half-length was defined as 20 mm.	74
5.11	On the influence of the mesh resolution n_{res} on the computed failure probability P_f . All results were computed using an adaptive quadrature scheme, eliminating quadrature errors. Compare with Fig. 5.10 for the considered coupon geometries in each row of subplots.	77
5.12	On the difference between $\tilde{\sigma}_{a,1}^{\text{nom}}$ and $\tilde{\sigma}_{a,1}^{\text{crit}}$. The shown case refers to the averaged nodal von Mises stresses in the notch root section for specimen type (a) from Fig. 5.10. Note that $n_{\text{res}}^{\text{max}}$ refers to $n_{\text{res}} = 60$ in this analysis.	78
5.13	On the combined influence of the mesh resolution n_{res} and the number of integration points n_{ip} on the computed failure probability P_f	79
5.14	Used test data for all three specimen types of all three materials from NACA reports, cf. [170–172]. The stresses σ_m^{crit} and σ_a^{crit} refer to the von Mises mean stress and stress amplitude in the notch root respectively.	82
5.15	Used finite element meshes for the fitting procedure including a contour plot of the von Mises stress field resulting from a tensile stress applied at the specimen top.	84
5.16	Calibration and prediction results for low-alloy steel SAE-4130 at $N_{\text{ref}} = 5 \cdot 10^6$ together with test data. The values on both axes refer to normalized von Mises stresses.	86
5.17	Calibration and prediction results for aluminum alloy AL2024-T3 at $N_{\text{ref}} = 5 \cdot 10^6$ together with test data. The values on both axes refer to normalized von Mises stresses.	87
5.18	Calibration and prediction results for aluminum alloy AL7075-T6 at $N_{\text{ref}} = 5 \cdot 10^6$ together with test data. The values on both axes refer to normalized von Mises stresses. The red-marked test in the right plot was not included in the computation of $\mathcal{L}(\theta_{\text{opt}}, \mathcal{T}_{\text{pred}})$ in Table 5.4.	88
5.19	On the separability of test data in the Haigh plane.	91
5.20	Test data for the NACA1 and NACA2(A) specimen geometry [170, 171] together with median lines and scatter band of the two probabilistic design Haigh diagrams. The respective model fit, which is defined as the true model in this study, is stated in the upper right corner.	94
5.21	Flowchart of a staircase test program using a combination of smooth and notched specimen geometries, cf. Alg. 1. After the test program is finished the results can be used to fit the model vector θ , see Section 5.1.1.	96
5.22	On the setup of the simulated staircase tests. The plot schematically shows a staircase test scheme conducted for one of the considered mean stress levels and one geometry. All shown tests refer to the same mean stress. Note that the depicted staircase steps have constant step size, while in the simulations a variable step size was used, cf. Eq. (5.49).	98
5.23	Influence of specimen geometry on parameter estimates. True median initial stresses and a medium step size of $s = 8\%$ have been used. A corresponding numerical representation in terms of different percentiles can be found in Table 5.7.	100

5.24	Influence of number of mean stress levels on parameter estimates. True median initial stresses and a medium step size of $s = 8\%$ have been used. A corresponding numerical representation in terms of different percentiles can be found in Table 5.8.	101
5.25	Influence of initial stresses and step size on parameter estimates. In all cases, 5 mean stress levels, i.e. $5 \times (5 + 4)$ have been used. The initial stress amplitudes were derived with Eq. (5.51). A corresponding numerical evaluation can be found in Table 5.9.	102
5.26	On the sensitivity of the median component fatigue strength $\sigma_{a,50\%}^{\text{notch}}$ at zero mean stress with respect to a perturbation in the fatigue strength scale parameter $\hat{\sigma}_e$ and shape parameter k respectively.	105
5.27	(a) Static nominal stress-strain curves at room temperature for both considered materials taken from page 31 in [175] (b) The derived relationship of true stress over true plastic strain. Note that all stresses are normalized to the respective value of σ_{UTS} , see Table 5.11.	109
5.28	Top view on the used finite element mesh for specimen NACA2A. Additionally the von Mises contour plots for both the mean stress and stress amplitude field, cf. Eqs. (5.56) and (5.57), resulting from a high σ_m^{nom} low σ_a^{nom} loading are shown.	111
5.29	On the determination of a p -quantile line in the nominal Haigh plane for a considered specimen geometry G based on a given model vector θ . Here, $\varepsilon = 5 \cdot 10^{-3}$ was used.	113
5.30	Calibration and prediction results for AL7075-T6 at $N_{\text{ref}} = 5 \cdot 10^6$ with respect to three different effective mean stress functions. The test data from the first two plots (gray background) was used for the model calibration with $V_1 = 16.4 \text{ cm}^3$ resulting in the parameter values given at the top. The remaining plots show pure predictions based on these calibrations.	115
5.31	Calibration and prediction results for AL2024-T3 at $N_{\text{ref}} = 5 \cdot 10^6$ with respect to three different effective mean stress functions. The test data from the first two plots (gray background) was used for the model calibration with $V_1 = 16.4 \text{ cm}^3$ resulting in the parameter values given at the top. The remaining plots show pure predictions based on these calibrations.	118
5.32	Comparison of linear-elastic and elasto-plastic failure predictions for NACA4A and NACA4B of AL2024-T3 using the von Mises effective mean stress function. The quantile lines of the elasto-plastic predictions are the same as those shown in Fig. 5.31. The quantile lines referring to the elastic model resulted from a fit to NACA1 and NACA2A test data while only using linear-elastic stress field solutions (no plasticity model). The linear-elastic fit resulted in the model parameters $\hat{\sigma}_e = 0.278$, $\hat{\sigma}_m = 2.123$, $n = 0.772$ and $k = 20.919$	122
5.33	Design Haigh diagrams for cylindrical specimens CS6, CN5 and CN1 of material PH12-10Mo, see Section 4.4. The underlying unit Haigh diagram for $V_1 = 1 \text{ cm}^3$ was fitted to the combined test data for $N_{\text{ref}} = 1 \cdot 10^8$, see Eq. (5.60). The annotation “ss” in the left subplot refers to two specimens that survived N_{ref} cycles under similar nominal stress conditions.	125

5.34	Visual comparison of the model fits between with $N_{\text{ref}} = 10^8$ for different mean stress models and effective mean stress functions, see also Table 5.14. The shaded areas always correspond to the area between the 0.05- and 0.95-quantile lines.	127
5.35	Parameter histograms of Θ_s^{BS} and Θ_s^{MCMC} generated using parametric bootstrapping (BS) and Markov chain Monte Carlo sampling (MCMC) respectively.	132
5.36	Unit Haigh diagram based on the original maximum likelihood fit (mle), compared with the model uncertainty adjusted unit Haigh diagrams based on parametric bootstrapping (BS) and Markov chain Monte Carlo sampling (MCMC) respectively. Each model is represented by a scale function and a corresponding scatter parameter given in the box on the bottom-left.	132
5.37	Design Haigh diagrams for CS6, CN5 and CN1 based on the original maximum likelihood fit and model uncertainty adjustments based on Markov chain Monte Carlo sampling (MCMC) and bootstrapping.	133
6.1	The full finite element section model including the disk and the blade. . .	138
6.2	The three considered finite element meshes of the analyzed compressor blade.	138
6.3	The first three compressor blade eigenmodes at $f = 30$ Hz.	139
6.4	Model uncertainty adjusted unit Haigh diagram (bootstrapping) of PH12-10Mo, see Section 5.7, and the translation to the design Haigh diagrams for the three compressor blade modes shown in Fig. 6.3. Note that the mean stress axis is parameterized with the rotor speed.	140
6.5	On the influence of the mesh resolution and the number of integration points on the median lines ($P_f = 50\%$) of the probabilistic Haigh diagram for each of the three modes.	141
6.6	The failure probability of a single compressor blade for mode 1 vibrations, occurring at $f = 30$ Hz for engine order 8 (EO8). The cumulative distribution function shown in the right diagram is a Weibull distribution with the stated scale and shape. It corresponds to the distribution associated with the dashed black line from the left plot.	142
6.7	Probability of failure for a compressor row with $N_b = 48$ blades as a function of the resonance response distribution of the blades. In this plot it was assumed that $P_f = 0.1\%$ was the accepted stage risk.	144

List of Tables

4.1	Chemical composition of SAE-4130 (typical values taken from [174]). . . .	44
4.2	Summary of used test data for SAE-4130. The stated K_t is derived from FE-calculations and refers to the von Mises stress. The number in parentheses given in the column with the number of tests (#Tests) states the number of runouts with respect to $N_{\text{ref}} = 5 \cdot 10^6$ cycles. For example, 48 tests with specimen NACA 1 were used, 11 of which collected more than $5 \cdot 10^6$ load cycles.	44
4.3	Tensile strength (σ_{UTS}), 0.2% yield strength (σ_{YS}) and Young's modulus (E) in rolling direction of the base sheets of the three materials considered in the NACA test campaigns. Note that the stated Young's modulus for SAE-4130 refers to compression, as it was not given as a tensile property in the reports.	46
4.4	Chemical composition of AL2024-T3 (typical values taken from [176]). . .	46
4.5	Summary of used test data for AL2024-T3, cf. Table 4.2.	46
4.6	Summary of used test data for AL7075-T6, cf. Table 4.2.	47
4.7	Chemical composition of AL7075-T6 (typical values taken from [177]). . .	48
4.8	Chemical composition of PH12-10Mo (average values), cf. [178].	48
4.9	Summary of available test data (Siemens) for PH12-10Mo. The stated K_t is derived from FE-calculations and refers to the von Mises stress. The number in parentheses given in the column with the number of tests (#Tests) states the number of runouts ($N_f > 10^8$). For example, 26 tests with specimen CS6 are available, 6 of which were runouts.	49
5.1	Overview of used test data for each material and specimen type. The numbers in parentheses state the number of runouts as stated in the NACA reports. For example: 51 data points of the NACA1 type for SAE-4130 were analyzed, 14 of which were runouts.	83
5.2	Comparison between different mean stress models and effective mean stress functions with respect to the calibration/prediction results for SAE-4130 shown in Fig. 5.16.	86
5.3	Comparison between different mean stress models and effective mean stress functions with respect to the calibration/prediction results for AL2024-T3 shown in Fig. 5.17.	87
5.4	Comparison between different mean stress models and effective mean stress functions with respect to the calibration/prediction results for AL7075-T6 shown in Fig. 5.18.	89
5.5	Comparison of model fits for the original data set (column σ_{UTS}) with fits based on test data corresponding to fully elastic material behavior (column σ_{YS}). The third row (#) states the total number of data points in the corresponding data set.	90
5.6	Total specimen volumes V based on the dimensions given in Fig. 5.20 and stress concentration factors K_t (based on finite element analyses of the considered specimen geometries.	94

5.7	Influence of specimen geometry on parameter estimates. The given quantiles refer to the histograms presented in Fig. 5.23. The relative numbers in the $Q_{.05}$ and $Q_{.95}$ columns correspond to the respective $Q_{.5}$ value, while the numbers in parenthesis in the first column denote the true parameter values, cf. Eq. (5.48).	100
5.8	Influence of number of mean stress levels on parameter estimates. The given quantiles refer to the histograms presented in Fig. 5.24. The relative numbers in the $Q_{.05}$ and $Q_{.95}$ columns correspond to the respective $Q_{.5}$ value, while the numbers in parenthesis in the top row denote the true parameter values, cf. Eq. (5.48).	101
5.9	Influence of initial stresses and step size on parameter estimates. The given quantiles refer to the histograms presented in Fig. 5.25. The relative numbers in the $Q_{.05}$ and $Q_{.95}$ columns correspond to the respective $Q_{.5}$ value, while the numbers in parenthesis in the top row denote the true parameter values, cf. Eq. (5.48).	103
5.10	Numerical evaluation of the sensitivity parameter κ_{12} for different combinations of specimen geometries, cf. Eq. (5.53).	106
5.11	Relevant material parameters for the two aluminum alloys, cf. [170, 175].	109
5.12	Comparison between different general mean stress models and effective mean stress functions with respect to the calibration/prediction results for AL7075-T6, cf. Fig. 5.30.	120
5.13	Comparison between different general mean stress models and effective mean stress functions with respect to the calibration/prediction results for AL2024-T3, cf. Fig. 5.31.	121
5.14	Comparison between different mean stress models in combination with different effective mean stress functions with respect to the calibration for PH12-10Mo shown in Fig. 5.33. The asterisk symbol * refers to values that had to be censored due to the use of Siemens data.	126

The author

Personal Data

Name	Mark Alexander Klawonn
Place of birth	Hagen, Germany
Nationality	German

Education

2014 – 2018	B.Sc. Mathematics, FernUniversität Hagen <ul style="list-style-type: none">• Specialized in Analysis and Numerics• Bachelor Thesis: “Spectral comparison of the standard Laplacian on equilateral finite metric graphs subjected to Kirchhoff and Anti-Kirchhoff vertex conditions”
2012 – 2014	M.Sc. Aerospace Engineering, RWTH Aachen <ul style="list-style-type: none">• Specialized in Aeronautics and Structure Dynamics• Master Thesis: “Analysis of aerodynamic nonlinearities on a 2D wind tunnel profile-model with movable control surface in transsonic flow”
2008 – 2012	B.Sc. Mechanical Engineering, RWTH Aachen <ul style="list-style-type: none">• Specialized in Aerospace Engineering• Bachelor Thesis: “Investigation of the interaction between wind-tunnel flow and a half-wing model based on wavelet time-frequency analysis”

Professional experience

2018 – 2021	PhD Researcher, Siemens (Energy) AG, Mülheim a. d. Ruhr <ul style="list-style-type: none">• Probabilistic treatment of high cycle loading phenomena
2014 – 2017	Research Associate, German Aerospace Center (DLR), Göttingen <ul style="list-style-type: none">• Dynamic simulation of wind turbines (loads and stability)
2011 – 2012	Intern, Airbus, Flaps and Leading Edge Movables, Bremen